

Dissertation zur Erlangung des Doktorgrades
der Fakultät für Chemie und Pharmazie
der Ludwig-Maximilians-Universität München

Nanostructured Iridium Oxide Electrocatalysts for PEM Electrolysis

Melisande Kost

aus

Attendorn, Deutschland

2025

Erklärung

Diese Dissertation wurde im Sinne von § 7 der Promotionsordnung vom 28. November 2011 von Herrn Prof. Dr. Thomas Bein betreut.

Eidesstattliche Versicherung

Diese Dissertation wurde eigenständig und ohne unerlaubte Hilfe bearbeitet.

München, den 21.03.2025

Melisande Kost

Dissertation eingereicht am 21.03.2025

1. Gutachter: Prof. Dr. Thomas Bein

2. Gutachter: Prof. Dr. Knut Müller-Caspary

Mündliche Prüfung am 12.06.2025

“May your dreams defy the laws of gravity.”

H. Jackson Brown Jr.

Abstract

In light of the growing demand for green and renewable energy, hydrogen has emerged as a promising energy carrier for the near future. Given its extensive range of applications, from basic chemical synthesis feedstock source to re-electrification with a fuel cell, the demand for green hydrogen is anticipated to grow significantly in the future.

This thesis presents a number of projects that facilitate the efficient conversion of electrical energy to chemical energy with the acidic proton exchange membrane electrolysis of water for the purpose of efficiently producing hydrogen. The aforementioned approaches place an emphasis on sustainability with respect to the materials utilized, or alternatively, demonstrate a significant reduction in the consumption of rare and non-abundant iridium metal, which serves as the active component of the employed catalysts. The synthesized materials were subjected to extensive examination with regard to their performance and stability through the utilization of a range of physical analytical techniques, including electrochemistry ranging from static wet-cell experiments to single cell electrolyzers, X-ray diffraction, X-ray photoelectron spectroscopy, and electron microscopy techniques. The overarching theme that emerges from this work is the impact of nanostructuring materials on their catalytic performance.

In the initial project discussed in this thesis, a SnO_2 filament morphology was electrospun and wet-chemically coated with $\text{IrO}(\text{OH})_x$ to create a composite material that acts as a catalyst for the oxygen evolution reaction. The filaments were oxidized at varying temperatures in air to ascertain the optimal temperature range for achieving high interconnectivity and crystallization of the IrO_2 layer, which resulted in enhanced conductivities and associated activities compared to the non-oxidized compound by establishing percolation pathways for electrons. Transmission electron microscopy was employed to elucidate the macroscopic processes undergone by iridium oxide at varying temperatures. An optimal temperature of 375 °C was identified, at which the interconnectivity and crystallinity were in an optimal state. At lower temperatures, the degree of crystallinity was insufficient for optimal conductivity and activity in the context of catalysis. Conversely, at higher temperatures, the increased degree of crystallinity and formation of larger crystallites resulted in the formation of isolated IrO_2

crystallites on the filament. This resulted in a reduction of conductivity and, consequently, in a decline of catalytic activity.

In the subsequent project, the insights gained from the initial project were integrated, and the impact of nanostructuring the iridium oxide phase on catalytic behavior was further elucidated. Specifically, the stability of an epitaxial catalyst-support system in comparison to a non-epitaxial catalyst was investigated with regard to the oxygen evolution reaction in proton exchange membrane electrolysis. IrO₂ and SnO₂ were utilized, both of which possess highly similar lattice parameters and exhibit a proclivity for epitaxy. Conversely, IrO₂ on TiO₂, which predominantly comprised the anatase structure, renders epitaxy nearly impossible. The impact of firm anchoring and good contact, which arises from the epitaxial growth of IrO₂ on SnO₂, on the stability and activity of the catalyst was examined, particularly at lower iridium contents. Electrochemical experiments conducted with a corresponding membrane electrode assembly demonstrated enhanced activity in comparison to non-epitaxially grown IrO₂ layers on nanoparticulate TiO₂ with a comparable iridium content. Further in-depth and long-term measurements are required to validate enhanced stability.

In the final and concluding project of this thesis, an investigation was conducted into the potential for coating novel materials with IrO₂ through nanostructuring. An iridium oxide layer with a thickness of only a few atom layers was deposited on a highly crystalline silicified DNA origami architecture using atomic layer deposition (ALD). Furthermore, ZnO and TiO₂ were also deposited on pure (non-silicified) DNA origami. Scanning electron microscopy demonstrated the successful complete and homogeneous coating of the various compounds, penetrating fully into the DNA origami crystal structure and indicating consistent coverage.

Proof-of-principle experiments for an application in acidic water electrolysis indicate that this DNA origami-based system exhibits promising stability, as evidenced by post-catalytic scanning electron microscopy imaging. Promising prospective applications of this system may be achieved through the skillful engineering of DNA origami crystals with larger pores or a consistent crystal film growth on suitable substrates.

Furthermore, the nanostructuring of the material was achieved by coating the DNA origami with a thin IrO₂ layer to split water. This development has opened up new paths for the functionalization of the material, paving the way for potential applications in areas such as photonic crystals. In conclusion, this work has demonstrated that nanostructuring of diverse support materials represents a promising strategy for the development of low-iridium

containing catalysts for the oxygen evolution reaction in proton exchange membrane water electrolysis. These catalysts are distinguished by high activity and stability. An additional emphasis is placed on enabling synthesis methods such as a wet chemical process which yielded reproducible coating of semiconductor oxide supports on a range of solvent volumes producing catalysts from a few mg up to 5 g to establish electrolysis for producing green hydrogen to ultimately meet global energy demand. The comprehensive electrochemical and materials science characterization results enhance our understanding regarding the factors contributing to activity and stability of low-iridium water electrolysis catalysts. This enables the overcoming of morphological constraints, and subsequent studies based on this work can advance the understanding of energy conversion processes with the ultimate goal of further reducing the iridium content of oxygen evolution catalysts.

Content

1. INTRODUCTION	2
1.1. THE ROLE OF HYDROGEN IN A CARBON NEUTRAL ECONOMY.....	2
1.2. WATER ELECTROLYSIS.....	5
1.2.1. Principles of Water Electrolysis	5
1.2.2. Catalysis of the Oxygen Evolution Reaction.....	6
1.2.3. Proton Exchange Membrane Electrolyzers	10
1.3. IRIIDIUM OXIDE CATALYSTS FOR PEM ELECTROLYSIS.....	13
1.4. METAL OXIDE-SUPPORTS FOR PEM.....	14
1.4.1. Electrospinning of Metal Oxide Nanofibers	16
1.5. EPITAXY IN CATALYSIS.....	19
1.6. ATOMIC LAYER DEPOSITION	21
1.6.1. Atomic Layer Deposition of Iridium Oxide Thin Films.....	23
1.7. REFERENCES	25
2. CHARACTERIZATION	40
2.1. NITROGEN PHYSISORPTION MEASUREMENTS	41
2.2. THERMOGRAVIMETRIC ANALYSIS	43
2.3. X-RAY PHOTOELECTRON SPECTROSCOPY	44
2.4. X-RAY DIFFRACTION	47
2.5. SPECTROSCOPIC ELLIPSOMETRY	48
2.6. ELECTRON MICROSCOPY	50
2.6.1. Scanning Electron Microscopy	50
2.6.2. Energy-Dispersive X-Ray Spectroscopy	52
2.6.3. Transmission Electron Microscopy.....	53
2.7. 2-POINT CONDUCTIVITY MEASUREMENTS.....	55
2.8. ELECTROCHEMICAL ANALYSIS.....	57
2.8.1. Electrical Impedance.....	57
2.8.2. Cyclic Voltammetry	59
2.8.3. Chronopotentiometry	61
2.9. REFERENCES	63
3. OPTIMIZED OXIDATION TEMPERATURE ENHANCES OER PERFORMANCE OF IRO₂-LOADED SNO₂ NANOFIBERS – ROLE OF CHARGE CARRIER PERCOLATION PATHWAYS	67
3.1. INTRODUCTION	68
3.2. RESULTS AND DISCUSSION.....	70
3.3. CONCLUSION AND OUTLOOK	79
3.4. EXPERIMENTAL PART.....	80

3.5.	REFERENCES	83
3.6.	APPENDIX	87
4.	CHEMICAL EPITAXY OF IRIIDIUM OXIDE ON TIN OXIDE ENHANCES STABILITY OF SUPPORTED OER CATALYST.....	94
4.1.	INTRODUCTION	95
4.2.	RESULTS AND DISCUSSION	98
4.3.	CONCLUSION	110
4.4.	EXPERIMENTAL PART.....	111
4.5.	REFERENCES	118
4.6.	APPENDIX	126
5.	FABRICATION OF FUNCTIONAL 3D NANOARCHITECTURES USING ATOMIC LAYER DEPOSITION ON DNA ORIGAMI CRYSTALS	143
5.1.	INTRODUCTION	145
5.2.	RESULTS AND DISCUSSION	147
5.3.	CONCLUSION	157
5.4.	EXPERIMENTAL PART.....	158
5.5.	REFERENCES	166
5.6.	APPENDIX	171
6.	CONCLUSION	185
7.	PUBLICATIONS AND PRESENTATIONS	189
7.1.	PUBLICATIONS	189
7.2.	PRESENTATIONS	189
8.	CURRICULUM VITAE	192

CHAPTER 1

Introduction

1. Introduction

1.1. The Role of Hydrogen in a Carbon Neutral Economy

The pressing conundrum confronting our global community is the urgent imperative to address climate change. A potential solution emerges through transitioning to a carbon-neutral future, where the adaptable energy vector molecule, hydrogen, receives a pivotal role in reshaping our energy landscape. Hydrogen stands out for its transformative potential without emitting carbon dioxide during utilization, making it a promising clean energy carrier. To date, hydrogen is mostly produced from fossil resources with CO₂-intensive downstream processing by steam reforming.^{1, 2} As the call to reduce greenhouse gas emissions intensifies, hydrogen not only emerges as a versatile and clean energy carrier but also as a feedstock chemical with diverse applications across various sectors.^{3, 4}

In the transportation sector, hydrogen fuel cells provide a clean alternative to traditional internal combustion engines, powering vehicles with environmental sustainability in mind. Industries can leverage hydrogen as a feedstock for chemical and material production or utilize it in steel manufacturing processes. Moreover, hydrogen contributes to power generation through re-electrification with fuel cells, offering a stable and environmentally friendly source of electricity. In essence, hydrogen's versatility as both an energy carrier and a feedstock chemical positions it as a key player in the multifaceted challenge of reducing carbon emissions across diverse sectors, ushering in a cleaner and more sustainable energy era.⁵⁻⁷

One of the key advantages of hydrogen is its potential as a storage medium for renewable energy. The critical intermittency of solar and wind power depicted in Figure 1-1 can be mitigated by using excess energy to produce hydrogen during surplus periods and storing it for later use. This makes hydrogen a valuable asset in balancing fluctuations in renewable energy generation and ensuring a stable and reliable power supply.⁷ To achieve carbon neutrality, the focus has shifted to producing green hydrogen, generated using renewable energy sources, resulting in a truly carbon-neutral energy carrier. This green hydrogen holds immense potential for decarbonizing challenging-to-electrify industries such as steel and cement production.^{6, 8}

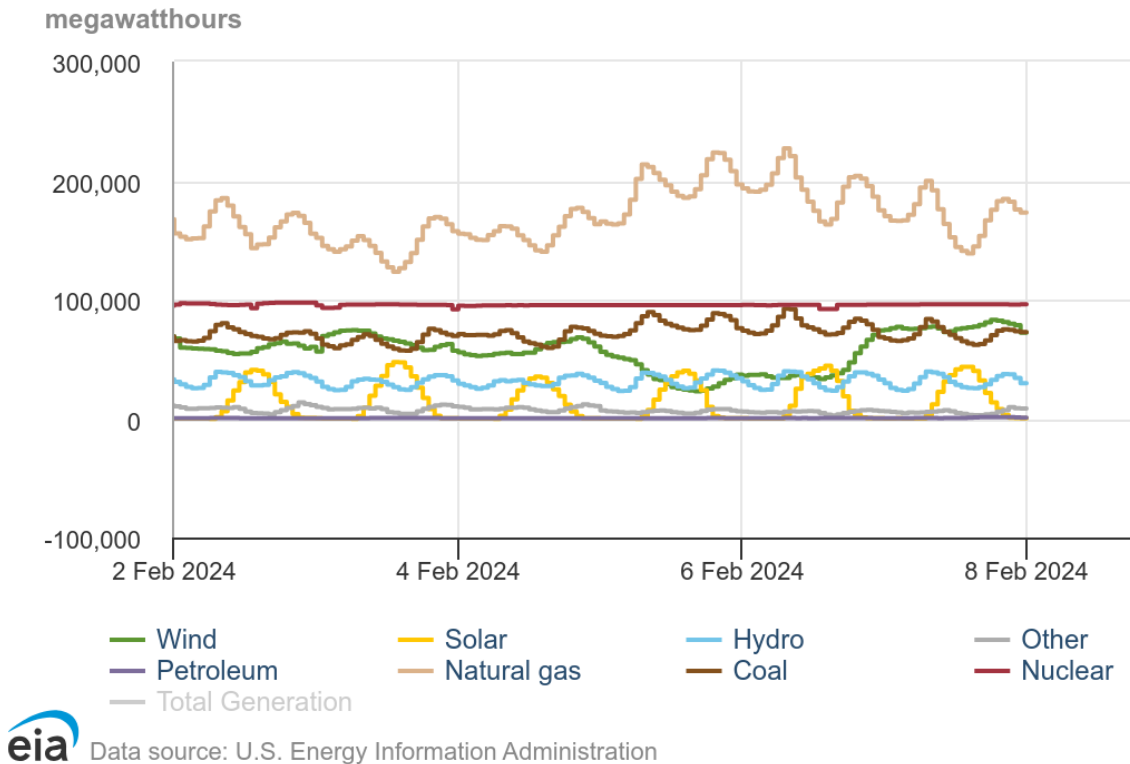


Figure 1-1: The urgency and importance of energy storage solutions is derived, among other things, from the intermittency of renewable energies. Solar energy can only be collected during sunshine hours and wind energy is also connected to it through thermal energy.⁹

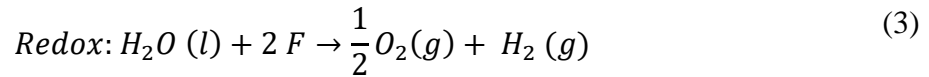
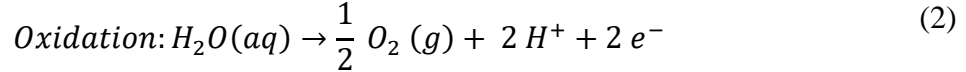
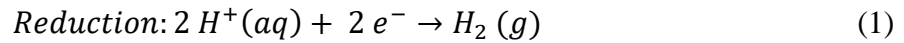
Especially sector coupling within the green hydrogen field harnesses the transformative potential of renewable energies to revolutionize various sectors of the economy. This strategy integrates the production of green hydrogen, derived from renewable sources such as wind or solar power, with multiple sectors like transportation, chemical and steel industry, as well as heating. By coupling these sectors as shown in Figure 1-2, excess renewable energy, often generated during periods of low demand, can be efficiently stored in the form of green hydrogen. This stored energy can then be utilized across different sectors, serving as a clean and versatile energy carrier. For instance, green hydrogen can be employed as a fuel for zero-emission vehicles, a feedstock for industrial processes, or a source of clean heat for buildings. This holistic approach not only enhances the overall efficiency of renewable energy systems but also facilitates the decarbonization of traditionally hard-to-abate sectors, contributing significantly to the transition towards a more sustainable and low-carbon future.^{5, 10, 11}

1.2. Water Electrolysis

1.2.1. Principles of Water Electrolysis

In general, electrolysis of water is a technology for the production of hydrogen that has an increasingly important role to play in the future to produce green hydrogen with energy from renewable sources. In dark electrolysis an applied current splits water into its gaseous components hydrogen and oxygen at a certain potential. This energy conversion technique allows for the conversion and storage of electric energy in the form of chemical energy. Re-electrification to meet increased energy demand utilizing a fuel cell is possible, albeit at certain energy losses.²¹ Therefore, water splitting is a powerful tool to stabilize the energy grid and mitigate times of low energy supply.²²

In principle, the overall reaction can be divided into half-cell reactions. The anodic oxygen evolution reaction (OER) and the cathodic hydrogen evolution reaction (HER) can be formulated as in the following²³:



where F represents 1 mol of (exchanged) electrical charge in (3), defined by the Faraday constant $F = N_A e = 96490 \frac{C}{mol}$ with N_A being the Avogadro constant and e the elementary charge.

The reduction presented in (1) shows a straightforward combination of two protons and two electrons to form hydrogen, which proceeds kinetically fast. In contrast, the oxygen evolution presented in principle in (2) involves four electron transfers, which substantially slow down the kinetics.²³

Besides the redox processes, diverse chemical and physical processes such as adsorption, electron transfer and others occur during electrolysis.²⁴ The potential of a cell with a reversible reaction represents the ideal limiting case and requires fast kinetics to be established. As a result, the Nernst equation in (4) is only valid for the electrode surface in equilibrium with species in solution. Therefore, the aforementioned chemical and physical processes have a

significant influence on the kinetics of the half-cell reactions.^{23, 25} Applying the Nernst equation the theoretical cell voltage of water electrolysis is 1.23 V:

$$E^{eq} = E^0 + \frac{RT}{zF} \ln \frac{c_R}{c_O} \quad (4)$$

with E^{eq} for the equilibrium potential, E^0 for the standard cell potential, c_O for the concentration of the oxidants (oxidized form), c_R for the concentration of the reductants (reduced form), T for the temperature, R for the universal gas constant, F for the Faraday constant and z for the number of exchanged electrons.^{23, 25} The presence of the above factors that directly influence the kinetics reveals that the theoretical potential is not sufficient for water splitting in reality. This results in the occurrence of the so-called overpotential η , which is defined as the difference between the actual electrode potential E and the equilibrium potential E_{eq} :^{23, 25}

$$\eta = E - E_{eq} \quad (5)$$

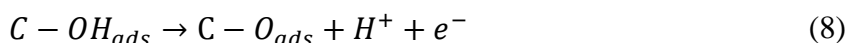
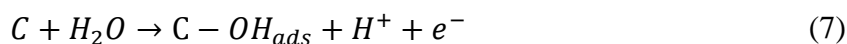
The current density at the electrode, described by the Butler-Volmer equation in (6), is linked to the overpotential and describes a key performance indicator of the electrolysis process:

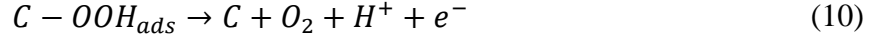
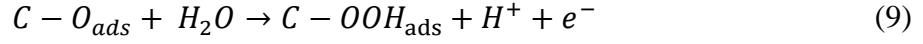
$$j = j_0 \times \left[\exp\left(\frac{\alpha z F \eta}{RT}\right) - \exp\left(-\frac{(1 - \alpha) z F \eta}{RT}\right) \right] \quad (6)$$

where j_0 describes the current density that is specific for the reversible reaction (exchange current density), α the transfer coefficient, z the number of electrons that are involved in the electrode reaction, F the Faraday constant and η the activation overpotential.^{23, 25}

1.2.2. Catalysis of the Oxygen Evolution Reaction

Due to the sluggish kinetics of the OER, a higher overpotential is apparent, causing the need for suitable electrocatalysts to increase the turnover rate of the OER. While the exact reaction mechanism is still not fully understood, one theory is presented in the following (C representing active sites):





With C representing the active site of the catalyst and O_{ads} and OH_{ads} describing the adsorbed oxygen atoms and hydroxyl groups. A hydroxyl ion of a water molecule is adsorbed on the active side of the catalyst and forms OH_{ads} . Oxygen can be produced by combination of two adsorbed oxygen atoms or via the formation of another intermediate OOH_{ads} . This species can react with water to form oxygen. The proposed mechanism of the OER shows the key role of the catalyst in the reaction mechanism.²⁶⁻²⁹

Each step in the proposed mechanism has an individual free reaction energy. With an ideal catalyst for the proposed reaction mechanism, all free reaction energies of the steps would be equivalent, which is not the case in reality due to different kinetic barriers and overpotentials. The resulting global overpotential of the overall reaction is determined by the reaction step with the highest free reaction energy. As a result, the OER activity can be described as the delta between the adsorption energies. This means that the overpotential can be described as in the following.³⁰

$$\eta^{OER} = \left\{ \max[\Delta G_{O_{ads}} - \Delta G_{HO_{ads}}], 3.2 \text{ eV} - \frac{[\Delta G_{O_{ads}} - \Delta G_{HO_{ads}}]}{e} \right\} - 1.23 \text{ eV} \quad (11)$$

with $\Delta G_{O_{ads}}$ describing the adsorption energy of O_{ads} and $\Delta G_{HO_{ads}}$ describing the adsorption energy of HO_{ads} .

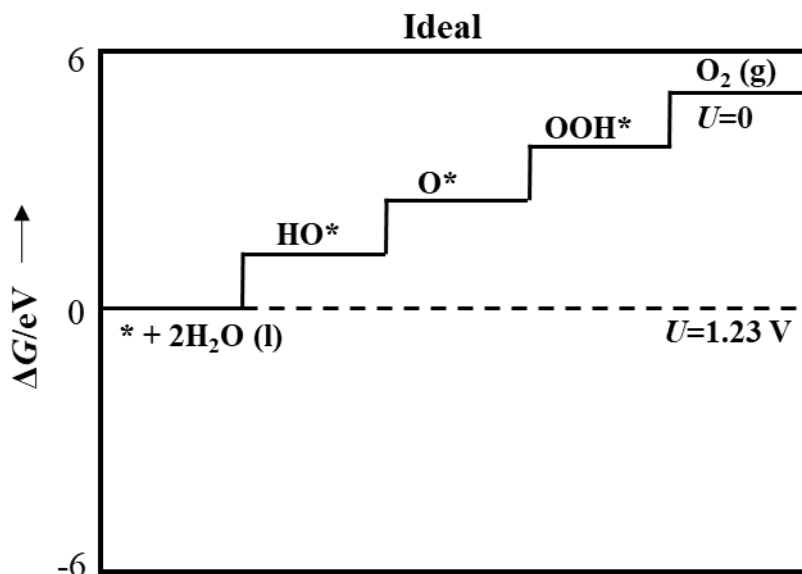


Figure 1-3 The standard free energies for the OER for an ideal catalyst with the theoretical potential of 1.23 V³⁰(* indicates an adsorption site on the catalyst). Reproduced with permission from Ref. [30]. Copyright 2011, WILEY-VCH Verlag GmbH & Co. KGaA, Weinheim.

The above-shown energy diagram in Figure 1-3 for an ideal OER catalyst reveals that at the equilibrium potential, an ideal OER catalyst should promote the oxygen evolution reaction. This means that the four charge-transfer steps require equivalent free reaction energies at zero potential:

$$\frac{4.92 \text{ eV}}{4} = 1.23 \text{ eV} \quad (12)$$

A thermodynamically ideal catalyst would fulfill these criteria, but in reality there is no catalyst that fulfills this, leading to overpotentials. By plotting the overpotentials of various catalysts for the OER against $\Delta G_{O_{ads}}^0 - \Delta G_{OH_{ads}}^0$, a volcano curve is obtained, shown in Figure 1-4. Such volcano curves are typical for catalyst activities.²⁶

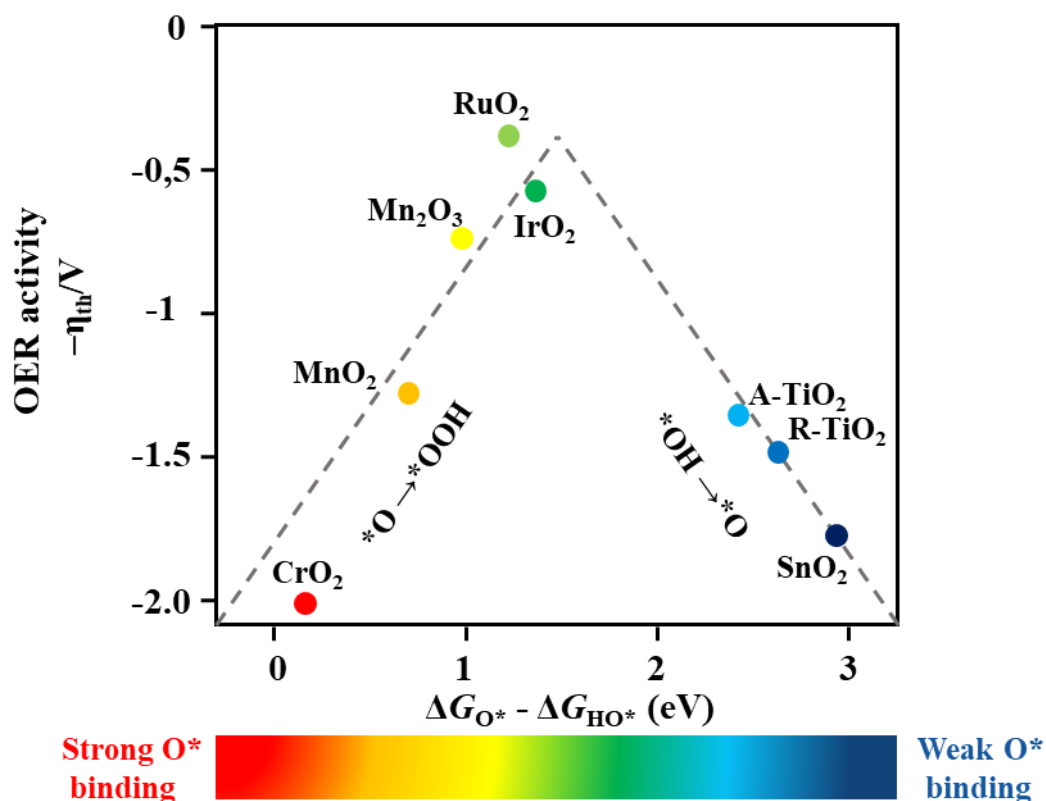


Figure 1-4: Volcano curve of diverse OER catalysts. A negative theoretical overpotential is plotted against the standard free energy of OER catalysts with activity trends towards the OER.³¹ Adapted from original image with permission from Ref. [31]. Copyright 2020, Wiley-VCH Verlag GmbH & Co. KGaA, Weinheim.

In a volcano curve, the activity is represented as a result of the binding energy of intermediates. Surfaces that bind oxygen strongly are limited by the formation of OOH_{ads} . On the other hand, surfaces that bind oxygen too weakly have a potential that is limited by the oxidation of OH_{ads} . Furthermore, the experimental overpotential also depends on the current density at the electrode at which the measurement was carried out. The effective surface areas of the electrodes used with oxide nanoparticles are also unknown.³⁰ Despite these limitations, the volcano curves are useful approximations for the development and optimization of OER catalysts. In particular, RuO_2 and IrO_2 stand out as especially promising OER catalysts for the acidic type of water splitting reaction with a proton exchange membrane (PEM) electrolyzer.²⁹

1.2.3. Proton Exchange Membrane Electrolyzers

PEM electrolysis is an electrochemical process used to split water into hydrogen and oxygen in an acidic environment. It is well suited to couple with sustainable and intermittent energy sources such as wind and solar.¹ At its core, the PEM electrolyzer consists of a proton exchange membrane separating two half cells as depicted in a simplified scheme of an membrane electrode assembly (MEA) in Figure 1-5.³² The electrolyte membrane, typically composed of a perfluorosulfonic acid polymer such as Nafion[®], plays a critical role in PEM electrolyzers. It serves as a selective barrier between the anode and cathode compartments, allowing only protons to pass through while blocking the transport of gases such as hydrogen and oxygen and minimizing hazardous gas crossover.^{33, 34} This selective permeability ensures that the protons generated at the anode can migrate to the cathode through the membrane, facilitating the electrolysis process.

One half cell is the anode which is the electrode where the OER occurs during electrolysis. It is typically coated with an electrocatalyst, often based on noble metals, such as iridium oxide or iridium-ruthenium (IrRu) alloys. These catalysts accelerate the oxidation of water molecules, splitting them into oxygen gas, protons, and electrons. The other half cell is the cathode which is the electrode where the HER takes place. It is coated with an electrocatalyst, commonly composed of platinum (Pt) or nickel (Ni). This catalyst promotes the reduction of protons and electrons from the anode compartment, facilitating the production of hydrogen gas.^{23, 32, 35} Further, bipolar plates which are conductive plates are placed between adjacent MEAs in the PEM electrolyzer stack. These plates serve multiple functions, including distributing electrical current evenly across the cell, facilitating the flow of reactants and products, and providing structural support to the MEAs. Bipolar plates are often made of lightweight and corrosion-resistant materials such as graphite or metal.³⁶ Other important components are gas diffusion layers (GDL). These are porous materials placed adjacent to the electrodes in the PEM electrolyzer. These layers facilitate the transport of water to the electrodes and the removal of product gases (hydrogen and oxygen). GDLs also help to maintain uniform gas distribution and promote efficient gas-electrode interactions, enhancing the overall performance of the electrolyzer.³⁷ Another important layer is the porous transport layer (PTL). The PTL is typically positioned adjacent to the catalyst layer in the MEA. The primary function of the PTL is to facilitate the transport and uniform distribution of reactants to the catalyst layer where electrochemical reactions occur. Therefore, the PTL prevents localized areas of high or low

reactant concentration which can lead to reduced efficiency. The porous structure of the PTL allows reactants to permeate through its surface and reach the catalyst layer efficiently. This ensures that a steady supply of reactants is available at the electrode surface, promoting continuous electrochemical reactions.^{32, 38}

Furthermore, current collectors are other necessary components. In principle, they are conductive elements that collect electrons generated at the electrodes and transport them to the external circuit, where they contribute to the overall electrical current flow. They are typically made of conductive materials such as graphite, carbon, or metal foils and are integrated into the electrode assemblies to ensure efficient electron transfer during electrolysis. As PEM is a dark electrolysis technique it requires a power supply to drive the electrolysis process. It delivers a direct current (DC) electrical potential across the electrodes, facilitating the separation of water molecules into hydrogen and oxygen gas. The power supply is ideally connected to renewable energy sources such as solar panels or wind turbines to enable the production of green hydrogen through electrolysis.^{32, 39}

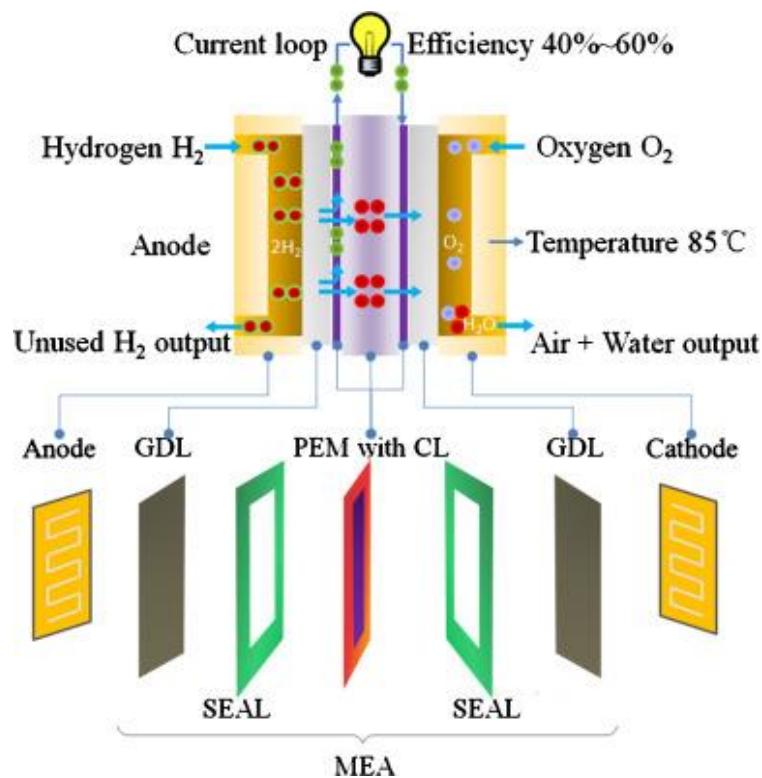


Figure 1-5: Schematic illustration of a simplified PEM electrolyzer comprising the cathode, separating membrane, and anode, as well as the GDL. Water is split into oxygen and protons at the anode. Produced protons can pass the membrane to the cathode where combination with electrons leads to the formation of hydrogen gas. The applied current is the driving force of the reactions.⁴⁰ Reproduced with permission from Ref. [40]. 2016 The Society of Manufacturing Engineers. Published by Elsevier Ltd. All rights reserved.

PEM electrolysis offers several advantages that contribute to its growing popularity in hydrogen production as this technique is known for its high efficiency, especially at partial loads. The electrolyzers can respond quickly to fluctuations in electricity supply, making them suitable for renewable energy integration. Moreover, PEM electrolyzers exhibit rapid start-up and shutdown capabilities, enabling flexibility in responding to dynamic energy demands and supply. This feature enhances their compatibility with intermittent renewable energy sources.^{32, 41-43} The solid polymer electrolyte membrane allows for a more compact and lightweight design compared to other electrolysis technologies. This is particularly advantageous for applications with space constraints. PEM electrolyzers produce high-purity hydrogen without the need for additional purification steps, which is crucial for applications requiring ultra-pure hydrogen, such as fuel cells.^{44, 45}

While PEM electrolysis has numerous advantages, it also comes with certain limitations: particularly, PEM electrolyzers rely on the use of precious and scarce metal catalysts due to their oxidizing nature, like platinum and iridium. The high costs of named materials contribute to the overall system cost, which remains a challenge for widespread adoption.^{41, 46} In addition to the use of precious metal catalysts, scientific efforts are also underway to replace them altogether with alternative catalyst systems such as, e.g., metal-organic-frameworks or non-noble transition metal-oxides and phosphides.^{47, 48}

Besides named cost factors, maintenance costs and the associated downtime of the electrolyzer should not be neglected in the final pricing of produced hydrogen with this technique. Improving the durability and lifespan of PEM electrolyzers is a key challenge. The durability of PEM electrolyzers is influenced by factors such as catalyst degradation and membrane stability.⁴⁹ Research is ongoing to improve the long-term performance and lifespan of PEM electrolysis systems. PEM electrolyzers are sensitive to impurities and contaminants in the feed water, thus maintaining high-purity water is essential to prevent degradation of the membrane and catalysts.⁵⁰

Successfully addressing named challenges further promotes an economic upscaling of PEM electrolysis to an industrially relevant level concerning engineering and cost issues derived by catalyst degradation, membrane stability, and corrosion, especially in high-current-density operations.⁵¹⁻⁵³

1.3. Iridium Oxide Catalysts for PEM Electrolysis

As the OER possesses overall complex 4-electron transfer processes, it necessitates highly efficient catalysts to enhance the turnover rate for the whole cell.⁵⁴ Among various explored catalyst materials, iridium oxide is a well-known OER catalyst due to its exceptional electrocatalytic properties, for instance, a good electrical conductivity, facilitating efficient electron transfer during the electrochemical reactions.^{55, 56} Further, this precious metal oxide shows remarkable stability as well as cycling durability under OER conditions and is less prone to dissolution. This makes this catalyst more attractive and corrosion resistant than, e.g., RuO₂. Despite exhibiting higher OER activity, at high potentials RuO₂ is oxidized to gaseous RuO₄ leading to decreased OER activity.^{57, 58} The unique electronic structure makes IrO₂ highly active for the OER, allowing for efficient water oxidation at relatively low overpotentials and achieve high current densities.^{59, 60} Further, iridium oxide exhibits a higher stability and durability during extended electrolysis operations compared to other possible catalysts like ruthenium oxide.

While demonstrating promising characteristics towards PEM, different challenges persist. As iridium is associated with high costs, economic feasibility of large-scale iridium-based catalyst deployment remains a challenge, necessitating cost-effective alternatives or catalyst designs that maximize utility and thus efficiency with reduced iridium content.^{61, 62} Despite novel catalyst development, scalability and cost-effective manufacturing processes are essential for adoption in large-scale PEM electrolysis systems.⁶³⁻⁶⁵

Further, the morphology of the iridium oxide component of the catalyst significantly influences the catalytic activity. Enhanced OER performance requires precise control of the iridium oxide phase in terms of particle size, crystallinity and surface structure, especially for catalysts with ultra-low iridium content.⁶⁶ Despite nanostructuring of iridium oxide particles, alloying with other metals, such as nickel, platinum, or cobalt, have been explored to enhance catalytic activity and reduce the overall iridium content, to address cost concerns.⁶⁷⁻⁷⁰ Alternative catalyst materials, such as earth-abundant elements or advanced nanomaterials such as perovskites, may lead to discoveries that offer comparable or maybe even superior performance to iridium oxide catalysts while addressing cost and availability concerns.⁷¹

Novel nanostructured catalyst support materials, like metal oxides and conductive substrates, are thought to improve the stability and dispersion of iridium oxide particles and contribute to

both activity and durability.^{42, 72, 73} Advancements in in-situ characterization techniques, such as in operando spectroscopy and microscopy, allows to study the dynamic behavior of iridium oxide-based catalysts during the OER.⁷⁴⁻⁷⁷ This aids in optimizing the overall catalyst design in terms of active component and interaction with its support for improved performance.

1.4. Metal Oxide-Supports for PEM

Despite the catalytic prowess, iridium oxide catalysts face challenges such as cost, scarcity, and stability concerns. This is where support structures such as semiconductor metal oxides come into play, offering solutions to enhance both the efficiency and longevity of the active component.⁷⁸ The support material is a critical component in PEM cells and is generally employed to load and disperse the active component forming the active catalyst layer which is sandwiched between the PEM and gas diffusion layer. The support should be optimized with regards to enhancement of the electron percolation in the system, promoting overall stability and long-term performance.⁷⁹

One of the primary functions of a support structure is to provide mechanical and chemical stability to the active component.⁸⁰ Semiconductor metal oxides, such as titanium oxide (TiO_2), tin oxide (SnO_2) or tantalum oxide (Ta_2O_5), are often chosen for their robust nature.⁷⁸ These materials act as a stable foundation for the deposition of the active component, e.g. iridium oxide, preventing its degradation over time.⁸¹ The support ensures that the catalyst remains anchored and protected during the harsh electrolysis operation conditions, which greatly benefits the long-term stability and durability of the overall system.⁸² In essence, the support structure should be chosen first and foremost for its corrosion resistance properties to withstand the highly oxidizing environment created during the electrolysis of water in PEM.

Moreover, advances in nanostructuring techniques aim to further enhance the catalytic performance by manipulating not only the size and shape of iridium nanoparticles but also the arrangement on metal oxide supports by optimization of the dispersion.⁸³ Nanostructuring the support itself aims to yield a high surface area and offers ample sites for the deposition of iridium oxide nanoparticles. This maximizes the density of active sites available for the OER, enhancing overall catalyst efficiency.⁸⁴ Various studies have demonstrated that the synergistic

effect of the active component and the support structure leads to improved efficiency, as more water molecules can interact with the catalyst, enhancing the overall electrolysis process.⁸⁵⁻⁸⁷

Uniform dispersion of iridium oxide nanoparticles on the stable support framework is critical for mitigating factors such as agglomeration and dissolution which can lead to catalyst degradation over time, as well as ensuring optimal catalytic performance.^{88, 89} Further, the interaction between iridium oxide and metal oxide supports at the atomic scale is expected to have a strong impact on overall OER efficiency and stability. This is crucial for achieving higher current densities and overall electrolyzer performance.^{74, 90, 91} However, achieving uniform loading and dispersion of iridium nanoparticles on the metal oxide support can be challenging. Researchers are exploring versatile synthesis methods such as incipient wetness impregnation, solvothermal, and wet-chemical loading to enhance the catalyst loading and ensure uniform distribution for optimal performance.⁹²⁻⁹⁴

While semiconductor metal oxides are not as conductive as metals, they contribute to the overall electrical conductivity of the system.⁹⁵ This is crucial for maintaining a steady flow of electrons during electrolysis. The support acts as a conductive pathway, facilitating the movement of charge carriers between the active component and the electrode, ensuring efficient electron transfer during the electrochemical reactions.⁹⁶ Doping is often employed to enhance the conductivity of the support material. By introducing elements or compounds that promote the density and/or mobility of electrons within the lattice structure, the doped support material becomes more effective in facilitating the transport of electrons from one electrode to another. This increased conductivity can lead to lower ohmic losses and, consequently, reduced overpotential in the PEM electrolysis cell, a key factor in improving the energy efficiency of the electrolysis process. By providing an environment that promotes efficient charge transfer, the support structure aids in reducing the amount of energy required for the electrolysis.^{41, 97}

Challenges persist in the development of metal oxide-supported iridium oxide catalysts for PEM electrolysis. For instance, the long-term stability and durability of these catalysts, especially under high current densities and varying operational conditions lead to dissolution of the active component and therefore a loss in active material.⁹⁸ Catalyst degradation, associated activity loss and high material costs necessitate continued research into novel materials like non-precious metal or mixed-precious metal catalysts, e.g. an iridium-tungsten composite catalyst⁹⁹ or a manganese perovskite oxide AMn_2O_3 ($\text{A}=\text{Ca}, \text{La}$) discovered by DFT calculations¹⁰⁰, tightly anchored precious-metal catalysts which eventually may lead to less

dissolution¹⁰¹, and engineering approaches to address high costs of components, e.g. corrosion resistant bipolar plates. Corrosion resistance plays a vital role for this key component that makes up 50 % of the stack cost. Even though graphite based bipolar plates do not withstand harsh environments, they are often employed. Potential substitutes are bipolar plates that consist of stainless steel, titanium and their alloys.¹⁰²

1.4.1. Electrospinning of Metal Oxide Nanofibers

Electrospinning is a powerful and versatile technique for producing nanofibrous structures with high surface areas. This method has found extensive use in many fields with a broad range of applications for nanofibrous scaffolds, e.g. for biomedical applications, air and water filtration systems, catalysis and many more utilizing different material classes such as polymers, composites, ceramics or semiconductor oxides.^{27, 103-105} Commonly studied metal oxide nanofibers include tin oxide (SnO₂), titanium dioxide (TiO₂) as also described in this work but also zinc oxide (ZnO), and cerium oxide (CeO₂), which can be employed as OER catalyst supports.¹⁰⁶⁻¹⁰⁸ Further, the scalability of electrospinning makes it a cost-effective technique. The ability to control nanofiber diameter, alignment, and density on a large scale is advantageous for industrial applications in catalysis.^{109, 110}

This technique allows for creating nanoscale polymeric fibers with an oriented fiber alignment ranging from nanometers to micrometers in diameter. This method's low cost and moderate equipment requirement are two of its main advantages. Three primary parts typically make up an electrospinning setup: a grounded metal collector, a high voltage power source, and a syringe and needle, also called spinneret, which is coupled to a syringe pump as shown in Figure 1-6.¹¹¹⁻¹¹³

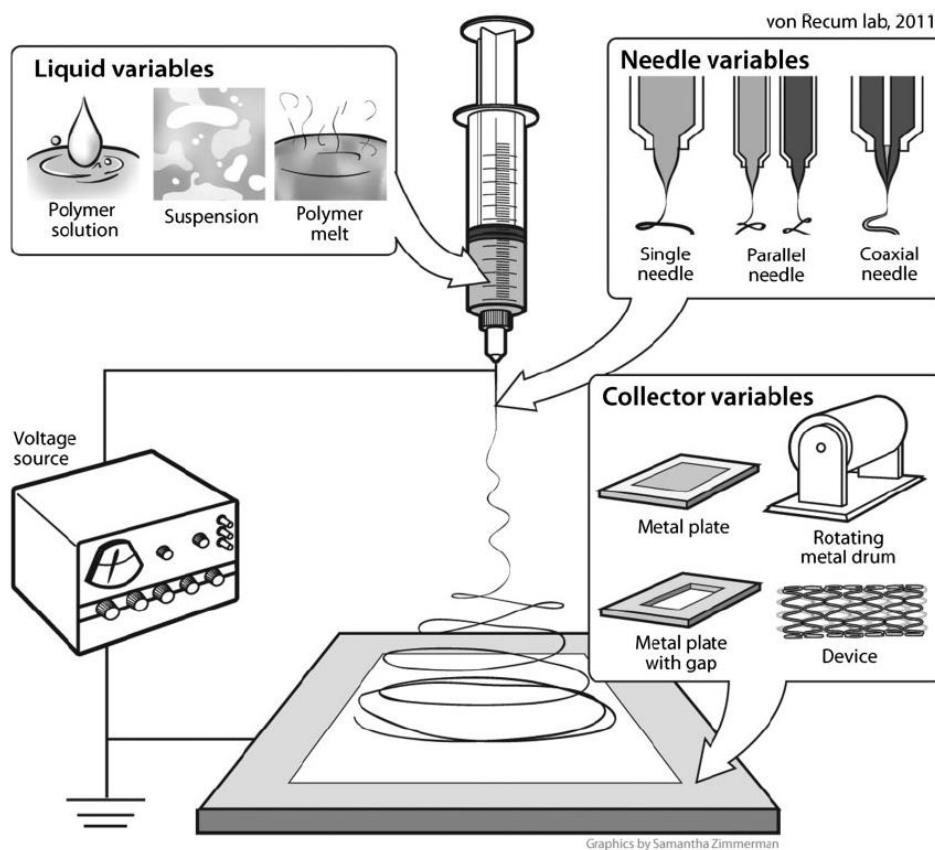


Figure 1-6: Principal electrospinning setup with diverse variables that impact the morphology of the resulting fibers.¹¹³ Reprinted with permission from ref [115]. Copyright © 2012 WILEY-VCH Verlag GmbH & Co. KGaA, Weinheim.

There are various steps involved in creating inorganic (such as metal oxide used in this work) electrospun nanofibers. The spinning solution requires a solvent, a carrier polymer and a precursor as crucial components. First, a precursor is dissolved in a suitable solvent. To obtain the appropriate viscosity of the spinning solution, it must be combined with an appropriate carrier polymer template in the second step. This spinning solution is then electrospun, and the produced filaments are deposited at the collector. Finally, in order to yield pure crystalline metal oxide nanofibers and combust the supporting polymer, the electrospun nanofibers are calcined.¹¹⁴

Throughout the process, a potential is applied in between the collector and the needle where the polymer solution is continuously forced through due to the continuous flow provided by a syringe pump. Due to its exposure to the potential, the droplet at the needle's tip becomes electrified and on the droplet's surface, charges are generated and dispersed uniformly. This droplet is subject to electrostatic forces, primarily the Coulombic force and electrostatic repulsion. The surface charges repel one another electrostatically, and Coulombic forces arise as a result of the external electric field. These two forces cause the droplet to change its shape

as it elongates into a cone, which is also referred to as the Taylor cone. To generate sufficient electrostatic forces to overcome surface tension, the applied voltage must exceed a threshold value, sometimes referred to as the critical voltage V_c . As a result, an electric liquid jet is released, stretching and whipping the material to create a long, thin thread that solidifies as it expands. The bending instability of the fibers occurs during the stretching process. The solution jet is further stretched as the solvent evaporates at the bending instability area due to electrostatic forces—the thread deposits as a mat on the grounded collector after being drawn to it. In an ideal setup with optimized variables one infinite fiber is formed on the collector.¹¹⁴
¹¹⁵ There are several kinds of collectors, as Figure 1-6 illustrates. One possibility to prevent the bending instability is to utilize a revolving spinning drum where the polymer jet is uniformly spun around. The size and shape of the electrospun fibers may be changed by adjusting a few factors, including the polymer concentration, the applied voltage, the needle size, the needle's distance from the collector, and the speed of the spinning drum. For example, increasing both the applied voltage and the distance between the injector and collector will result in a decrease in the diameters of the nanofibers whereas for instance a higher polymer concentration leads to an increase in fiber diameter.¹¹⁶

In recent years, electrospinning has gained significant attention in the field of PEM electrolysis, by employing corrosion resistant metal oxide nanofibers as catalyst support structures.^{117, 118} Their tunable characteristics, such as high surface area, porosity, composition and morphology, make them ideal for catalyst supports.¹¹⁸⁻¹²⁰ Especially the precise tuning of porosity and composition is crucial for tailoring catalyst support structures to meet specific catalytic requirements, such as optimizing active sites and improving mass transfer.^{117, 121, 122} But also enhanced dispersion of catalytic materials is advantageous as it facilitates efficient reaction kinetics.¹²³

Despite numerous advantages, electrospinning faces challenges related to process optimization. Achieving reproducibility and scalability while maintaining desired nanofiber characteristics requires careful consideration of processing parameters as described earlier in this chapter.¹²⁴ The integration of the active component into electrospun metal oxide nanofibers is a critical aspect. Ensuring uniform distribution and strong interaction between the active component and the support is essential for maximizing catalytic activity and stability.¹²⁵

1.5. Epitaxy in Catalysis

One concept to ensure strong interaction between active component and support is epitaxy. This term describes a regularly oriented growth of one crystalline substance on another. It is a fundamental fabrication technique, for instance in the semiconductor industry.¹²⁶ The precise control over the crystal structure and thickness of epitaxial layers allows for the development of materials with tailored properties, such as enhanced carrier mobility and improved light-emitting efficiency, or a higher catalytic activity towards the OER as described in this work.¹²⁷

101

Besides homoepitaxy, where an epitaxial layer made of the same material as the substrate is grown, the growth of an epitaxial layer made of material distinct from the substrate is possible in heteroepitaxy. Depending on the interfacial circumstances and lattice parameters, heteroepitaxial films can have either strained or relaxed lattice structures as illustrated in Figure 1-7.^{128, 129}

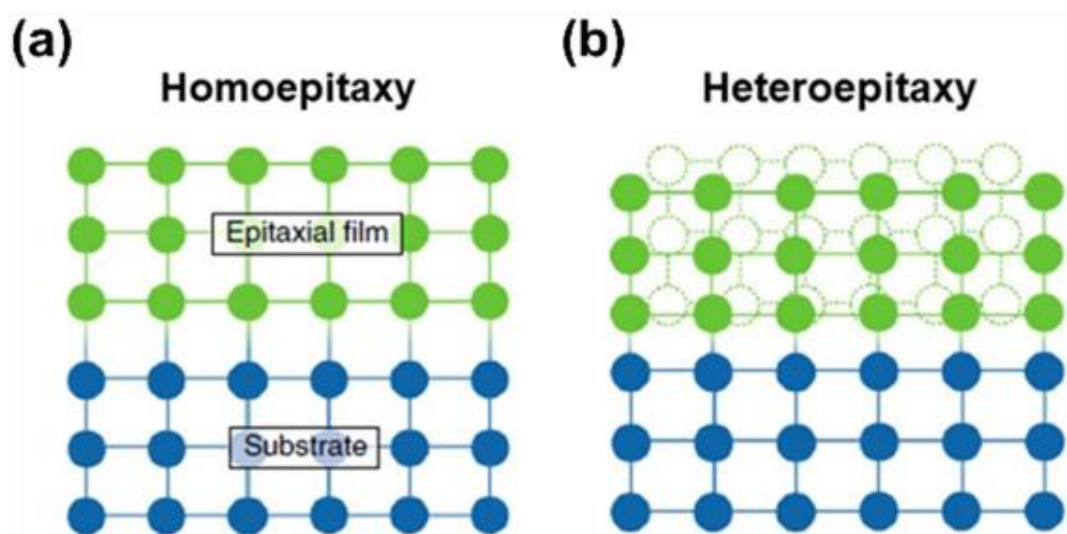


Figure 1-7: Homoepitaxy leads to matched crystal lattices (a) whereas heteroepitaxy can either have a strained or relaxed lattice match (b).¹²⁹ Reprinted from ref [131] with permission from. Copyright © 2019, Taylor & Francis.

To achieve named epitaxial growth, several fabrication techniques are available, including evaporation, sputtering,¹³⁰ liquid phase epitaxy,¹³¹ pulsed laser deposition (PLD),¹³² molecular beam epitaxy (MBE),¹³³ atomic layer epitaxy, more generally known as atomic layer deposition (ALD), and metal-organic chemical vapor deposition (MOCVD) epitaxy.¹³⁴ MBE involves the deposition of atoms or molecules one at a time in ultra-high vacuum conditions, ensuring precise control over the growth.¹³³ ALD processes including Al_2O_3 , ZnO , TiO_2 ,¹³⁵ NiO ¹³⁶, and

IrO_2 ¹³⁷ are split into partial processes and require high vacuum conditions and inert gases throughout the process as well as volatile-metal-organic precursors. This technique allows for high precision growth of individual layers and is explained in detail in chapter 1.6. MOCVD, on the other hand, is not as precise as ALD but also relies on chemical reactions between volatile metal-organic precursors and gases to deposit thin films on a substrate to produce e.g. GaN, AlN, InN or their alloys.^{138, 139}

Besides the deposition technique itself, the choice of substrate is critical in epitaxial growth. The substrate's crystal lattice and orientation determine the arrangement of atoms in the epitaxial layer. Normally, single crystal substrates are used to achieve high-quality epitaxial films. The lattice match between the substrate and the epitaxial layer is essential for minimizing defects, strain and ensuring the desired electronic and optical properties.¹⁴⁰

Besides the wide application purposes in semiconductors, epitaxy has become more and more important to catalyst fabrication. The application of epitaxial thin films in catalysis has gained attention due to their potential to enhance the stability, durability and catalytic activity of respective epitaxial catalysts.¹⁴¹ For instance, SrIrO_3 was grown by PLD and employed to the OER. Here, a low overpotential of 270 mV for continuous 30 h of testing in acidic electrolyte was recorded at a current density of 10 mA cm^{-2} . This epitaxially grown catalyst outperformed many known IrO_x and RuO_x systems in regard of high activity.¹³² However, the demanding synthesis conditions of PLD require a pulsed laser as well as ultra-high vacuum conditions which makes widespread applications challenging. Further, single-crystalline NiFeCu oxide with epitaxial dendrites has been employed as catalyst for the OER in PEM electrolysis. The structure was found to promote fast electron transport for the catalyst as well as retard the diffusion of the oxygen atoms to the inner metallic current collector, leading to a more efficient and steady operation than commercial RuO_2 with an anode current density at industrial scale (300 mA cm^{-2}).¹⁴²

By controlling the arrangement of atoms in the epitaxial layer, the density of states and electronic properties of the catalyst can be modulated. This control over the electronic structure directly influences the catalytic activity and selectivity, providing a new feature for designing efficient catalysts.¹⁴³ By preferred growth of facets, the creation of specific active sites on the catalyst surface is facilitated. This tailoring of active sites can enhance catalytic selectivity and efficiency.¹⁴⁴ The precise engineering of catalytic surfaces has a great impact on the electronic structure. It was demonstrated in iron oxides $\text{FeO}(111)$, $\text{Fe}_3\text{O}_4(111)$ and $\alpha\text{-Fe}_2\text{O}_3(0001)$ films

grown epitaxially onto Pt(111) for dehydrogenation of ethylbenzene to styrene. Here, the electronic surface structure varies greatly with surface orientation and results in α -Fe₂O₃(0001) containing surface defects being active, and always inactive Fe₃O₄(111) catalysts.¹⁴⁵

This high level of control is crucial for catalysis, where the interaction between the catalyst and reactants determines the reaction kinetics and thus the overall performance of a reaction.¹⁴⁶ Maintaining the stability of a catalyst in a harsh oxidative environment such as PEM is one of the key challenges in electrocatalysis. The suggested increased stability is attributed to the strong interaction between the epitaxial layer and the substrate, resulting from a coherent interface that resists degradation over time as stated in the examples described above. For instance, the deposition or growth of thin epitaxial layers of iridium-based materials on a substrate with a similar crystal structure such as (doped) TiO₂ or SnO₂, may lead to a higher utilization of iridium in terms of activity and stability. This may enable development of catalysts with lower iridium contents that comprise comparable activity and stability vs. non-epitaxial catalysts with greater iridium contents.

1.6. Atomic Layer Deposition

ALD is a gas-phase thin-film technique, offering high precision and control over layer growth with applications in various fields, including catalysis and energy conversion. Its sequential, self-limiting reactions, atomic-scale precision, conformal coating capabilities, material versatility, and suitability for nanoscale structures make it an important tool in the development of advanced materials and technologies. It is an evolution of chemical vapor deposition (CVD) but differs fundamentally in the introduction of gaseous precursors for solid formation into the reactor alternately rather than simultaneously. These reactions are surface-limited, as each precursor chemisorbs onto the substrate surface (and reactor) by reacting with surface functional groups. In the 1960s, Aleskovskii and co-workers conducted pioneering research on ALD initially termed "Molecular Layering," in Russia.¹⁴⁷ This work laid the groundwork for subsequent advancements of controlled growth of luminescent ZnS and Al₂O₃ insulator films for electroluminescent flat-panel displays by Finnish researchers Suntola and colleagues who introduced the name "atomic layer epitaxy" (ALE).¹⁴⁸ In the early 2000s ALE became ALD as most grown films were amorphous and did not comprise epitaxial relationships to the

1.6. Atomic Layer Deposition

substrate they were grown on. Nowadays, a wide range of possible ALD processes are known from metals, oxides, nitrides to chalcogenides.¹⁴⁹

In contrast to CVD, ALD operates on the basis of at least two self-limiting gas-solid reactions, termed chemisorption reactions. This characteristic allows for the uniform coating of structures with high aspect ratios (how tall an object is vs. how wide it is). These reactions occur in sequence, with each step separated by the removal of unreacted precursors and side-products from the reaction chamber. Consequently, one ALD cycle typically comprises two half-cycles with four consecutive steps, as depicted in Figure 1-8.^{135, 150}

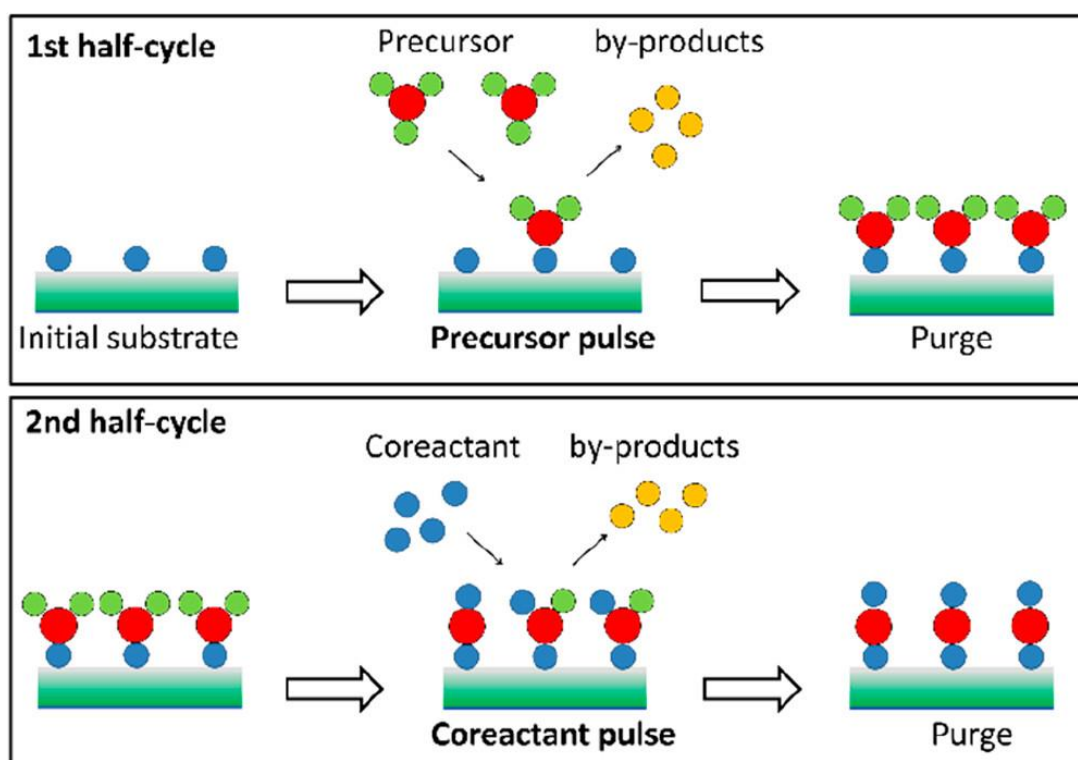


Figure 1-8: Schematic illustration of a single ALD cycle. During the first half-cycle the substrate is exposed to the precursor. A purge step is following to remove excess precursor and byproduct molecules. In the second half-cycle, the co-reactant is introduced followed by another purge for the deposition of one material (sub-)monolayer.¹³⁵ Reprinted from ref [137] with permission from. Copyright © 2021, Taylor & Francis.

The typical steps of an ALD cycle comprise precursor dosing, purging, co-reactant dosing, and purging. During precursor dosing, a gaseous precursor is introduced into the reaction chamber, where it chemisorbs onto the substrate surface. In the next step, the excess precursor and by-products are removed with purging of an inert gas like nitrogen or argon. After purging, the co-reactant is dosed into the chamber, reacting with the precursor to form a (sub-)monolayer of the desired material. Finally, the chamber is purged again to remove any remaining by-product and unreacted co-reactant, completing the ALD cycle. Layer growth is achieved by

repeating the cycle sequentially and offers precise control over film thickness and composition, making ALD a highly effective technique for thin film deposition.¹⁵⁰

In many cases, achieving a full and dense monolayer in a single cycle is challenging due to the steric hindrance of bulky precursor molecules, which shield other potential reactive sites from additional precursor. Consequently, thickness control down to sub-monolayer coverage is attainable, a feature of particular significance in the synthesis of supported catalysts. Moreover, as growth is limited by available surface sites rather than mass transport, ALD enables the conformal coating of all surfaces with nearly equal thickness. This attribute makes ALD a powerful and distinctive tool for modifying the surface properties of advanced materials.¹⁵⁰

One of ALD's remarkable features is its ability to provide conformal coating over complex and three-dimensional surfaces. The self-limiting reactions enable the uniform growth of films insensitive to surface topology because the principle of ALD depends on surface adsorption resulting in excellent coverage even on irregular or trench structures with high-aspect-ratios of advanced nanostructures such as semiconductor devices which often have high aspect ratios and complexity and require implementation of many different layers at nanoscale dimensions.^{151, 152} The great versatility in material choice enhances its utility across diverse fields, including electronics, energy storage and catalysis.¹⁵³ For instance, ALD has been employed to coat mesoporous IrTiO_x with two different IrO_x layer thicknesses over the entire external and internal surface of the oxides' pore systems resulting in two different iridium loadings. The authors found an optimized ALD layer thickness, as differences in electrical sheet conductivities and mass-based activities were apparent. They explained this observation with the predominance of well-accessible active IrO_x sites and high iridium utilization of homogeneously distributed Ir species.¹⁵⁴

1.6.1. Atomic Layer Deposition of Iridium Oxide Thin Films

As previously noted, even and thin coverage enable high mass utilization as active sites are accessible to reactants and uniform reactivity across the catalyst is promoted. This may contribute to the stability and durability of the catalyst as uniform coverage of tightly anchored iridium oxide is expected to reduce degradation as described in chapter 1.5.

ALD has been utilized for the growth of IrO_x with a range of possible precursors such as $(\text{EtCp})\text{Ir}^{\text{I}}\text{CHD}$ ¹⁵⁴, $\text{tris}(2,4\text{-pentanedionato})\text{iridium}$ ¹⁵⁵, $[\text{Ir}(\text{acac})_3]$ with oxygen and hydrogen¹⁵⁶, and $\text{Ir}(\text{acac})_3$ with ozone¹³⁷. These thin films have demonstrated low impurity contents, good adhesion to substrates, and controllable thickness. The electrocatalytic properties of IrO_x thin films have been studied and it was found that these films exhibit promising Tafel slopes, sheet conductivities as well as OER activities, making them suitable for the OER.¹⁵⁴ Additionally, low impurity contents further enhance their suitability for the OER in PEM electrolysis as this process is prone to poisoning.^{153, 154} Specifically, introducing impurities to PEM systems can lead to noble metal catalyst poisoning and stack failure.¹⁵⁷ Further, competing chemical reactions can be excluded with suitable catalyst layers, such as the chlorine evolution reaction which leads to degradation of the electrode.¹⁵⁸

Despite the great promise, challenges persist in the application of ALD thin film iridium oxide for the OER. ALD processes can be resource-intensive and involve the use of expensive precursors such as $\text{Ir}(\text{acac})_3$.^{66, 137} Transitioning ALD from laboratory-scale depositions to scalable manufacturing processes poses challenges upon maintaining the precision with higher throughput such as enabled by spatial ALD. Here, individual steps of the full cycle are physically separated in space rather than introduced sequentially as in ordinary ALD. The substrate is moved underneath the reactor and specific zones are spatially separated by inert gas shields.¹⁵⁹ The combination of ALD thin-film iridium oxide coating with advanced electrode materials also synthesized by ALD is feasible, such as titania/silica hybrid nanowires¹⁶⁰, Al_2O_3 helical nanotubes¹⁶¹, or TiO_2 nanorods¹⁶². The latter nanostructured supports offer precise control of their interface at the nanoscale as well as high surface areas.¹³⁶

1.7. References

1. Carmo, M.; Fritz, D.; Mergel, J.; Stolten, D., A comprehensive review on PEM electrolysis. *International Journal of Hydrogen Energy* **2013**, *38*, 4901-4934.
2. Rostrup-Nielsen, J. R.; Sehested, J.; Nørskov, J. K., Hydrogen and synthesis gas by steam- and CO₂ reforming. In *Advances in Catalysis*, Academic Press: 2002; Vol. 47, pp 65-139.
3. Abdin, Z.; Zafaranloo, A.; Rafiee, A.; Mérida, W.; Lipiński, W.; Khalilpour, K. R., Hydrogen as an energy vector. *Renewable and Sustainable Energy Reviews* **2020**, *120*, 109620.
4. Jain, I. P., Hydrogen the fuel for 21st century. *International Journal of Hydrogen Energy* **2009**, *34* (17), 7368-7378.
5. Giehl, J.; Hohgräve, A.; Lohmann, M.; Müller-Kirchenbauer, J., Economic analysis of sector coupling business models: Application on green hydrogen use cases. *International Journal of Hydrogen Energy* **2023**, *48* (28), 10345-10358.
6. He, G.; Mallapragada, D. S.; Bose, A.; Heuberger-Austin, C. F.; Genç, E., Sector coupling via hydrogen to lower the cost of energy system decarbonization. *Energy & Environmental Science* **2021**, *14* (9), 4635-4646.
7. Ramsebner, J.; Haas, R.; Ajanovic, A.; Wietschel, M., The sector coupling concept: A critical review. *WIREs Energy and Environment* **2021**, *10* (4).
8. Nhuchhen, D. R.; Sit, S. P.; Layzell, D. B., Decarbonization of cement production in a hydrogen economy. *Applied Energy* **2022**, *317*, 119180.
9. Administration, U. S. E. I. Real-time Operating Grid - U.S. Energy Information Administration (EIA). <https://www.eia.gov/electricity/gridmonitor/index.php> (accessed 09.02.2024).
10. De Blasio, N., Geopolitical and Market Implications of Renewable Hydrogen: New Dependencies in a Low-Carbon Energy World. *Energy* **2020**.
11. He, G.; Mallapragada, D. S.; Bose, A.; Heuberger-Austin, C. F.; Genç, E., Sector coupling via hydrogen to lower the cost of energy system decarbonization. *Energy & Environmental Science* **2021**, *14* (9), 4635-4646.
12. Han, J.-R.; Park, S.-J.; Kim, H.; Lee, S.; Lee, J. M., Centralized and distributed hydrogen production using steam reforming: challenges and perspectives. *Sustainable Energy & Fuels* **2022**, *6* (8), 1923-1939.

1.7. References

13. Du, Y.; Li, B.; Xu, G.; Wang, L., Recent advances in interface engineering strategy for highly-efficient electrocatalytic water splitting. *InfoMat* **2023**, 5 (1).
14. Joy, J.; Mathew, J.; George, S. C., Nanomaterials for photoelectrochemical water splitting – review. *International Journal of Hydrogen Energy* **2018**, 43 (10), 4804-4817.
15. Jiang, C.; Moniz, S. J. A.; Wang, A.; Zhang, T.; Tang, J., Photoelectrochemical devices for solar water splitting – materials and challenges. *Chemical Society Reviews* **2017**, 46 (15), 4645-4660.
16. Arunkumar, P.; Aarthi, U.; Rengaraj, S.; Won, C. S.; Babu, K. M. S., Review of solid oxide electrolysis cells: a clean energy strategy for hydrogen generation. *Nanomaterials and Energy* **2019**, 8 (1), 2-22.
17. Schiller, G.; Ansar, A.; Lang, M.; Patz, O., High temperature water electrolysis using metal supported solid oxide electrolyser cells (SOEC). *Journal of Applied Electrochemistry* **2009**, 39 (2), 293-301.
18. Appleby, A. J.; Crepy, G.; Jacquelin, J., High efficiency water electrolysis in alkaline solution. *International Journal of Hydrogen Energy* **1978**, 3 (1), 21-37.
19. Yu, Z. Y.; Duan, Y.; Feng, X. Y.; Yu, X.; Gao, M. R.; Yu, S. H., Clean and Affordable Hydrogen Fuel from Alkaline Water Splitting: Past, Recent Progress, and Future Prospects. *Advanced Materials* **2021**, 33 (31), 2007100.
20. Minke, C.; Suermann, M.; Bensmann, B.; Hanke-Rauschenbach, R., Is iridium demand a potential bottleneck in the realization of large-scale PEM water electrolysis? *International Journal of Hydrogen Energy* **2021**, 46 (46), 23581-23590.
21. Grimaud, A.; Rossmeisl, J.; Strasser, P., Water splitting and sustainable H₂ production. *Energy-X* **2019**, 10-16.
22. Zhang, B.; Zheng, Y.; Ma, T.; Yang, C.; Peng, Y.; Zhou, Z.; Zhou, M.; Li, S.; Wang, Y.; Cheng, C., Designing MOF nanoarchitectures for electrochemical water splitting. *Advanced Materials* **2021**, 33 (17), 2006042.
23. Naterer, G. F.; Dincer, I.; Zamfirescu, C., Hydrogen Production from Nuclear Energy. **2013**.
24. Sapountzi, F. M.; Gracia, J.; Weststrate, C.; Fredriksson, H.; Niemantsverdriet, H., Electrocatalysts for the generation of hydrogen, oxygen and synthesis gas. *Progress in Energy and Combustion Science* **2017**, 58, 1-35.
25. Arning, M. D.; Minter, S. D., 18 - Electrode Potentials. In *Handbook of Electrochemistry*, Zoski, C. G., Ed. Elsevier: Amsterdam, 2007; pp 813-827.

26. Song, J.; Wei, C.; Huang, Z.-F.; Liu, C.; Zeng, L.; Wang, X.; Xu, Z. J., A review on fundamentals for designing oxygen evolution electrocatalysts. *Chemical Society Reviews* **2020**, 49 (7), 2196-2214.
27. Boddula, R.; Asiri, A. M., *Methods for Electrocatalysis: Advanced Materials and Allied Applications*. Springer: 2020.
28. Fabbri, E.; Schmidt, T. J., Oxygen Evolution Reaction—The Enigma in Water Electrolysis. *ACS Catalysis* **2018**, 8 (10), 9765-9774.
29. Suen, N.-T.; Hung, S.-F.; Quan, Q.; Zhang, N.; Xu, Y.-J.; Chen, H. M., Electrocatalysis for the oxygen evolution reaction: recent development and future perspectives. *Chemical Society Reviews* **2017**, 46 (2), 337-365.
30. Man, I. C.; Su, H.-Y.; Calle-Vallejo, F.; Hansen, H. A.; Martínez, J. I.; Inoglu, N. G.; Kitchin, J.; Jaramillo, T. F.; Nørskov, J. K.; Rossmeisl, J., Universality in Oxygen Evolution Electrocatalysis on Oxide Surfaces. *ChemCatChem* **2011**, 3 (7), 1159-1165.
31. Chen, H.; Shi, L.; Liang, X.; Wang, L.; Asefa, T.; Zou, X., Optimization of Active Sites via Crystal Phase, Composition and Morphology for Efficient Low-Iridium Oxygen Evolution Catalysts. *Angewandte Chemie International Edition* **2020**, 59.
32. Shiva Kumar, S.; Himabindu, V., Hydrogen production by PEM water electrolysis – A review. *Materials Science for Energy Technologies* **2019**, 2 (3), 442-454.
33. Afshari, E.; Khodabakhsh, S.; Jahantigh, N.; Toghyani, S., Performance assessment of gas crossover phenomenon and water transport mechanism in high pressure PEM electrolyzer. *International Journal of Hydrogen Energy* **2021**, 46 (19), 11029-11040.
34. Schalenbach, M.; Carmo, M.; Fritz, D. L.; Mergel, J.; Stolten, D., Pressurized PEM water electrolysis: Efficiency and gas crossover. *International Journal of Hydrogen Energy* **2013**, 38 (35), 14921-14933.
35. Tee, S. Y.; Win, K. Y.; Teo, W. S.; Koh, L. D.; Liu, S.; Teng, C. P.; Han, M. Y., Recent Progress in Energy-Driven Water Splitting. *Advanced Science* **2017**, 4 (5), 1600337.
36. Hermann, A.; Chaudhuri, T.; Spagnol, P., Bipolar plates for PEM fuel cells: A review. *International journal of hydrogen Energy* **2005**, 30 (12), 1297-1302.
37. Park, S.; Lee, J.-W.; Popov, B. N., A review of gas diffusion layer in PEM fuel cells: Materials and designs. *International Journal of Hydrogen Energy* **2012**, 37 (7), 5850-5865.
38. Phillips, R. K.; Rezaei Niya, S. M.; Hoorfar, M. In *Characterization of the Porous Transport Layer (PTL)*, Electrochemical Society Meeting Abstracts 225, The Electrochemical Society, Inc.: 2014; pp 565-565.

1.7. References

39. Wang, Y.; Pham, L.; de Vasconcellos, G. P. S.; Madou, M., Fabrication and characterization of micro PEM fuel cells using pyrolyzed carbon current collector plates. *Journal of Power Sources* **2010**, *195* (15), 4796-4803.
40. Chen, J.; Liu, H.; Huang, Y.; Yin, Z., High-rate roll-to-roll stack and lamination of multilayer structured membrane electrode assembly. *Journal of Manufacturing Processes* **2016**, *23*, 175-182.
41. Böhm, D.; Beetz, M.; Schuster, M.; Peters, K.; Hufnagel, A. G.; Döblinger, M.; Böller, B.; Bein, T.; Fattakhova-Rohlfing, D., Efficient OER Catalyst with Low Ir Volume Density Obtained by Homogeneous Deposition of Iridium Oxide Nanoparticles on Macroporous Antimony-Doped Tin Oxide Support. *Advanced Functional Materials* **2019**, *30* (1).
42. Böhm, D.; Beetz, M.; Gebauer, C.; Bernt, M.; Schröter, J.; Kornherr, M.; Zoller, F.; Bein, T.; Fattakhova-Rohlfing, D., Highly conductive titania supported iridium oxide nanoparticles with low overall iridium density as OER catalyst for large-scale PEM electrolysis. *Applied Materials Today* **2021**, *24*, 101134.
43. Ahmed, K. W.; Jang, M. J.; Park, M. G.; Chen, Z.; Fowler, M., Effect of Components and Operating Conditions on the Performance of PEM Electrolyzers: A Review. *Electrochem* **2022**, *3* (4), 581-612.
44. Wang, T.; Cao, X.; Jiao, L., PEM water electrolysis for hydrogen production: fundamentals, advances, and prospects. *Carbon Neutrality* **2022**, *1* (1).
45. Wang, Y.; Yuan, H.; Martinez, A.; Hong, P.; Xu, H.; Bockmiller, F. R., Polymer electrolyte membrane fuel cell and hydrogen station networks for automobiles: Status, technology, and perspectives. *Advances in Applied Energy* **2021**, *2*, 100011.
46. Bernt, M.; Hartig-Weiß, A.; Tovini, M. F.; El-Sayed, H. A.; Schramm, C.; Schröter, J.; Gebauer, C.; Gasteiger, H. A., Current Challenges in Catalyst Development for PEM Water Electrolyzers. *Chemie Ingenieur Technik* **2020**, *92* (1-2), 31-39.
47. Chen, Z.; Higgins, D.; Yu, A.; Zhang, L.; Zhang, J., A review on non-precious metal electrocatalysts for PEM fuel cells. *Energy & Environmental Science* **2011**, *4* (9), 3167-3192.
48. Hughes, J. P.; Clipsham, J.; Chavushoglu, H.; Rowley-Neale, S. J.; Banks, C. E., Polymer electrolyte electrolysis: A review of the activity and stability of non-precious metal hydrogen evolution reaction and oxygen evolution reaction catalysts. *Renewable and Sustainable Energy Reviews* **2021**, *139*, 110709.
49. Möckl, M.; Ernst, M. F.; Kornherr, M.; Allebrod, F.; Bernt, M.; Byrknes, J.; Eickes, C.; Gebauer, C.; Moskovtseva, A.; Gasteiger, H. A., Durability Testing of Low-Iridium PEM

Water Electrolysis Membrane Electrode Assemblies. *Journal of The Electrochemical Society* **2022**, *169* (6), 064505.

50. Becker, H.; Murawski, J.; Shinde, D. V.; Stephens, I. E. L.; Hinds, G.; Smith, G., Impact of impurities on water electrolysis: a review. *Sustainable Energy & Fuels* **2023**, *7* (7), 1565-1603.
51. Khatib, F. N.; Wilberforce, T.; Ijaodola, O.; Ogungbemi, E.; El-Hassan, Z.; Durrant, A.; Thompson, J.; Olabi, A. G., Material degradation of components in polymer electrolyte membrane (PEM) electrolytic cell and mitigation mechanisms: A review. *Renewable and Sustainable Energy Reviews* **2019**, *111*, 1-14.
52. Rakousky, C.; Reimer, U.; Wippermann, K.; Carmo, M.; Lueke, W.; Stolten, D., An analysis of degradation phenomena in polymer electrolyte membrane water electrolysis. *Journal of Power Sources* **2016**, *326*, 120-128.
53. Feng, Q.; Yuan, X. Z.; Liu, G.; Wei, B.; Zhang, Z.; Li, H.; Wang, H., A review of proton exchange membrane water electrolysis on degradation mechanisms and mitigation strategies. *Journal of Power Sources* **2017**, *366*, 33-55.
54. Siracusano, S.; Van Dijk, N.; Payne-Johnson, E.; Baglio, V.; Aricò, A., Nanosized IrO_x and IrRuO_x electrocatalysts for the O₂ evolution reaction in PEM water electrolyzers. *Applied Catalysis B: Environmental* **2015**, *164*, 488-495.
55. Slavcheva, E.; Radev, I.; Bliznakov, S.; Topalov, G.; Andreev, P.; Budevski, E., Sputtered iridium oxide films as electrocatalysts for water splitting via PEM electrolysis. *Electrochimica Acta* **2007**, *52* (12), 3889-3894.
56. Yu, H.; Danilovic, N.; Wang, Y.; Willis, W.; Poozhikunnath, A.; Bonville, L.; Capuano, C.; Ayers, K.; Maric, R., Nano-size IrO_x catalyst of high activity and stability in PEM water electrolyzer with ultra-low iridium loading. *Applied Catalysis B: Environmental* **2018**, *239*, 133-146.
57. Rheinländer, P. J.; Durst, J., Transformation of the OER-Active IrO_x Species under Transient Operation Conditions in PEM Water Electrolysis. *Journal of The Electrochemical Society* **2021**, *168* (2), 024511.
58. Audichon, T.; Napporn, T. W.; Canaff, C.; Morais, C. u.; Comminges, C. m.; Kokoh, K. B., IrO₂ coated on RuO₂ as efficient and stable electroactive nanocatalysts for electrochemical water splitting. *The Journal of Physical Chemistry C* **2016**, *120* (5), 2562-2573.

1.7. References

59. Xu, X.; Jiang, J.; Shi, W.; Süß, V.; Shekhar, C.; Sun, S.; Chen, Y.; Mo, S.-K.; Felser, C.; Yan, B., Strong spin-orbit coupling and Dirac nodal lines in the three-dimensional electronic structure of metallic rutile IrO₂. *Physical Review B* **2019**, 99 (19), 195106.
60. Zhou, Z.-H.; Sun, W.; Zaman, W. Q.; Cao, L.-M.; Yang, J., Highly active and stable synergistic Ir–IrO₂ electro-catalyst for oxygen evolution reaction. *Chemical Engineering Communications* **2018**, 205 (7), 966-974.
61. Wang, C.; Lee, K.; Liu, C. P.; Kulkarni, D.; Atanassov, P.; Peng, X.; Zenyuk, I. V., Design of PEM water electrolyzers with low iridium loading. *International Materials Reviews* **2024**, 09506608231216665.
62. Ni, J.; Shi, Z.-P.; Wang, X.; Wang, Y.-B.; Wu, H.-X.; Liu, C.-P.; Ge, J.-J.; Xing, W., Recent Development of Low Iridium Electrocatalysts toward Efficient Water Oxidation. *Journal of Electrochemistry* **2022**, 28 (9), 2214010.
63. Xu, H.; Ci, S.; Ding, Y.; Wang, G.; Wen, Z., Recent advances in precious metal-free bifunctional catalysts for electrochemical conversion systems. *Journal of Materials Chemistry A* **2019**, 7 (14), 8006-8029.
64. Zhang, T.; Zhu, Y.; Lee, J. Y., Unconventional noble metal-free catalysts for oxygen evolution in aqueous systems. *Journal of Materials Chemistry A* **2018**, 6 (18), 8147-8158.
65. Pan, S.; Li, H.; Liu, D.; Huang, R.; Pan, X.; Ren, D.; Li, J.; Shakouri, M.; Zhang, Q.; Wang, M., Efficient and stable noble-metal-free catalyst for acidic water oxidation. *Nature communications* **2022**, 13 (1), 2294.
66. Abbott, D. F.; Lebedev, D.; Waltar, K.; Povia, M.; Nachtegaal, M.; Fabbri, E.; Copéret, C.; Schmidt, T. J., Iridium Oxide for the Oxygen Evolution Reaction: Correlation between Particle Size, Morphology, and the Surface Hydroxo Layer from Operando XAS. *Chemistry of Materials* **2016**, 28 (18), 6591-6604.
67. Hegge, F.; Lombeck, F.; Cruz Ortiz, E.; Bohn, L.; von Holst, M.; Kroschel, M.; Hübner, J.; Breitwieser, M.; Strasser, P.; Vierrath, S., Efficient and stable low iridium loaded anodes for PEM water electrolysis made possible by nanofiber interlayers. *ACS Applied Energy Materials* **2020**, 3 (9), 8276-8284.
68. Alia, S. M.; Shulda, S.; Ngo, C.; Pylypenko, S.; Pivovar, B. S., Iridium-based nanowires as highly active, oxygen evolution reaction electrocatalysts. *ACS Catalysis* **2018**, 8 (3), 2111-2120.
69. Lewinski, K. A.; van der Vliet, D.; Luopa, S. M., NSTF advances for PEM electrolysis- the effect of alloying on activity of NSTF electrolyzer catalysts and performance of NSTF based PEM electrolyzers. *Ecs Transactions* **2015**, 69 (17), 893.

70. Fu, C.; O'Carroll, T.; Shen, S.; Luo, L.; Zhang, J.; Xu, H.; Wu, G., Metallic-Ir-based Anode Catalysts in PEM Water Electrolyzers: Achievements, Challenges, and Perspectives. *Current Opinion in Electrochemistry* **2023**, 101227.
71. Tang, J.; Xu, X.; Tang, T.; Zhong, Y.; Shao, Z., Perovskite-Based Electrocatalysts for Cost-Effective Ultrahigh-Current-Density Water Splitting in Anion Exchange Membrane Electrolyzer Cell. *Small Methods* **2022**, 6 (11), 2201099.
72. Böhm, D.; Beetz, M.; Schuster, M.; Peters, K.; Hufnagel, A. G.; Döblinger, M.; Böller, B.; Bein, T.; Fattakhova-Rohlfing, D., Efficient OER Catalyst with Low Ir Volume Density Obtained by Homogeneous Deposition of Iridium Oxide Nanoparticles on Macroporous Antimony-Doped Tin Oxide Support. *Advanced Functional Materials* **2020**, 30 (1), 1906670.
73. Hartig-Weiss, A.; Miller, M.; Beyer, H.; Schmitt, A.; Siebel, A.; Freiberg, A. T.; Gasteiger, H. A.; El-Sayed, H. A., Iridium oxide catalyst supported on antimony-doped tin oxide for high oxygen evolution reaction activity in acidic media. *ACS Applied Nano Materials* **2020**, 3 (3), 2185-2196.
74. Mom, R. V.; Falling, L. J.; Kasian, O.; Algara-Siller, G.; Teschner, D.; Crabtree, R. H.; Knop-Gericke, A.; Mayrhofer, K. J.; Velasco-Vélez, J.-J. s.; Jones, T. E., Operando structure–activity–stability relationship of iridium oxides during the oxygen evolution reaction. *ACS Catalysis* **2022**, 12 (9), 5174-5184.
75. Su, H.; Zhou, W.; Zhou, W.; Li, Y.; Zheng, L.; Zhang, H.; Liu, M.; Zhang, X.; Sun, X.; Xu, Y., In-situ spectroscopic observation of dynamic-coupling oxygen on atomically dispersed iridium electrocatalyst for acidic water oxidation. *Nature Communications* **2021**, 12 (1), 6118.
76. Weber, T.; Vonk, V.; Escalera-López, D.; Abbondanza, G.; Larsson, A.; Koller, V.; Abb, M. J.; Hegedüs, Z.; Bäcker, T.; Lienert, U., Operando stability studies of ultrathin single-crystalline IrO₂ (110) films under acidic oxygen evolution reaction conditions. *ACS Catalysis* **2021**, 11 (20), 12651-12660.
77. Jiang, K.; Luo, M.; Peng, M.; Yu, Y.; Lu, Y.-R.; Chan, T.-S.; Liu, P.; de Groot, F. M.; Tan, Y., Dynamic active-site generation of atomic iridium stabilized on nanoporous metal phosphides for water oxidation. *Nature communications* **2020**, 11 (1), 2701.
78. Ledendecker, M.; Geiger, S.; Hengge, K.; Lim, J.; Cherevko, S.; Mingers, A. M.; Göhl, D.; Fortunato, G. V.; Jalalpoor, D.; Schüth, F., Towards maximized utilization of iridium for the acidic oxygen evolution reaction. *Nano research* **2019**, 12, 2275-2280.

1.7. References

79. Du, L.; Shao, Y.; Sun, J.; Yin, G.; Liu, J.; Wang, Y., Advanced catalyst supports for PEM fuel cell cathodes. *Nano Energy* **2016**, *29*, 314-322.
80. Bagheri, S.; Muhd Julkapli, N.; Bee Abd Hamid, S., Titanium dioxide as a catalyst support in heterogeneous catalysis. *The scientific world journal* **2014**, *2014*.
81. Yu, Y.; Li, H.; Wang, H.; Yuan, X.-Z.; Wang, G.; Pan, M., A review on performance degradation of proton exchange membrane fuel cells during startup and shutdown processes: Causes, consequences, and mitigation strategies. *Journal of Power Sources* **2012**, *205*, 10-23.
82. Zhao, Y.; Yang, K. R.; Wang, Z.; Yan, X.; Cao, S.; Ye, Y.; Dong, Q.; Zhang, X.; Thorne, J. E.; Jin, L., Stable iridium dinuclear heterogeneous catalysts supported on metal-oxide substrate for solar water oxidation. *Proceedings of the National Academy of Sciences* **2018**, *115* (12), 2902-2907.
83. Bizzotto, F.; Quinson, J.; Schröder, J.; Zana, A.; Arenz, M., Surfactant-free colloidal strategies for highly dispersed and active supported IrO₂ catalysts: Synthesis and performance evaluation for the oxygen evolution reaction. *Journal of Catalysis* **2021**, *401*, 54-62.
84. Moriau, L.; Bele, M.; Marinko, Ž.; Ruiz-Zepeda, F.; Koderman Podboršek, G.; Šala, M.; Šurca, A. K.; Kovač, J.; Arčon, I.; Jovanovič, P.; Hodnik, N.; Suhadolnik, L., Effect of the Morphology of the High-Surface-Area Support on the Performance of the Oxygen-Evolution Reaction for Iridium Nanoparticles. *ACS Catalysis* **2021**, *11* (2), 670-681.
85. Wang, C.; Yang, F.; Feng, L., Recent advances in iridium-based catalysts with different dimensions for acidic oxygen evolution reaction. *Nanoscale Horizons* **2023**.
86. Pittkowski, R. K.; Abbott, D. F.; Nebel, R.; Divanis, S.; Fabbri, E.; Castelli, I. E.; Schmidt, T. J.; Rossmeisl, J.; Krtić, P., Synergistic effects in oxygen evolution activity of mixed iridium-ruthenium pyrochlores. *Electrochimica Acta* **2021**, *366*, 137327.
87. Zhou, Z.-H.; Sun, W.; Zaman, W.; Cao, L.; Yang, J., Highly active and stable synergistic Ir–IrO₂ electro-catalyst for oxygen evolution reaction. *Chemical Engineering Communications* **2018**, *205*, 1-9.
88. Tovini, M. F.; Damjanovic, A. M.; El-Sayed, H. A.; Speder, J.; Eickes, C.; Suchsland, J.-P.; Ghielmi, A.; Gasteiger, H. A., Degradation mechanism of an IrO₂ anode co-catalyst for cell voltage reversal mitigation under transient operation conditions of a PEM fuel cell. *Journal of The Electrochemical Society* **2021**, *168* (6), 064521.
89. da Silva, G. C.; Mayrhofer, K. J. J.; Ticianelli, E. A.; Cherevko, S., The degradation of Pt/IrO_x oxygen bifunctional catalysts. *Electrochimica Acta* **2019**, *308*, 400-409.
90. Czioska, S.; Boubnov, A.; Escalera-López, D.; Geppert, J.; Zagalskaya, A.; Röse, P.; Saraçi, E.; Alexandrov, V.; Krewer, U.; Cherevko, S.; Grunwaldt, J.-D., Increased Ir–Ir

Interaction in Iridium Oxide during the Oxygen Evolution Reaction at High Potentials Probed by Operando Spectroscopy. *ACS Catalysis* **2021**, *11* (15), 10043-10057.

91. van der Merwe, M.; Garcia-Diez, R.; Lahn, L.; Wibowo, R. E.; Frisch, J.; Gorgoi, M.; Yang, W.; Ueda, S.; Wilks, R. G.; Kasian, O.; Bär, M., The Chemical and Electronic Properties of Stability-Enhanced, Mixed Ir-TiO_x Oxygen Evolution Reaction Catalysts. *ACS Catalysis* **2023**, *13* (23), 15427-15438.

92. Munnik, P.; de Jongh, P. E.; de Jong, K. P., Recent Developments in the Synthesis of Supported Catalysts. *Chemical Reviews* **2015**, *115* (14), 6687-6718.

93. Lim, A.; Kim, J.; Lee, H. J.; Kim, H.-J.; Yoo, S. J.; Jang, J. H.; Park, H. Y.; Sung, Y.-E.; Park, H. S., Low-loading IrO₂ supported on Pt for catalysis of PEM water electrolysis and regenerative fuel cells. *Applied Catalysis B: Environmental* **2020**, *272*, 118955.

94. Li, L.; Li, G.; Zhang, Y.; Ouyang, W.; Zhang, H.; Dong, F.; Gao, X.; Lin, Z., Fabricating nano-IrO₂@ amorphous Ir-MOF composites for efficient overall water splitting: a one-pot solvothermal approach. *Journal of Materials Chemistry A* **2020**, *8* (48), 25687-25695.

95. He, H., Metal oxide semiconductors and conductors. In *Solution Processed Metal Oxide Thin Films for Electronic Applications*, Elsevier: 2020; pp 7-30.

96. Yang, G.; Yu, S.; Li, Y.; Li, K.; Ding, L.; Xie, Z.; Wang, W.; Zhang, F.-Y., Role of electron pathway in dimensionally increasing water splitting reaction sites in liquid electrolytes. *Electrochimica Acta* **2020**, *362*, 137113.

97. Neagu, D.; Irvine, J. T., Enhancing electronic conductivity in strontium titanates through correlated A and B-site doping. *Chemistry of materials* **2011**, *23* (6), 1607-1617.

98. Wang, Q.; Cheng, Y.; Tao, H. B.; Liu, Y.; Ma, X.; Li, D. S.; Yang, H. B.; Liu, B., Long-Term Stability Challenges and Opportunities in Acidic Oxygen Evolution Electrocatalysis. *Angewandte Chemie International Edition* **2023**, *62* (11), e202216645.

99. Gao, J.; Huang, X.; Cai, W.; Wang, Q.; Jia, C.; Liu, B., Rational Design of an Iridium–Tungsten Composite with an Iridium-Rich Surface for Acidic Water Oxidation. *ACS Applied Materials & Interfaces* **2020**, *12* (23), 25991-26001.

100. Yamada, I.; Fujii, H.; Takamatsu, A.; Ikeno, H.; Wada, K.; Tsukasaki, H.; Kawaguchi, S.; Mori, S.; Yagi, S., Bifunctional oxygen reaction catalysis of quadruple manganese perovskites. *Advanced Materials* **2017**, *29* (4), 1603004.

101. Kost, M.; Kornherr, M.; Zehetmaier, P.; Illner, H.; Jeon, D. S.; Gasteiger, H.; Döblinger, M.; Fattakhova-Rohlfing, D.; Bein, T., Chemical Epitaxy of Iridium Oxide on Tin Oxide Enhances Stability of Supported OER Catalyst. *Small* *n/a* (n/a), 2404118.

1.7. References

102. Chen, Y.; Liu, C.; Xu, J.; Xia, C.; Wang, P.; Xia, B. Y.; Yan, Y.; Wang, X., Key Components and Design Strategy for a Proton Exchange Membrane Water Electrolyzer. *Small Structures* **2023**, *4* (6), 2200130.
103. Liu, L.; Xu, W.; Ding, Y.; Agarwal, S.; Greiner, A.; Duan, G., A review of smart electrospun fibers toward textiles. *Composites Communications* **2020**, *22*, 100506.
104. Repanas, A.; Andriopoulou, S.; Glasmacher, B., The significance of electrospinning as a method to create fibrous scaffolds for biomedical engineering and drug delivery applications. *Journal of Drug Delivery Science and Technology* **2016**, *31*, 137-146.
105. Teo, W. E.; Ramakrishna, S., A review on electrospinning design and nanofibre assemblies. *Nanotechnology* **2006**, *17* (14), R89.
106. Li, C.; Chen, R.; Zhang, X.; Shu, S.; Xiong, J.; Zheng, Y.; Dong, W., Electrospinning of CeO₂-ZnO composite nanofibers and their photocatalytic property. *Materials Letters* **2011**, *65* (9), 1327-1330.
107. Blachowicz, T.; Ehrmann, A., Recent developments in electrospun ZnO nanofibers: A short review. *Journal of Engineered Fibers and Fabrics* **2020**, *15*, 1558925019899682.
108. Xu, F.; Tan, H.; Fan, J.; Cheng, B.; Yu, J.; Xu, J., Electrospun TiO₂-based photocatalysts. *Solar RRL* **2021**, *5* (6), 2000571.
109. Al-Mezrakchi, R. Y. H., An investigation into scalability production of ultra-fine nanofiber using electrospinning systems. *Fibers and Polymers* **2018**, *19* (1), 105-115.
110. Huang, Y.; Song, J.; Yang, C.; Long, Y.; Wu, H., Scalable manufacturing and applications of nanofibers. *Materials Today* **2019**, *28*, 98-113.
111. Li, Y.; Zhu, J.; Cheng, H.; Li, G.; Cho, H.; Jiang, M.; Gao, Q.; Zhang, X., Developments of advanced electrospinning techniques: A critical review. *Advanced Materials Technologies* **2021**, *6* (11), 2100410.
112. Long, Y.-Z.; Yan, X.; Wang, X.-X.; Zhang, J.; Yu, M., Electrospinning: the setup and procedure. In *Electrospinning: Nanofabrication and applications*, Elsevier: 2019; pp 21-52.
113. Merritt, S. R.; Exner, A. A.; Lee, Z.; von Recum, H. A., Electrospinning and imaging. *Advanced Engineering Materials* **2012**, *14* (5), B266-B278.
114. Someswararao, M.; Dubey, R.; Subbarao, P.; Singh, S., Electrospinning process parameters dependent investigation of TiO₂ nanofibers. *Results in Physics* **2018**, *11*, 223-231.
115. Teo, W. E.; Ramakrishna, S., A review on electrospinning design and nanofibre assemblies. *Nanotechnology* **2006**, *17* (14), R89-R106.
116. Fong H., C. I., Reneker D. H., Beaded nanofibers formed during electrospinning. *Polymer* **1999**, *40*, 4585-4592.

117. Kim, I. D.; Rothschild, A., Nanostructured metal oxide gas sensors prepared by electrospinning. *Polymers for Advanced Technologies* **2011**, 22 (3), 318-325.
118. Figen, A. K.; Filiz, B. C., Polymeric and metal oxide structured nanofibrous composites fabricated by electrospinning as highly efficient hydrogen evolution catalyst. *Journal of colloid and interface science* **2019**, 533, 82-94.
119. Huang, C.; Thomas, N. L., Fabrication of porous fibers via electrospinning: strategies and applications. *Polymer Reviews* **2020**, 60 (4), 595-647.
120. Kanzler, C. H.; Urban, S.; Zalewska-Wierzbicka, K.; Hess, F.; Rohrlack, S. F.; Wessel, C.; Ostermann, R.; Hofmann, J. P.; Smarsly, B. M.; Over, H., Electrospun metal oxide nanofibres for the assessment of catalyst morphological stability under harsh reaction conditions. *ChemCatChem* **2013**, 5 (9), 2621-2626.
121. Hoogesteijn von Reitzenstein, N.; Bi, X.; Yang, Y.; Hristovski, K.; Westerhoff, P., Morphology, structure, and properties of metal oxide/polymer nanocomposite electrospun mats. *Journal of Applied Polymer Science* **2016**, 133 (33).
122. Rauf, M.; Wang, J.-W.; Zhang, P.; Iqbal, W.; Qu, J.; Li, Y., Non-precious nanostructured materials by electrospinning and their applications for oxygen reduction in polymer electrolyte membrane fuel cells. *Journal of Power Sources* **2018**, 408, 17-27.
123. Zhu, Q.-L.; Xu, Q., Immobilization of ultrafine metal nanoparticles to high-surface-area materials and their catalytic applications. *Chem* **2016**, 1 (2), 220-245.
124. Muthukrishnan, L., An overview on electrospinning and its advancement toward hard and soft tissue engineering applications. *Colloid and Polymer Science* **2022**, 300 (8), 875-901.
125. Li, Y.; Zhang, Y.; Qian, K.; Huang, W., Metal–support interactions in metal/oxide catalysts and oxide–metal interactions in oxide/metal inverse catalysts. *ACS Catalysis* **2022**, 12 (2), 1268-1287.
126. Li, Q.; Lau, K. M., Epitaxial growth of highly mismatched III-V materials on (001) silicon for electronics and optoelectronics. *Progress in Crystal Growth and Characterization of Materials* **2017**, 63 (4), 105-120.
127. Otero-Martínez, C.; Ye, J.; Sung, J.; Pastoriza-Santos, I.; Pérez-Juste, J.; Xia, Z.; Rao, A.; Hoyer, R. L.; Polavarapu, L., Colloidal metal-halide perovskite nanoplatelets: thickness-controlled synthesis, properties, and application in light-emitting diodes. *Advanced Materials* **2022**, 34 (10), 2107105.
128. Bromann, K.; Brune, H.; Röder, H.; Kern, K., Interlayer mass transport in homoepitaxial and heteroepitaxial metal growth. *Physical review letters* **1995**, 75 (4), 677.

1.7. References

129. Ji, J.; Kwak, H.-M.; Yu, J.; Park, S.; Park, J.-H.; Kim, H.; Kim, S.; Kim, S.; Lee, D.-S.; Kum, H. S., Understanding the 2D-material and substrate interaction during epitaxial growth towards successful remote epitaxy: a review. *Nano Convergence* **2023**, *10* (1), 1-21.
130. Jiang, H.; Klemmer, T.; Barnard, J.; Payzant, E., Epitaxial growth of Cu on Si by magnetron sputtering. *Journal of Vacuum Science & Technology A: Vacuum, Surfaces, and Films* **1998**, *16* (6), 3376-3383.
131. Kuphal, E., Liquid phase epitaxy. *Applied Physics A* **1991**, *52* (6), 380-409.
132. Seitz, L. C.; Dickens, C. F.; Nishio, K.; Hikita, Y.; Montoya, J.; Doyle, A.; Kirk, C.; Vojvodic, A.; Hwang, H. Y.; Norskov, J. K., A highly active and stable IrO_x/SrIrO₃ catalyst for the oxygen evolution reaction. *Science* **2016**, *353* (6303), 1011-1014.
133. Cho, A. Y.; Arthur, J., Molecular beam epitaxy. *Progress in solid state chemistry* **1975**, *10*, 157-191.
134. Davey, J. E.; Pankey, T., Epitaxial GaAs films deposited by vacuum evaporation. *Journal of Applied Physics* **1968**, *39* (4), 1941-1948.
135. Weber, M.; Boysen, N.; Graniel, O.; Sekkat, A.; Dussarrat, C.; Wiff, P.; Devi, A.; Muñoz-Rojas, D., Assessing the Environmental Impact of Atomic Layer Deposition (ALD) Processes and Pathways to Lower It. *ACS Materials Au* **2023**, *3* (4), 274-298.
136. Matienzo, D. D.; Settapani, D.; Instuli, E.; Kallio, T., Active IrO₂ and NiO thin films prepared by atomic layer deposition for oxygen evolution reaction. *Catalysts* **2020**, *10* (1), 92.
137. Hämäläinen, J.; Kemell, M.; Munnik, F.; Kreissig, U.; Ritala, M.; Leskelä, M., Atomic Layer Deposition of Iridium Oxide Thin Films from Ir(acac)₃ and Ozone. *Chemistry of Materials* **2008**, *20*.
138. Zilko, J. L., Metal organic chemical vapor deposition: technology and equipment. In *Handbook of thin film deposition processes and techniques*, Elsevier: 2001; pp 151-203.
139. Watson, I. M., Metal organic vapour phase epitaxy of AlN, GaN, InN and their alloys: A key chemical technology for advanced device applications. *Coordination Chemistry Reviews* **2013**, *257* (13), 2120-2141.
140. Phillips, J. M., Substrate selection for thin-film growth. *MRS Bulletin* **1995**, *20* (4), 35-39.
141. Wadayama, T.; Todoroki, N.; Yamada, Y.; Sugawara, T.; Miyamoto, K.; Iijima, Y., Oxygen reduction reaction activities of Ni/Pt (111) model catalysts fabricated by molecular beam epitaxy. *Electrochemistry communications* **2010**, *12* (8), 1112-1115.

142. Cui, P.; Wang, T.; Zhang, X.; Wang, X.; Wu, H.; Wu, Y.; Ba, C.; Zeng, Y.; Liu, P.; Jiang, J., Rapid Formation of Epitaxial Oxygen Evolution Reaction Catalysts on Dendrites with High Catalytic Activity and Stability. *ACS Nano* **2023**, *17* (22), 22268-22276.
143. De Heer, W. A.; Berger, C.; Wu, X.; Sprinkle, M.; Hu, Y.; Ruan, M.; Strosio, J. A.; First, P. N.; Haddon, R.; Piot, B., Epitaxial graphene electronic structure and transport. *Journal of Physics D: Applied Physics* **2010**, *43* (37), 374007.
144. Rajan, Z. S. H. S.; Binniger, T.; Kooyman, P. J.; Susac, D.; Mohamed, R., Organometallic chemical deposition of crystalline iridium oxide nanoparticles on antimony-doped tin oxide support with high-performance for the oxygen evolution reaction. *Catalysis Science & Technology* **2020**, *10* (12), 3938-3948.
145. Weiss, W.; Ranke, W., Surface chemistry and catalysis on well-defined epitaxial iron-oxide layers. *Progress in Surface Science* **2002**, *70* (1), 1-151.
146. Zhao, Y.; Wang, Y.; Cheng, X.; Dong, L.; Zhang, Y.; Zang, J., Platinum nanoparticles supported on epitaxial TiC/nanodiamond as an electrocatalyst with enhanced durability for fuel cells. *Carbon* **2014**, *67*, 409-416.
147. Malygin, A. A.; Drozd, V. E.; Malkov, A. A.; Smirnov, V. M., From V. B. Aleskovskii's "Framework" Hypothesis to the Method of Molecular Layering/Atomic Layer Deposition *Chemical Vapor Deposition* **2015**, *21* (10-11-12), 216-240.
148. Suntola, T., Atomic layer epitaxy. *Materials Science Reports* **1989**, *4* (5), 261-312.
149. Puurunen, R. L., A Short History of Atomic Layer Deposition: Tuomo Suntola's Atomic Layer Epitaxy. *Chemical Vapor Deposition* **2014**, *20* (10-11-12), 332-344.
150. Leskelä, M.; Ritala, M., Atomic layer deposition (ALD): from precursors to thin film structures. *Thin solid films* **2002**, *409* (1), 138-146.
151. Ahn, J.; Ahn, C.; Jeon, S.; Park, J., Atomic layer deposition of inorganic thin films on 3D polymer nanonetworks. *Applied Sciences* **2019**, *9* (10), 1990.
152. Kim, H., Atomic layer deposition of metal and nitride thin films: Current research efforts and applications for semiconductor device processing. *Journal of Vacuum Science & Technology B: Microelectronics and Nanometer Structures Processing, Measurement, and Phenomena* **2003**, *21* (6), 2231-2261.
153. Laube, A.; Hofer, A.; Ressel, S.; Chica, A.; Bachmann, J.; Struckmann, T., PEM water electrolysis cells with catalyst coating by atomic layer deposition. *international journal of hydrogen energy* **2021**, *46* (79), 38972-38982.
154. Frisch, M.; Raza, M. H.; Ye, M.-Y.; Sachse, R.; Paul, B.; Gunder, R.; Pinna, N.; Kraehnert, R., ALD-Coated Mesoporous Iridium-Titanium Mixed Oxides: Maximizing

1.7. References

Iridium Utilization for an Outstanding OER Performance. *Advanced Materials Interfaces* **2022**, 9 (6), 2102035.

155. Park, N.-Y.; Kim, M.; Kim, Y.-H.; Ramesh, R.; Nandi, D. K.; Tsugawa, T.; Shigetomi, T.; Suzuki, K.; Harada, R.; Kim, M., Atomic layer deposition of iridium using a tricarbonyl cyclopropenyl precursor and oxygen. *Chemistry of Materials* **2022**, 34 (4), 1533-1543.

156. Mattinen, M.; Hämäläinen, J.; Vehkamäki, M.; Heikkilä, M. J.; Mizohata, K.; Jalkanen, P.; Räisänen, J.; Ritala, M.; Leskelä, M., Atomic Layer Deposition of Iridium Thin Films Using Sequential Oxygen and Hydrogen Pulses. *The Journal of Physical Chemistry C* **2016**, 120 (28), 15235-15243.

157. Corbin, J.; Jones, M.; Lyu, C.; Loh, A.; Zhang, Z.; Zhu, Y.; Li, X., Challenges and progress in oxygen evolution reaction catalyst development for seawater electrolysis for hydrogen production. *RSC Advances* **2024**, 14 (9), 6416-6442.

158. Exner, K. S., Controlling Stability and Selectivity in the Competing Chlorine and Oxygen Evolution Reaction over Transition Metal Oxide Electrodes. *ChemElectroChem* **2019**, 6 (13), 3401-3409.

159. Munoz-Rojas, D.; Maindron, T.; Esteve, A.; Piallat, F.; Kools, J.; Decams, J.-M., Speeding up the unique assets of atomic layer deposition. *Materials Today Chemistry* **2019**, 12, 96-120.

160. Chen, X.; Knez, M.; Berger, A.; Nielsch, K.; Gösele, U.; Steinhart, M., Formation of Titania/Silica Hybrid Nanowires Containing Linear Mesocage Arrays by Evaporation-Induced Block-Copolymer Self-Assembly and Atomic Layer Deposition. *Angewandte Chemie International Edition* **2007**, 46 (36), 6829-6832.

161. Ma, H.; Wei, Y.; Wang, J.; Lin, X.; Wu, W.; Wu, Y.; Zhang, L.; Liu, P.; Wang, J.; Li, Q.; Fan, S.; Jiang, K., Freestanding macroscopic metal-oxide nanotube films derived from carbon nanotube film templates. *Nano Research* **2015**, 8 (6), 2024-2032.

162. Shi, J.; Sun, C.; Starr, M. B.; Wang, X., Growth of titanium dioxide nanorods in 3D-confined spaces. *Nano letters* **2011**, 11 (2), 624-631.

163. Marichy, C.; Bechelany, M.; Pinna, N., Atomic layer deposition of nanostructured materials for energy and environmental applications. *Advanced materials* **2012**, 24 (8), 1017-1032.

CHAPTER 2

Characterization

2. Characterization

For the characterization of nanomaterials, several different analytical techniques can be applied. Scanning electron microscopy (SEM) with energy dispersive X-ray spectroscopy (EDX) and transmission electron microscopy (TEM) allow for the imaging of a specimen and can be used to gain information about the particle size, morphology and crystal structure, pore structure and chemical composition. Further information about the surface area, pore size distribution and pore volume of porous materials can be obtained with nitrogen sorption measurements. The temperature range for crystallization of amorphous iridium oxide was determined using thermogravimetric analysis (TGA). X-ray photoelectron spectroscopy (XPS) allows the oxidation states of the sample components to be determined.

Furthermore, two-electrode were used to determine the conductivity of the samples for an initial assessment of the performance of the OER catalysts. Electrochemical measurements such as cyclic voltammetry (CV) in a static measurement cell and chronopotentiometry (CP) allowed for an assessment of the activity and provided initial insights into the stability of the catalysts.

2.1. Nitrogen Physisorption Measurements

A fundamental tool to characterize porous materials is nitrogen physisorption. This technique can be used to assess the surface area, pore size and volume, pore distribution, and adsorption properties of nanostructured materials such as semiconductor oxides for water splitting applications.¹ The surface area of a carrier material is a critical parameter for the subsequent coating with the active component, as it can be used to estimate the required quantity of material to coat the surface of the carrier with a specific thickness.²

The term adsorption is defined by the International Union of Pure and Applied Chemistry (IUPAC) as the enrichment of one or more components at an interface. The distinction is made between chemisorption and physisorption. In physisorption, weak interactions, such as van-der-Waals forces, result in the occupation of the respective interface between porous sample (adsorbent) and gas molecules (adsorbate), a reversible process in contrast to the irreversible chemisorption. At temperatures corresponding to the boiling point of the respective gas (77 K, the boiling point of nitrogen), an adsorption and desorption isotherm is recorded at different relative pressures p/p^0 , where p is the equilibrium pressure and p^0 is the saturation vapor pressure.² IUPAC has defined six main classes of sorption isotherms which are visualized in Figure 2-1, with micropores defined as pores below a diameter of 2 nm, mesopores with a diameter between 2 and 50 nm and macropores which exceed a diameter of 50 nm:

Type I isotherms show a steep increase in adsorbed volume at low relative pressures due to their small pore diameter typical for microporous materials. The micropores are thus filled and reach a maximum value defined by the accessible micropore volume. *Type I* isotherms can be further subdivided into *Type Ia* for materials with narrow micropores (< 1 nm) and *Type Ib* for materials with a range of wider micropores and narrow mesopores (< 2.5 nm).

Type II is typically observed with non-porous or macroporous materials, and is characterized by a monolayer adsorption followed by unrestricted multilayer adsorption.

Type III does not show a distinct monolayer adsorption owing to dominant adsorbate-adsorbate interactions.

Type IV isotherms with apparent hysteresis loop is indicative of capillary condensation, a characteristic of mesoporous materials. The initial part of this loop is attributed to monolayer adsorption. The initial monolayer-multilayer adsorption takes the same path as the

corresponding part of a *type II* isotherm and is then followed by pore condensation. Here, the adsorbing gas condenses to a liquid-like phase within the pore at a pressure p that is smaller than the saturation pressure p^0 . Here, IUPAC distinguishes between *type IVa* isotherms which are accompanied by hysteresis of the capillary condensation, which occurs for pore widths exceeding ≈ 4 nm. In contrast, *type IVb* isotherms, which are entirely reversible, are observed for mesopores with smaller conical or cylindrical pore shapes.

Type V isotherms resemble those of *type III*, a consequence of the reduced adsorbate-adsorbent interactions. The hysteresis loop can be attributed to capillary condensation within the mesopores. *Type VI* isotherms, on the other hand, demonstrate a stepwise multilayer adsorption process on a highly uniform and non-porous surface, with each step in the uptake representing the capacity for an adsorbed monolayer on the surface.^{1, 3}

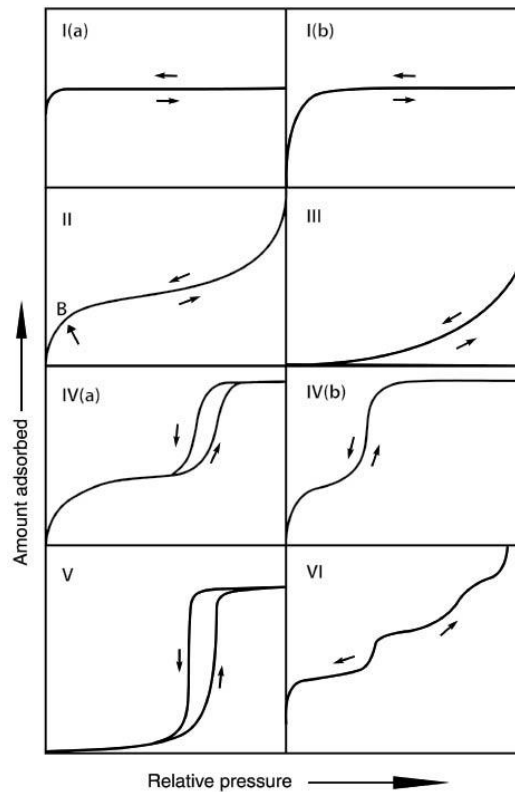


Figure 2-1: IUPAC classification of physisorption isotherms.³ Reprinted with permission of ref [3]. Copyright © 2015 IUPAC & De Gruyter.

One theory to interpret the results of sorption measurements is represented by the BET (Brunauer-Emmett-Teller) equation. It is based on three fundamental assumptions:

- (a) adsorptive species within each layer do not interact

- (b) the energy of adsorption remains constant across all layers, with the exception of the first layer due to adsorbent-adsorbate interactions
- (c) the number of adsorbed layers becoming infinite at $p/p^0 = 1$.

The BET can be expressed as:

$$\frac{p}{n^a (p^0 - p)} = \frac{1}{n_m^a C} + \frac{(C - 1) p}{n_m^a C p^0} \quad (1)$$

With n^a describing the adsorbed amount of nitrogen at the relative pressure $\frac{p}{p^0}$, n_m^a the monolayer capacity, p the equilibrium pressure and p^0 the saturation pressure. In BET theory, C is exponentially related to the enthalpy of adsorption of the first adsorbed layer. Further, the value of C can be applied to describe the shape of the isotherm according to the BET theory, with a high value indicating strong adsorbent-adsorbate interactions.^{1, 4, 5}

The BET theory is also used to calculate the surface area via the monolayer capacity. Therefore, the average area, a_m (molecular cross-section area), which is occupied by the adsorbate molecule in the monolayer is essential and calculated as in the following:

$$A_s(BET) = n_m^a L a_m \quad (2)$$

$$a_s(BET) = \frac{A_s(BET)}{m} \quad (3)$$

$A_s(BET)$ represents the total surface area, $a_s(BET)$ the specific surface area, m the mass of the adsorbent, and L the Avogadro constant and n_m^a is the monolayer capacity.¹

2.2. Thermogravimetric Analysis

Thermogravimetric analysis (TGA) is an analytical method to track changes in a material's weight as a function of temperature or time under controlled atmospheric conditions, offering insights into diverse material transformations including melting, crystallization, decomposition, volatilization, oxidation, and reduction processes.⁶

Through a controlled temperature program, the sample's weight is continuously monitored and depicted as a thermogravimetric curve, revealing the correlation between mass loss and temperature or time. Distinct features of the curve, such as inflection points and gradients, yield

vital information regarding the nature and extent of transformations occurring within the material.⁶ A typical TGA apparatus usually comprises a sample pan and a scale housed within a heated chamber. The sample is positioned in the pan, and the chamber is heated at a controlled rate. The incorporated scale records the mass changes upon thermal transitions. In general, TGA instruments can operate under various atmospheric conditions, including inert (e.g., nitrogen or argon) or oxidative (e.g., air) environments, enabling targeted investigation of specific chemical reactions or degradation phenomena.^{6, 7}

Changes in weight are a result of dehydration of sample, desorption of adsorbed species, thermal decomposition to volatile products, formation of oxides with associated weight gain, pyrolysis upon gas exchange from oxygen to nitrogen with associated weight loss, or explosive decomposition with recoil effect with associated apparent weight gain and subsequent weight loss.⁷

In this work, TGA was used to determine the temperature for crystallization of amorphous IrO_x to IrO_2 . Temperature differences as small as 5-10 °C in calcination temperature in air influence the resulting iridium oxide phase and lead to differences in conductivity, activity and cycling stability of respective catalysts.

In these TGA experiments, dried catalyst powder which was either SnO_2 or TiO_2 supported IrO_x was heated with a temperature ramp of 10 °C/min to a maximum temperature of 900 °C in synthetic air flow of 25 ml min⁻¹.

2.3. X-Ray Photoelectron Spectroscopy

X-ray photoelectron spectroscopy (XPS) represents a fundamental technique in surface analysis, providing a wealth of information regarding the elemental composition, chemical and oxidation states, as well as electronic structures of materials. This method operates on the principle of the photoelectric effect, wherein irradiation of a sample's surface with X-rays induces the emission of photoelectrons as illustrated in Figure 2-2.

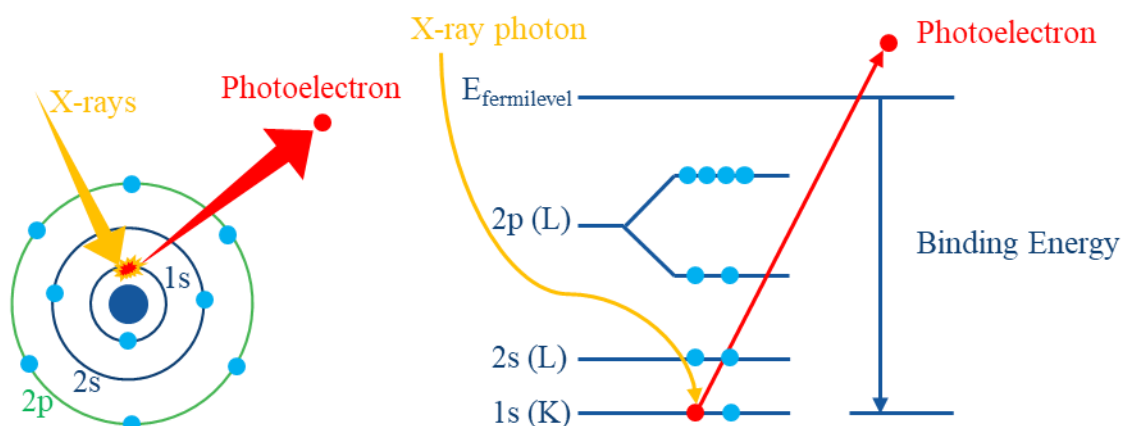


Figure 2-2: Photoelectron generation upon irradiation of sample with X-rays and emitted photoelectron.

These emitted electrons, whose kinetic energies are characteristic for each element present and their chemical bonding environments, are then analyzed to deduce vital information about the surface chemistry of the material under investigation.⁸ A typical XPS instrumentation as illustrated in Figure 2-3, comprising an X-ray source, a hemispherical electron/energy analyzer, a multi-channel detector plate and a sample stage in a high-vacuum environment to prevent electron scattering and ensure accurate analysis.⁹

One of the key strengths of XPS lies in its ability to provide quantitative elemental analysis, allowing determination of the concentration of elements present on the surface of respective materials. XPS is surface sensitive due to the short inelastic mean free path, λ , of electrons in condensed materials. By measuring the intensity of characteristic photoelectron peaks corresponding to each element, XPS can accurately quantify elemental composition down to the parts per thousand level depending on the apparatus' specifications. This capability is particularly useful in characterizing thin films, coatings, and multilayered structures, where precise elemental composition is critical for gaining a deeper understanding of material properties and performance.⁸

Furthermore, XPS offers valuable insights into the chemical bonding environment of surface atoms. The energy and shape of XPS peaks provide information about the oxidation states and chemical states of elements within a material. By comparing experimental spectra to reference spectra and employing sophisticated data analysis techniques, researchers can identify specific chemical species and their distribution on the material's surface. This capability is essential for studying surface reactions, catalysts, and interfaces in various applications, including heterogeneous catalysis, semiconductor devices, and corrosion protection coatings.^{10, 11}

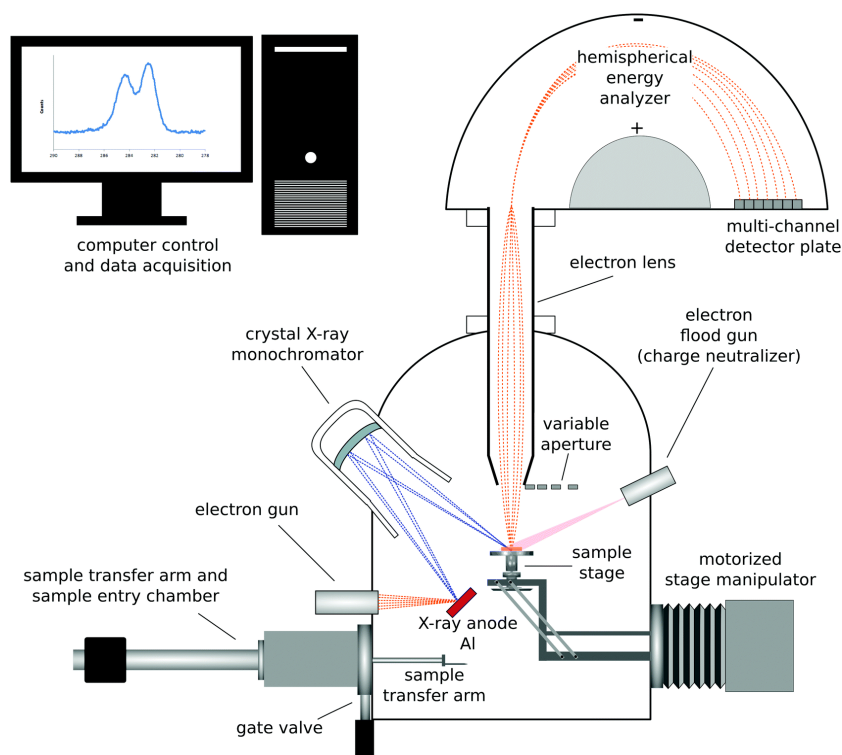


Figure 2-3: Schematic drawing of a monochromatized XPS instrument.⁹ Reprinted with permission of ref [9] Copyright © 2021, Royal Society of Chemistry.

In addition to elemental and chemical state analysis, XPS enables the investigation of surface contamination and adsorption phenomena. Surface-sensitive measurements can reveal the presence of adsorbed species, such as water, gases, or organic contaminants, which can significantly impact material performance and stability. XPS depth profiling techniques, such as angle-resolved XPS and sputter depth profiling, allow to probe surface composition as a function of depth, providing valuable information about surface segregation, diffusion processes, and interfacial reactions.¹² In this work, XPS was used to determine the oxidation state of iridium species. The measurements were carried out by using a VSW TA10 X-ray source set at 15 mA and 12 kV providing non-monochromatized Mg K α radiation ($h\nu = 1253.6$ eV) and a VSW HA100 hemispherical analyzer. The spectra were recorded with a pass energy of 22 eV and a dwell time of 0.1 s per measurement point. The samples were prepared by drop-casting a dispersion of the respective sample in a (1:1 v/v) water to isopropanol ratio on ITO glass. After drying, the samples were transferred to the UHV chamber.

XPS is a crucial tool in catalyst development due to its ability to provide detailed surface chemical information and the high surface-sensitivity, making it ideal for characterizing the active sites of catalysts, which are often located on the surface.¹³ For instance, XPS can help to understand the relation between surface chemistry and electrocatalytic activity. As an

example, lanthanum ferrite based electrolysis cathodes were examined with XPS. Under cathodic polarization the formation of metallic iron on the surface of the cathode could be observed, which was accompanied by a strong improvement of the water splitting activity of the electrolysis cell. This suggests that the underlying water splitting mechanism in presence of metallic iron species is fundamentally different and opens novel paths towards the design of electrodes with increased activities.¹⁴

2.4. X-Ray Diffraction

X-ray diffraction (XRD) is one of the most powerful techniques to determine the structure of crystalline specimens, including crystallite size, shape, and sample purity. First, X-rays are generated when a highly energetic beam of electrons is directed onto a metal target. Upon colliding with the metal, electrons lose energy and change their momentum. This leads to the emission of continuous radiation called Bremsstrahlung. Electrons with energies beyond a specific threshold can knock out electrons from inner shells of the target metal. Subsequently, electrons from outer shells, i.e. higher energy levels, fill these voids upon releasing characteristic X-ray emission. A monochromatic beam is produced with filters and collimated towards the sample.

Laue and Bragg discovered the principle of X-ray diffraction which occurs when X-ray beams are directed onto crystalline materials. Their theory explaining this phenomenon relies on the constructive interference of X-rays through scattering at the lattice planes of the crystal as illustrated in Figure 2-4.¹⁵

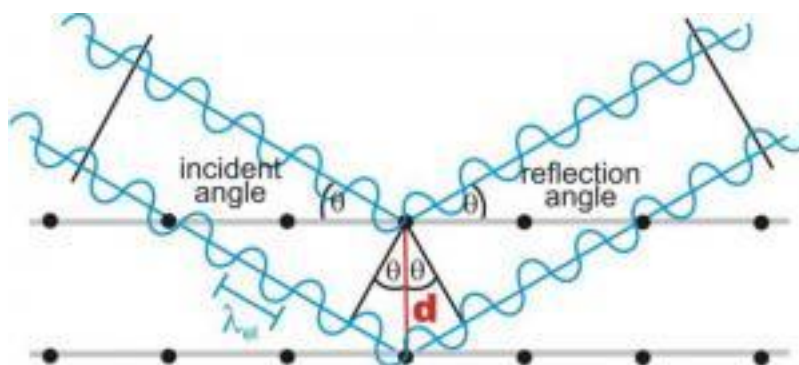


Figure 2-4: Schematic drawing of X-ray diffraction on a periodic lattice according to Bragg's law.¹⁶ Copyright © 2025 Yale University.

These principles are based on Bragg's law, which states that:

$$2d\sin\theta = n\lambda \quad (4)$$

In this equation, d represents the distance between the crystal planes, λ is the wavelength of the X-rays, and θ is the angle between the incident X-rays and the crystal planes. According to the aforementioned equation (4), the product of the integer n with the X-ray wavelength λ must be equivalent to the phase shift $2d\sin\theta$ for constructive interference to occur.¹⁵

The Scherrer equation can be applied to determine the crystallite size D based on the broadening of the measured reflections:

$$D = \frac{K\lambda}{\beta\cos(\theta)} \quad (5)$$

with K as a geometrical factor also called the Scherrer coefficient, β being the full width at half maximum (FWHM) of the respective reflection, λ being the wavelength of the X-rays and θ the Bragg diffraction angle of the respective diffraction peak.

In this thesis, XRD was utilized to determine the crystallinity and crystalline sizes of the catalyst support and the active components with a STOE Stadi P diffractometer in transmission geometry.

2.5. Spectroscopic Ellipsometry

Spectroscopic Ellipsometry (SE) is an optical technique used for characterizing thin films, providing critical information about film thickness and optical constants. SE is used in various fields, including semiconductor manufacturing, materials science, and electrochemistry. It is particularly valuable for real-time monitoring of thin film growth and etching processes, providing critical insights into film thickness, growth rates, and interface quality. It is further a suitable method to evaluate ALD growth rates and was the method of choice to elucidate film thicknesses of ZnO, TiO₂ and IrO₂ on silicon substrate. In this manner the growth per cycle was determined and the absolute number of cycles required to achieve a certain film thickness could be determined. In principle, this technique is based on measuring the relative phase change of polarized light upon reflection from a sample surface, making it highly sensitive and non-destructive.¹⁷ A schematic set up is presented in Figure 2-5:

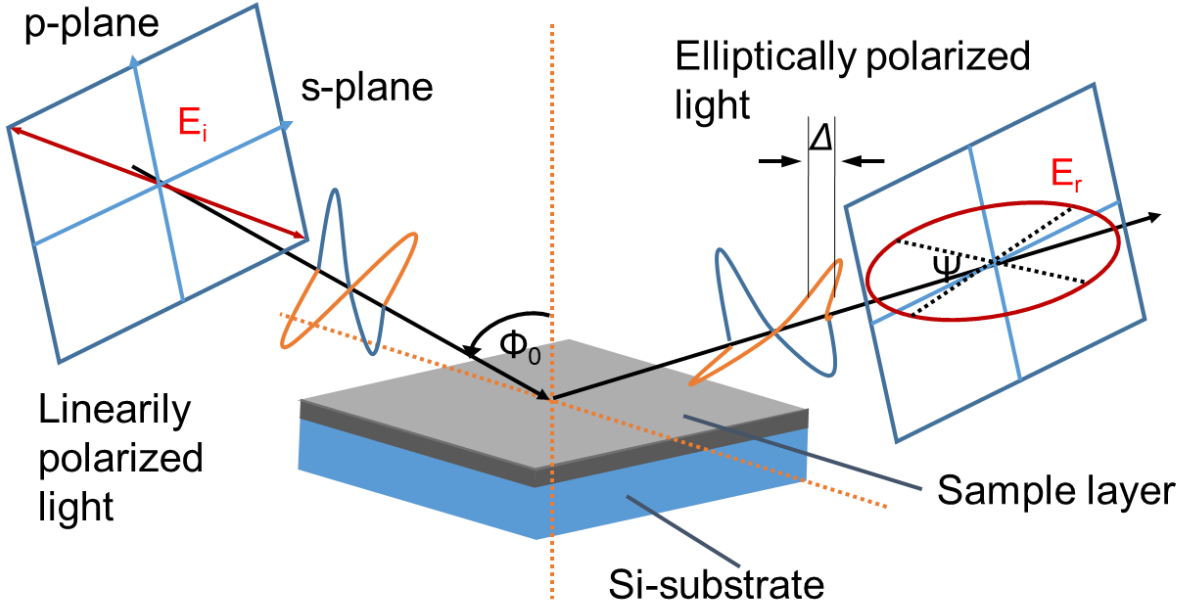


Figure 2-5: Schematic setup of spectroscopic ellipsometry measurement with electric field vectors of incident and reflected light.

SE measures two key parameters: the amplitude ratio Ψ and the phase difference Δ . These parameters are related to the complex reflectance ratio ρ , which is influenced by the film's thickness and refractive index. Typically, directed polarized light is emitted by a light source and is reflected off the sample. Upon reflection, the light beam gets elliptically polarized due to different reflectivity for the components of the incident beam. These components are perpendicular (s-plane) and parallel (p-plane) to the plane of incidence.¹⁸ The amplitudes of the s and p components following reflection and normalization are designated as r_s and r_p , respectively, illustrated in Figure 2-6.

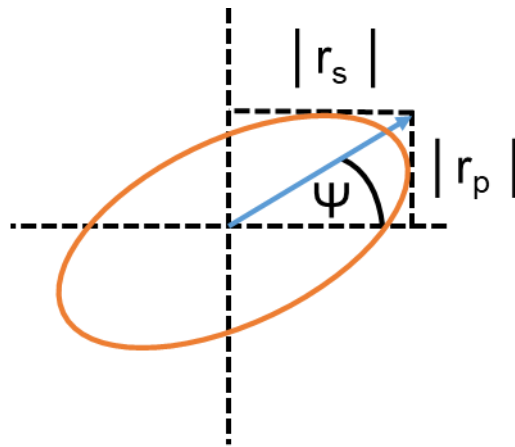


Figure 2-6: Field vector projection of elliptically polarized light with amplitudes of components r_s and r_p .

The change in polarization can be described by the complex ratio ρ of the reflection coefficients r_s and r_p , which provides the foundation for the fundamental equation of ellipsometry with the amplitude ratio Ψ and the phase difference Δ as described in Equation 6:

$$\rho = \frac{r_p}{r_s} = \tan(\Psi)e^{i\Delta} \quad (6)$$

Ellipsometry is an indirect method, as the optical constants cannot be calculated directly from the measured Ψ and Δ . Consequently, the analysis of ellipsometry data necessitates the formulation of an optical model, which is defined by the optical constants and layer thickness of the sample under investigation. An iterative procedure, based on least-squares optimization, is employed to vary the unknown optical constants and thickness parameters and to calculate the values of Ψ and Δ using the Fresnel equations. The resulting values of Ψ and Δ , which are in the best possible agreement with the experimental data, are then used to calculate the optical constants and thickness parameters of the sample.^{18, 19} All SE measurements were recorded on an J.A. Woollam M-200D instrument on Si(100) substrates. TiO₂ and ZnO layers were modeled using a Cauchy function whereas IrO₂ layers were modeled using a dual Lorentz oscillator model.

2.6. Electron Microscopy

2.6.1. Scanning Electron Microscopy

SEM represents a highly effective method for the topographical and morphological characterization of materials. The high resolution of this technique allows for nanoscale imaging, which makes it a valuable tool for examining nanoparticles, nanomaterials, and thin films for electrocatalyst development. This method is based on the scanning of a focused electron beam across the surface of the specimen in question. The interaction between the incident electrons and the specimen surface in a high vacuum chamber results in the generation of signals that are subsequently detected and utilized to construct high-resolution, three-dimensional images.²⁰

An acceleration voltage of about 1 to 30 keV is applied to a heated filament to generate primary electrons (PE) in the electron gun. These electrons are focused and directed onto the sample by a condenser and objective lens system and various apertures. The electron beam then scans

over the sample's surface moderated by a scanning generator. Upon bombardment of the specimen with accelerated PE, among others, secondary electrons (SE) are emitted from within the sample or backscattered electrons (BSE) are generated. The inelastically scattered PE generate SE which are detected in an Everhart-Thornley detector held at a positive voltage. This attracts low energy SE and converts them to light using a scintillator inside the detector. The low-intensity signal is then amplified with a photomultiplier and used as an intensity signal of corresponding pixels in the image. Additionally, BSE are generated through elastic interactions between PE and the specimen atoms, typically possessing a higher energy level (>50 eV) than SE. The intensity of BSE is dependent on the atomic number (Z) of the atoms at which they scatter, thereby allowing for the qualitative determination of the specimen's composition. BSE are detected by application of a negative voltage to the detector to deflect low-energy electrons like SE.²¹ A schematic setup of an SEM is illustrated in Figure 2-7.

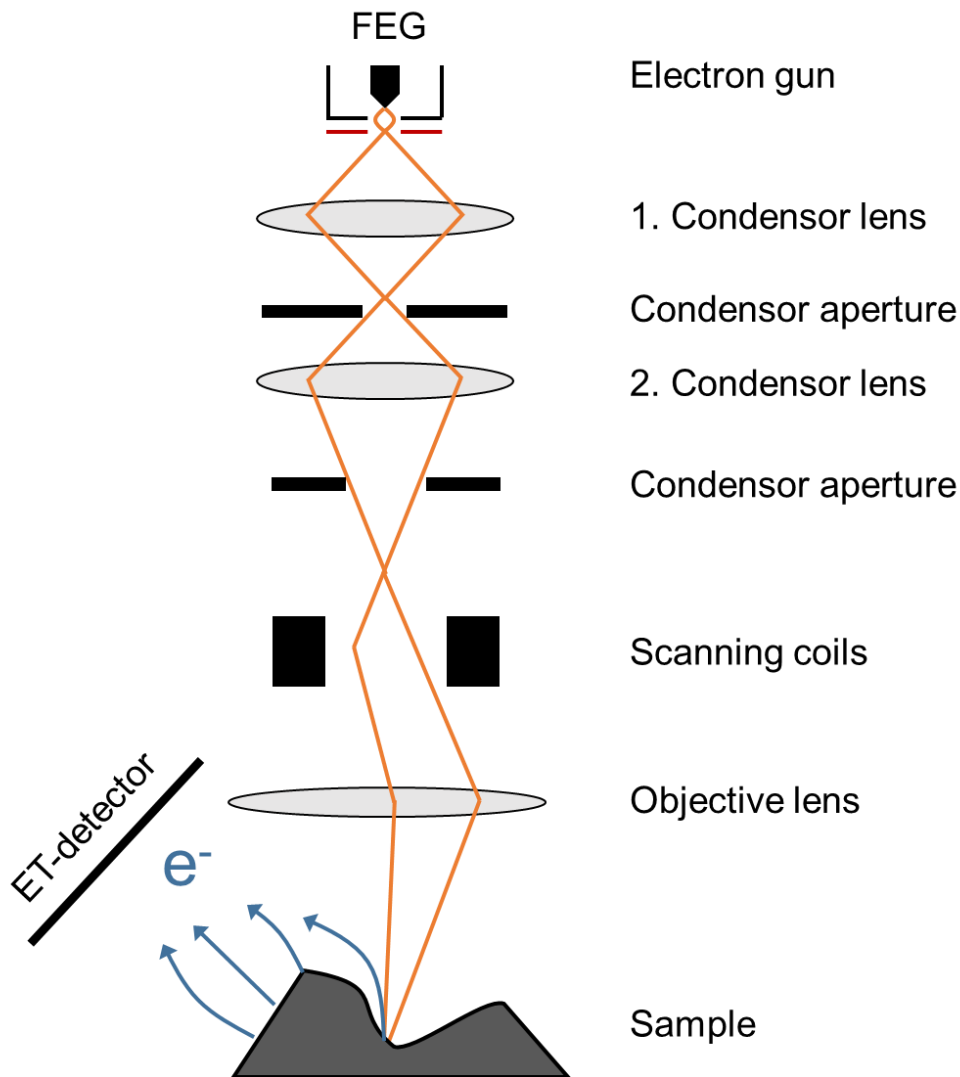


Figure 2-7: Scheme of a scanning electron microscope with beam path illustrated.

2.6.2. Energy-Dispersive X-Ray Spectroscopy

EDX is an analytical technique that can be employed for the qualitative and quantitative characterization of the investigated material. The generation of characteristic X-ray radiation upon interaction of high-energy PE and the inner-shell electrons of a sample is the fundamental principle underlying the operation of EDX as illustrated in Figure 2-8.

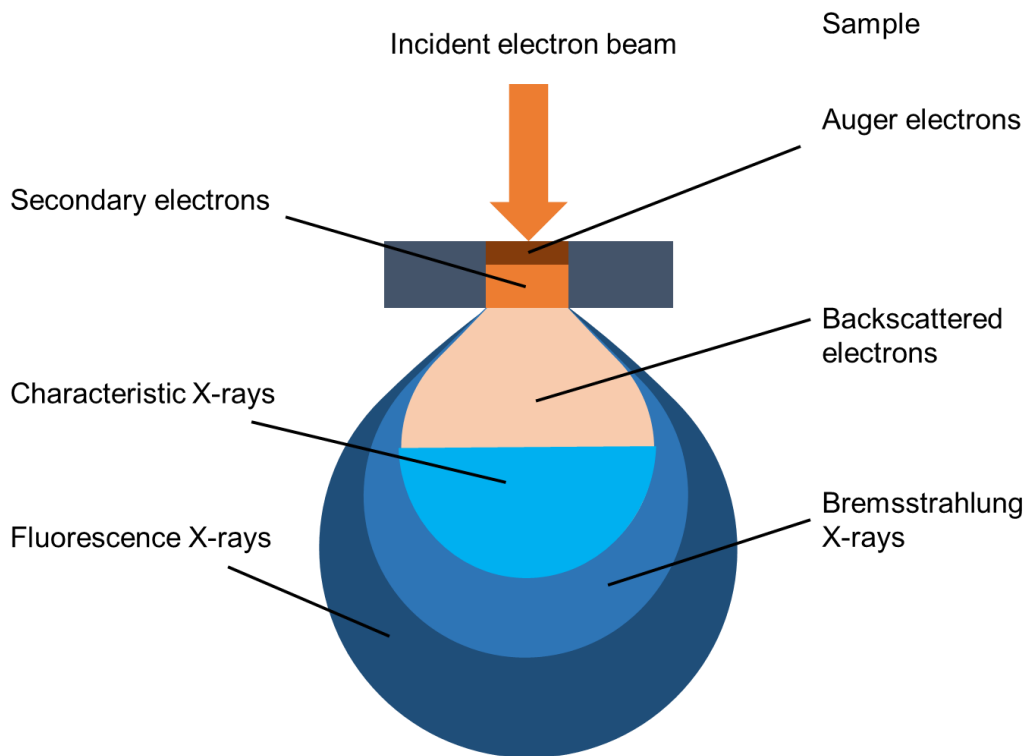


Figure 2-8: Interaction volume of incident electron beam with the sample generating Auger-, secondary and backscattered electrons and characteristic X-rays as well as fluorescence X-rays.

When electrons from the atomic core levels are emitted, remaining vacancies are filled by electrons of the same atom. The resulting energy is then released as an X-ray photon, which is subsequently detected by an energy-dispersive detector. The detector records the energy spectrum of the emitted X-rays, which allows for the identification of the elemental distribution and quantitative investigation of a specimen on an atom-specific level. The distinction between K-, L-, and M lines of characteristic X-rays is contingent upon the shell of the excited electron. EDX can be applied in two distinct modes: point analysis, whereby a spectrum is obtained from the point irradiated with the primary beam, and X-ray mapping, whereby the electron probe is scanned over a specified area to visualize the spatial distribution of elements on a microscopic scale. Furthermore, EDX can provide quantitative information, as the intensity of the

characteristic X-rays is approximately proportional to the concentration of the corresponding element. It should be noted that quantitative analysis by SEM/EDX is only accurate when several requirements are met. Firstly, the specimen must have a flat surface, with the electron beam entering perpendicularly. Secondly, the elemental distribution in the X-ray generating area must be uniform.²² In this work, EDX was the method of choice to determine the elemental composition of specimens qualitatively and determine the iridium content of samples quantitatively.

2.6.3. Transmission Electron Microscopy

TEM is a microscopy technique that enables the observation of the structure, morphology and phase composition of nanoscale structures with unparalleled resolution, reaching up to 45 pm (high-resolution transmission electron microscopy, HRTEM).²³ This even enables the observation of individual atoms (under favorable circumstances) and provides detailed information about the arrangement of atoms in a crystal lattice.²⁴

The essential components of a transmission electron microscope (TEM) are illustrated in Figure 2-9 and include an electron source, which is commonly either LaB₆, a tungsten filament or a field-emission gun. Typically, the acceleration voltage is within the range of 80 to 400 kV, with electrons ejected from the source traveling through a condenser lens system to control the intensity and convergence of the beam. Subsequently, the electrons traverse a thin specimen, which is optimally ≤ 100 nm in thickness, thereby enabling the electrons to pass through the specimen. The image of the specimen is then projected onto the image plane by the objective lens and magnified by a projector lens system, resulting in the final image on a fluorescent screen or another type of image detector. An alternative analytical method is to magnify and focus the diffraction pattern in the back focal plane of the objective lens onto the screen.

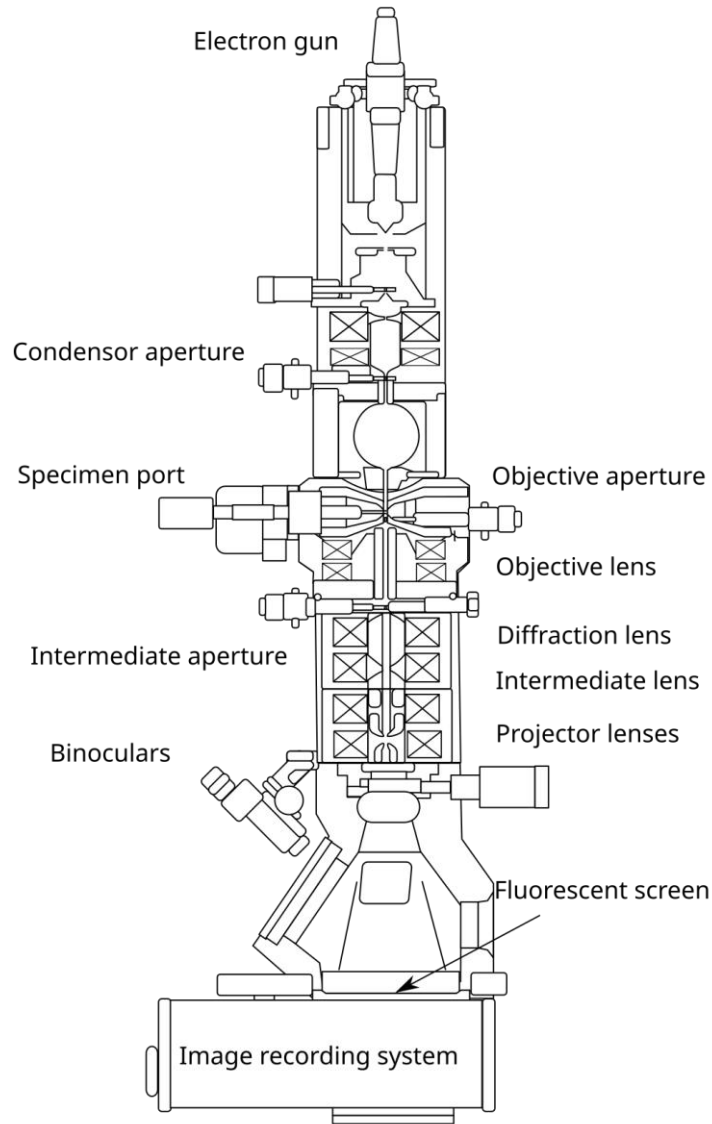


Figure 2-9: Schematic setup of a transmission electron microscope.²⁵

An optional selected area electron diffraction (SAED) aperture may be inserted into the beam path at the position of the projected image plane of the objective lens. This allows for the generation of a diffraction pattern from a specific area of the sample, which can then be analyzed. By adjusting the aperture, one can focus on (select) a particular region, thereby obtaining a detailed local diffraction pattern. These diffraction patterns can be analyzed to determine crystal symmetry, lattice parameters, and orientation relationships.

Another method within TEM is represented by scanning transmission electron microscopy (STEM), which enables the combination of scanning the sample like in SEM with a much higher resolution of a highly focused primary beam. Subsequently, high-angle scattered electrons are recorded by a ring detector situated in proximity to the optical axis, thereby

facilitating imaging with a high mass contrast and enabling the differentiation between heavy and light elements in the so-called high-angle annular dark-field mode (HAADF).²⁶

2.7. 2-Point Conductivity Measurements

The through-the-plane (TP) 2-point probe is one of the most commonly employed techniques for conductivity measurements.²⁷ As the conductivity of an OER catalyst layer strongly influences the electrochemical performance at elevated current densities, the conductivity is a key feature of the electrocatalyst.

DC two-plane (TP) conductivity measurements offer a rapid and (fairly) reliable assessment of bulk conductivity in a diverse range of materials. Although the TP conductivity method is relatively straightforward and cost-effective, it is susceptible to influences such as electrode polarization, contact resistance, and sample inhomogeneity, which may affect the accuracy of the measurements. It is of great importance to give these factors the appropriate attention in order to obtain reliable results.²⁸ TP conductivity measurements are utilized to assess the electrical conductivity of a material in a direction perpendicular to a dominant plane, such as the surfaces of a flat pressed powder pellet. A scheme is shown in

Figure 2-10. This method is also of interest for materials exhibiting layered structures or anisotropic electrical properties. The underlying principle of TP measurements is based on the following formula²⁹:

$$\sigma = \frac{1}{\rho} \quad (7)$$

Where σ represents the conductivity which is equal to the inverse of the resistivity ρ .³⁰ Thereby, the resistivity is defined in the continuum form of (7):²⁹

$$E = \rho \times J \quad (8)$$

With the electric field E , the current density J and the resistivity ρ .

The electric field E across the two ends of the material is given by:²⁹

$$E = \frac{V}{l} \quad (9)$$

With potential V and length l .

The current density J equals:²⁹

$$J = \frac{I}{A} = \frac{I}{w \times h} \quad (10)$$

With current I and area A derived from the sample dimensions' w (width) and h (height). The resistivity ρ is determined by the current measured at the respective voltage. In addition, l (length) of the sample need to be known:²⁹

$$\rho = \frac{V \times A}{I \times l} \quad (11)$$

The conductivity σ as the inverse of the resistivity can be written as:

$$\sigma = \frac{I \times l}{V \times A} \quad (12)$$

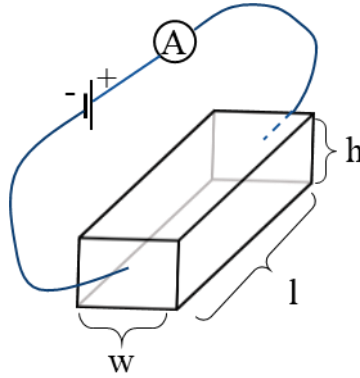


Figure 2-10: Scheme of TP conductivity setup. A potential is applied across the electrodes, and the resulting current passing through the material perpendicular to its planes is measured.

In this work, conductivity measurements of epitaxial nanoparticulate $\text{IrO}_2@\text{SnO}_2$ and $\text{IrO}_x/\text{TiO}_2$ catalysts as well as nanofibrous $\text{IrO}_2@\text{TiO}_2$ were carried out on an in-house constructed dc-conductivity measurement cell on loosely compressed powders by recording I – V curves between -5 to +5 V by an AUTOLAB 302N.

2.8. Electrochemical Analysis

2.8.1. Electrical Impedance

Electrochemical impedance spectroscopy (EIS) was employed to determine the electrolyte resistance in cyclic voltammetry experiments. The results allow for a correction of the iR -drop in the measurements and yield comparable current densities for OER catalysts. Besides, it is a powerful and versatile technique that allows for the characterization of electrochemical processes, including charge transfer reactions, mass transport phenomena, and bilayer capacitance, and provides insight into the kinetics and mechanisms of these processes.³¹

The experimental setup consists of immersing an electrode or material of interest in an electrolyte solution, usually in a three-electrode configuration. The application of a small amplitude alternating current (AC) signal to an electrochemical system over a range of frequencies results in a current response. The response of the system is then analyzed in the frequency domain, yielding an impedance spectrum. The impedance spectrum typically consists of real (resistance) and imaginary (reactance) components and is represented as a Nyquist or Bode plot. In an AC system, current and voltage are closely related, and periodic waves of them have the same frequency. In the Bode and Nyquist plots, the total impedance Z can be expressed by Z as the length of the vector and Φ as the angle, with the real part of the impedance Z' on the abscissa and the imaginary part Z'' on the ordinate as shown in Figure 2-11.

Thereby, the impedance can be obtained by applying a fixed potential wave of known frequency to the system and recording the resulting current wave. Z , Z' , Z'' and Φ can be calculated from the recorded data.

The relationship of the current to the applied potential in an AC system and the resulting impedance are expressed in the following equations:³²

$$\text{Potential:} \quad E_t = E_0 \sin(\omega t) \quad (13)$$

$$\text{Current:} \quad I_t = I_0 \sin(\omega t + \Phi) \quad (14)$$

$$\text{Impedance:} \quad Z(\omega) = \frac{E_t}{I_t} = Z_0 \frac{\sin(\omega t)}{\sin(\omega t + \Phi)} \quad (15)$$

E_t and I_t represent the potential and current at time t and Φ is the phase shift of the responding current versus the potential.

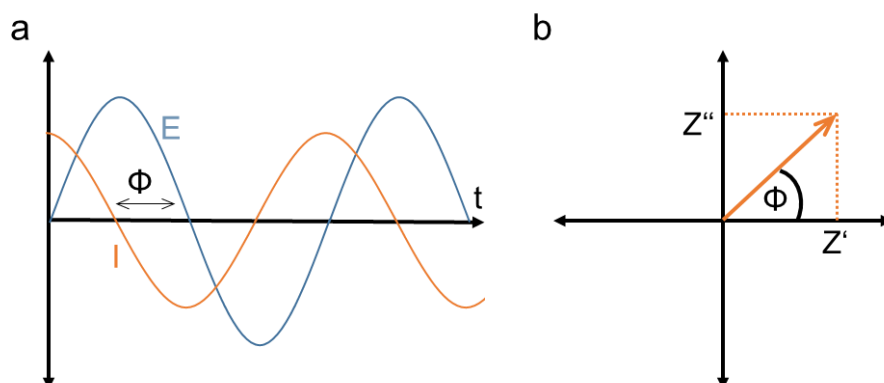


Figure 2-11: (a) Periodic waves of potential E and resulting current I with phase shift Φ . (b) Impedance Z in vector representation with Z'' at the abscissa and Z' on the ordinate with angle Φ .

Representation of obtained data can be displayed as a Bode or Nyquist diagram as illustrated in Figure 2-12. In the complex representation of the impedance, the Nyquist plot, the x-axis (Z') or real part represents the resistive part of the impedance and the y-axis as the imaginary axis ($-Z''$) the reactive part, which can be attributed to, for example, capacitive behavior. The Bode diagram, on the other hand, shows the phase shift and the amplitude gain in two different graphs.³³

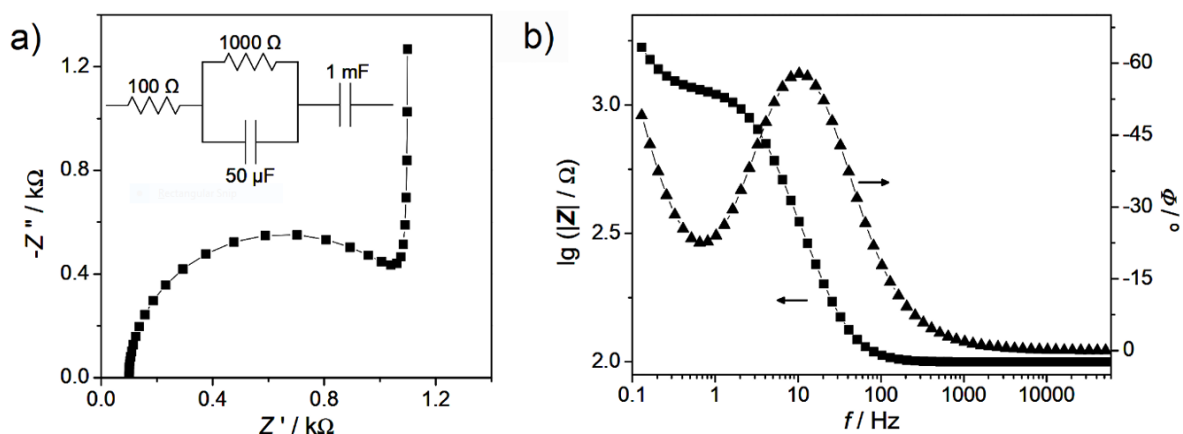


Figure 2-12: Typical electrochemical impedance spectrum in a complex plane in the (a) Nyquist representation and (b) Bode diagram with impedance magnitude (squares) and phase angles (triangles) representation for the circuit shown in the inset in (a)³⁴. Reproduced with permission from Ref. [34]. Copyright 2004, Springer-Verlag Berlin Heidelberg.

In this work EIS was used to determine the resistance of the electrolyte before and after further electrochemical measurements in the high frequency region under non-faradaic conditions (open circuit) at 0.5 V vs. RHE to determine the iR correction.

2.8.2. Cyclic Voltammetry

CV stands as a fundamental and widely utilized electroanalytical technique, providing valuable insights into the electrochemical behavior of materials and systems. This versatile method allows the study of redox processes, determination of electrochemical parameters, and characterization of materials in various applications.

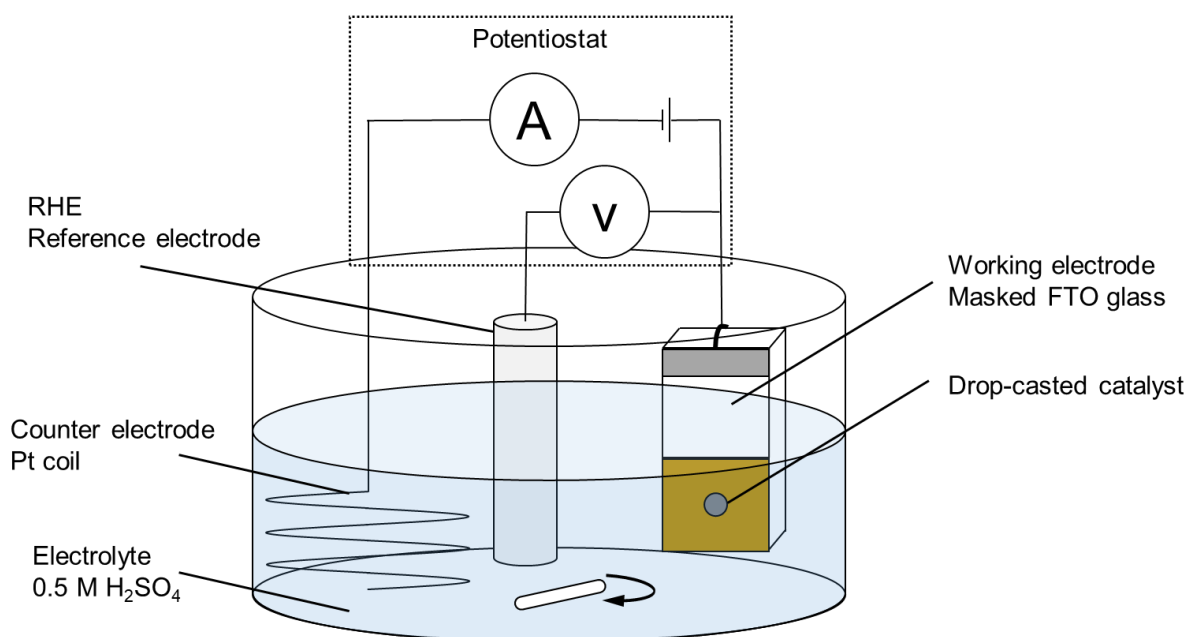


Figure 2-13: Three-electrode set-up for electrochemical measurements as used for this work. Stirring was applied in projects described in chapters 3 and 5. No stirring was used in the project described in chapter 4.

CV measurements are typically performed in three-electrode set-ups with a working electrode (WE), a counter electrode (CE) and a reference electrode (RE) as schematically depicted in Figure 2-13. At the WE, the electrochemical reaction of interest is investigated. In this work, fluorine-doped tin oxide (FTO) was used as conductive and transparent WE. In static wet cell measurements, FTO WE offer the advantage of transparency, allowing optical monitoring of processes occurring at the electrode-electrolyte interface. In addition, the rough surface area is beneficial for adhesion of the drop-casted electrocatalyst.

During the CV measurement, a potential is applied and the resulting current response is monitored by a potentiostat. The potential is varied linearly with time, creating a cyclic voltammogram that depicts the current as a function of the applied potential. In a typical CV experiment, the potential is swept between a lower and upper potential limit at a defined scan rate v , which is the rate at which the applied potential is changed. The resulting voltammogram

can exhibit distinct features, including oxidation and reduction peaks corresponding to specific electrochemical processes. A schematic current response of a redox couple comprising a single electrode reaction is illustrated in Figure 2-14 showing a Gauss-type peak, which allows the identification of the peak voltage (E_p) and peak current (i_p).³⁵

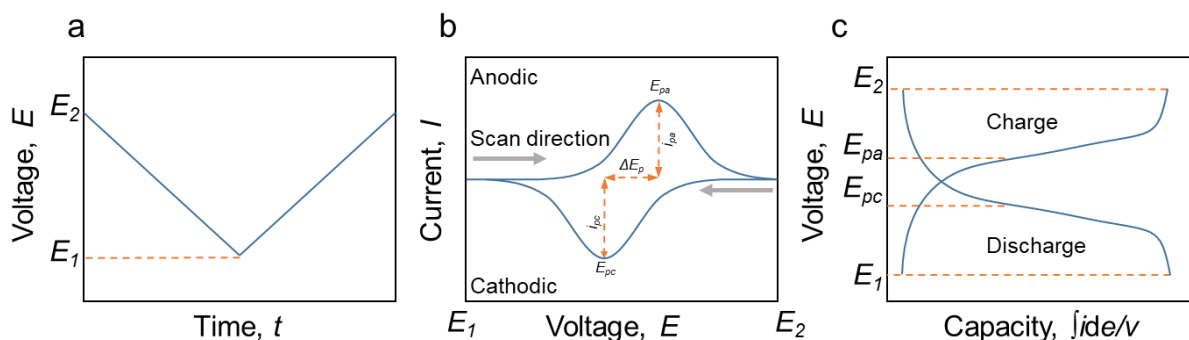


Figure 2-14: (a) Chain saw shape of cyclical potential sweep with the voltage changing over time and (b) resulting cyclic voltammogram with current dependent of applied voltage and (c) voltage versus integral current curves.

The ratio of peak currents and their difference of peak voltage (ΔE_p) in cathodic and anodic segments can be analyzed to ascertain the reversibility of the electrochemical system. The electrochemical capacity of the reaction can be calculated by integrating the current curve with respect to potential and scan rate. The area under the peaks provides quantitative information about the amount of charge involved in the redox reactions. By applying the voltage versus capacity profiles, it can be determined that the discharge and charge plateaus will correspond to the cathodic and anodic peak voltages, respectively, as depicted in Figure 2-14c. In the case of a known mass of the redox-active electrode, the ordinate can be specified as the specific current (in units of $A\ g^{-1}$) and the integral value will provide the specific capacity (in units of $mAh\ g^{-1}$). In the context of catalytic reactions in liquids, the exposed surface area of the electrode is a more significant factor than the electrode mass itself. Accordingly, it is more practical to employ the current density (in units of $A\ cm^{-2}$) in lieu of the specific current.³⁶

As the scan rate controls how fast the applied potential is changed, it is a powerful tool to access the electrochemically active surface area (ECSA). If the scan rate is increased, higher currents are observed as a result of a reduction in the diffusion layer thickness. This allows for the determination of the actual ECSA of an electrode immersed in an electrolyte solution through the use of CV. At a potential where only capacitive currents flow and no electrochemical reaction takes place, the measured current i_{cap} is proportional to the scan rate dE/dt and the electrode capacitance C according to Equation (16) below:

$$i_{cap} = C \frac{dE}{dt} \quad (16)$$

Plotting i_{cap} versus dE/dt yields a line with slope C , allowing determination of the electrode capacitance, which is proportional to the ECSA.

In the case of a given potential where the measured current is attributed to a charge transfer between redox-active species, the Randles-Sevcik equation, shown in Equation (17), describes the dependence of the peak current i_p on the scan rate ν . In the case of electrochemically reversible electron transfer processes involving freely diffusing redox species, a linear relationship should be observed between the peak current i_p and the square root of the scan rate ($\sqrt{\nu}$). For a known scan rate and peak current, the diffusion coefficient (D_0 , in $\text{cm}^2 \text{s}^{-1}$) of the diffusing species can be obtained by considering the electrode surface area (A , cm^2) and the bulk concentration of the analyte (C^0 , in mol cm^{-3}). Furthermore, the Faraday constant F , the number of charges n exchanged, the temperature T , and the molar gas constant R complete the equation. The equation is written as follows:³⁷

$$i_p = 0.446nFAC^0 \sqrt{\frac{nF\nu D_0}{RT}} \quad (17)$$

In this study, the CV method was selected as the primary technique for determining the specific and mass-based activity of the iridium catalysts as a key performance indicator. To assess the cycling stability of the materials, multiple cycles were performed (ranging from 20 to 50 cycles between 1.0 and 1.8 V vs. RHE).

2.8.3. Chronopotentiometry

CP is a common technique to assess the long-term stability of a catalyst. Here, the potential difference between two electrodes in an electrochemical cell is measured while the current is kept constant, leading to time dependent changes in potential, whereby information about the rate of electrochemical reactions, the formation of reaction intermediates, reaction kinetics, ion transport, and the evolution of electroactive species can be derived. This is enabled by the potentiostat that maintains a constant potential difference between the WE and RE by adjusting the potential of the CE to a level at which the flux of the electroactive species is sufficient to supply the desired current.³⁸ Typically, a three-electrode-setup as shown in Figure 2-13 in Chapter 2.8.2 is used for this measurement.

Performing CP at various current densities allows for the determination of the exchange current densities of an electrode as well as the Tafel-slope, which relates the rate of an electrochemical reaction to the overpotential.

2.9. References

1. Sing, K. S., Reporting physisorption data for gas/solid systems with special reference to the determination of surface area and porosity (Recommendations 1984). *Pure and applied chemistry* **1985**, 57 (4), 603-619.
2. Sing, K., The use of nitrogen adsorption for the characterisation of porous materials. *Colloids and Surfaces A: Physicochemical and Engineering Aspects* **2001**, 187-188, 3-9.
3. Thommes, M.; Kaneko, K.; Neimark, A.; Olivier, J.; Rodriguez-Reinoso, F.; Rouquerol, J.; Sing, K., Physisorption of gases, with special reference to the evaluation of surface area and pore size distribution (IUPAC Technical Report). *Pure and Applied Chemistry* **2015**, 87.
4. Rouquerol, J.; Avnir, D.; Fairbridge, C.; Everett, D.; Haynes, J.; Pernicone, N.; Ramsay, J.; Sing, K.; Unger, K., Recommendations for the characterization of porous solids (Technical Report). *Pure and applied chemistry* **1994**, 66 (8), 1739-1758.
5. McMillan, W.; Teller, E., The Assumptions of the BET Theory. *The Journal of Physical Chemistry* **1951**, 55 (1), 17-20.
6. Bottom, R., Thermogravimetric analysis. *Principles and applications of thermal analysis* **2008**, 87-118.
7. A. W. Coats, J. P. R., Thermogravimetric Analysis - A Review. *Analyst* **1963**, 88, 906-924.
8. Seah, M., The quantitative analysis of surfaces by XPS: A review. *Surface and Interface Analysis* **1980**, 2 (6), 222-239.
9. Baio, J. E.; Graham, D. J.; Castner, D. G., Surface analysis tools for characterizing biological materials. *Chemical Society Reviews* **2020**, 49 (11), 3278-3296.
10. Bagus, P. S.; Ilton, E.; Nelin, C. J., Extracting chemical information from XPS spectra: a perspective. *Catalysis Letters* **2018**, 148, 1785-1802.
11. Krishna, D. N. G.; Philip, J., Review on surface-characterization applications of X-ray photoelectron spectroscopy (XPS): Recent developments and challenges. *Applied Surface Science Advances* **2022**, 12, 100332.
12. Ballerini, G.; Ogle, K.; Barthés-Labrousse, M.-G., The acid–base properties of the surface of native zinc oxide layers: An XPS study of adsorption of 1, 2-diaminoethane. *Applied surface science* **2007**, 253 (16), 6860-6867.

13. Nguyen, L.; Tao, F. F.; Tang, Y.; Dou, J.; Bao, X.-J., Understanding Catalyst Surfaces during Catalysis through Near Ambient Pressure X-ray Photoelectron Spectroscopy. *Chemical Reviews* **2019**, *119* (12), 6822-6905.
14. Opitz, A. K.; Nenning, A.; Rameshan, C.; Rameshan, R.; Blume, R.; Hävecker, M.; Knop-Gericke, A.; Rupprechter, G.; Fleig, J.; Klötzer, B., Enhancing Electrochemical Water-Splitting Kinetics by Polarization-Driven Formation of Near-Surface Iron(0): An In Situ XPS Study on Perovskite-Type Electrodes. *Angewandte Chemie International Edition* **2015**, *54* (9), 2628-2632.
15. Holder, C. F.; Schaak, R. E., Tutorial on powder X-ray diffraction for characterizing nanoscale materials. ACS Publications: 2019; Vol. 13, pp 7359-7365.
16. Yale West Campus Materials Characterization Core XRD Principle. <https://ywcmatsci.yale.edu/principle-0>.
17. Riedling, K.; Riedling, K., Basics of Ellipsometry. *Ellipsometry for Industrial Applications* **1988**, 1-18.
18. Fujiwara, H., *Spectroscopic ellipsometry: principles and applications*. John Wiley & Sons: 2007.
19. Gonçalves, D.; Irene, E. A., Fundamentals and applications of spectroscopic ellipsometry. *Química Nova* **2002**, *25*, 794-800.
20. Mohammed, A.; Abdullah, A. In *Scanning electron microscopy (SEM): A review*, Proceedings of the 2018 International Conference on Hydraulics and Pneumatics—HERVEX, Băile Govora, Romania, 2018; pp 7-9.
21. Zhou, W.; Apkarian, R.; Wang, Z. L.; Joy, D., Fundamentals of scanning electron microscopy (SEM). *Scanning microscopy for nanotechnology: techniques and applications* **2007**, 1-40.
22. Frankel, R.; Aitken, D., Energy-dispersive x-ray emission spectroscopy. *Applied Spectroscopy* **1970**, *24* (6), 557-566.
23. Sawada, H.; Shimura, N.; Hosokawa, F.; Shibata, N.; Ikuhara, Y., Resolving 45-pm-separated Si–Si atomic columns with an aberration-corrected STEM. *Microscopy* **2015**, *64* (3), 213-217.
24. A. Amelinckx, D. v. D., J. van Landuyt, G. van Tendeloo, *Electron Microscopy: Principles and Fundamentals*. John Wiley & Sons: Hoboken, NJ, 1997.
25. <https://en.wikipedia.org/wiki/Transmission-electron-microscopy>, a. J.
26. Egerton, R. F., *Physical principles of electron microscopy: an introduction to TEM, SEM, and AEM*. Springer: 2006; Vol. 2.

27. Larsen, T.; Larsen, T.; Andreasen, S. J.; Christiansen, J. D. C., Pressure-independent through-plane electrical conductivity measurements of highly filled conductive polymer composites. *International Journal of Hydrogen Energy* **2023**, *48* (33), 12493-12500.
28. Horszczaruk, E.; Sikora, P.; Łukowski, P., Application of Nanomaterials in Production of Self-Sensing Concretes: Contemporary Developments and Prospects. *Archives of Civil Engineering* **2016**, *62*.
29. Electrical Measurement, Signal Processing, and Displays. **2003**.
30. Wei, Q.; Suga, H.; Ikeda, I.; Mukaida, M.; Kirihara, K.; Naitoh, Y.; Ishida, T., An accurate method to determine the through-plane electrical conductivity and to study transport properties in film samples. *Organic Electronics* **2016**, *38*, 264-270.
31. Lazanas, A. C.; Prodromidis, M. I., Electrochemical impedance spectroscopy— a tutorial. *ACS Measurement Science Au* **2023**, *3* (3), 162-193.
32. Callegaro, L., *Electrical impedance: principles, measurement, and applications*. CRC Press: 2012.
33. Magar, H. S.; Hassan, R. Y.; Mulchandani, A., Electrochemical impedance spectroscopy (EIS): Principles, construction, and biosensing applications. *Sensors* **2021**, *21* (19), 6578.
34. Arnau, A., *Piezoelectric Transducers and Applications*. 2004.
35. Yamada, H.; Yoshii, K.; Asahi, M.; Chiku, M.; Kitazumi, Y., Cyclic voltammetry part 1: fundamentals. *Electrochemistry* **2022**, *90* (10), 102005-102005.
36. Marken, F.; Neudeck, A.; Bond, A. M., Cyclic voltammetry. *Electroanalytical methods: guide to experiments and applications* **2010**, 57-106.
37. Ko, J. M.; Park, H. C., Principles and applications of cyclic voltammetry. *Polymer Science and Technology* **1999**, *10* (4), 519-524.
38. Lingane, P. J.; Peters, D. G., Chronopotentiometry. *CRC Critical Reviews in Analytical Chemistry* **1971**, *1* (4), 587-634.

CHAPTER 3

Optimized Oxidation Temperature Enhances OER Performance of IrO₂-Loaded SnO₂ Nanofibers – Role of Charge Carrier Percolation Pathways

3. Optimized Oxidation Temperature Enhances OER Performance of IrO₂-Loaded SnO₂ Nanofibers – Role of Charge Carrier Percolation Pathways

This chapter was submitted by:

Melisande Kost, Jean Felix Dushimineza, Knut Müller-Caspary and Thomas Bein*

Department of Chemistry and CeNS, Ludwig-Maximilians-Universität München, Germany

* Corresponding author: Thomas Bein (thomas.bein@cup.lmu.de)

Abstract

The potential for further reducing iridium content in large-scale proton-exchange membrane (PEM) electrolysis is examined using a fibrous support morphology to enhance electron percolation. Focusing on high activity, stability, and conductivity, ultra-small, interconnected IrO_x/IrO₂ nanoparticles anchored to electrospun SnO₂ nanofibers (IrO_x/IrO₂@SnO₂) are investigated, with particular attention to the crystallinity of the iridium phase. Scanning transmission electron microscopy (STEM), conducted both before and after use as an electrocatalyst for the oxygen evolution reaction (OER), reveals how the oxidation temperature impacts the crystallinity and stability of the iridium oxide phase. The results suggest that further reductions in iridium content may be achieved by optimizing synthesis parameters. The data show that the highest iridium utilization is achieved at an oxidation temperature of 375°C, with improved conductivity and electrochemical activity. TEM data indicate that higher oxidation temperatures result in fragmentation of conduction pathways, negatively affecting catalyst performance. Furthermore, TEM analysis indicates the onset of IrO₂ crystallization between 365 and 375°C, with cyclic voltammetry (CVA) emphasizing the critical role of conductivity in ensuring efficient charge carrier transport to active sites. This study not only deepens our understanding of iridium-based catalysts but also identifies practical strategies to enhance cost-effectiveness and efficiency in PEM electrolysis technologies.

3.1. Introduction

3.1. Introduction

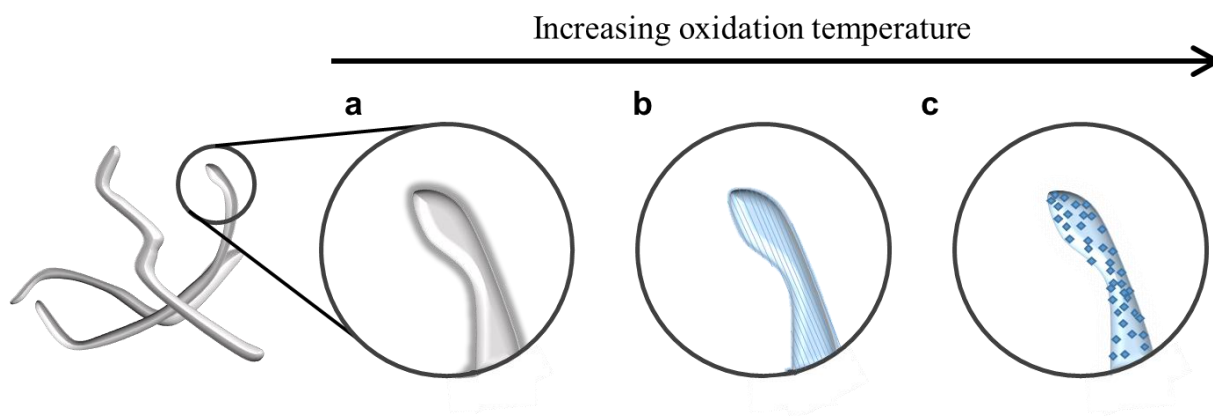
In the renewable energy landscape, water electrolysis has emerged as a key pathway for clean hydrogen fuel production.¹ Among the various electrolysis methods, proton-exchange membrane (PEM) electrolysis stands out due to its exceptional efficiency, achieving current densities above 2 Acm⁻², which supports high hydrogen output pressures. It also features low gas crossover and a compact design, making it highly suitable for large-scale hydrogen generation.^{2,3}

However, this promising approach is hindered by its dependence on rare components, particularly the catalyst for the anodic oxygen evolution reaction (OER), which is limited by sluggish kinetics.⁴ IrO₂ remains the state-of-the-art OER catalyst, due to its exceptional activity and stability. This valuable compound is derived from metallic iridium, which can only be extracted as a scarce byproduct of mining operation,⁵ underscoring the critical need to reduce iridium usage while maintaining catalytic performance. Achieving this balance requires maximizing charge carrier transport to active sites through interconnected IrO₂ clusters or ultra-thin IrO₂ layers, thereby ensuring adequate conductivity derived from percolation paths through the metallic IrO₂ phase.⁶⁻⁸

To tackle these challenges, various possibilities for nanostructuring of electrocatalysts are being examined. This includes selecting corrosion-stable substrate material, employing doping to increase conductivity^{7, 9-13}, tailoring the morphology of the substrate and the active component to maximize the active surface area^{5, 6, 14-16}, selecting a suitable catalytically active compound¹⁷⁻²², and optimizing the deposition method for the active component on the substrate.^{5, 23-26} The morphology, oxidation state, lattice distortion, and crystallinity of the active material are particularly critical for improving performance.^{8, 27-30}

Here, we present a novel approach that integrates electrospun SnO₂ nanofilaments as support structures for iridium nanoclusters, deposited via a wet-chemical process. The iridium oxide nanoclusters were oxidized at different temperatures to optimize percolation pathways, thereby minimizing iridium content while exposing a maximum of catalytically active sites.³¹ A sufficient oxidation temperature provides optimal energy input to promote phase transition of amorphous to crystalline iridium oxide nanoparticles on the nanofilament surface.³² Oxidations temperature that exceed the optimal temperature window lead to formation of isolated nanocrystals as presented in Scheme 3-1.

3. Optimized Oxidation Temperature Enhances OER Performance of IrO₂-Loaded SnO₂ Nanofibers – Role of Charge Carrier Percolation Pathways

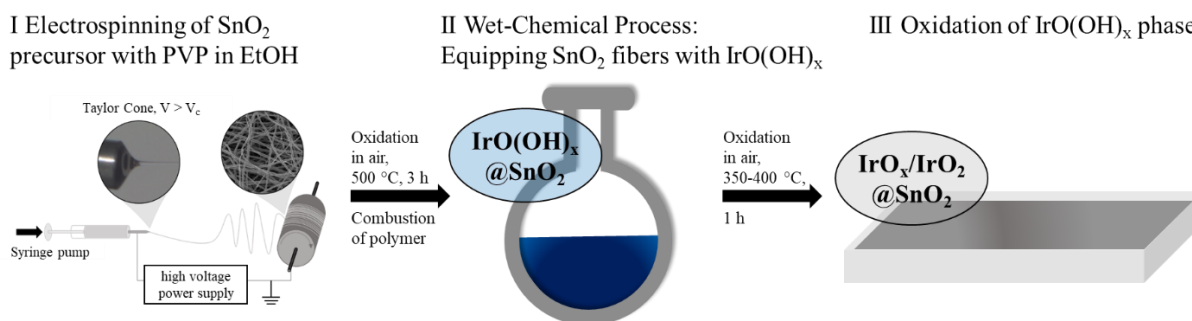


Scheme 3-1: Crystallization processes of the iridium oxide phase occurring with increasing oxidation temperature on supporting SnO₂ nanofibers. At insufficient oxidation temperature, the IrO_x phase remains amorphous (a). An increase in oxidation temperature leads to crystallization of evenly distributed IrO₂ layer (b). Even higher temperatures lead to crystal growth and fragmentation of the IrO₂ layer, generating isolated nanocrystals (c).

The characterization of the IrO₂ nanoparticles is facilitated by employing advanced techniques, including high-resolution TEM coupled with electrochemical studies. We investigate the potential rearrangement and clustering of iridium nanoparticles during oxidation and electrochemical processes, thereby providing insights into structural changes and their impact on performance. By correlating structural and electronic features with catalytic activity, our comprehensive approach advances both fundamental understanding and possible practical solutions for developing efficient (and cost-effective) PEM electrolysis catalysts.

3.2. Results and Discussion

To prepare the catalyst support material, SnO₂ nanofibers were fabricated by electrospinning as shown in step I in Scheme 3-2. The uniform deposition of amorphous polymer-containing filaments on the collector roll was carried out in an electrospinning setup with a multinozzle tip, to increase the production rate. A spinning solution based on a tin alkoxide was electrospun to obtain a fibrous mat. After oxidation, the final crystalline support structure of SnO₂ filaments was obtained. The second critical step was the slow hydrolysis of aqueous iridium(III) chloride solution at elevated pH values in the presence of the SnO₂ fibers, which led to the deposition of nanoparticulate amorphous IrO(OH)_x clusters on the filament surface (referred to as IrO(OH)_x@SnO₂). Due to the instability of the amorphous IrO(OH)_x species under PEM conditions³², this phase was initially converted to the dehydrated form IrO_x by an oxidation process. This phase is characterized by its improved stability. At sufficiently high temperatures, the amorphous IrO_x phase crystallizes to form rutile IrO₂.³³ In a previous study, we found that due to similar lattice constants IrO₂ can be grown epitaxially on (nanoparticulate) SnO₂, leading to strongly enhanced stability under electrocatalytic operating conditions.³⁴



Scheme 3-2: The workflow for catalyst synthesis consists of three essential steps. First the electrospinning and oxidation of the SnO₂ nanofibers is performed. This is followed by coating the fibers with the hydrous IrO(OH)_x phase, which is oxidized in the last step to yield the final product.

The morphology and composition of the catalyst were examined using electron microscopy as presented in Figure 3-1. The spinning process yields fibers with a thickness of 100 – 500 nm. In addition to the formation of threads, the process also leads to the production of bead-like structures. Upon iridium-loading and oxidation using the processes described above, mechanical stress arising from stirring somewhat shortens the long, brittle filaments.

3. Optimized Oxidation Temperature Enhances OER Performance of IrO₂-Loaded SnO₂ Nanofibers – Role of Charge Carrier Percolation Pathways

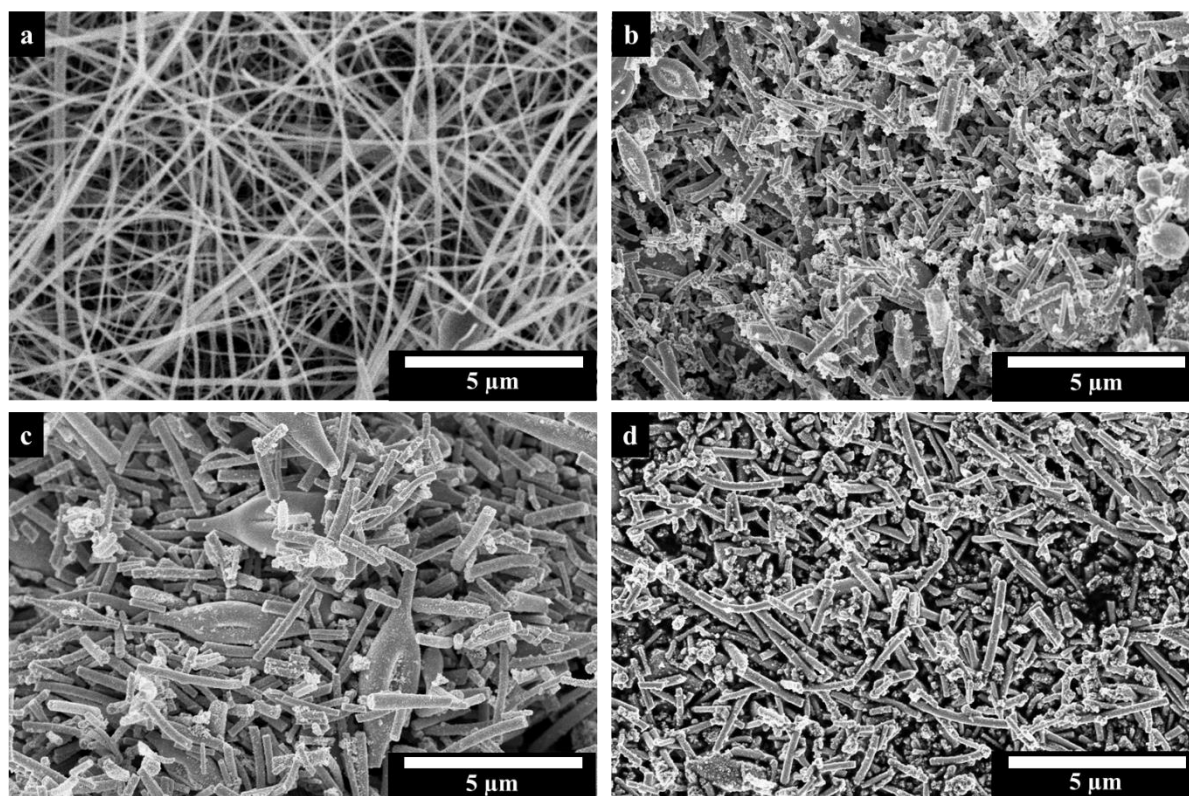


Figure 3-1: Secondary electron images of electrospun nanofibers acquired in an SEM. (A) Pure SnO₂ filaments after oxidation at 500 °C for 3 hours, after loading with 35 wt% Ir nominal and oxidation at (B) 375 °C, (C) 385 °C, and (D) 400 °C for 1 hour, respectively.

The crystallinity of the loaded filaments was examined with powder X-ray diffraction (PXRD). Resulting patterns of IrO_x/IrO₂@SnO₂ with a nominal Ir loading of 35 wt%, after oxidation at various temperatures in air, are presented in Figure 3-2. The phase composition of the SnO₂ filamentous support is a mixture of small crystals of predominantly cassiterite (c-SnO₂) and a small fraction of the meta-stable scrutinyite (s-SnO₂) and becomes clearly identifiable with very long acquisition times (supporting information Figure S3-2). The PXRD patterns of IrO_x/IrO₂@SnO₂ exhibit an anisotropic tail of the first reflection at 27° 2θ (Cu K_{α1}) that we attribute to the iridium oxide phase.³⁴ The PXRD patterns of IrO_x/IrO₂@SnO₂ samples appear to show only reflections of orthorhombic scrutinyite as well as tetragonal SnO₂, which is isostructural with rutile. Upon closer examination, cassiterite-SnO₂ reflections show tails that coincide with the reflection positions of crystalline IrO₂. This is due to the very similar lattice parameters of iridium oxide and tin oxide, both of which crystallize in the rutile structure.³⁴ The reflections of the s-SnO₂ become less distinct after oxidation at higher temperatures, indicating phase transition to the rutile polymorph.

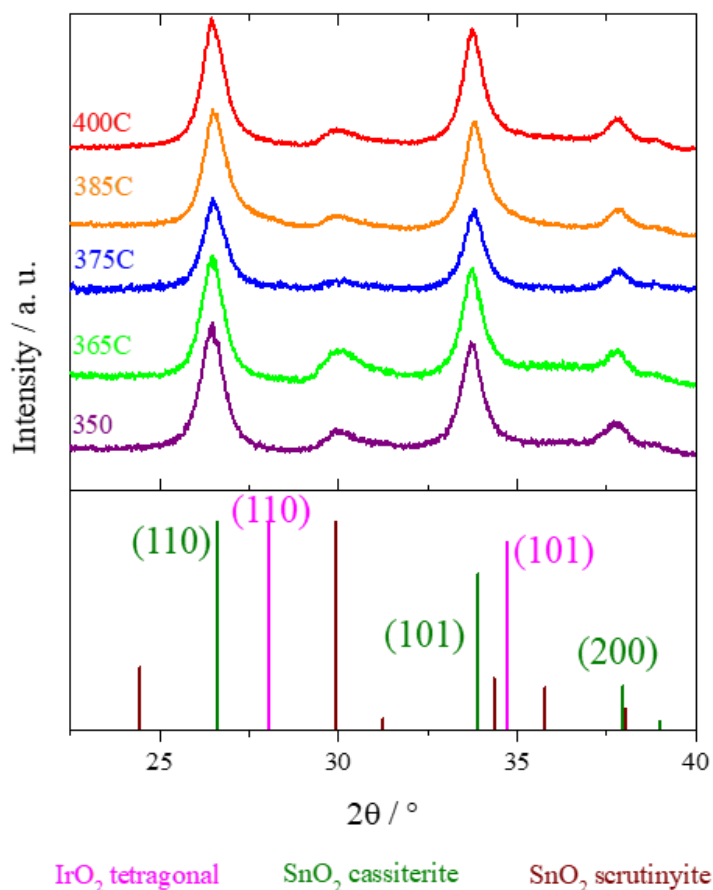


Figure 3-2: PXRD data of specimen calcined for 1 hour at different temperatures with an acquisition time of 1.5 h between 20° and 40° 2 θ .

Energy dispersive X-ray spectroscopy (EDX) data indicate that the nominal loading amount of 35 wt% was nearly matched with the resulting 33 wt% of iridium content (see supporting information Figure S3-1), indicating an efficient loading process. The nanoparticulate iridium oxide phase is evenly distributed throughout the sample on a micrometer scale. (supplementary Table S3-1, supplementary Figure S3-1). Particle sizes observed by STEM are 1-2 nm. Significant changes in the STEM data were observed starting from 375 °C, over 385 °C, to particularly 400 °C. At 375 °C, uniform coverage of the SnO₂ substrate with iridium oxide is observed, with no clear evidence of individual crystallites but rather interconnected iridium oxide. This is derived from high-resolution HAADF-STEM data (Figure 3-3a). In addition, the data indicate that the iridium oxide layer structure undergoes a gradual coarsening process after oxidation at 385 °C. This is attributed to the initial growth of isolated IrO₂, which could lead to a reduction in interconnectivity (Figure 3-3b). Upon oxidation at 400 °C, the formation of distinct nanocrystals on the surface of the SnO₂ support is observed. These mostly isolated nanocrystals of IrO₂, eventually lead to the disruption of the interconnected electrical

3. Optimized Oxidation Temperature Enhances OER Performance of IrO₂-Loaded SnO₂ Nanofibers – Role of Charge Carrier Percolation Pathways

percolation pathways (Figure 3-3c). The three samples show comparable electron diffraction patterns (Figure 3-2d,e,f). The diffuse diffraction rings confirm the fine polycrystalline nature of the samples (Figure 3-3d,e,f). Occasional stronger reflections within those diffuse rings stem from comparably larger crystallites (Figure 3-3d,e,f). We note that additional reflections may appear at scattering angles below twice the Bragg angle of low-order reflections corresponding to low-index zone axes $\langle 110 \rangle$ due to double-diffraction. They arise from multiple scattering in TEM due to differently oriented grains along the beam path. See supporting information for data of specimens calcined at 350 and 365 °C (Supporting Figure S3-3).

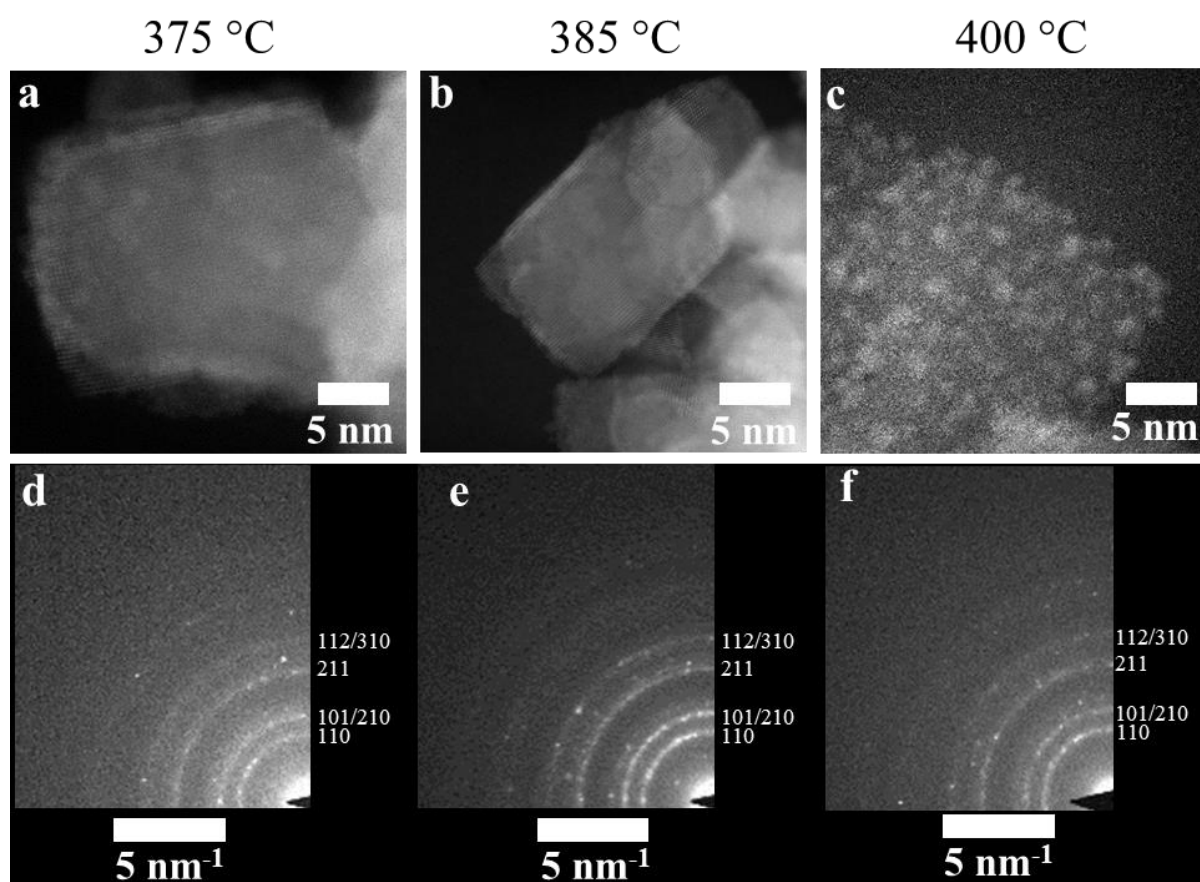


Figure 3-3: TEM HAADF images (a-c) and diffraction data (d-f) of samples loaded with 35 wt% nominal iridium after oxidation for 1 h in air at 375 °C (a and d), 385 °C (b and e) and 400 °C (c and f). As the temperature increases, the degree of fragmentation rises, thereby disrupting the conduction pathways.

In addition to the observed structural differences, differences in electrical conductivity, electrochemical activity, and stability of catalysts oxidized at various temperatures were also identified. The electrical conductivity has a significant impact on the efficiency and voltage losses in industrial electrolyzers operating at high current densities. The reference nanofibrous SnO₂ support exhibits a low conductivity of 1.6×10^{-1} mS cm⁻¹ (Figure 3-6a). As anticipated, the conductivity of the powders increased following coating with the conductive IrO_x layer.

3.2. Results and Discussion

However, the extent of this increase varied depending on the oxidation temperature. At a nominal loading of 35 wt% Ir, low conductivities of 0.2 and 5 mS cm⁻¹ were observed for a dried catalyst and after oxidation at 350 °C, indicating that the crystalline structure of the amorphous dehydrated IrO_x did not undergo significant changes. At 365 °C, a conductivity of 682 mS cm⁻¹ was obtained for IrO₂@SnO₂, representing a significant increase within a small temperature window. Crystalline IrO₂ exhibits higher electrical conductivity than the amorphous phase³⁵, suggesting that at 365 °C the crystallization of amorphous IrO_x is initiated. The sample calcined at 375 °C exhibited a slightly higher electrical conductivity, reaching a maximum of 1 S cm⁻¹. The relatively narrow temperature range of only 10 °C is sufficient to initiate the optimum crystallization of the amorphous IrO_x phase into IrO₂, which is expected to strongly impact the efficiency of the catalyst in an electrolyzer. Notably, further elevated oxidation temperatures of 385 and 400 °C were observed to result in a reduction in conductivity, with measured values of 5 and 2 mS cm⁻¹, respectively. These observations can be attributed to the growth of isolated separate IrO₂ crystals, which impede the conductive percolation pathways for charge carriers. These observations are in accordance with the differences in structure and morphology of the IrO_x/IrO₂@SnO₂ catalysts described in the preceding TEM section. While the initially present amorphous IrO_x displays a relatively continuous morphology on the SnO₂ surface, this phase generally exhibits a lower conductivity than the crystalline IrO₂.

Furthermore, comparative in-situ STEM-HAADF measurements were conducted in which nanowires were transferred to a chip of an *in-situ* TEM heating holder and heated in a high-vacuum environment inside the TEM. Figure 3-4 compiles STEM Z-contrast images of one wire-edge region taken during the course of increasing temperatures. As indicated on the right, each close-up view contains the projection through both the SnO₂-substrate and the IrO_x-film at the bottom, followed by the transition into the pristine IrO_x-film, finally ending in the vacuum region at the top (see Figure S3-7 for wider FOV).

3. Optimized Oxidation Temperature Enhances OER Performance of IrO₂-Loaded SnO₂ Nanofibers – Role of Charge Carrier Percolation Pathways

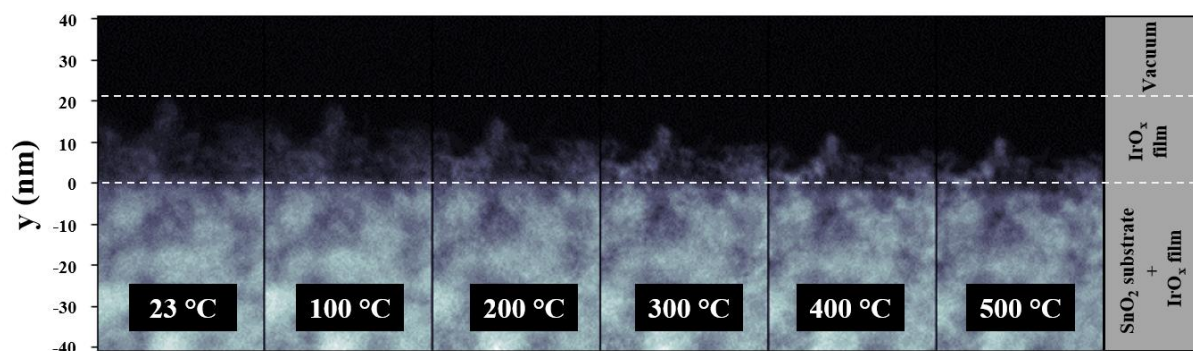


Figure 3-4: STEM-HAADF images of an IrO_x@SnO₂-wire edge successively heated from 23 °C up to 500 °C inside the TEM. At each indicated temperature step, a STEM-HAADF image of the same region has been acquired.

The most obvious effect of heating is a gradual shrinking of the Ir-film thickness with increasing temperature at a rate of 2 nm/100 °C (see Figure S3-8 for supporting information). Recalling that Z-contrast imaging provides a measure of the local mass density, Figure 3-4 reveals that the Ir-oxide film is rather homogeneous at room temperature, whereas its shrinking upon heating is accompanied by gradual granulation as indicated by the concentration of mass in local grains starting at about 300 °C. Also within the substrate region, the contrast between bright and dark areas increases, indicating segregation of the Ir-oxide film to form IrO₂ crystallites.

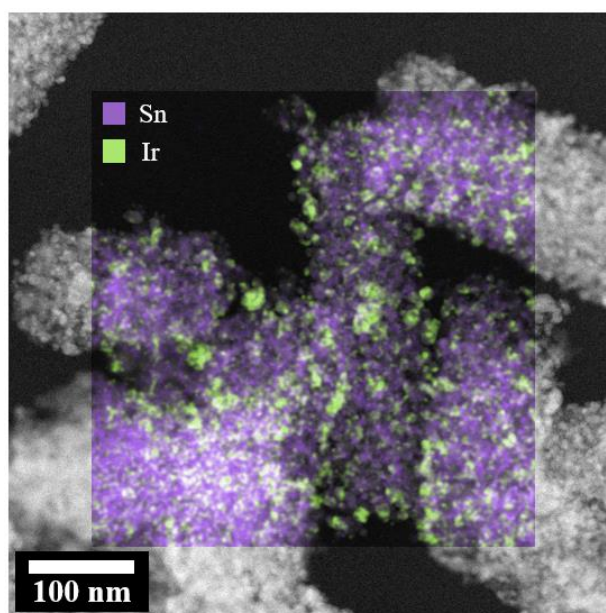


Figure 3-5: STEM-HAADF image of IrO_x@SnO₂ wires heated to 800 °C inside the TEM. Within the colored tile, an EDX-map overlay shows the spatial distribution of the elements Sn (purple) and Ir (green).

In Figure 3-5 we demonstrate that the thermal treatment drives the system to a state of complete IrO₂ segregation, which effectively breaks the electronic percolation pathways through the

3.2. Results and Discussion

conducting Ir-oxide phase. In this case, the specimen has been heated up to 800 °C inside the TEM so as to drive the crystallite formation. The energy-dispersive X-ray (EDX) map clearly reveals the homogeneous Sn distribution (purple) and the separated IrO₂ crystallites (green). Although the TEM study sheds light on the thermally-induced processes, we note that the conditions inside the TEM differ from *ex-situ* experiments shown in Figure 3-4. While we assume that the structural changes observed by TEM are representative and that they reveal the overall trends, they might occur at different temperatures in different atmospheres *ex-situ*.

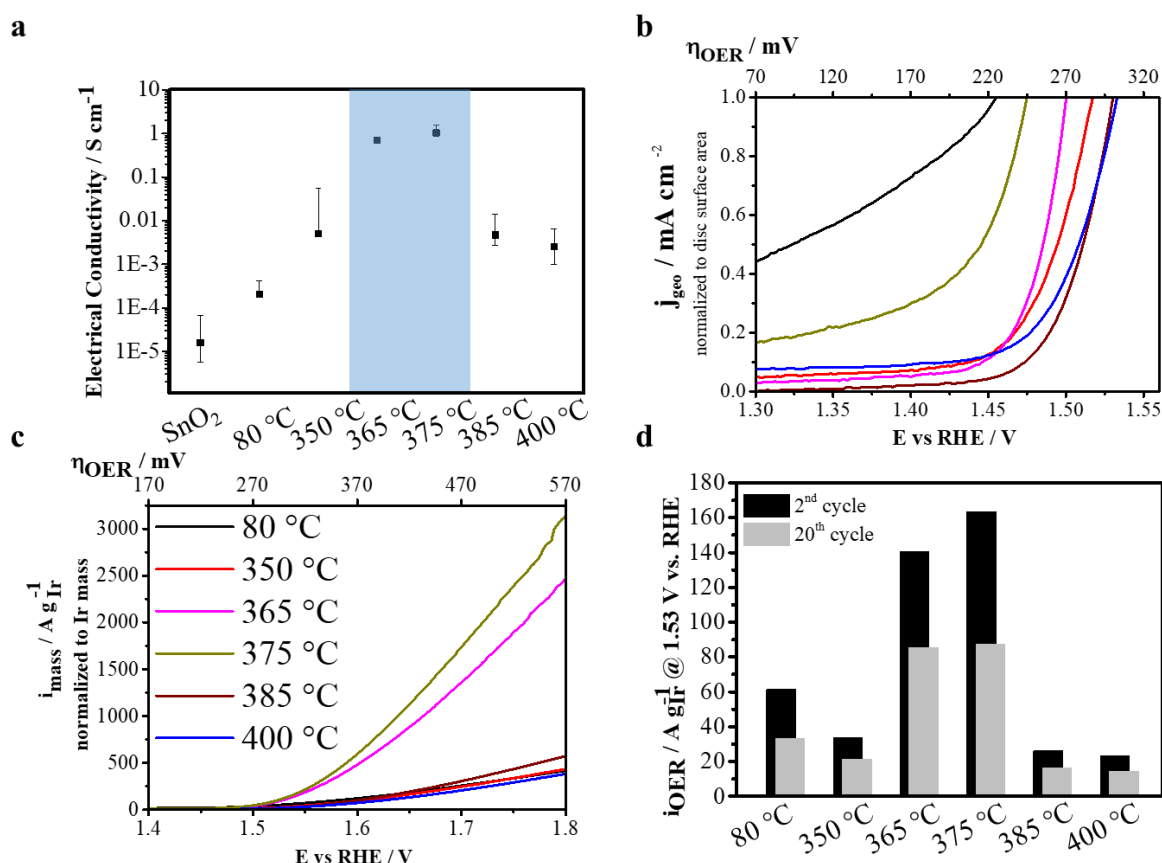


Figure 3-6: Conductivity and cyclic voltammetry (CVA) data of samples after calcination at different temperatures. Through-plane electrical conductivity of pressed powders measured in a home-built DC conductivity cell (a) (the entry “SnO₂” shows the conductivity of the pristine uncoated fibrous SnO₂ support). JV curves of IrO_x/IrO₂@SnO₂, also showing the onset potentials at 1 mA cm⁻² during CVA measurements on the stationary FTO electrode at the 2nd cycle (b). Electrochemical characterization on stationary FTO electrodes with only anodic scans shown, with current normalized to the total weight of Ir in the electrode layer, between 1.4 and 1.8 V versus RHE (2nd scan) (c) (b has the same color scheme as that used in c). Extracted mass-based activities at 2nd and 20th cycle at an overpotential of 300 mV (1.53 mV versus RHE) (d).

In addition to the differences in conductivity as a result of different oxidation temperatures, the electrochemical activity of the IrO_x/IrO₂@SnO₂ catalysts on the stationary FTO electrode also differs significantly (Figure 3-6b,c,d, Figure 3-7). All of the investigated IrO_x/IrO₂@SnO₂

3. Optimized Oxidation Temperature Enhances OER Performance of IrO₂-Loaded SnO₂ Nanofibers – Role of Charge Carrier Percolation Pathways

catalysts exhibited a relatively low onset potential of 1.45 V versus RHE (dried at 80 °C) and 1.47 V versus RHE (365 and 375 °C) at a defined current density of 1 mAcm⁻² of OER. Onset potentials of 1.52 V versus RHE for 350 °C as well as 1.53 V versus RHE (385 and 400 °C) were obtained (Figure 3-6b). These observations can be attributed to the initial presence of partially hydrated amorphous IrO_x at lower oxidation temperatures, which is one of the most electrocatalytically active compounds.³⁶ However, this phase is known to degrade rapidly upon repeated cycling, as evidenced by the significant decline in mass-specific activity after only 20 cycles (Figure 3-6d, for further data after 20 cycles see supporting information Figure S3-4).

Samples subjected to oxidation temperatures below 365 °C demonstrated comparable activities and cycling stabilities, as evidenced by the results of electrocatalytic measurements (Figure 3-6c,d). At a defined onset potential of 300 mV versus RHE, the mass-based activities of specimens dried at 80 °C exhibited a maximum of 61.4 A g_{Ir}⁻¹. At a higher oxidation temperature of 350 °C, the activity decreased to a maximum value of 33.7 A g_{Ir}⁻¹. The highest observable activities were found for samples oxidized at 365 and 375 °C, with a maximum mass-based activity of 163.5 A g_{Ir}⁻¹ for the sample calcined at 375 °C, and slightly lower activity of 140.6 A g_{Ir}⁻¹ for the specimen calcined at 365 °C. Oxidation temperatures of 385 and 400 °C resulted in lower activities, being within a similar range as samples oxidized below 365 °C, with activities of 26.2 and 23.2 A g_{Ir}⁻¹, respectively. We attribute the notable activity observed for IrO_x/IrO₂@SnO₂ oxidized at 365 and 375 °C, as illustrated in Figure 3-6c,d, to the growth of a most favorable overall morphology for electrocatalysis, comprising interconnected highly conducting crystalline IrO₂ nanoparticles (that may be interconnected by an amorphous IrO_x phase), which provides optimal conductive percolation networks for charge carriers as well as a high concentration of catalytically active sites. These results corroborate those obtained from the acquired conductivity and STEM data, thereby underscoring the crucial importance of optimizing the oxidation temperature for the purpose of catalyst optimization and enhancing catalytic activity.

STEM imaging was used to detect potential structural changes within the catalysts after electrochemical operation. Data of samples oxidized between 375 and 400 °C indicate the presence of a stable iridium oxide phase that appears to be firmly anchored to the substrate as shown in Figure 3-7. See supplementary information for further data with different magnifications and lower oxidation temperatures of 350 and 365 °C (Supplementary Figure S3-5 and 6). The images obtained are strikingly similar to those of the catalyst prior to electrocatalysis, illustrating morphological stability. The striking interconnectivity of the IrO₂

3.2. Results and Discussion

domains is still evident in the sample oxidized at 375 °C. There is no evidence of a significant detachment or dissolution of the catalytically active components. Moreover, no appreciable coarsening of the nanocrystals is observed. The sample oxidized at 385 °C features an incipient coarsening into larger, more isolated nanocrystallites, being consistent with the above electrochemical experiments. Overall, the STEM images illustrate that the iridium oxide phases exhibit minimal alteration in comparison to their state prior to electrochemical experimentation. This confirms that the crystalline IrO₂ phase remains stable within the highly acidic and oxidizing anodic environment of the electrochemical water splitting reaction.

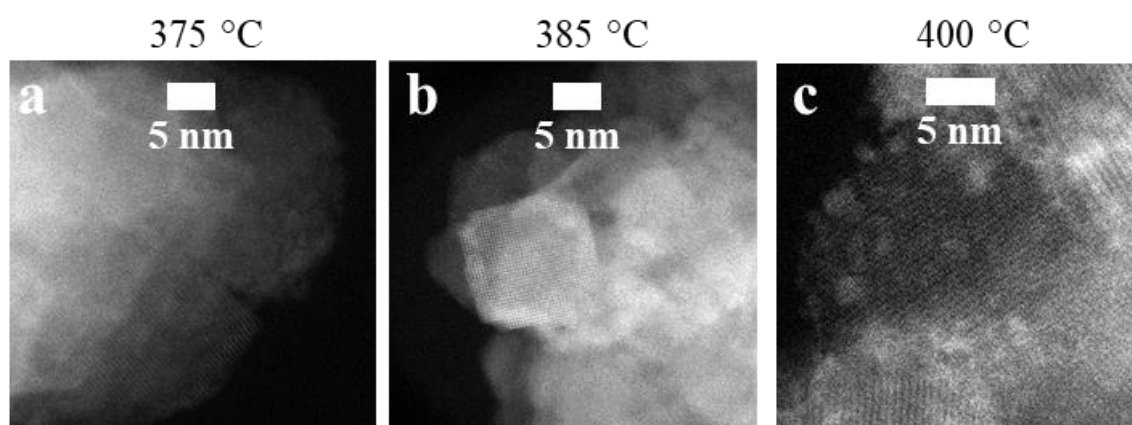


Figure 3-7: STEM imaging after 20 cycles between 1 and 1.8 V versus RHE of samples oxidized for 1 h at 375 °C (a), 385 °C (b) and 400 °C (c).

3.3. Conclusion and Outlook

This study examines the impact of oxidation temperature on the crystallinity, conductivity, and OER activity of supported IrO_x catalysts. Optimizing the oxidation temperature window for the fibrous SnO₂ support and its active components enables the controlled growth of interconnected IrO₂ nanocrystals with tailored crystal structures and surface coverage. The resulting crystalline IrO₂ phase, firmly anchored and interconnected, achieves electronic conductivity at low overpotentials and current densities, even with an Ir content of only 35 wt%. This is significantly lower than conventional catalysts such as Umicore's Elyst Ir75, which contain 75 wt% iridium, demonstrating substantial material efficiency.³⁷ Further tuning of catalyst coverage, thickness, and dominant facets through temperature control holds great promise for performance optimization.

A key advantage of this new route is that it eliminates the need for SnCl₄, thereby avoiding chlorine usage. When combined with a chlorine-free iridium precursor, the competing chlorine evolution reaction can be entirely excluded, enhancing the suitability of these materials for PEM electrolysis applications. The fibrous filament morphology supports low-resistance current conduction and shows potential for MEA integration. Moreover, there are prospects for a more compact core-shell synthesis process *via* direct co-spinning of iridium oxide phases, reducing mechanical and thermal stress on the filaments. Overall, this approach enables lower iridium usage while maintaining comparable catalytic activity, paving the way for cost-effective and efficient solutions in hydrogen generation.

3.4. Experimental Part

3.4. Experimental Part

Electrospinning and oxidation of SnO₂ fibers

For a typical preparation, 440 mg of Sn(OEt)₂ (Thermo Fischer) is placed in a round-bottom flask with a magnetic stirrer and stirred at 100 rpm. Subsequently, 0.8 ml of bi-distilled water is added dropwise, followed immediately by the addition of 4.2 ml of acetic acid (100%). The solution should be stirred at 50 °C until it becomes transparent. Subsequently, 10 ml of an ethanolic polyvinylpyrrolidone solution (10 wt%, Sigma Aldrich, Mw = 150 kDa) heated to 50 °C is added. Subsequently, the resulting solution is stirred for one hour at 50 °C and then drawn into a syringe and transferred to the electrospinning apparatus. The electrospinning process is conducted at a voltage of 13 kV, with a flow rate of 5 ml/h and a drum roll speed of 400 rpm. The distance between the needle tip and the drum roll collector is 12.5 centimeters. The resulting fiber mat is then carefully removed with a razor blade and transferred to an aluminum oxide dish for oxidation. The target temperature of 500 °C is reached with a heating ramp of 2 °C min⁻¹ and maintained for a period of three hours.

Loading of IrO(OH)_x nanoparticles and oxidation to IrO₂ on SnO₂ fibers

In order to achieve the iridium coating of the nanofilament SnO₂ support, a wet chemical synthesis previously described in detail (EP3764443B1; EP4019666A1) was adapted to prepare the amorphous IrO(OH)_x@SnO₂ catalyst precursor phase with a nominal content of 35 wt% Ir for SnO₂ supported IrO(OH)_x, respectively. To this end, the nominal amount of IrCl₃·xH₂O was dissolved in bi-distilled water at 80 °C, yielding a brown-yellow transparent solution. Following the dissolution of the iridium precursor, the respective amounts of SnO₂ filaments were added to the solution and stirred for one hour. In a typical reaction for 35 wt% Ir loading on SnO₂, 626 mg IrCl₃·xH₂O (43 wt% Ir according to ICP-OES) was dissolved in 100 ml of bi-distilled water, and 500 mg of SnO₂ was added. Following the dispersion of the supports, the pH of the compound solution was adjusted to 11.5 with 1 M NaOH for a period of 2 h. The mixture was then left to stir for a further 2 d at 80 °C, with the pH maintained between 11 and 11.5 as the color changed to dark blue. Subsequently, the product was subjected to four wash cycles with bi-distilled water, followed by centrifugation at 25,000 rcf for 20 min.

Two-plane conductivity measurements

Conductivity measurements of IrO₂@SnO₂ were conducted using an in-house constructed DC-conductivity measurement cell at an estimated moderate pressure of 1 MPa (to avoid crushing the tin oxide filaments). The measurements were recorded as *I-V* curves between -1 and +1 V with an AUTOLAB 302N potentiostat/galvanostat (METROHM AUTOLAB B.V.). While the conductivity measurements were conducted on moderately compressed materials, the results allow for a reliable relative comparison of transport properties.

Powder X-ray diffraction (PXRD)

PXRD experiments were conducted using a Ge (111) monochromated (Cu K α 1) STOE Stadi P diffractometer in transmission geometry with a solid-state strip detector (Dectris Mythen 1k). The XRD patterns of the samples were collected using an omega- 2θ scan in the 2θ range from 20° to 80°, with a step size of 1° and a fixed integration time of 60 s per step, and a resolution of 0.05°.

Transmission electron microscopy (TEM)

TEM and scanning TEM (STEM) measurements were performed at an FEI Titan Themis 80-300 (S)TEM, operated at 300 kV, equipped with an XFEG field emission gun and the chemiSTEM SuperX detection system for energy-dispersive X-ray (EDX) spectroscopy. The specimens were prepared on carbon TEM-grids via dry application from powder or from the FTO WE with catalyst powder post electro-catalysis. *In-situ* heating experiments were performed with a DENSsolutions Lightning HB+ holder, for which nanowires were transferred to electron-transparent SiN-membranes of MEMS chips. Selected-area TEM diffraction patterns were recorded on a CCD-camera of model CETA-M. High-angle annular dark field (HAADF) STEM images were acquired using a semi-convergence angle of the scanning probe of 23.3 mrad and a Fischione Model 3000 ring detector covering scattering angles of 35-200 mrad at the used camera length of 195 mm.

3.4. Experimental Part

Scanning electron microscopy (SEM)

Scanning electron microscopy (SEM) images were recorded with an FEI Helios Nanolab G3 UC scanning electron microscope, equipped with a field emission gun, and operated at an accelerating voltage of 2–5 kV. The specimens were prepared from powders deposited on carbon-based Leit tabs adhered to a stainless-steel sample holder. Energy-dispersive X-ray spectroscopy (EDX) measurements were recorded at an operating voltage of 20 kV with an X-MaxN Silicon Drift Detector, which has an 80 mm² detector area, and AZTec acquisition software, both of which are manufactured by Oxford Instruments. To quantify the iridium content via EDX in the SEM, the iridium content resulting from four measurements, each covering an area of between 40 and 100 μm^2 , was averaged.

Electrochemical characterization

Electrochemical characterization was conducted with a three-electrode configuration within a quartz cell at ambient temperature. The cell was filled with 20 ml of 0.5 M H₂SO₄ (SIGMA-ALDRICH, Titripur® volumetric standard) electrolyte. A PGSTAT302N potentiostat/galvanostat (Metrohm Autolab B.V.) equipped with an FRA32 M impedance analyzer was connected to a hydroflex reversible hydrogen electrode (Gaskatel Gesellschaft für Gassysteme durch Katalyse und Elektrochemie mbH) electrode for cyclic voltammetry and galvanostatic (chronopotentiometry) measurements, respectively.

To prepare the catalyst layers on FTO substrates, the volume of a dispersion of catalyst powders with different Ir loadings was calculated to deposit 10 μg Ir-content on a masked area of 0.196 cm⁻² on each electrode. The iridium content, as determined by EDX, was employed to calculate the nominal loading values of Ir in the electrode layers. Cyclic voltammetry (CVA) measurements were conducted with *iR* correction (95%) in a potential window of 1.0–1.8 V versus RHE with a scan rate of 20 mV s⁻¹ in 20 scans. Prior to each CVA measurement, impedance spectroscopy was conducted at 0.5 V versus RHE to ascertain the corresponding electrolyte resistance from the high-frequency region (R_s).

3.5. References

1. Awad, M.; Said, A.; Saad, M. H.; Farouk, A.; Mahmoud, M. M.; Alshammari, M. S.; Alghaythi, M. L.; Abdel Aleem, S. H. E.; Abdelaziz, A. Y.; Omar, A. I., A review of water electrolysis for green hydrogen generation considering PV/wind/hybrid/hydropower/geothermal/tidal and wave/biogas energy systems, economic analysis, and its application. *Alexandria Engineering Journal* **2024**, 87, 213-239.
2. Ababao, P. M.; Oh, I., Recent Advances in Catalyst Materials for PEM Water Electrolysis. *Journal of the Korean Electrochemical Society* **2023**, 26 (2), 19-34.
3. Carmo, M.; Fritz, D.; Mergel, J.; Stolten, D., A comprehensive review on PEM electrolysis. *International Journal of Hydrogen Energy* **2013**, 38, 4901-4934.
4. Song, J.; Wei, C.; Huang, Z.-F.; Liu, C.; Zeng, L.; Wang, X.; Xu, Z. J., A review on fundamentals for designing oxygen evolution electrocatalysts. *Chemical Society Reviews* **2020**, 49 (7), 2196-2214.
5. Böhm, D.; Beetz, M.; Schuster, M.; Peters, K.; Hufnagel, A. G.; Döblinger, M.; Böller, B.; Bein, T.; Fattakhova-Rohlfing, D., Efficient OER Catalyst with Low Ir Volume Density Obtained by Homogeneous Deposition of Iridium Oxide Nanoparticles on Macroporous Antimony-Doped Tin Oxide Support. *Advanced Functional Materials* **2020**, 30 (1), 1906670.
6. Abbott, D. F.; Lebedev, D.; Waltar, K.; Povia, M.; Nachtegaal, M.; Fabbri, E.; Copéret, C.; Schmidt, T. J., Iridium Oxide for the Oxygen Evolution Reaction: Correlation between Particle Size, Morphology, and the Surface Hydroxo Layer from Operando XAS. *Chemistry of Materials* **2016**, 28 (18), 6591-6604.
7. Böhm, D.; Beetz, M.; Gebauer, C.; Bernt, M.; Schröter, J.; Kornherr, M.; Zoller, F.; Bein, T.; Fattakhova-Rohlfing, D., Highly conductive titania supported iridium oxide nanoparticles with low overall iridium density as OER catalyst for large-scale PEM electrolysis. *Applied Materials Today* **2021**, 24, 101134.
8. Clapp, M.; Zalitis, C. M.; Ryan, M., Perspectives on current and future iridium demand and iridium oxide catalysts for PEM water electrolysis. *Catalysis Today* **2023**, 420, 114140.
9. Abbou, S.; Chattot, R.; Martin, V.; Claudel, F.; Solà-Hernandez, L.; Beauger, C.; Dubau, L.; Maillard, F., Manipulating the Corrosion Resistance of SnO₂ Aerogels through Doping for Efficient and Durable Oxygen Evolution Reaction Electrocatalysis in Acidic Media. *ACS Catalysis* **2020**, 10 (13), 7283-7294.

3.5. References

10. da Silva, G. C.; Venturini, S. I.; Zhang, S.; Löffler, M.; Scheu, C.; Mayrhofer, K. J. J.; Ticianelli, E. A.; Cherevko, S., Oxygen Evolution Reaction on Tin Oxides Supported Iridium Catalysts: Do We Need Dopants? *ChemElectroChem* **2020**, 7 (10), 2330-2339.
11. Du, Y.; Wang, W.; Zhao, H.; Liu, Y.; Li, S.; Wang, L., The rational doping of P and W in multi-stage catalysts to trigger Pt-like electrocatalytic performance. *Journal of Materials Chemistry A* **2020**, 8 (47), 25165-25172.
12. Kim, M.; Kwon, C.; Eom, K.; Kim, J.; Cho, E., Electrospun Nb-doped TiO₂ nanofiber support for Pt nanoparticles with high electrocatalytic activity and durability. *Sci Rep* **2017**, 7, 44411.
13. Neagu, D.; Irvine, J. T., Enhancing electronic conductivity in strontium titanates through correlated A and B-site doping. *Chemistry of materials* **2011**, 23 (6), 1607-1617.
14. Abd Rahman, N.; Tang, Z. S.; Bolong, N.; Saad, I.; Ayog, J. L.; Mohd Jaini, Z.; Yunus, R.; Rahmat, S. N., The Morphology of Electrospun Titanium Dioxide Nanofibers and Its Influencing Factors. *MATEC Web of Conferences* **2016**, 47.
15. Bernicke, M.; Ortel, E.; Reier, T.; Bergmann, A.; Ferreira de Araujo, J.; Strasser, P.; Kraehnert, R., Iridium Oxide Coatings with Templated Porosity as Highly Active Oxygen Evolution Catalysts: Structure-Activity Relationships. *ChemSusChem* **2015**, 8 (11), 1908-15.
16. Chen, H.; Shi, L.; Liang, X.; Wang, L.; Asefa, T.; Zou, X., Optimization of Active Sites via Crystal Phase, Composition and Morphology for Efficient Low-Iridium Oxygen Evolution Catalysts. *Angewandte Chemie International Edition* **2020**, 59.
17. Cherevko, S.; Geiger, S.; Kasian, O.; Kulyk, N.; Grote, J.-P.; Savan, A.; Shrestha, B. R.; Merzlikin, S.; Breitbach, B.; Ludwig, A.; Mayrhofer, K. J. J., Oxygen and hydrogen evolution reactions on Ru, RuO₂, Ir, and IrO₂ thin film electrodes in acidic and alkaline electrolytes: A comparative study on activity and stability. *Catalysis Today* **2016**, 262, 170-180.
18. Pan, S.; Li, H.; Liu, D.; Huang, R.; Pan, X.; Ren, D.; Li, J.; Shakouri, M.; Zhang, Q.; Wang, M., Efficient and stable noble-metal-free catalyst for acidic water oxidation. *Nature communications* **2022**, 13 (1), 2294.
19. Vazhayil, A.; Vazhayal, L.; Thomas, J.; Ashok C, S.; Thomas, N., A comprehensive review on the recent developments in transition metal-based electrocatalysts for oxygen evolution reaction. *Applied Surface Science Advances* **2021**, 6, 100184.
20. Xu, H.; Yuan, J.; He, G.; Chen, H., Current and future trends for spinel-type electrocatalysts in electrocatalytic oxygen evolution reaction. *Coordination Chemistry Reviews* **2023**, 475, 214869.

3. Optimized Oxidation Temperature Enhances OER Performance of IrO₂-Loaded SnO₂ Nanofibers – Role of Charge Carrier Percolation Pathways

21. Yan, Y.; Xia, B. Y.; Zhao, B.; Wang, X., A review on noble-metal-free bifunctional heterogeneous catalysts for overall electrochemical water splitting. *J. Mater. Chem. A* **2016**, *4*.
22. Zhang, T.; Zhu, Y.; Lee, J. Y., Unconventional noble metal-free catalysts for oxygen evolution in aqueous systems. *Journal of Materials Chemistry A* **2018**, *6* (18), 8147-8158.
23. Jürgensen, L.; Frank, M.; Pyeon, M.; Czympiel, L.; Mathur, S., Subvalent Iridium Precursors for Atom-Efficient Chemical Vapor Deposition of Ir and IrO₂ Thin Films. *Organometallics* **2017**, *36* (12), 2331-2337.
24. Matienzo, D. D.; Settipani, D.; Instuli, E.; Kallio, T., Active IrO₂ and NiO thin films prepared by atomic layer deposition for oxygen evolution reaction. *Catalysts* **2020**, *10* (1), 92.
25. Ogawa, S.; Hara, M.; Suzuki, S.; Joshi, P.; Yoshimura, M., Controlled Deposition of Iridium Oxide Nanoparticles on Graphene. *Electrochemistry* **2020**, 88.
26. Rajan, Z. S. H. S.; Binninger, T.; Kooyman, P. J.; Susac, D.; Mohamed, R., Organometallic chemical deposition of crystalline iridium oxide nanoparticles on antimony-doped tin oxide support with high-performance for the oxygen evolution reaction. *Catalysis Science & Technology* **2020**, *10* (12), 3938-3948.
27. Cheng, J.; Yang, J.; Kitano, S.; Juhasz, G.; Higashi, M.; Sadakiyo, M.; Kato, K.; Yoshioka, S.; Sugiyama, T.; Yamauchi, M.; Nakashima, N., Impact of Ir-Valence Control and Surface Nanostructure on Oxygen Evolution Reaction over a Highly Efficient Ir–TiO₂ Nanorod Catalyst. *ACS Catalysis* **2019**, *9* (8), 6974-6986.
28. Siracusano, S.; Baglio, V.; Grigoriev, S.; Merlo, L.; Fateev, V.; Aricò, A., The influence of iridium chemical oxidation state on the performance and durability of oxygen evolution catalysts in PEM electrolysis. *Journal of Power Sources* **2017**, *366*, 105-114.
29. Retuerto, M.; Salam, P.; Mostafa, M.; Calle-Vallejo, F.; Rojas, S., How Oxidation State and Lattice Distortion influence the Oxygen Evolution Activity in Acid of Iridium Double Perovskites. *Journal of Materials Chemistry A* **2021**, *9*.
30. Lee, W. H.; Ko, Y.-J.; Kim, J. H.; Choi, C. H.; Chae, K. H.; Kim, H.; Hwang, Y. J.; Min, B. K.; Strasser, P.; Oh, H.-S., High crystallinity design of Ir-based catalysts drives catalytic reversibility for water electrolysis and fuel cells. *Nature Communications* **2021**, *12* (1), 4271.
31. Bernsmeier, D.; Bernicke, M.; Schmack, R.; Sachse, R.; Paul, B.; Bergmann, A.; Strasser, P.; Ortel, E.; Kraehnert, R., Oxygen Evolution Catalysts Based on Ir-Ti Mixed Oxides with Templated Mesopore Structure: Impact of Ir on Activity and Conductivity. *ChemSusChem* **2018**, *11* (14), 2367-2374.

3.5. References

32. Banti, A.; Papazisi, K.; Balomenou, S.; Tsiplakides, D., Effect of Calcination Temperature on the Activity of Unsupported IrO₂ Electrocatalysts for the Oxygen Evolution Reaction in PEM Water Electrolyzers. *Molecules* **2023**, 28.
33. Cherevko, S.; Reier, T.; Zeradjanin, A. R.; Pawolek, Z.; Strasser, P.; Mayrhofer, K. J. J., Stability of nanostructured iridium oxide electrocatalysts during oxygen evolution reaction in acidic environment. *Electrochemistry Communications* **2014**, 48, 81-85.
34. Kost, M.; Kornherr, M.; Zehetmaier, P.; Illner, H.; Jeon, D. S.; Gasteiger, H.; Döblinger, M.; Fattakhova-Rohlfing, D.; Bein, T., Chemical Epitaxy of Iridium Oxide on Tin Oxide Enhances Stability of Supported OER Catalyst. *Small* n/a (n/a), 2404118.
35. Bernt, M.; Schramm, C.; Schröter, J.; Gebauer, C.; Byrknes, J.; Eickes, C.; Gasteiger, H. A., Effect of the IrO_x Conductivity on the Anode Electrode/Porous Transport Layer Interfacial Resistance in PEM Water Electrolyzers. *Journal of The Electrochemical Society* **2021**, 168 (8), 084513.
36. Bernt, M.; Hartig-Weiß, A.; Tovini, M. F.; El-Sayed, H. A.; Schramm, C.; Schröter, J.; Gebauer, C.; Gasteiger, H. A., Current Challenges in Catalyst Development for PEM Water Electrolyzers. *Chemie Ingenieur Technik* **2020**, 92 (1-2), 31-39.
37. Lee, G. R.; Kim, J.; Hong, D.; Kim, Y. J.; Jang, H.; Han, H. J.; Hwang, C.-K.; Kim, D.; Kim, J. Y.; Jung, Y. S., Efficient and sustainable water electrolysis achieved by excess electron reservoir enabling charge replenishment to catalysts. *Nature Communications* **2023**, 14 (1).

3. Optimized Oxidation Temperature Enhances OER Performance of IrO₂-Loaded SnO₂ Nanofibers – Role of Charge Carrier Percolation Pathways

3.6. Appendix

EDX data

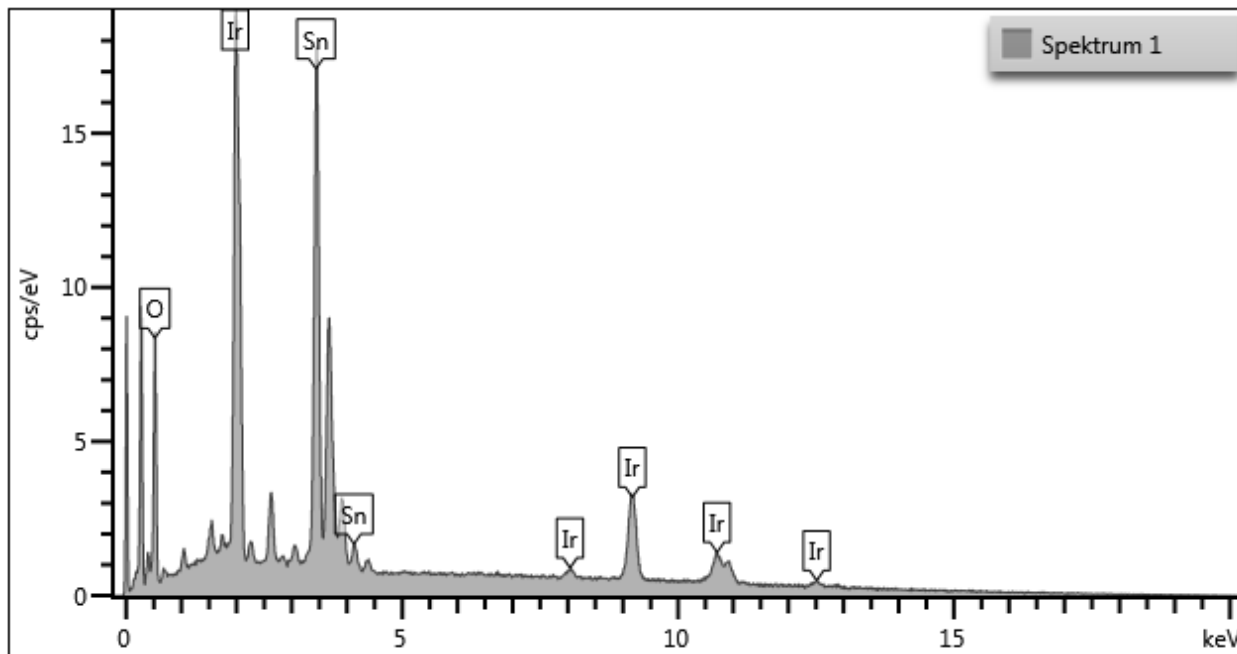


Figure S3-1: Spectrum of IrO₂@SnO₂ with 35 wt% Ir content calcined at 375 °C (with a nominal amount of 35 wt% iridium) contains 33 wt% according to EDX.

Table S3-1: Weight fraction of individual catalyst components according to EDX measurements in an SEM after calcination at 375 °C. Nominal value for iridium component was 35 wt%.

Element	Weight %
O	16.1
Sn	50.6
Ir	33.2
Sum	100.0

XRD

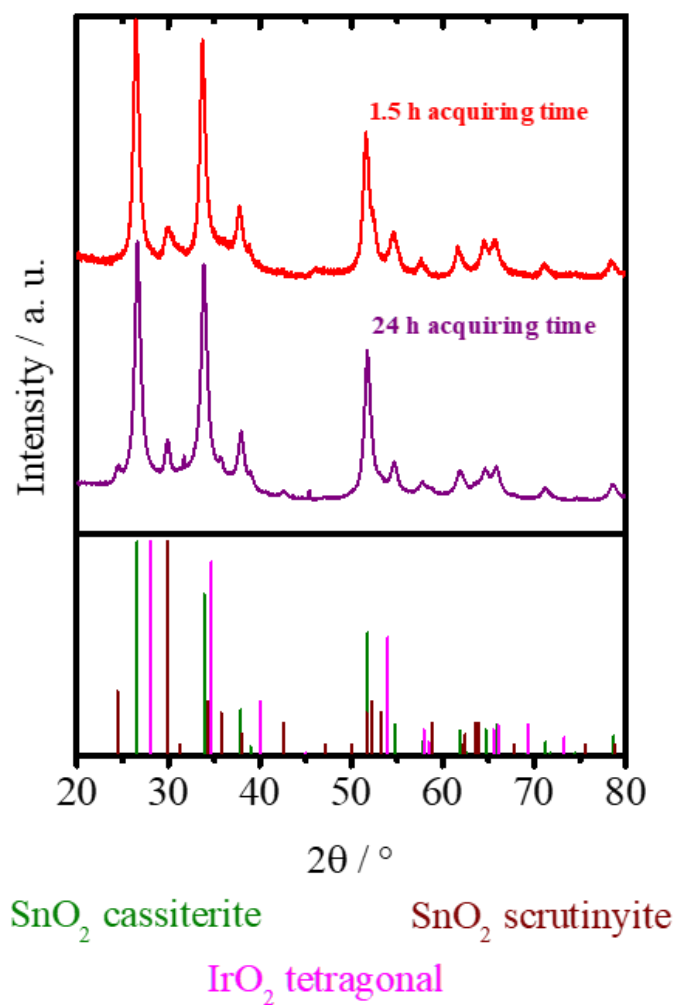


Figure S3-2: Detailed comparison of PXRD patterns acquired for 1.5 h and 24 h of $\text{IrO}_2@\text{SnO}_2$ with 35wt% Ir content calcined at 400 °C for 1 h. Especially at lower 2θ values, the reflections are separated more sharply.

3. Optimized Oxidation Temperature Enhances OER Performance of IrO₂-Loaded SnO₂ Nanofibers – Role of Charge Carrier Percolation Pathways

STEM data before electrocatalysis

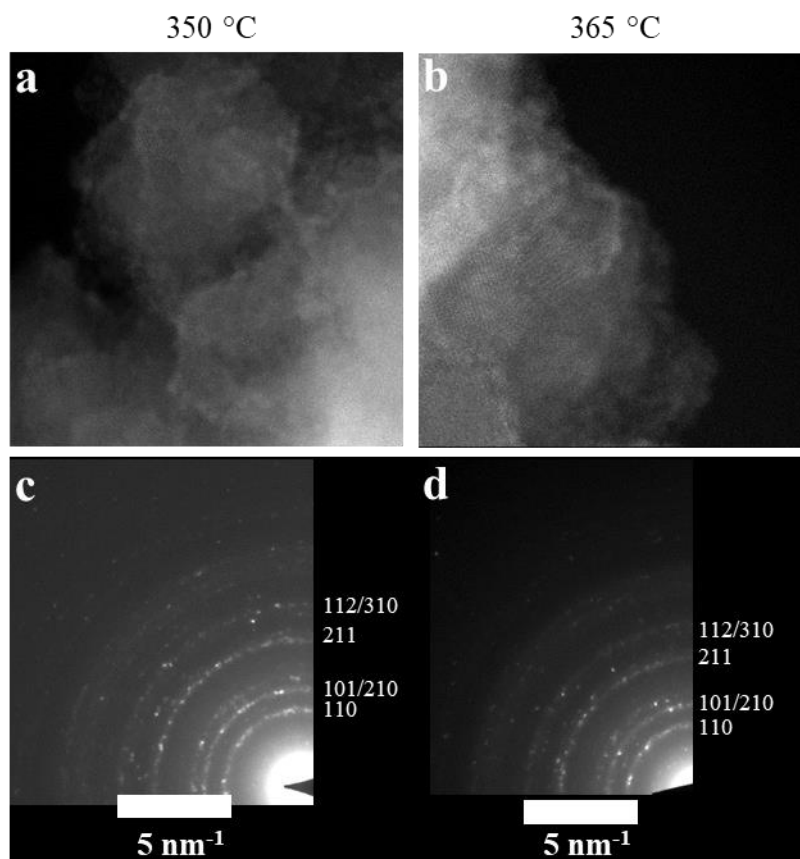


Figure S3-3: STEM and electron diffraction data of IrO_x@SnO₂ fibers calcined at 350 (a and c) and 365 °C (b and d).

3.6. Appendix

Electrochemical data

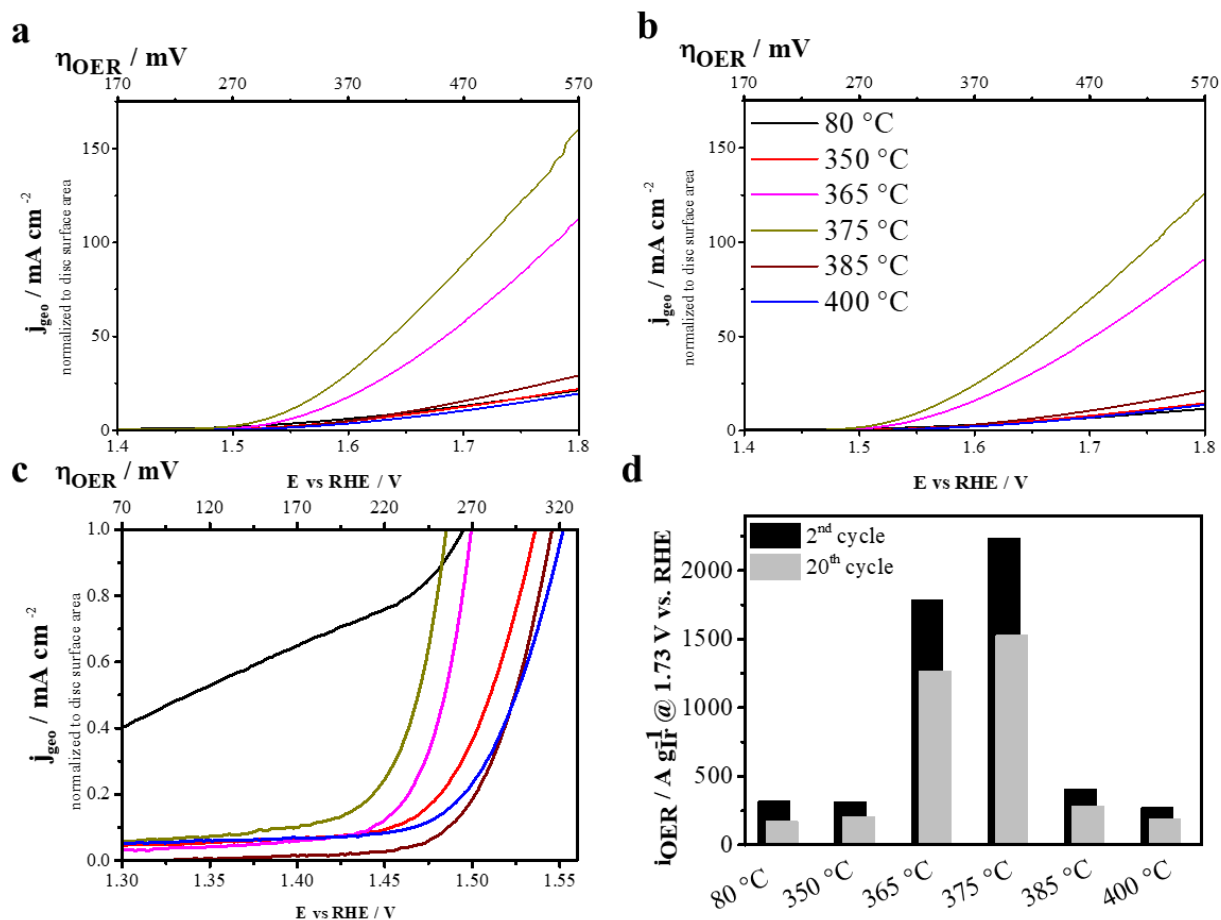


Figure S3-4: CVA data of $\text{IrO}_x/\text{IrO}_2@\text{SnO}_2$ after calcination at different temperatures. Electrochemical characterization on stationary FTO electrodes with only anodic scans shown, with current normalized to the total weight of Ir in the electrode layer between 1.4 and 1.8 V versus RHE. JV curves of 2nd (a) and 20th scan of $\text{IrO}_x/\text{IrO}_2@\text{SnO}_2$ samples oxidized at different temperatures (b). JV curves of $\text{IrO}_x/\text{IrO}_2@\text{SnO}_2$, also showing the onset potentials at 1 mA cm^{-2} during CVA measurements on the stationary FTO electrode at the 20th cycle (c) (a and c have the same color scheme as indicated in b). Extracted mass-based activities at 2nd and 20th cycle at an overpotential of 500 mV (1.73 mV versus RHE) (d).

3. Optimized Oxidation Temperature Enhances OER Performance of IrO₂-Loaded SnO₂ Nanofibers – Role of Charge Carrier Percolation Pathways

STEM data after electrocatalysis

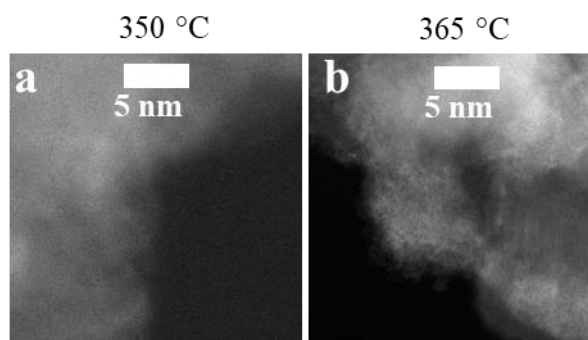


Figure S3-5. STEM images of IrO_x@SnO₂ with 35wt% Ir content calcined at 350 °C (a) and 365 °C (b) at high magnification.

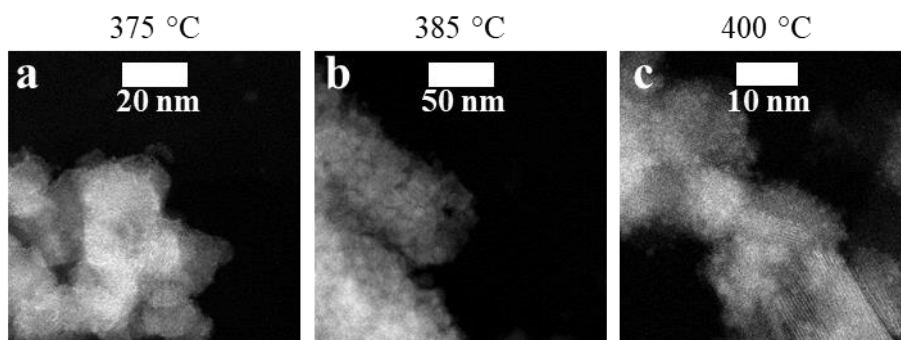


Figure S3-6: STEM imaging of IrO₂@SnO₂ with 35wt% Ir content at different magnifications, of catalysts oxidized at 375 °C (a), 385 °C (b), and 400 °C (c) after a cycle from 0 to 1.8 V versus RHE followed by 19 cycles between 1.3 and 1.8 V versus RHE.

3.6. Appendix

In-situ STEM data evaluation

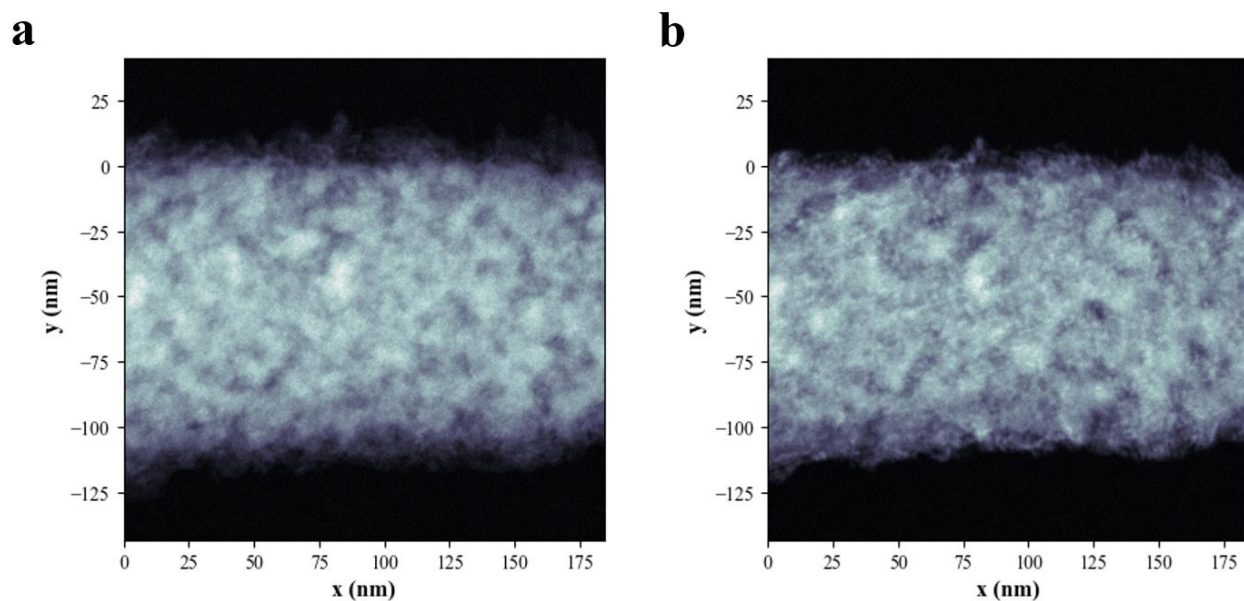


Figure S3-7: STEM-HAADF image of an $\text{IrO}_x@\text{SnO}_2$ -wire section (a) at 23 °C and (b) at 500 °C after in-situ heating.

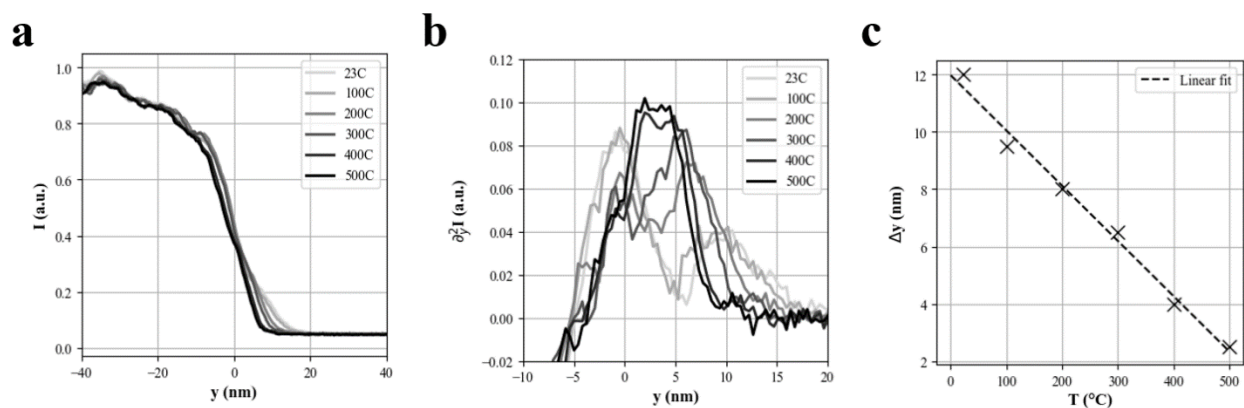


Figure S3-8: (a) Line profile from HAADF-intensity in S7a integrated along the wire axis for each temperature step. (b) Second derivative of line profiles depicted in (a). Peak positions serve as markers of the Ir-oxide film onset at the SnO_2 -substrate edge and vacuum region. (c) Peak-separation distance estimated from (b) as a measure of the IrO_2 -film thickness for each temperature step. The decrease of peak-separation distance with increasing temperature is about 2 nm/100 °C.

CHAPTER 4

Chemical Epitaxy of Iridium Oxide on Tin Oxide Enhances Stability of Supported OER Catalyst

4. Chemical Epitaxy of Iridium Oxide on Tin Oxide Enhances Stability of Supported OER Catalyst

This chapter is based on the following publication:

Melisande Kost, Matthias Kornherr, Peter Zehetmaier, Hannah Illner, Djung Sue Jeon, Hubert Gasteiger, Markus Döblinger*, Dina Fattakhova-Rohlfing*, Thomas Bein*, *Small* 2024, 20, 2404118

<https://doi.org/10.1002/sml.202404118>

Abstract

Significantly reducing the iridium content in oxygen evolution reaction (OER) catalysts while maintaining high electrocatalytic activity and stability is a key priority in the development of large-scale proton exchange membrane (PEM) electrolyzers. In practical catalysts, this is usually achieved by depositing thin layers of iridium oxide on a dimensionally stable metal oxide support material that reduces the volumetric packing density of iridium in the electrode assembly. By comparing two support materials with different structure types, it is shown that the chemical nature of the metal oxide support can have a strong influence on the crystallization of the iridium oxide phase and the direction of crystal growth. Epitaxial growth of crystalline IrO₂ is achieved on the isostructural support material SnO₂, both of which have a rutile structure with very similar lattice constants. Crystallization of amorphous IrO_x on an SnO₂ substrate results in interconnected, ultrasmall IrO₂ crystallites that grow along the surface and are firmly anchored to the substrate. Thereby, the IrO₂ phase enables excellent conductivity and remarkable stability of the catalyst at higher overpotentials and current densities at a very low Ir content of only 14 at%. The chemical epitaxy described here opens new horizons for the optimization of conductivity, activity and stability of electrocatalysts and the development of other epitaxial materials systems.

4.1. Introduction

Electrolysis of water in a proton exchange membrane electrolyzer (PEM electrolyzer) is one of the most promising technologies for efficient hydrogen production. PEM electrolysis offers numerous advantages, such as high adaptability to a decentralized power grid with a fast response to operating fluctuations, high efficiency, high current density of over 2 A cm^{-2} that allows high hydrogen output pressure, low gas cross-over, and compact design.^[1, 2] However, these advantages are offset by the high capital cost of critical components such as the Nafion membrane, porous titanium transport layer, and catalysts needed to accelerate the oxygen evolution (OER) reaction. In particular, the cost and scarcity of suitable OER catalyst layers remains one of the main factors limiting the economic feasibility and widespread application of PEM electrolyzers. Despite intensive efforts to develop efficient catalysts based on cheap and abundant elements, iridium remains the only OER catalyst that provides sufficient electrocatalytic activity and long-term corrosion stability in the harsh operating environment of a commercial PEM electrolyzer stack.^[3-5] In terms of overall availability, iridium is one of the scarcest materials, with an annual production of about seven tons.^[6] Therefore, a more than 40-fold reduction in iridium content from $\approx 2 \text{ mgIr cm}^{-2}$ to only $\approx 0.05 \text{ mgIr cm}^{-2}$ in a membrane electrode assembly (MEA) is required to achieve competitiveness of PEM electrolyzers.^[7, 8] At the same time, a certain technologically necessary thickness of electrode layers is required to ensure their reliable assembly and operation.^[7]

A widely used approach to reduce the areal Ir loading in practical MEAs is to disperse a small amount of an electrocatalytically active iridium phase on a cheap, dimensionally stable material that forms a mechanical backbone for the MEA architecture.^[9] The supported catalysts are usually fabricated by depositing thin iridium oxide films^[10-13] or nanoparticles^[14-17] on particles of the carrier material by scalable processes such as sol-gel coating, wet chemical precipitation or chemical vapor deposition. Methods such as atomic layer deposition or pulsed laser deposition are excellently suited to the deposition of self-limiting, ordered, epitaxially grown IrO_2 phases.^[18, 19] However, these methods are less promising for the production of practical catalysts for industrial applications due to their challenging scalability and associated costs. The coating process has a crucial influence on the performance of supported catalysts via the thickness, homogeneity, and distribution of the iridium oxide film and has therefore been intensively studied.^[20-24] Optimization of the support morphology, which strongly affects the volumetric Ir density, has also been the subject of extensive research.^[9, 14, 25-27]

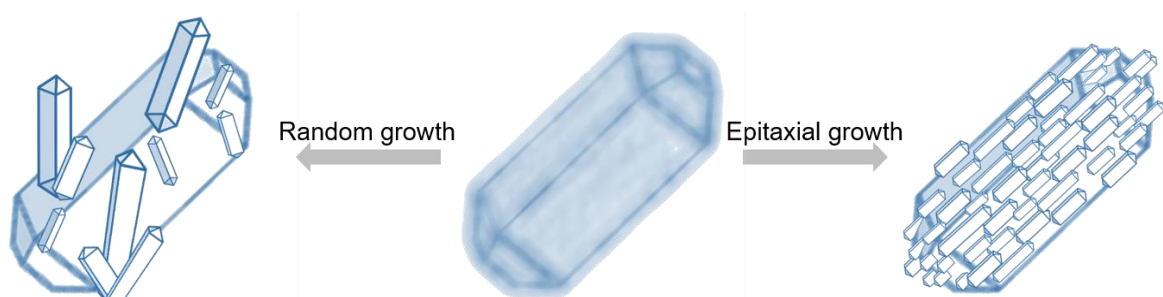
4.1. Introduction

The electrical conductivity of the supported catalysts is another important aspect of research activity, as it is fundamental to minimizing ohmic losses in industrial electrolyzers. Many efforts have been aimed at increasing the electrical conductivity of the support materials by structural doping.^[4, 28-30] However, due to problems with long-term stability under harsh OER conditions, the practical choice of support materials is generally limited to corrosion-resistant metal oxides (MO), with the electrically insulating TiO₂ remaining the most popular support material.^[14, 31-36] It was also shown that pristine SnO₂ can be a suitable corrosion-stable substrate material under PEM conditions.^[37] The charge carrier percolation in such insulating materials is only possible via a conductive IrO_x phase. Therefore, optimization of the volume fraction, distribution, homogeneity, interconnectivity, and conductivity of the IrO_x coating is the most important means to improve the macroscopic conductivity of IrO_x/MO-supported catalysts.^[26]

Crystallinity and morphology of the IrO_x phase strongly affect its conductivity and electrocatalytic activity. The amorphous phase, which exists in various hydrogenated states and is often referred to as IrO(OH)_x, has very high initial electrocatalytic activity but low long-term stability and lower electrical conductivity.^[38, 39] This differs from the crystalline IrO₂ phase, which has lower catalytic activity but much better long-term stability and higher electrical conductivity than its amorphous counterpart, especially during prolonged polarization.^[26, 40] Increased crystallinity of the IrO_x phase can have a positive effect on catalyst performance and is one of the goals of catalyst development. However, the conversion of amorphous to crystalline IrO_x is accompanied by significant morphological changes that can have a negative impact on catalyst performance. In particular, the uncontrolled growth of elongated IrO₂ crystals poses the greatest challenge to the dimensional stability and functionality of the catalyst architecture. When the direction of crystal growth is orthogonal to the surface of the support material, crystallization disrupts the continuity of the IrO_x phase, leading to a loss of conductivity and resulting performance degradation.^[14] An optimized IrO_x coating could be envisioned as an interconnected layer of ultrasmall IrO₂ crystallites along the support surface, with a firm attachment to the MO support. In principle, these features might be obtained by an epitaxial growth process (Scheme 4-1). Epitaxial crystallization in a chemical process was demonstrated, for example, for Deacon catalysts, for which the formation of an epitaxial RuO₂ layer on isostructural rutile supports was observed.^[41-43] However, no examples of such a growth mode are yet known for practical IrO_x-based catalysts for industrial applications. The work of Rajan et al.^[44] showed evidence of epitaxial anchoring of

4. Chemical Epitaxy of Iridium Oxide on Tin Oxide Enhances Stability of Supported OER Catalyst

IrO_2 nanoparticles on rutile antimony-doped tin oxide. However, the involved processing methods are difficult to scale up to an industrial scale. Therefore, it remains to be shown whether epitaxial growth of IrO_x catalyst can be achieved by an easily scalable chemical synthesis route and whether a high degree of control over the synthesis can be achieved to obtain the properties mentioned above. Isostructural materials with similar lattice parameters are good prerequisites to facilitate epitaxial growth.^[45] From this perspective, corrosion-stable SnO_2 is a possible choice as a catalyst support for crystalline IrO_2 , as both materials have rutile structure and a lattice mismatch of less than 5% for all lattice constants. To address this challenge, we compared the crystallization of IrO_x films deposited on TiO_2 with predominantly anatase structure with growth on SnO_2 support materials under otherwise identical conditions, and investigated the effects of the support material on the catalyst structure and properties.



Scheme 4-1: Simplified scheme of possible crystallization processes. Crystallization of an amorphous $\text{IrO}(\text{OH})_x$ coating on a crystalline MO substrate: random growth of IrO_2 crystals (left) versus epitaxial growth along the substrate surface (right).

4.2. Results and Discussion

For the preparation of the supported OER catalysts, a simple wet-chemical coating procedure was applied, which has already been successfully used for the preparation of IrO_x catalysts on TiO_2 support on an industrial scale.^[14, 36, 46, 47] In the first step, the controlled hydrolysis of an aqueous iridium(III) chloride solution in the presence of high surface area metal oxide (MO) supports leads to the formation of very thin homogeneous amorphous $\text{IrO}(\text{OH})_x$ layers on the particle surface (referred to as $\text{IrO}(\text{OH})_x@\text{MO}$). In order to focus exclusively on the influence of the support material on the catalyst performance while keeping the other parameters similar, crystalline TiO_2 (anatase) and SnO_2 nanoparticles with a very similar morphology and an average particle size of about 50 nm were used as catalyst supports (Figures S4-1 and S4-2, Supporting Information). The molar ratio between the Ir salt and MO particles was varied to obtain $\text{IrO}_x@\text{SnO}_2$ and $\text{IrO}_x@\text{TiO}_2$ catalysts with low Ir loadings of 7 at% and 14 at%, referred to as $\text{IrO}_x@\text{MO}_7$ at% and $\text{IrO}_x@\text{MO}_{14}$ at%, respectively (for comparison, the industrial benchmark catalyst $\text{IrO}_x@\text{TiO}_2$ Elyst Ir75 has a much higher loading of 75 wt% Ir,^[48] respectively 56 at% Ir (Ir:Ti)). Amorphous $\text{IrO}(\text{OH})_x$ is unstable under PEM electrolysis conditions and should be converted to a more stable IrO_x phase by thermal treatment, which has a key impact on catalyst performance. Our previous studies of $\text{IrO}_x@\text{TiO}_2$ catalysts have shown that rapid calcination and high calcination temperatures above 400 °C lead to uncontrolled growth of IrO_2 crystals on the TiO_2 surface, which disrupts the continuity of the conductive catalyst layer, while considerably lower calcination temperatures are insufficient for the required conversion of the amorphous phase to the crystalline phase. Mild oxidation in molten NaNO_3 at 375 °C^[14, 49, 50] proved to be the optimal thermal treatment for the $\text{IrO}_x@\text{TiO}_2$ catalyst, resulting in maximum conductivity and electrochemical performance.^[14, 51, 52] For better comparability, the same treatment was applied to both the TiO_2 and SnO_2 -supported catalysts studied in this work.

Powder X-ray diffraction (PXRD) patterns of $\text{IrO}_x@\text{TiO}_2$ and $\text{IrO}_x@\text{SnO}_2$ with 14 at% Ir loading after oxidation at 375 °C in molten NaNO_3 are shown in Figure 4-1a,c. The phase composition of the TiO_2 support consists of a mixture of small crystals of predominantly anatase (92 wt%, ≈ 84 nm in the *a-b* plane, and ≈ 37 nm along *c*) and a minor fraction of rutile (8 wt%, ≈ 35 nm in size), as determined by Rietveld refinement (Figure S4-3 and Table S4-1, Supporting Information). The PXRD patterns of $\text{IrO}_x@\text{TiO}_2$ exhibit a broad intensity maximum at $q = 2.36 \text{ 1/\AA}$, or $12^\circ 2\theta$ (Ag $\text{K}\alpha_1$) as shown in Figure 4-1a. The contribution of

IrO_x can be extracted by subtracting the PXRD patterns of the pure TiO_2 support from the corresponding PXRD patterns of $\text{IrO}_x/\text{TiO}_2$ (Figure 4-1a, inset). To obtain a more detailed structural understanding of the IrO_x coverage on TiO_2 , the electron diffraction patterns (Figure S4-4, Supporting Information) of individual IrO_x agglomerates and the extracted IrO_x contribution from the PXRD patterns (Figure 4-1a, inset) were evaluated. By Fourier sine transform, these evaluations yield the reduced pair distribution function (PDF), which represents the probability of finding atom pairs as a function of distance (Figure 4-1b). The PDFs derived from electron diffraction and PXRD are quite similar and both exhibit a double maximum at about 3.1 and 3.55 Å. These values are close to the Ir–Ir distances in crystalline rutile and hollandite.^[53, 54] The presence of a double maximum with approximately equal intensities suggests a short-range order closer to hollandite (with a larger fraction of edge-sharing IrO_6 octahedra) and the presence of a mixed valence state of Ir^{3+} and Ir^{4+} . Assuming a direct relationship between the valence state of Ir and its connectivity or atomic distances, this suggests the presence of Ir^{3+} and Ir^{4+} in approximately equal amounts. Beyond about 8.5 Å, the PDFs become featureless, consistent with the impression from HAADF-STEM images (Figure 4-2a,c) that amorphous (sub-) nanometer particles are loosely agglomerated.

4.2. Results and Discussion

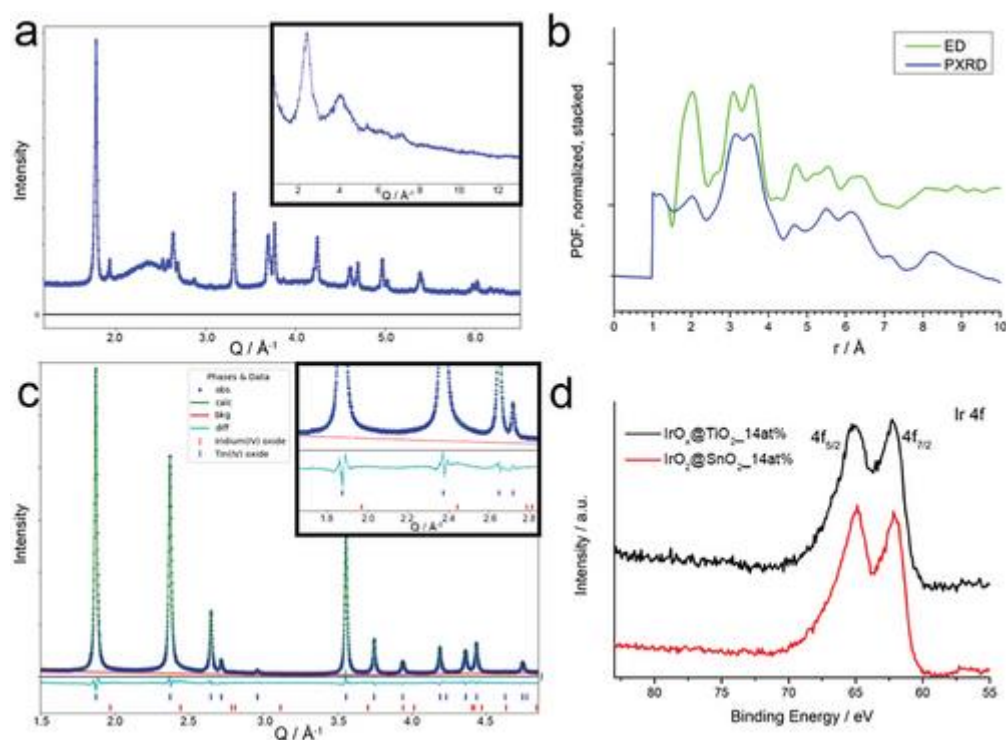


Figure 4-1: Physicochemical characterization of IrO_x@MO. a) PXRd pattern (Ag Ka₁) of TiO₂-supported IrO_x (14 at% Ir). Inset: Extracted contribution of IrO_x after subtracting a PXRd pattern of the pure TiO₂ substrate from the pattern of TiO₂-supported IrO_x. b) Pair distribution functions derived from an electron diffraction pattern of small IrO_x agglomerates (green) and from the IrO_x signal extracted from PXRd (blue). c) PXRd pattern of SnO₂-supported IrO_x (14 at% Ir). The magnified inset depicts the base of some reflections showing anisotropic tails, coinciding with reflection positions of crystalline IrO₂. d) Iridium 4f XPS spectra of SnO₂ and TiO₂-supported iridium oxide species with 14 at% Ir content, respectively.

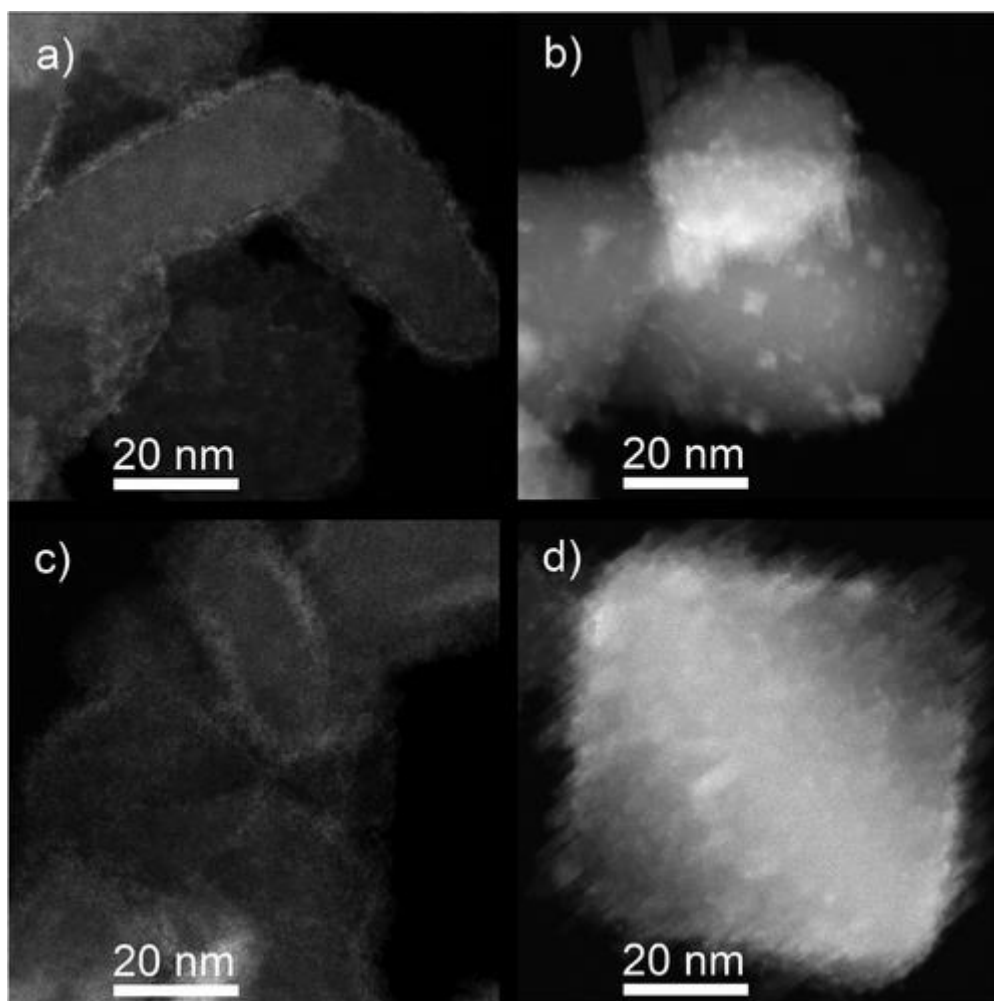


Figure 4-2: Atomic number sensitive STEM-HAADF images of Ir-loaded supports. The left images depict TiO_2 substrates with a) 7 at% Ir, and c) 14 at% Ir, while the right images show SnO_2 substrates with b) 7 at% Ir, and d) 14 at% Ir.

The PXRD patterns of $\text{IrO}_x@ \text{SnO}_2$ samples (Figure 4-1c) appear to show only reflections of tetragonal SnO_2 , which is isostructural with rutile. Closer inspection reveals that some of the SnO_2 reflections have tails that coincide with the reflection positions of crystalline IrO_2 (Figure 4-1c, inset), which also has rutile structure and similar lattice parameters. A Rietveld refinement (Table S4-2, Supporting Information) gives a size of about 40 nm for the SnO_2 support particles (≈ 85 wt%). The crystallite size of IrO_2 was refined anisotropically, yielding rod-shaped IrO_2 nanocrystals elongated along the c-axis, with an average size of $\approx 1.6 \text{ nm} \times 14 \text{ nm}$. The amount of IrO_2 of ≈ 10.3 at% determined by Rietveld refinement is lower than the nominal amount of Ir in the sample (14 at%), which may be due to the fact that the amorphous phase of IrO_x was not included in the refinement. Some of the IrO_x material remained non-crystalline (Figure S4-8, Supporting Information), but part of the discrepancy may also be related to a dependence on the background fit.

4.2. Results and Discussion

Further insight into the oxidation states of iridium was obtained by XPS (Figure 4-1d). In general, the spin-orbit splitting ratio for the $4f_{7/2}$ and $4f_{5/2}$ components of the 4f doublet is 4:3, but this usual intensity distribution is not present in the spectra obtained, supporting the presence of more than one Ir species. Due to the small difference in the binding energies of Ir^{3+} and Ir^{4+} of less than 1 eV and the presence of multiple satellite peaks at the same binding energies, a fit of the individual components is only possible with extensive constraints. Their ratio can therefore not be determined precisely.^[55, 56] Different peak widths and intensity ratios of the $4f_{7/2}$ to $4f_{5/2}$ are attributed to different proportions of oxidation states in both samples. In addition, the slightly broader peak width in the $\text{IrO}_x/\text{TiO}_2$ sample compared to the work of Pfeifer et al. indicates a higher fraction of the amorphous phase.^[55] This peak broadening is not as pronounced in the $\text{IrO}_x/\text{SnO}_2$ sample, suggesting a higher degree of crystallinity. The survey spectra of both samples are displayed and described in the Supporting Information (Figure S4-5, Supporting Information).

The morphology, nanostructure, and composition of the samples were characterized by electron microscopy. As expected, the morphology of the nanoparticle supports remained unchanged after the loading and oxidation processes (Figure S4-5, Supporting Information). Energy-dispersive X-ray spectroscopy (EDX) data confirm that the nominal loading amount of iridium is uniformly distributed over the sample on a micrometer scale (Tables S4-3–S4-6 and Figures S4-7–S4-10, Supporting Information). The particle sizes observed by TEM are in agreement with the PXRD results (Figure S4-3, Supporting Information). Imaging at higher magnification using atomic number sensitive scanning transmission electron microscopy in high-angle annular dark-field mode (STEM-HAADF) shows a different morphology for IrO_x particles on the surface of SnO_2 and TiO_2 substrates (Figure 4-2). On the TiO_2 substrate (Figure 4-2a,c), the IrO_x appears as loosely agglomerated, extremely fine particles extending into the sub-nm range. At a loading of 14 at% Ir, the particles form a coherent layer (Figure 4-3a). At an increased Ir-loading of 14 at%, a continuous film is observed (Figure 4-2c). In edge-on orientations, the IrO_x coating has a thickness of 1–2 nm and 2–3 nm for 7 at% and 14 at% Ir, respectively.

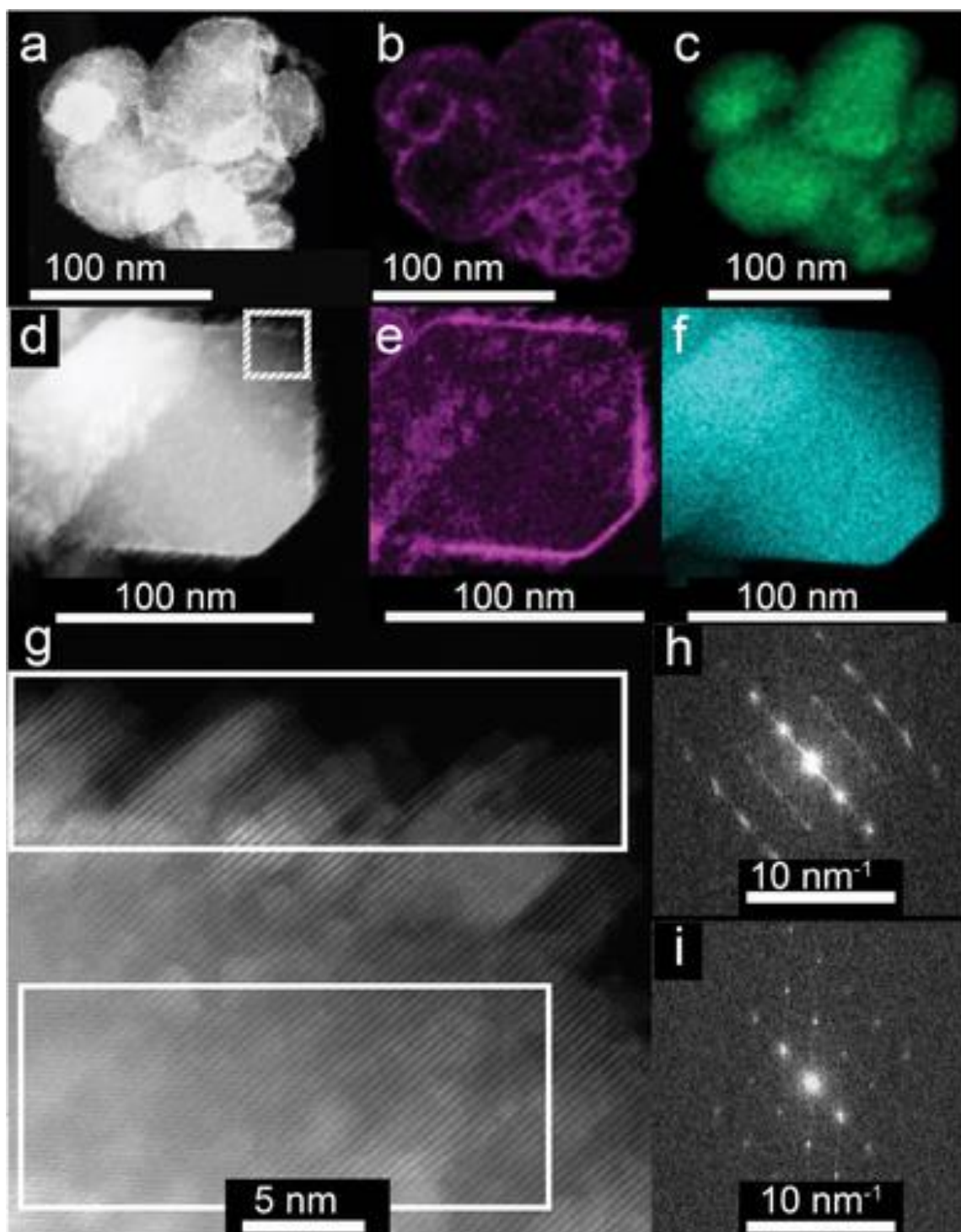


Figure 4-3: Transmission electron microscopy imaging of $\text{IrO}_x@\text{MO}$ samples. a) STEM-HAADF image of $\text{IrO}_x@\text{TiO}_2_{14}$ at%; b,c) corresponding elemental EDX maps showing the distribution of iridium (purple) and titanium (green). d) STEM-HAADF image of $\text{IrO}_2@\text{SnO}_2_{14}$ at% Ir. e,f) Corresponding elemental EDX maps showing the distribution of iridium (purple) and tin (cyan). g) High-resolution STEM-HAADF image of the small hatched rectangle in (d). The Fourier transform (FT) of the white upper rectangular area is shown in (h), the FT of the white lower rectangle is shown in (i). A comparison with the EDX maps e,f) shows that the upper rectangular area is free of Sn while the lower rectangular area is dominated by the SnO_2 support. Both FTs show a tetragonal arrangement of peaks whose intensities indicate a slight tilt out of zone axis. The peak positions are in agreement with the $hk0$ reciprocal plane of h) IrO_2 and i) SnO_2 , the lattice plane distances of IrO_2 being around 5% smaller than those of SnO_2 .

4.2. Results and Discussion

In contrast to the TiO₂-supported catalyst, mostly nanocrystals are observed on the SnO₂ support (Figure 4-2b,d) in addition to smaller particles that do not exhibit a clear lattice fringe contrast (compare to Figure S4-8, Supporting Information). On each crystal face of the SnO₂ support, most surface crystals exhibit the same crystallographic orientation. At a low Ir loading of 7 at%, the surface crystals appear to be isolated. At 14 at% Ir, the connectivity of the surface particles improves significantly, but a homogeneous surface film is not consistently observed.

The IrO_x/IrO₂ particle coating is illustrated by STEM-EDX maps (Figure 4-3) for both support materials loaded with 14 at% Ir. For the TiO₂ support, the Ir and Ti-maps (Figure 4-3b,c) confirm a continuous IrO_x film with a fairly constant thickness, consistent with HAADF-STEM observations. For SnO₂ substrates, the EDX maps and HAADF-STEM images show a more inhomogeneous surface coating reflecting the presence of surface nanocrystals instead of amorphous IrO_x (Figure 4-3e,f and Figures S4-8–S4-10, Supporting Information). A closer examination of such a region (hatched rectangle in Figure 4-3d, magnified in Figure 4-3g) reveals similar lattice spacings and orientations of surface crystals and support. This is verified by Fourier transformation (FT) of a region composed entirely of Ir-containing surface crystals (upper white rectangle in Figure 4-3g) and a region dominated by the SnO₂ support (lower white rectangle in Figure 4-3g shown in Figure 4-3h,i), respectively. Both FTs show maxima at similar positions, in agreement with the *hk0* plane of IrO₂ (Figure 4-3h), and the *hk0* plane of SnO₂ (Figure 4-3i), both of which have rutile structure and similar lattice constants ($\Delta a/a < 5\%$).^[53] In this study, all characterized SnO₂ facets were covered by crystalline epitaxial IrO₂. Additional examples of the epitaxial relationship between SnO₂ and IrO₂ are shown in the supporting information (Figures S4-8–S4-10, Supporting Information). The latter examples highlight the rod-like elongation of IrO₂ crystals along the *c*-axis, as expected from the Rietveld refinement of SnO₂ loaded with 14 at% Ir (Figure 4-1c and Table S4-2, Supporting Information). The mechanical stability and integrity of epitaxial films during catalytic use has yet to be demonstrated.

4. Chemical Epitaxy of Iridium Oxide on Tin Oxide Enhances Stability of Supported OER Catalyst

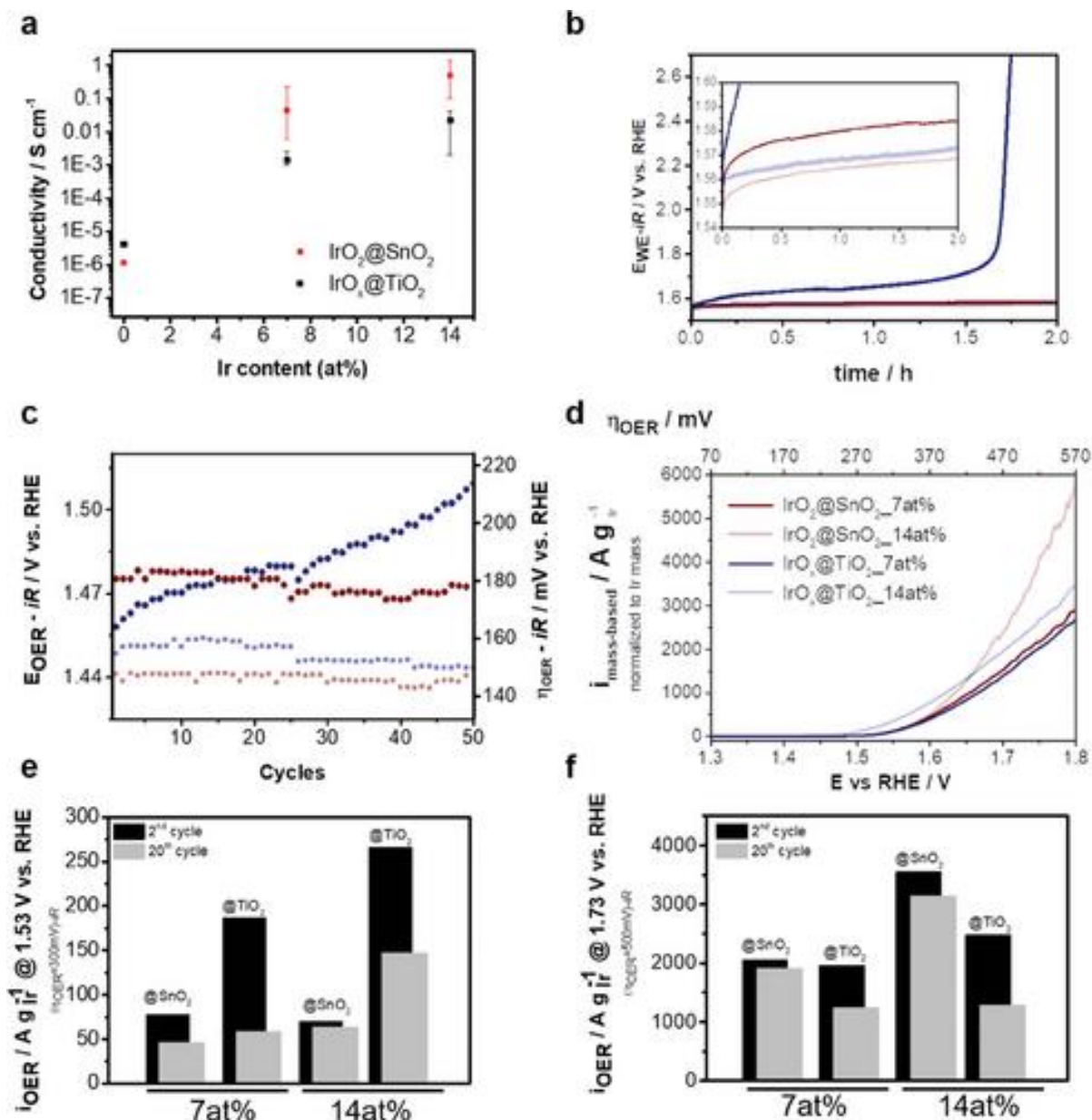


Figure 4-4: Electrical and electrochemical characterization of $\text{IrO}_x@\text{SnO}_2$ and $\text{IrO}_x@\text{TiO}_2$ catalysts with different Ir content: a) through-plane electrical conductivity of pressed powders measured in a home-built DC conductivity cell. b–f) Electrochemical characterization on b,d–f) stationary FTO electrodes and c) rotating disc electrode (RDE). Figure 4-4b–d) have the same color scheme indicated in the legend of Figure 4-4d. b) Electrode potential during galvanostatic polarization of the catalyst layer on a stationary FTO electrode for 2 h at a constant current density of 10 mA cm^{-2} ; c) electrode potentials at current density of 1 mA cm^{-2} during cyclic voltammetry (CVA) of catalyst layers on the RDE for 50 cycles); d) CVA on the stationary FTO electrode (only anodic scan is shown, with current normalized to the total weight of Ir in the electrode layer) between 1.3 and 1.8 V versus RHE (2nd scan) visualizes more positive onset potential and increased activity at higher overpotentials of SnO_2 -supported IrO_2 catalysts; mass-based activity after the 2nd and the 20th cycles is additionally shown for the overpotentials of e) 300 mV and of f) 500 mV.

In an in-situ study, Lebedev et al. described the coordination environment and oxidation state changes under OER conditions of atomically dispersed iridium on indium tin oxide. Changes in the oxidation state of the iridium species were observed and high-resolution electron

4.2. Results and Discussion

microscopy studies indicated aggregation of iridium single sites to small clusters under OER conditions. However, the mechanism of this agglomeration process and the impact on the catalyst activity remain unclear to date.^[57]

Here, TEM data of our catalyst after prolonged electrochemical characterization (conditions see below) show retained rod-like elongation of the IrO₂ nanocrystals and epitaxially oriented, layered IrO₂ along the c-axis and indicate a high mechanical stability of this phase under electrochemical conditions (see Figure S4-11, Supporting Information).

In addition to the structure, differences in electrical conductivity, electrochemical activity and stability of catalysts on the different MO substrates have also been observed. The electrical conductivity has a crucial impact on the efficiency and voltage losses in industrial electrolyzers operating at high current densities.^[14, 26, 58] Uncoated powders of the support materials are practically insulating after oxidative treatment in NaNO₃ (1.2 10^{-6} S cm⁻¹ and 4.2 10^{-6} S cm⁻¹ for the SnO₂ and TiO₂ powders, respectively) (Figure 4-4a). As expected, the conductivity of the powders increases after coating with the conductive IrO_x layer, but to a different extent depending on the substrate material. In contrast to IrO_x@TiO₂, the conductivity of IrO₂@SnO₂ catalysts is generally higher. At nominal loading of 7 at% Ir, conductivity of around 44 mS cm⁻¹ was obtained for SnO₂-supported and of 1.4 mS cm⁻¹ for TiO₂-supported catalyst. At 14 at% Ir loading, a conductivity of 503 mS cm⁻¹ was obtained for IrO₂@SnO₂, in contrast to a far lower conductivity of 22.3 mS cm⁻¹ measured for IrO₂@TiO₂. These observations are in line with the differences in structure and morphology of the IrO_x@MO catalysts described above. Even though the amorphous IrO_x is fairly continuous on the TiO₂ surface, this phase generally exhibits lower conductivity than the crystalline IrO₂ formed on the surface of SnO₂ particles.^[26, 59]

In addition to the differences in conductivity, IrO_x@MO catalysts show also markedly different electrochemical activity on a rotating disk electrode (RDE) and on the stationary FTO electrode (Figure 4-4b–f). Samples with comparable iridium contents showed no significant differences in their activity and stability with respect to thoroughly washed out sodium nitrate or remaining residues. All investigated IrO_x@TiO₂ catalysts with different Ir loading have a relatively low onset potential of 1.50 V versus RHE (7 at% Ir) and 1.47 V versus RHE (14 at% Ir) acquired at a defined current density of 1 mA cm⁻² of OER (Figure S4-12, Supporting Information). This can be attributed to the presence of partially hydrated amorphous IrO_x, which is one of the most electrocatalytically active compounds.^[26] However, this phase is known to degrade

rapidly upon repeated cycling, which was also observed in our measurements as a significant drop in mass-specific activity after only 20 cycles (Figure 4-4e) with a concomitant sharp increase in electrode polarization (Figure 4-4c). The unusual behavior of IrO₂@TiO₂_7 at% observable in Figure 4-4b,c is attributed to the randomized growth, which can lead to different crystallinity and crystal orientation, as opposed to epitaxial growth, which allows reproducible crystallization along the substrate surface and is a further indication of the more stable behavior of an epitaxial system. Precautions were taken to avoid the measurement artifacts discussed in El-Sayed et al.^[60] (see Experimental Section for more details).

Compared to IrO_x@TiO₂, the catalysts on the SnO₂ substrate show a later onset of the OER reaction and lower electrochemical activity at low overpotentials such as 300 mV. An overview of the electrocatalytic activity of IrO_x@MO powders, presented as mass-specific activity at an overpotential of 300 mV for the second and twentieth cycles (Figure 4-4e), shows that the catalysts on titania support have a higher initial mass-specific activity than the catalysts on SnO₂ support at lower overpotentials. However, at overpotentials equal or higher than 500 mV, the electrochemical activity of the IrO₂@SnO₂ catalysts is much better than that of the IrO_x@TiO₂ catalysts, with much higher initial mass-specific currents and a significantly better current retention after 20 cycles (Figure 4-4f). Although the performance at such an overpotential does not depend only on the pure electrocatalytic activity of the active phase, but also includes contributions from other processes (such as mass transfer or the ohmic resistance of the electrocatalytic layer), the improved performance at high potentials is of great technological importance, as it would allow for an increase in the pressure of the generated gases.

The SnO₂-supported catalysts exhibit little loss of mass-specific activity from the second to twentieth cycle in cyclic voltammetry (CVA) measurements, regardless of overpotential, and show a very stable electrode potential during prolonged cycling on RDE and on stationary FTO electrodes (Figure 4-4c,e,f).

In order to evaluate and validate the applicability of the SnO₂ supported IrO_x catalyst for PEM water electrolysis at the industrially relevant MEA level, single-cell MEA measurements with an active area of 5 cm² were conducted at a temperature of 80 °C and ambient pressure. Since the possibility to operate at high current densities of more than 2 A cm⁻² is one advantage of PEM water electrolyzers in comparison to other electrolysis technologies.^[61] Figure 4-5a,b shows the first and the last of five consecutive polarization curves with current densities

4.2. Results and Discussion

of up to 4 A cm^{-2} for the $\text{IrO}_x@\text{SnO}_2$ catalyst with 14 at% iridium, together with the respective high frequency resistances (HFRs). A low iridium loading of $0.3 \text{ mg}_{\text{Ir}} \text{ cm}^{-2}$ was employed together with Nafion 212 serving as proton exchange membrane. Using a titanium powder-sintered porous transport layer with protective platinum coating in the anodic cell compartment, an average cell voltage of 1.78 V (corresponding to a cell voltage efficiency of 70.4% based on the lower heating value of hydrogen) is obtained at a current density of 4 A cm^{-2} in the first polarization curve. Constant HFR-values of $\approx 50 \text{ m}\Omega \text{ cm}^2$ at all applied current densities without significant changes at increasing number of polarization cycles indicate no significant loss of the electrical conductivity within the anode electrode assembly. The iridium-based OER mass activity at an *iR*-corrected cell voltage of 1.43 V decreases from $65 \pm 4 \text{ A g}_{\text{Ir}}^{-1}$ in the first polarization curve to $34 \pm 4 \text{ A g}_{\text{Ir}}^{-1}$ (min./max. errors of two measured cells) in the fifth polarization curve. In a previous study with a similar single-cell setup and the same measurement conditions, a considerably lower MEA mass activity of $12 \text{ A g}_{\text{Ir}}^{-1}$ was obtained at an *iR*-corrected potential of 1.43 V for a crystalline IrO_2 catalyst supported on TiO_2 (75 wt% Ir, anode Ir-loading of $\approx 2.33 \text{ mg}_{\text{Ir}} \text{ cm}^{-2}$). In comparison, $440 \text{ A g}_{\text{Ir}}^{-1}$ were measured for an amorphous $\text{IrO}(\text{OH})_x@\text{TiO}_2$ catalyst (45 wt% Ir, anode Ir-loading of $\approx 0.27 \text{ mg}_{\text{Ir}} \text{ cm}^{-2}$).^[26] It has to be noted that direct comparisons of mass activities in units of $\text{A g}_{\text{Ir}}^{-1}$ with literature data have to be conducted carefully, since the obtained values do not only depend on the potential that is used for evaluation and the operation conditions like temperature or pressure, but also on the catalyst system, the OER active species, and the mass specific catalyst utilization. Although the iridium-based OER mass activity of the $\text{IrO}_x@\text{SnO}_2$ catalyst with 14 at% iridium in this work decreases in the course of the measurement, the cell performance at high current densities remains promising after five polarization cycles. While a detailed analysis and comparison of single-cell measurements for the different $\text{IrO}_x@\text{MO}$ catalysts exceeds the scope of this work, a profound investigation of the activity and long-term stability at the MEA level will be required in the future since a direct comparison of electrochemical tests in liquid cell configurations (e.g., with a rotating disc electrode) with measurements in an MEA setup yields discrepancies in obtained catalyst stabilities.^[8, 62] Importantly, the herein presented performance assessment at the MEA level indicates that a controlled oriented epitaxial growth of IrO_2 nanocrystals on appropriate substrate materials can open a promising pathway for future catalyst design and optimization at very low noble metal contents.

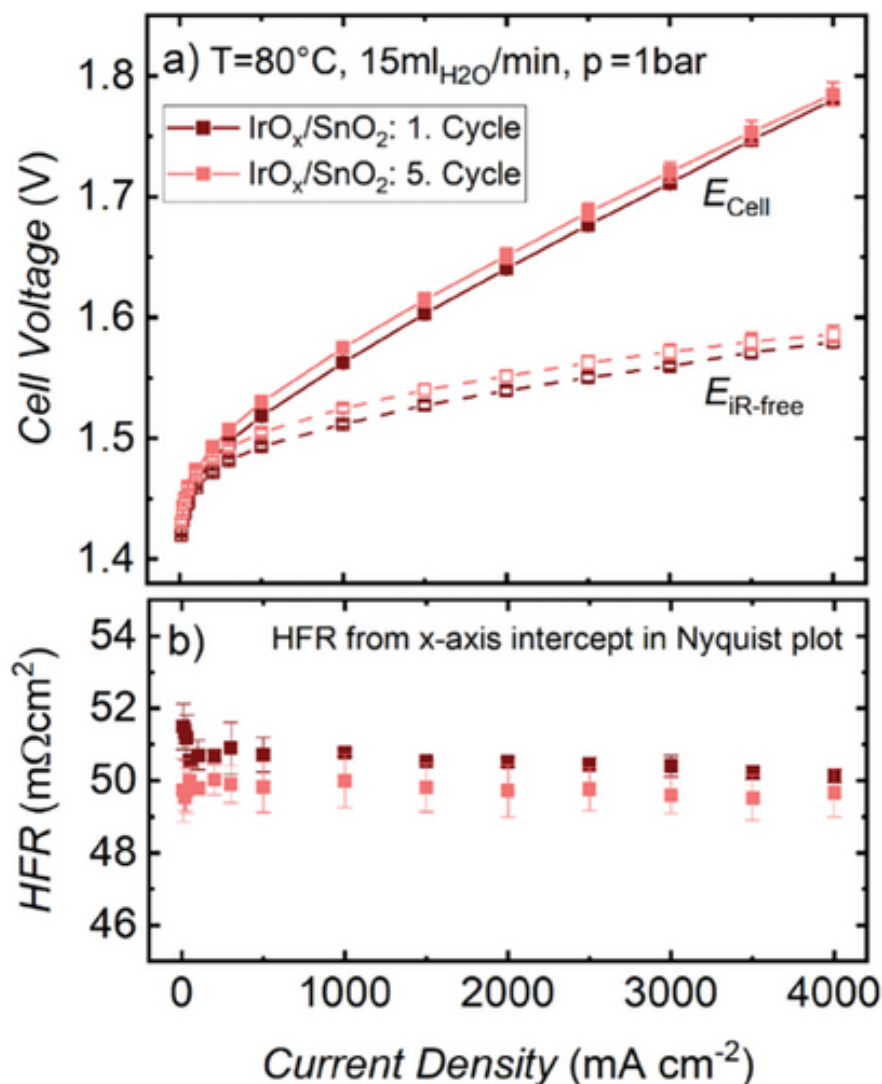


Figure 4-5: Single-cell PEM water electrolysis performance of MEAs with 5 cm^2 active area utilizing the $\text{IrO}_x/\text{SnO}_2$ catalyst with 14 at% iridium as catalyst material and a platinized Ti-PTL on the anode side: a) First and last cycle out of five ambient pressure polarization curves showing the cell potential (full symbols, solid lines) together with the iR -corrected cell voltage (open symbols, dashed lines) at current densities of up to 4 A cm^{-2} . b) High frequency resistance (HFR) values determined from electrochemical impedance spectroscopy measurements at each investigated current density. Data show average potentials and HFRs with min./max. errors from two repeated measurements. Anode and cathode catalyst loadings were $0.28/0.29\text{ mgIr cm}^{-2}$ and $0.37/0.39\text{ mgPt cm}^{-2}$ and a Nafion 212 membrane was used.

4.3. Conclusion

4.3. Conclusion

In this work, the influence of the substrate material on crystallinity, conductivity, OER activity and stability of supported IrO_x catalysts is demonstrated. The specific choice of the SnO_2 support and the active IrO_2 component in terms of their crystal structure with similar lattice parameters enables a decisive lowering of the nucleation energy barrier and allows for a controlled epitaxial growth of interconnected nanocrystals of IrO_2 on SnO_2 . The firmly anchored crystalline IrO_2 phase enables excellent electronic conductivity and remarkable stability at larger overpotentials and current densities, at a very low Ir content of only 14 at%.

The low-temperature synthesis presented here provides a promising basis for the epitaxial growth of a catalytically active phase on the isostructural support material. In contrast to physical deposition methods, which are mostly applied to single-crystalline substrates, this could provide a high degree of control over the epitaxial system through a scalable chemical pathway for a nanocrystalline substrate.^[63] With the appropriate choice of substrate and temperature treatment, it may be possible to further optimize performance by tuning the coverage, thickness, and dominant facets of the catalyst. We envision that the chemical epitaxy described here can be extended to other epitaxial material systems, thereby adding a promising new strategy for the design of high-performance catalyst materials and beyond.

4.4. Experimental Part

IrO(OH)_x@TiO₂ and IrO(OH)_x@SnO₂ Precursor Phases

Commercially available TiO₂ and SnO₂ were obtained from Sigma Aldrich. For iridium coating of these supports, a wet chemical synthesis described elsewhere in detail (EP3764443B1; EP4019666A1) was adapted to prepare the amorphous IrO(OH)_x@SnO₂/TiO₂ catalyst precursor phases with nominal contents of 7 and 14 at% Ir for TiO₂ and SnO₂ supported IrO(OH)_x, respectively. For this purpose, the nominal amount of IrCl₃ · xH₂O was dissolved in bi-distilled H₂O at 50 °C yielding a brown-yellow transparent solution. After the dissolution of the iridium precursor, the respective amounts of TiO₂ or SnO₂ support were added to this solution and stirred for 1 h. In a typical reaction for 14 at% Ir loading on SnO₂, 202 mg IrCl₃ · xH₂O (43 wt% Ir according to ICP-OES) was dissolved in 50 ml deionized H₂O and 1 g SnO₂ was added. After the dispersion of the supports, the pH of the compound solution was adjusted to 9.7 with 1 M NaOH and the solution subsequently heated to 75 °C for 2 h. After heating, the pH was then readjusted to a pH between 11 and 11.5. This mixture was then left stirring for 2 d at 75 °C and the pH was kept between 11 and 11.5 while the color changed to dark blue. Eventually, the product was washed four times with deionized H₂O followed by centrifugation at 25 k rcf for 20 min, respectively.

Oxidation of IrO(OH)_x@SnO₂/TiO₂ to IrO_x@TiO₂ and IrO₂@SnO₂

In 1923, Adams and Shriner introduced the well-known molten salt oxidation in NaNO₃, Adams fusion, for the preparation of platinum oxide nanoparticles.^[46] On this basis, Oakton et al. further described the preparation of a TiO₂/IrO₂ OER catalyst from a mixture of molecular precursors.^[64] This process was adapted for the transformation of the previously mentioned thin IrO(OH)_x layer on the SnO₂/TiO₂ nanoparticles to IrO_x nanoparticles.

For instance, per 1 g of IrO(OH)_x@MO powder, 1 g NaNO₃ (VWR, ≥ 99.9%) was added and mixed with 40 ml deionized H₂O. The precursors were intermixed and the dispersion was homogenized by treatment in an ULTRA-TURRAX for 30 min at a speed of 24k rpm. Subsequently, the reaction mixture was dried in ceramic calcination trays on a hot plate by evaporation at 120 °C. After drying, the trays were transferred to a laboratory oven (NABERTHERM, model N15/65SHA). All mixtures were first heated to 150 °C for 1 h (6

4.4. Experimental Part

°C min⁻¹ heating ramp) in air to remove residual water. The targeted crystallinity of IrO_x adopted by Böhm et al. was achieved by further heating to a temperature of 375 °C and a holding time of 1 h (3 °C min⁻¹ heating ramp) in air.^[14] After cooling down, the resulting IrO_x@MO was encapsulated in the NaNO₃ melt, which was removed by three consecutive washing steps with bidistilled H₂O followed by centrifugation. Finally, the product was dried in a laboratory oven (NABERTHERM, model N15/65SHA) at 85 °C overnight to obtain a powder product.

Two-Point Conductivity Measurements

Conductivity measurements of IrO₂@SnO₂ and IrO_x@TiO₂ were performed on an in-house constructed dc-conductivity measurement cell with an estimated pressure of 1 MPa by recording *I*–*V* curves between –1 to +1 V with an AUTOLAB 302N potentiostat/galvanostat (METROHM AUTOLAB B.V.).

It should be mentioned that the conductivity measurements were performed on loosely pressed powders, which do not give the highest absolute values (note, e.g., the much higher conductivities reported by Bernt and Gasteiger,^[65] which were measured at 1040 MPa), but the measurement conditions allow for a comparison of the relative sample conductivities.

X-Ray Photoelectron Spectroscopy

The XPS measurements were carried out by using a VSW TA10 X-ray source providing nonmonochromatized Mg K α radiation ($h\nu = 1253.6$ eV) set at 15 mA and 12 kV and a VSW HA100 hemispherical analyzer. The spectra were recorded with a pass energy of 22 eV and a dwell time of 0.1 s per measurement point. The samples were prepared by drop-casting a dispersion of the respective sample in a (1:1 v/v) water to isopropanol ratio on ITO glass. After drying, the samples were transferred to the UHV chamber.

Powder X-Ray Diffraction (PXRD)

For most PXRD experiments, a Ge (111)–monochromated (Cu K α_1) STOE Stadi P diffractometer in transmission geometry with the solid state strip detector Dectris Mythen 1k was used. Powder XRD patterns of the samples were collected with an omega- 2θ scan in the

4. Chemical Epitaxy of Iridium Oxide on Tin Oxide Enhances Stability of Supported OER Catalyst

2θ range from 20° to 80° with a step size of 1° and fixed integration time of 60 s per step and a resolution of 0.05° . For PDF analysis, a Ge (111)–monochromated (Ag $K\alpha_1$) STOE Stadi P diffractometer in Debye-Scherrer geometry and a Dectris Mythen 1k solid state strip detector was used up to a limit of $q = 14.9 \text{ \AA}^{-1}$. For the latter, a scaled PXRD pattern of pure TiO_2 support was subtracted from a pattern of TiO_2 loaded with 14 at% Ir, whereby both patterns were recorded with the same parameters. The PDF was calculated with the software package GSAS II.^[66] Rietveld refinements were also performed using GSAS II. Results and parameters of Rietveld refinements are presented in Table S4-1 (Supporting Information) (TiO_2 loaded with 14 at% Ir) and Table S4-2 (Supporting Information) (SnO_2 loaded with 14 at% Ir). For the former, the contribution of IrO_x was treated as background.

High-Resolution Transmission Electron Microscopy (HRTEM), High-Angle Annular Dark-Field Scanning Transmission Electron Microscopy (HAADF-STEM) and Electron Diffraction (ED)

All experiments were performed at 300 kV with an FEI Titan Themis 60-300 transmission electron microscope with aberration correction of the probe-forming lens, further equipped with a SuperX windowless, four quadrant silicon drift detector with a solid angle of 0.7 sr for EDX. TEM specimens were prepared by dispersing powders on a thin carbon-film or a double-layer graphene coated copper grid.

Evaluation Procedure of Electron Diffraction Patterns for the Calculation of Pair Distribution Functions (PDFs)

Electron diffraction patterns were recorded at close to parallel beam conditions with a small selected area diffraction aperture (diameter $\approx 150 \text{ nm}$). Before azimuthal intensity integration, reflections from nearby crystalline material and beam stopper contrast were masked. Typically, the resulting 1 D intensity profiles were fit up to $q \approx 14 \text{ \AA}^{-1}$. For Fourier sine transformation resulting in the PDF, the software eRDF Analyser was used with standard settings.^[67]

Scanning Electron Microscopy (SEM)

Scanning electron microscopy (SEM) images were recorded with an FEI Helios Nanolab G3 UC scanning electron microscope equipped with a field emission gun operated at 2–5 kV.

4.4. Experimental Part

Specimens were prepared from powders deposited on carbon-based Leit tabs adhered onto a stainless-steel sample holder. EDX measurements were recorded at an operating voltage of 20 kV with an X-Max^N Silicon Drift Detector with an 80 mm² detector area (OXFORD INSTRUMENTS) and AZTec acquisition software (OXFORD INSTRUMENTS). For quantification of the iridium content by EDX in the SEM, the iridium content of four measurements of areas with sizes between 40 and 100 μm² was averaged. By thoroughly cleaning the sample after the oxidation step, sodium could be removed, which can potentially serve as a dopant. However, electrochemical measurements of samples with residual sodium did not reveal any advantage of these samples (see Figure S4-6 for sample spectrum in Supporting Information).

Electrochemical Characterization

Electrochemical characterization was performed in a three-electrode setup in a quartz cell at room temperature. The cell was filled with 20 ml 0.5 M H₂SO₄ (SIGMA-ALDRICH, Titripur volumetric standard) electrolyte. A PGSTAT302N potentiostat/galvanostat (METROHM AUTOLAB B.V.) equipped with an FRA32 M impedance analyzer was connected to a Hydroflex reversible hydrogen electrode (GASKATEL Gesellschaft für Gassysteme durch Katalyse und Elektrochemie mbH) or Hg/HgSO₄/K₂SO₄(sat.) (REF601, RADIOMETER ANALYTICAL-HACH COMPANY) reference electrode for cyclic voltammetry and galvanostatic (chronopotentiometry) measurements, respectively.

To avoid artifacts related to the formation of trapped oxygen bubbles in porous electrode layers described in the work of El-Sayed et al.,^[60] cyclic voltammetry (CVA) measurements were used as the main method to determine the electrochemical activity of catalysts, which allows to reduce oxygen bubbles during each cathodic scan.

To prepare the catalyst layers on fluorine-doped tin oxide (FTO) substrates, the volume of a dispersion of catalyst powders with different Ir loadings was calculated to deposit 10 μg_{Ir} on a masked area of 0.196 cm⁻² on each electrode. The iridium content measured with EDX was used to calculate the nominal loading values of Ir in the electrode layers. The CVA measurements were performed with *iR*-correction (95%) in a potential window of 1.0–1.8 V versus RHE with a scan rate of 20 mV s⁻¹ in 20 scans. Before each CVA measurement, impedance spectroscopy was performed at 0.5 V versus RHE to determine the corresponding electrolyte resistance from the high-frequency region (*R_s*).

4. Chemical Epitaxy of Iridium Oxide on Tin Oxide Enhances Stability of Supported OER Catalyst

Rotating disc electrode (RDE) measurements were performed using a MSR Electrode rotator with mirror-polished 5 mm diameter glassy carbon disc insets (PINE RESEARCH INSTRUMENTATION) connected to an Autolab PGSTAT302N potentiostat/galvanostat equipped with a FRA32 M impedance analyzer (METROHM AUTOLAB B.V.) and a double-walled glass cell with Luggin-capillary for the reference electrode. The temperature of the electrolyte at 60.0 ± 0.5 °C was regulated by a KISS 104A circulation thermostat (PETER HUBER KÄLTEMASCHINENBAU AG) and monitored with an immersed K-element temperature sensor. The Nernst potential for water oxidation was kept constant by continuous O₂ (AIR LIQUIDE, AlphaGaz 2 N5 purity) purging of the electrolyte (0.5 M H₂SO₄, SIGMA-ALDRICH, Titripur volumetric standard). The respective catalysts were dispersed in a solution of Nafion perfluorinated resin (SIGMA-ALDRICH, 5 wt% in lower aliphatic alcohols and water (15-20% water)) in an H₂O/*i*PrOH mixture (1:1 v/v) at a dilution ratio of 1:100. The concentration of the catalyst dispersion was adjusted so that 10 µg of iridium was contained in 10 µl of dispersion. Subsequently, 10 µl of the dispersion was drop-cast onto a glassy carbon disk with a diameter of 5 mm and immediately dried at 60 °C. The rotation rate was 1600 rpm. The electrolyte resistance was determined before and after each RDE measurement in the high-frequency region of recorded impedance spectra at 0.5 V versus RHE. The applied measurement protocol consisted of 50 CVA cycles starting from 1.0 V versus Hydroflex RHE (GASKATEL Gesellschaft für Gassysteme durch Katalyse und Elektrochemie mbH). The upper vertex potential was defined to be at a current density of $j = 1 \text{ mA cm}^{-2}$ ($i_{\text{abs}} = 0.2 \text{ mA}$, $A = 0.196 \text{ cm}^2$). The reported current densities were determined from the *iR*-corrected anodic scan for a given overpotential η_{OER} of the respective scan cycle.

To identify redox features and to compare the electrocatalytically active surface area of catalyst samples, additional CVA measurements over the potential range of 0.05–1.52 V versus RHE were performed during the RDE measurements. Three cycles were therefore recorded before each RDE measurement (as described above) and after 50 RDE CVA cycles.

Membrane Electrode Assembly (MEA) Preparation, Single-Cell Assembly and Electrochemical Testing

To fabricate membrane electrode assemblies (MEAs), the decal transfer method was used. First, catalyst ink was prepared by mixing catalyst material (IrO_x) supported on SnO₂ (at 14 at% Ir, as synthesized, for anode electrodes) or platinum supported on Vulcan XC72 carbon

4.4. Experimental Part

(45.8 wt% Pt/C, TEC10V50E from Tanaka Japan, for cathode electrodes)) with 1-propanol ($\geq 99.9\%$ purity, from Sigma Aldrich, Germany, for anode ink) or 2-propanol ($\geq 99.9\%$ purity, from Sigma Aldrich, Germany, for cathode ink) and ionomer solution (D2021 Nafion solution, 20 wt% ionomer, from IonPower, USA). An ionomer content of 11 wt% was set for the anodes while an ionomer to carbon ratio of $I/C = 0.6/1$ g/g_C was chosen for the cathodes. ZrO₂ beads with a diameter of 5 mm were added and the ink was mixed on a roller mixer (from Ratek, Australia) at 180 rpm for approximately 18 hours. Subsequently, the ink was coated onto a PTFE decal foil (50 μm nominal thickness, from Angst+Pfister, Germany) with a Mayer rod and an automatic coater (from Erichsen GmbH & Co. KG, Germany). The wet coating thickness of the Mayer rod was chosen according to the targeted loadings of $0.30 \pm 0.03 \text{ mg}_{\text{Ir}} \text{ cm}^{-2}$ and $0.35 \pm 0.05 \text{ mg}_{\text{Pt}} \text{ cm}^{-2}$ for anodes and cathodes, respectively. After drying at room temperature, electrodes with an area of 5 cm^2 were punched out of the coating. To fabricate MEAs, a Nafion 212 membrane (51 μm nominal thickness, from IonPower, USA) as well as the anode and cathode electrodes were dried for approximately 20 min at a temperature of 80°C to minimize residual moisture and then hot-pressed together for 3 min at a temperature of 155°C and a pressure of 2.5 MPa. After removal of the decals, the respective electrode loadings could be determined from the known ink compositions and the weighed electrode and decal masses before and after the decal transfer.

Cell measurements were carried out in a single-cell hardware. The design has already been reported in detail elsewhere.^[68] On the anode side, titanium powder-sintered sheets ($\approx 40\%$ porosity, from Mott Corporation, USA) with a protective platinum coating ($0.5 \pm 0.1 \mu\text{m}$ coating thickness, platinized by Umicore Galvanotechnik, Germany) and a thickness of 265–270 μm were used as porous transport layers. Prior to cell assembly, PTLs were cleaned by sonification in ultrapure water ($18 \text{ M}\Omega \text{ cm}$) and subsequent immersion in $0.1 \text{ M H}_2\text{SO}_4$ at 80°C for one hour. For the cathodic gas diffusion layer (GDL), carbon fiber paper (TGP-H-120, no MPL, 5 wt% PTFE, from Toray, Japan) with a thickness of 370–375 μm was used. One PTFE subgasket (10 μm nominal thickness, from Goodfellow, UK) was applied on each side of the MEA. The thickness of the gaskets (virgin PTFE, from Angst+Pfister, Germany) was chosen so that a GDL compression of $\approx 20\text{--}22\%$ was obtained.

Single-cell testing at ambient pressure with 5 cm^2 active area was performed with an in-house built test station. Electrochemical measurements were conducted with a VSP-300 potentiostat (from BioLogic, France) equipped with two 10 A booster boards. The measurement protocol consisted of a warm-up step to a temperature of 80°C for cell hardware and feed water, cell

conditioning and electrochemical characterization. The anode compartment was flushed with deionized water at a flow rate of $15 \text{ ml H}_2\text{O min}^{-1}$, which was kept constant throughout the whole experiment. After reaching a stable temperature, a cyclic voltammetry (CV) measurement was conducted consisting of 3 potential cycles between 1.3 V and 0.05 V at a scan rate of 50 mV s^{-1} , while dry H_2 was flushed through the cathode compartment at a flow rate of $50 \text{ ml H}_2 \text{ min}^{-1}$ to ensure a stable potential comparable to a reversible hydrogen electrode (RHE). Subsequently, the current was ramped to 1 A cm^{-2} and held constant for 30 minutes to condition the cell. In the following, five consecutive polarization curves were measured, consisting of a potentiostatic step in blocking conditions at a cell potential of 1.3 V, including a potentiostatic impedance measurement with a perturbation voltage of $\pm 10 \text{ mV}$, and current density steps from 0.01 to 4 A cm^{-2} . Each current was held for 5 minutes followed by a galvanostatic impedance measurement (perturbation currents between $\pm 20 \text{ mA}$ and $\pm 500 \text{ mA}$) to determine the high frequency resistances (HFRs) from the x-axis intercept in the obtained Nyquist plots. To perform an iR -correction of the measured cell potentials, the product of the HFR and the respective current density was subtracted from the measured cell voltages.

4.5. References

4.5. References

1. Wang, T.; Cao, X.; Jiao, L., PEM water electrolysis for hydrogen production: fundamentals, advances, and prospects. *Carbon Neutrality* 2022, 1 (1).
2. Chatenet, M.; Pollet, B. G.; Dekel, D. R.; Dionigi, F.; Deseure, J.; Millet, P.; Braatz, R. D.; Bazant, M. Z.; Eikerling, M.; Staffell, I.; Balcombe, P.; Shao-Horn, Y.; Schäfer, H., Water electrolysis: from textbook knowledge to the latest scientific strategies and industrial developments. *Chemical Society Reviews* 2022, 51 (11), 4583-4762.
3. Carmo, M.; Fritz, D.; Mergel, J.; Stolten, D., A comprehensive review on PEM electrolysis. *International Journal of Hydrogen Energy* 2013, 38, 4901-4934.
4. Vazhayil, A.; Vazhayal, L.; Thomas, J.; Ashok C, S.; Thomas, N., A comprehensive review on the recent developments in transition metal-based electrocatalysts for oxygen evolution reaction. *Applied Surface Science Advances* 2021, 6, 100184.
5. González-Huerta, R. G.; Ramos-Sanchez, G.; Balbuena, P., Oxygen evolution in Co-doped RuO₂ and IrO₂: Experimental and theoretical insights to diminish electrolysis overpotential. *Journal of Power Sources* 2014, 268, 69–76.
6. Brooks, D., Will there be enough iridium to meet demand from the hydrogen economy. *Precious Metals* 2022, 43, 93.
7. Bernt, M.; Siebel, A.; Gasteiger, H. A., Analysis of Voltage Losses in PEM Water Electrolyzers with Low Platinum Group Metal Loadings. *Journal of The Electrochemical Society* 2018, 165 (5), F305-F314.
8. Bernt, M.; Hartig-Weiß, A.; Tovini, M. F.; El-Sayed, H. A.; Schramm, C.; Schröter, J.; Gebauer, C.; Gasteiger, H. A., Current Challenges in Catalyst Development for PEM Water Electrolyzers. *Chemie Ingenieur Technik* 2020, 92 (1-2), 31-39.
9. Böhm, D.; Beetz, M.; Schuster, M.; Peters, K.; Hufnagel, A. G.; Döblinger, M.; Böller, B.; Bein, T.; Fattakhova-Rohlfing, D., Efficient OER Catalyst with Low Ir Volume Density Obtained by Homogeneous Deposition of Iridium Oxide Nanoparticles on Macroporous Antimony-Doped Tin Oxide Support. *Advanced Functional Materials* 2020, 30 (1), 1906670.
10. Cherevko, S.; Geiger, S.; Kasian, O.; Kulyk, N.; Grote, J.-P.; Savan, A.; Shrestha, B. R.; Merzlikin, S.; Breitbach, B.; Ludwig, A., Oxygen and hydrogen evolution reactions on Ru,

RuO₂, Ir, and IrO₂ thin film electrodes in acidic and alkaline electrolytes: A comparative study on activity and stability. *Catalysis Today* 2016, 262, 170-180.

11. Jürgensen, L.; Frank, M.; Pyeon, M.; Czympiel, L.; Mathur, S., Subvalent Iridium Precursors for Atom-Efficient Chemical Vapor Deposition of Ir and IrO₂ Thin Films. *Organometallics* 2017, 36 (12), 2331-2337.

12. Kristóf, J.; Szilágyi, T.; Horváth, E.; De Battisti, A.; Frost, R. L.; Rédey, Á., Investigation of IrO₂/Ta₂O₅ thin film evolution. *Thermochimica acta* 2004, 413 (1-2), 93-99.

13. Ledendecker, M.; Geiger, S.; Hengge, K.; Lim, J.; Cherevko, S.; Mingers, A. M.; Göhl, D.; Fortunato, G. V.; Jalalpoor, D.; Schüth, F., Towards maximized utilization of iridium for the acidic oxygen evolution reaction. *Nano research* 2019, 12, 2275-2280.

14. Böhm, D.; Beetz, M.; Gebauer, C.; Bernt, M.; Schröter, J.; Kornherr, M.; Zoller, F.; Bein, T.; Fattakhova-Rohlfing, D., Highly conductive titania supported iridium oxide nanoparticles with low overall iridium density as OER catalyst for large-scale PEM electrolysis. *Applied Materials Today* 2021, 24, 101134.

15. Böhm, D.; Beetz, M.; Schuster, M.; Peters, K.; Hufnagel, A. G.; Döblinger, M.; Böller, B.; Bein, T.; Fattakhova-Rohlfing, D., Efficient OER Catalyst with Low Ir Volume Density Obtained by Homogeneous Deposition of Iridium Oxide Nanoparticles on Macroporous Antimony-Doped Tin Oxide Support. *Advanced Functional Materials* 2019, 30 (1).

16. Moriau, L.; Bele, M.; Marinko, Z. i.; Ruiz-Zepeda, F.; Koderman Podboršek, G.; Šala, M.; Šurca, A. K.; Kovač, J.; Arčon, I.; Jovanovič, P., Effect of the morphology of the high-surface-area support on the performance of the oxygen-evolution reaction for iridium nanoparticles. *ACS catalysis* 2020, 11 (2), 670-681.

17. Wu, X.; Feng, B.; Li, W.; Niu, Y.; Yu, Y.; Lu, S.; Zhong, C.; Liu, P.; Tian, Z.; Chen, L., Metal-support interaction boosted electrocatalysis of ultrasmall iridium nanoparticles supported on nitrogen doped graphene for highly efficient water electrolysis in acidic and alkaline media. *Nano Energy* 2019, 62, 117-126.

18. Lee, K.; Flores, R. A.; Liu, Y.; Wang, B. Y.; Hikita, Y.; Sinclair, R.; Bajdich, M.; Hwang, H. Y., Epitaxial Stabilization and Oxygen Evolution Reaction Activity of Metastable Columbite Iridium Oxide. *ACS Applied Energy Materials* 2021, 4 (4), 3074-3082.

4.5. References

19. Matienzo, D. D.; Settipani, D.; Instuli, E.; Kallio, T., Active IrO₂ and NiO Thin Films Prepared by Atomic Layer Deposition for Oxygen Evolution Reaction. *Catalysts* 2020, 10 (1), 92.
20. Ogawa, S.; Hara, M.; Suzuki, S.; Joshi, P.; Yoshimura, M., Controlled Deposition of Iridium Oxide Nanoparticles on Graphene. *Electrochemistry* 2020, 88.
21. Malinovic, M.; Paciok, P.; Koh, E. S.; Geuß, M.; Choi, J.; Pfeifer, P.; Hofmann, J. P.; Göhl, D.; Heggen, M.; Cherevko, S.; Ledendecker, M., Size-Controlled Synthesis of IrO₂ Nanoparticles at High Temperatures for the Oxygen Evolution Reaction. *Advanced Energy Materials* n/a (n/a), 2301450.
22. Badam, R.; Hara, M.; Huang, H.-H.; Yoshimura, M., Synthesis and electrochemical analysis of novel IrO₂ nanoparticle catalysts supported on carbon nanotube for oxygen evolution reaction. *International Journal of Hydrogen Energy* 2018, 43 (39), 18095-18104.
23. Karade, S. S.; Sharma, R.; Gyergyek, S.; Morgen, P.; Andersen, S. M., IrO₂/Ir Composite Nanoparticles (IrO₂@Ir) Supported on TiN_xO_y Coated TiN: Efficient and Robust Oxygen Evolution Reaction Catalyst for Water Electrolysis. *ChemCatChem* 2023, 15 (4), e202201470.
24. Han, B.; Risch, M.; Belden, S.; Lee, S.; Bayer, D.; Mutoro, E.; Shao-Horn, Y., Screening Oxide Support Materials for OER Catalysts in Acid. *Journal of The Electrochemical Society* 2018, 165, F813-F820.
25. Kale, S. B.; Babar, P. T.; Kim, J.-H.; Lokhande, C. D., Synthesis of one dimensional Cu₂S nanorods using a self-grown sacrificial template for the electrocatalytic oxygen evolution reaction (OER). *New Journal of Chemistry* 2020, 44 (21), 8771-8777.
26. Bernt, M.; Schramm, C.; Schröter, J.; Gebauer, C.; Byrknes, J.; Eickes, C.; Gasteiger, H. A., Effect of the IrO_x Conductivity on the Anode Electrode/Porous Transport Layer Interfacial Resistance in PEM Water Electrolyzers. *Journal of The Electrochemical Society* 2021, 168 (8), 084513.
27. Godínez-Salomón, F.; Albiter, L. A.; Alia, S. M.; Pivovar, B. S.; Camacho-Forero, L. E.; Balbuena, P. B.; Mendoza-Cruz, R.; Arellano-Jimenez, M. J.; Rhodes, C. P., Self-Supported Hydrous Iridium–Nickel Oxide Two-Dimensional Nanoframes for High Activity Oxygen Evolution Electrocatalysts. *ACS Catalysis* 2018.

28. Du, Y.; Wang, W.; Zhao, H.; Liu, Y.; Li, S.; Wang, L., The rational doping of P and W in multi-stage catalysts to trigger Pt-like electrocatalytic performance. *Journal of Materials Chemistry A* 2020, 8 (47), 25165-25172.
29. Solà-Hernández, L.; Claudel, F.; Maillard, F.; Beauger, C., Doped tin oxide aerogels as oxygen evolution reaction catalyst supports. *International Journal of Hydrogen Energy* 2019, 44 (45), 24331-24341.
30. Yoo, H.; Oh, K.; Lee, Y. R.; Row, K. H.; Lee, G.; Choi, J., Simultaneous co-doping of RuO₂ and IrO₂ into anodic TiO₂ nanotubes: A binary catalyst for electrochemical water splitting. 2016, 10 (42), 6657-6664.
31. Daiane Ferreira Da Silva, C.; Claudel, F.; Martin, V.; Chattot, R.; Abbou, S.; Kumar, K.; Jiménez-Morales, I.; Cavaliere, S.; Jones, D.; Rozière, J.; Solà-Hernandez, L.; Beauger, C.; Faustini, M.; Peron, J.; Gilles, B.; Encinas, T.; Piccolo, L.; Barros De Lima, F. H.; Dubau, L.; Maillard, F., Oxygen Evolution Reaction Activity and Stability Benchmarks for Supported and Unsupported IrOx Electrocatalysts. *ACS Catalysis* 2021, 11 (7), 4107-4116.
32. Kasian, O.; Li, T.; Mingers, A. M.; Schweinar, K.; Savan, A.; Ludwig, A.; Mayrhofer, K., Stabilization of an iridium oxygen evolution catalyst by titanium oxides. *Journal of Physics: Energy* 2021, 3 (3), 034006.
33. Pham, C. V.; Bühler, M.; Knöppel, J.; Bierling, M.; Seeberger, D.; Escalera-López, D.; Mayrhofer, K. J. J.; Cherevko, S.; Thiele, S., IrO₂ coated TiO₂ core-shell microparticles advance performance of low loading proton exchange membrane water electrolyzers. *Applied Catalysis B: Environmental* 2020, 269, 118762.
34. Lv, H.; Zhang, G.; Hao, C.; Mi, C.; Zhou, W.; Yang, D.; Li, B.; Zhang, C., Activity of IrO₂ supported on tantalum-doped TiO₂ electrocatalyst for solid polymer electrolyte water electrolyzer. *RSC Advances* 2017, 7 (64), 40427-40436.
35. Mazúr, P.; Polonský, J.; Paidar, M.; Bouzek, K., Non-conductive TiO₂ as the anode catalyst support for PEM water electrolysis. *International Journal of Hydrogen Energy* 2012, 37, 12081–12088.
36. Möckl, M.; Ernst, M. F.; Kornherr, M.; Allebrod, F.; Bernt, M.; Byrknes, J.; Eickes, C.; Gebauer, C.; Moskovtseva, A.; Gasteiger, H. A., Durability Testing of Low-Iridium PEM

4.5. References

Water Electrolysis Membrane Electrode Assemblies. *Journal of The Electrochemical Society* 2022, 169 (6), 064505.

37. da Silva, G. C.; Venturini, S. I.; Zhang, S.; Löffler, M.; Scheu, C.; Mayrhofer, K. J. J.; Ticianelli, E. A.; Cherevko, S., Oxygen Evolution Reaction on Tin Oxides Supported Iridium Catalysts: Do We Need Dopants? *ChemElectroChem* 2020, 7 (10), 2330-2339.

38. Reier, T.; Teschner, D.; Lunkenbein, T.; Bergmann, A.; Selve, S.; Kraehnert, R.; Schlögl, R.; Strasser, P., Electrocatalytic Oxygen Evolution on Iridium Oxide: Uncovering Catalyst-Substrate Interactions and Active Iridium Oxide Species. *Journal of The Electrochemical Society* 2014, 161 (9), F876-F882.

39. Geiger, S.; Kasian, O.; Shrestha, B. R.; Mingers, A. M.; Mayrhofer, K. J. J.; Cherevko, S., Activity and Stability of Electrochemically and Thermally Treated Iridium for the Oxygen Evolution Reaction. *Journal of The Electrochemical Society* 2016, 163 (11), F3132-F3138.

40. Nga Ngo, T. H.; Love, J.; O'Mullane, A. P., Investigating the Influence of Amorphous/Crystalline Interfaces on the Stability of IrO₂ for the Oxygen Evolution Reaction in Acidic Electrolyte. *ChemElectroChem* 2023, 10 (24).

41. Teschner, D.; Farra, R.; Yao, L.; Schlögl, R.; Soerijanto, H.; Schomäcker, R.; Schmidt, T.; Szentmiklósi, L.; Amrute, A.; Mondelli, C.; Pérez-Ramírez, J.; Novell-Leruth, G., An integrated approach to Deacon chemistry on RuO₂-based catalysts. *Journal of Catalysis - J CATAL* 2012, 285.

42. Mondelli, C.; Amrute, A. P.; Krumeich, F.; Schmidt, T.; Pérez-Ramírez, J., Shaped RuO₂/SnO₂-Al₂O₃ Catalyst for Large-Scale Stable Cl₂ Production by HCl Oxidation. *ChemCatChem* 2011, 3.

43. Seki, K., Development of RuO₂/Rutile-TiO₂ Catalyst for Industrial HCl Oxidation Process. *Catalysis Surveys from Asia* 2010, 14 (3), 168-175.

44. Rajan, Z. S. H. S.; Binninger, T.; Kooyman, P. J.; Susac, D.; Mohamed, R., Organometallic chemical deposition of crystalline iridium oxide nanoparticles on antimony-doped tin oxide support with high-performance for the oxygen evolution reaction. *Catalysis Science & Technology* 2020, 10 (12), 3938-3948.

45. Lee, Y.; Scheurer, C.; Reuter, K., Epitaxial Core-Shell Oxide Nanoparticles: First-Principles Evidence for Increased Activity and Stability of Rutile Catalysts for Acidic Oxygen Evolution. *ChemSusChem* 2022, 15 (10).
46. Adams, R.; Shriner, R. L., Platinum Oxide As A Catalyst In The Reduction Of Organic Compounds. Iii. Preparation And Properties Of The Oxide Of Platinum Obtained By The Fusion Of Chloroplatinic Acid With Sodium Nitrate 1. *Journal of the American Chemical Society* 1923, 45 (9), 2171-2179.
47. Kemmer M., Gebauer. C. Catalyst for the Oxygen Evolution Reaction During Water Electrolysis. 2021, <https://worldwide.espacenet.com/patent/search?q=pn%3DPL3764443T3>, last accessed: 03.07.2024
48. Moriau, L.; Smiljanić, M.; Lončar, A.; Hodnik, N., Supported Iridium-based Oxygen Evolution Reaction Electrocatalysts - Recent Developments. *ChemCatChem* 2022, 14 (20).
49. Gimenez, P.; Fereres, S., Effect of Heating Rates and Composition on the Thermal Decomposition of Nitrate Based Molten Salts. 2015; Vol. 69, p 654-662.
50. Hoshino, Y.; Utsunomiya, T.; Abe, O., The thermal decomposition of sodium nitrate and the effects of several oxides on the decomposition. *Bulletin of the Chemical Society of Japan* 1981, 54 (5), 1385-1391.
51. Wu, H.; Wang, Y.; Shi, Z.; Wang, X.; Yang, J.; Xiao, M.; Ge, J.; Xing, W.; Liu, C., Recent developments of iridium-based catalysts for the oxygen evolution reaction in acidic water electrolysis. *Journal of Materials Chemistry A* 2022, 10 (25), 13170-13189.
52. Oakton, E.; Lebedev, D.; Povia, M.; Abbott, D. F.; Fabbri, E.; Fedorov, A.; Nachtegaal, M.; Copéret, C.; Schmidt, T. J., IrO₂-TiO₂: A High-Surface-Area, Active, and Stable Electrocatalyst for the Oxygen Evolution Reaction. *ACS Catalysis* 2017, 7 (4), 2346-2352.
53. Bolzan, A. A.; Fong, C.; Kennedy, B. J.; Howard, C. J., Structural studies of rutile-type metal dioxides. *Acta Crystallographica Section B: Structural Science* 1997, 53 (3), 373-380.
54. Willinger, E.; Massué, C.; Schlögl, R.; Willinger, M. G., Identifying Key Structural Features of IrO_x Water Splitting Catalysts. *Journal of the American Chemical Society* 2017, 139 (34), 12093-12101.
55. Pfeifer, V.; Jones, T. E.; Velasco Vélez, J. J.; Massué, C.; Greiner, M. T.; Arrigo, R.; Teschner, D.; Girgsdies, F.; Scherzer, M.; Allan, J.; Hashagen, M.; Weinberg, G.; Piccinin, S.;

4.5. References

- Hävecker, M.; Knop-Gericke, A.; Schlögl, R., The electronic structure of iridium oxide electrodes active in water splitting. *Physical Chemistry Chemical Physics* 2016, 18 (4), 2292-2296.
56. Freakley, S. J.; Ruiz-Esquius, J.; Morgan, D. J., The X-ray photoelectron spectra of Ir, IrO₂ and IrCl₃ revisited. *Surface and Interface Analysis* 2017, 49 (8), 794-799.
57. Lebedev, D.; Ezhov, R.; Heras-Domingo, J.; Comas-Vives, A.; Kaeffer, N.; Willinger, M.; Solans-Monfort, X.; Huang, X.; Pushkar, Y.; Coperet, C., Atomically Dispersed Iridium on Indium Tin Oxide Efficiently Catalyzes Water Oxidation. *ACS Cent Sci* 2020, 6 (7), 1189-1198.
58. Xu, H.; Yuan, J.; He, G.; Chen, H., Current and future trends for spinel-type electrocatalysts in electrocatalytic oxygen evolution reaction. *Coordination Chemistry Reviews* 2023, 475, 214869.
59. Mahmoud, S.; Al-Shomar, S.; Akl, A., Electrical Characteristics and Nanocrystalline Formation of Sprayed Iridium Oxide Thin Films. *Advances in Condensed Matter Physics* 2010, 2010, 1-6.
60. El-Sayed, H. A.; Weiß, A.; Olbrich, L. F.; Putro, G. P.; Gasteiger, H. A., OER Catalyst Stability Investigation Using RDE Technique: A Stability Measure or an Artifact? *Journal of The Electrochemical Society* 2019, 166 (8), F458-F464.
61. Shiva Kumar, S.; Himabindu, V., Hydrogen production by PEM water electrolysis – A review. *Materials Science for Energy Technologies* 2019, 2 (3), 442-454.
62. Fathi Tovini, M.; Hartig-Weiß, A.; Gasteiger, H. A.; El-Sayed, H. A., The Discrepancy in Oxygen Evolution Reaction Catalyst Lifetime Explained: RDE vs MEA - Dynamicity within the Catalyst Layer Matters. *Journal of The Electrochemical Society* 2021, 168 (1), 014512.
63. Albertin, S.; Merte, L. R.; Lundgren, E.; Martin, R.; Weaver, J. F.; Dippel, A.-C.; Gutowski, O.; Hejral, U., Oxidation and Reduction of Ir(100) Studied by High-Energy Surface X-ray Diffraction. *The Journal of Physical Chemistry C* 2022, 126 (11), 5244-5255.
64. Oakton, E.; Lebedev, D.; Povia, M.; Abbott, D. F.; Fabbri, E.; Fedorov, A.; Nachtegaal, M.; Copéret, C.; Schmidt, T. J., IrO₂-TiO₂: A High-Surface-Area, Active, and Stable Electrocatalyst for the Oxygen Evolution Reaction. *ACS Catalysis* 2017, 7 (4), 2346-2352.

65. Bernt, M.; Gasteiger, H. A., Influence of Ionomer Content in IrO₂/TiO₂ Electrodes on PEM Water Electrolyzer Performance. *Journal of The Electrochemical Society* 2016, 163 (11), F3179-F3189.
66. Toby, B.; Dreele, R., GSAS-II: The Genesis of a Modern Open-Source All-Purpose Crystallography Software Package. *Journal of Applied Crystallography* 2013, 46, 544-549.
67. Shanmugam, J.; Borisenko, K. B.; Chou, Y.-J.; Kirkland, A. I., eRDF Analyser: An interactive GUI for electron reduced density function analysis. *SoftwareX* 2017, 6, 185-192.
68. Bernt, M.; Gasteiger, H., Influence of Ionomer Content in IrO₂/TiO₂ Electrodes on PEM Water Electrolyzer Performance. *Journal of The Electrochemical Society* 2016, 163, F3179-F3189.

4.6. Appendix

4.6. Appendix

Supporting Figures and Tables:

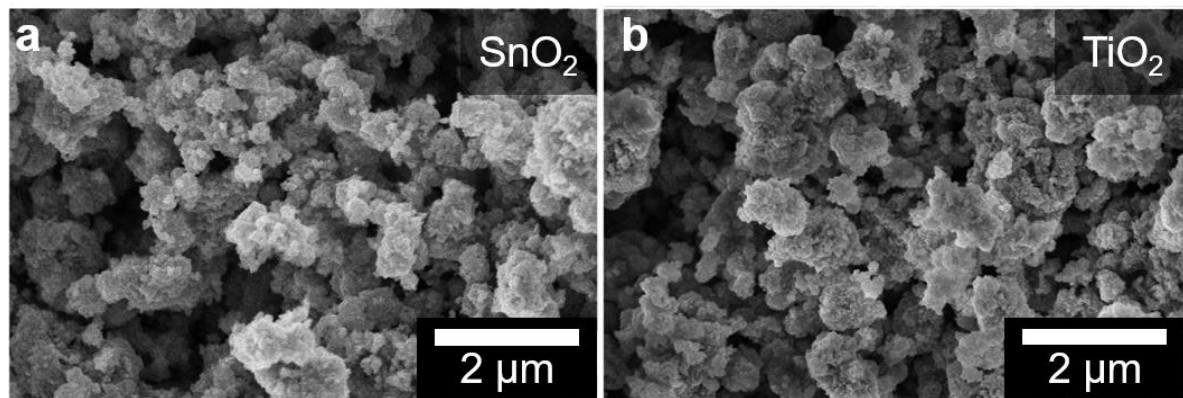


Figure S4-1: Scanning electron microscopy images of crystalline nanoparticles reveal similar structures of (a) SnO₂ nanoparticles and (b) TiO₂ nanoparticles.

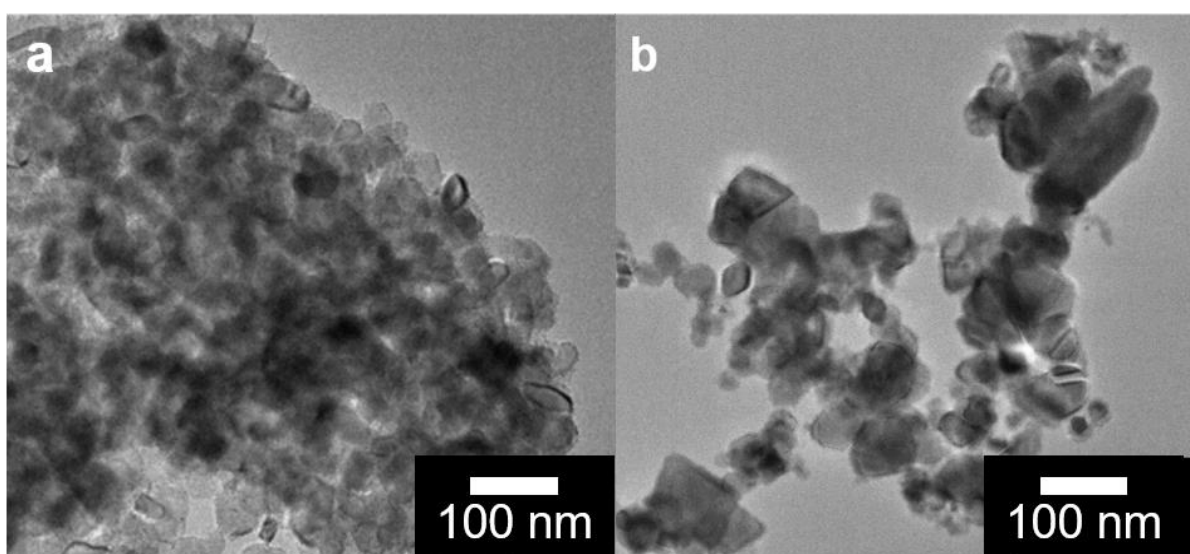


Figure S4-2: Transmission electron microscopy images show particle sizes of roughly 50 nm of support structures for (a) SnO₂ with 21 at% Ir coating and (b) IrO_x@TiO₂_7_at%.

4. Chemical Epitaxy of Iridium Oxide on Tin Oxide Enhances Stability of Supported OER Catalyst

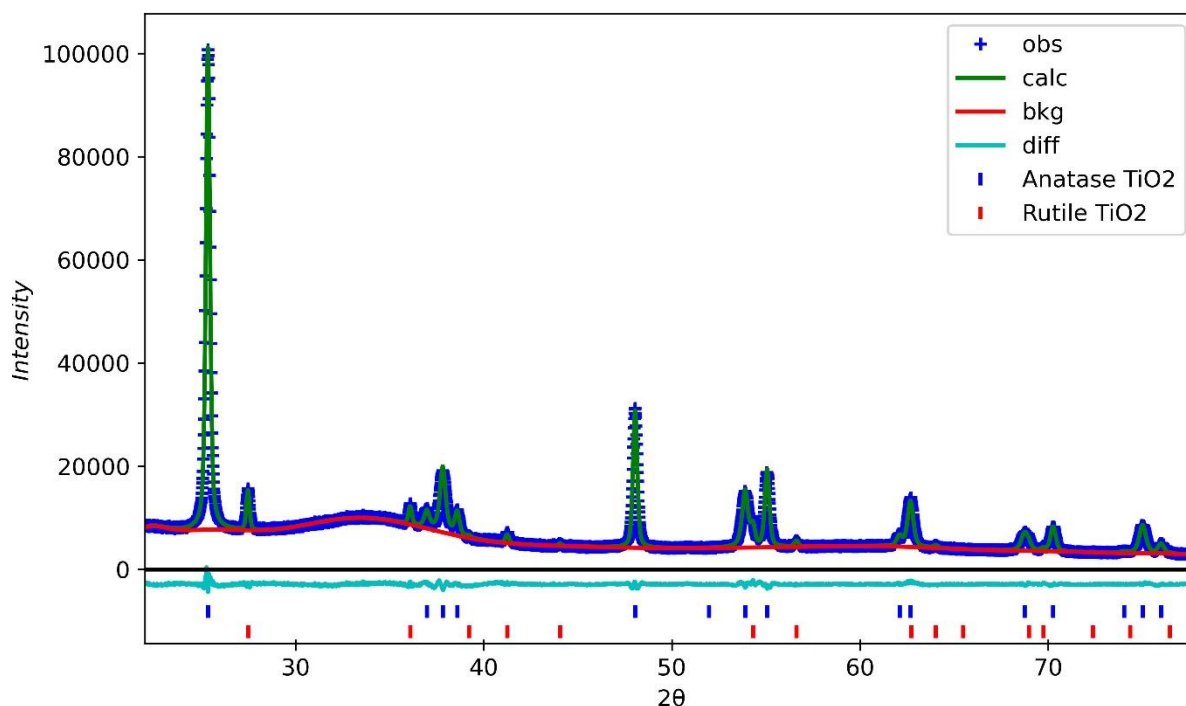


Figure S4-3: PXRD pattern (Cu $K\alpha_1$) of $\text{IrO}_x@\text{TiO}_2$ _14t_%. The pattern is dominated by anatase reflections, see Table S4-1.

Table S4-1: Rietveld refinement of $\text{IrO}_x@\text{TiO}_2$ _14_at% (Figure S4-3). For this characterization of the TiO_2 support, the amount of amorphous IrO_x phase was not refined but included into the preceding background fit. The isotropic temperature factors of Ti and O in the two compounds were constrained to be equal, respectively. The large obtained RF value of 8.3% for rutile is likely related to the large statistical error in intensities, as rutile makes up less than 8 wt% of the crystalline phases.

Temperature / K	293 K
TiO ₂ (Anatase)	
Crystal system, space group	Tetragonal, $I4_1/amd$ (141)
Lattice parameters	$a = 3.78943(2)$, $c = 9.5232(1)$
Crystallite size (equatorial, axial) / nm	84.2(5) , 37.0(2)
Weight fraction	0.9256(8)
No. of reflections, RF / %, RF ² / %	15, 1.66, 3.34
TiO ₂ (Rutile)	
Crystal system	Tetragonal, $P 4_2/mnm$ (136)

4.6. Appendix

Lattice parameters	$a = 4.5996(3)$ $c = 2.9634(2)$
Crystallite size / nm	35(3)
Weight fraction	0.0744(8)
No. of reflections, RF / %, RF ² / %	15, 8.32, 8.12
Diffractometer, Monochromator	STOE Stadip, (111) Ge
X-ray radiation, λ / Å	Cu – K α_1 , 1.540562
Detector range	22°-78°
Background	Chebyshev-1, 19 parameters
No. of observations	3734
No. of parameters	13
wR / %, R / %	2.48, 1.96

Table S4-2: Rietveld refinement of SnO₂ loaded with 14 at% Ir. The XRD pattern used for refinement is shown in Figure 4-2(c). Because of the extremely small crystallite size of IrO₂, its temperature factors were constrained to the values of the respective cation and anion of SnO₂. Atomic positions of IrO₂ were also fixed, instead the values of a reference were adopted.¹

Temperature / K	293
SnO ₂ (rutile structure)	
Crystal system, space group	Tetragonal, P 4 ₂ /mnm (136)
Lattice parameters / Å	$a = 4.74450(7)$, $c = 3.19105(5)$
Crystallite size (equatorial, axial) / nm	45.9(1), 38.5(2)
Weight fraction, phase fraction	0.854(2), 0.897(2)
No. of reflections, RF / %, RF ² / %	17, 1.27, 2.51
IrO ₂ (rutile structure)	
Crystal system	Tetragonal, P 4 ₂ /mnm (136)

4. Chemical Epitaxy of Iridium Oxide on Tin Oxide Enhances Stability of Supported OER Catalyst

Lattice parameters / Å	a = 4.51(2), c = 3.131(5)
Crystallite size (equatorial, axial) / nm	1.6(5), 14(3)
Weight fraction, phase fraction	0.146(2), 0.103 (2)
No. of reflections, RF / %, RF ² / %	16, 1.23, 2.69
Diffractometer, Monochromator	STOE Stadip, (111) Ge
X-ray radiation, λ / Å	Cu – Kα ₁ , 1.540562
Detector range	20.0°- 80.28°
Background	Chebyshev-1, 5 parameters
No. of observations	4020
No. of parameters	22
wR / %, R / %	4.84, 3.65

4.6. Appendix

Electron Diffraction Patterns:

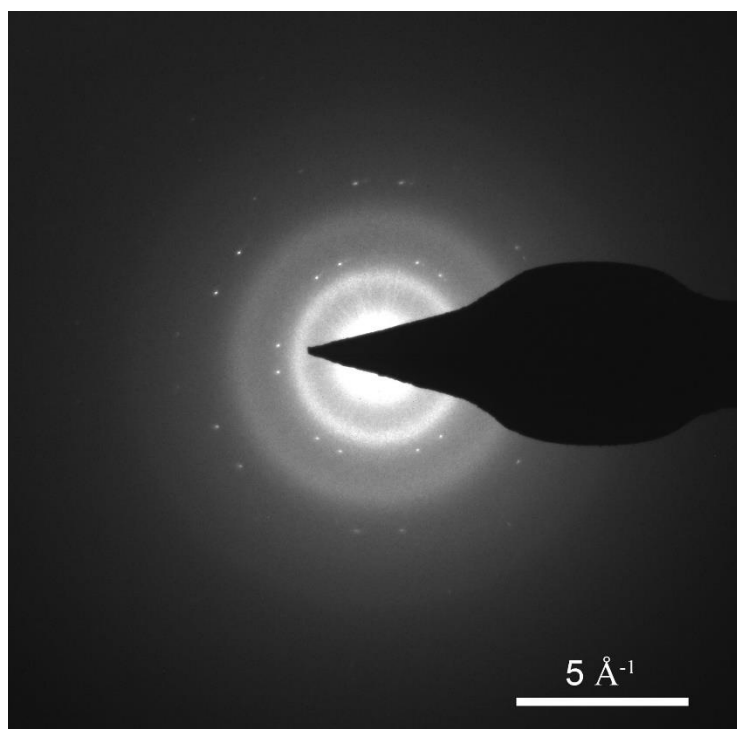


Figure S4-4: Electron diffraction pattern of a larger IrO_x agglomerate ($\approx 80 \text{ nm}$) on the TiO_2 support loaded with 21 at% Ir. The reflections, which were masked for azimuthal intensity integration, stem from a double-layer graphene TEM sample support.

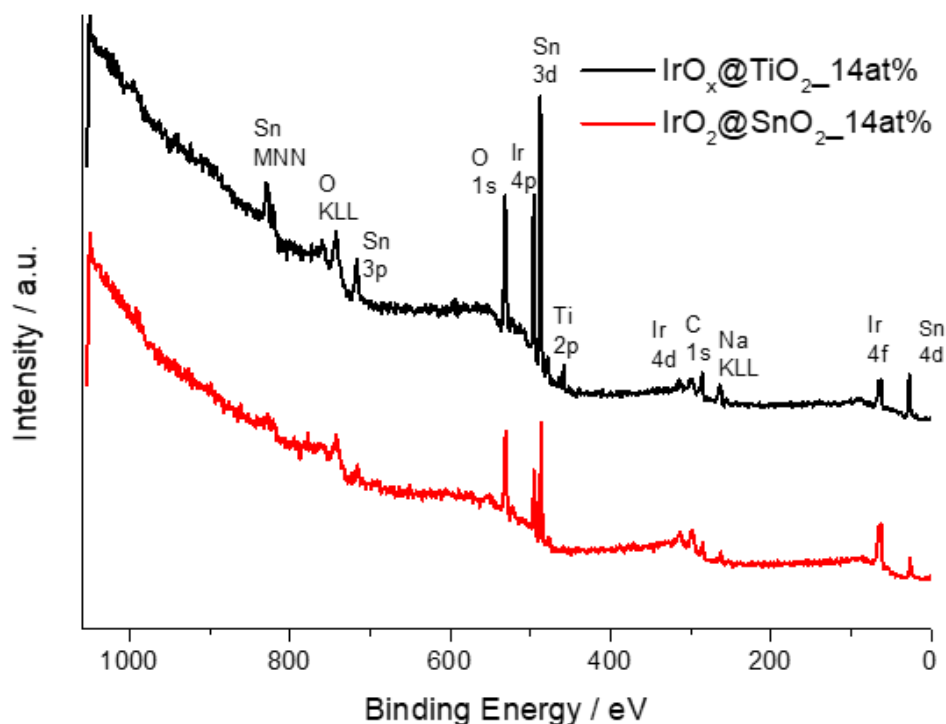


Figure S4-5: XPS survey data of $\text{IrO}_2@\text{SnO}_2_{14\text{at}\%}$ and $\text{IrO}_x@\text{TiO}_2_{14\text{at}\%}$ samples after oxidation over the full measurement range. Residual sodium could be detected in XPS.

The survey spectra of both $\text{IrO}_x@\text{SnO}_2_{14\text{at}\%}$ and $\text{IrO}_x@\text{TiO}_2_{14\text{at}\%}$ show the core level peaks of Ir and O, and Sn or Ti, respectively. A Sn signal can also be seen in the $\text{IrO}_x@\text{TiO}_2_{14\text{at}\%}$ sample, which is due to the sample preparation on FTO glass, as the substrate surface is not uniformly covered with the sample. A quantitative analysis of the elemental composition is therefore not meaningful. The observed carbon peak can be assigned to adventitious carbon species on the surface. A small peak is also visible in both samples, which can be assigned to Na KLL, indicating the presence of residual Na after oxidation in NaNO_3 .

4.6. Appendix

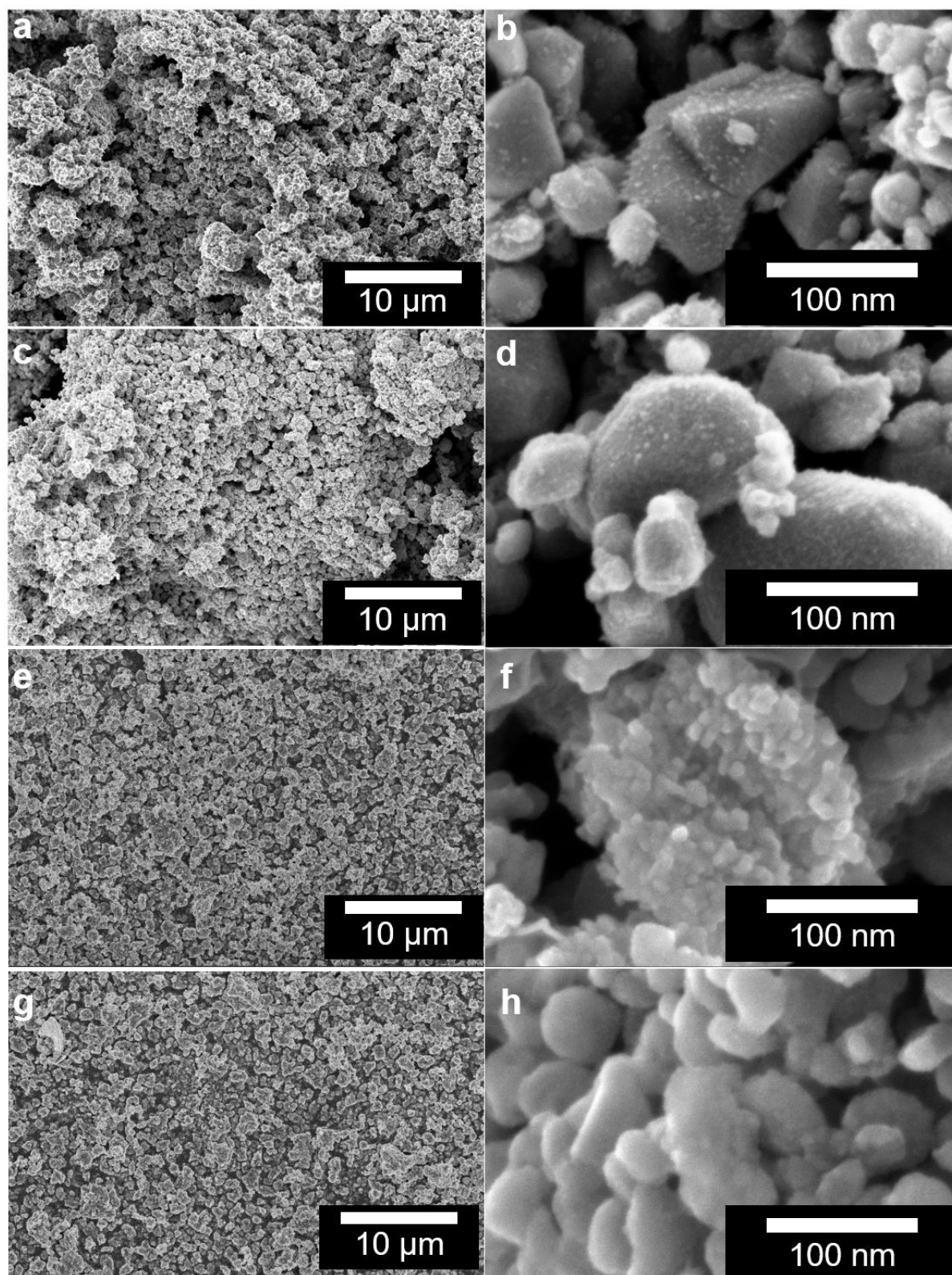


Figure S4-6: SEM images of sample morphologies after the loading and oxidation processes. (a, b) show 7 at% $\text{IrO}_2@\text{SnO}_2$, with anisotropic surface particles revealed in (b). In (c, d) $\text{IrO}_2@\text{SnO}_2_{14_at\%}$ is shown with detectable directional growth in (d). The comparable iridium loadings of $\text{IrO}_x@\text{TiO}_2_{7_at\%}$ (e, f) and $\text{IrO}_x@\text{TiO}_2_{14_at\%}$ (g, h) show no indication of anisotropic surface particles.

4. Chemical Epitaxy of Iridium Oxide on Tin Oxide Enhances Stability of Supported OER Catalyst

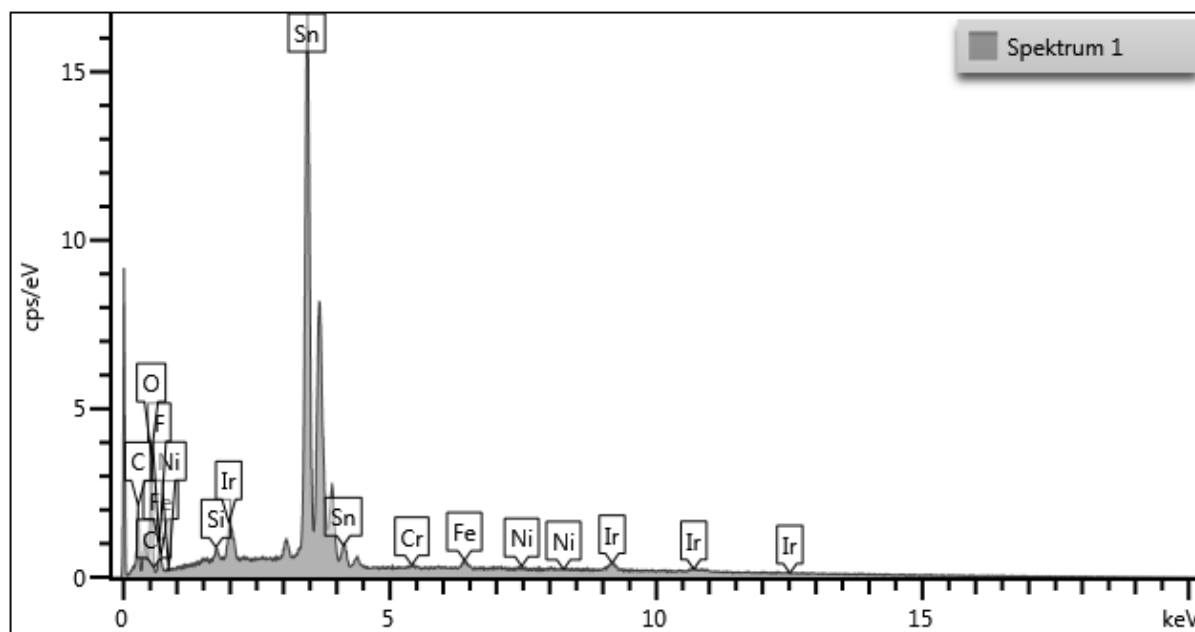


Figure S4-7: EDX sample spectrum of IrO₂@SnO₂_7_at% after oxidation and thoroughly washing. Residual sodium can be fully removed from the sample washing with water.

4.6. Appendix

Additional HAADF-STEM Images and EDX Maps

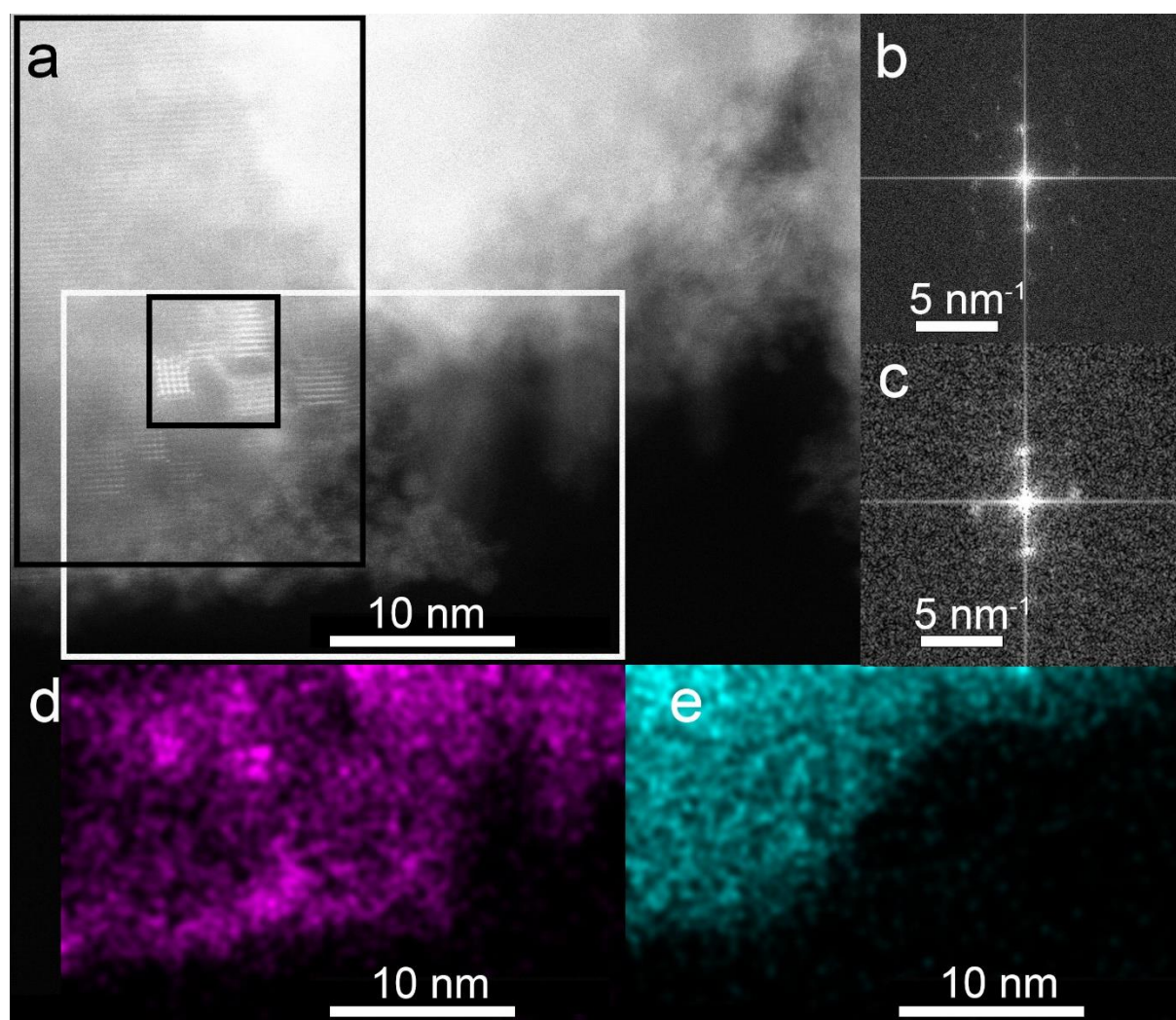


Figure S7-8: (a) STEM-HAADF image of SnO_2 support loaded with 21 at% Ir. The left region shows lattice fringes, all aligned in the same orientation. On the right, the particles on the SnO_2 support appear smaller and mostly non-crystalline. The Fourier Transform (FT) of the large black rectangle is shown in (b), and the FT of the small black rectangle is shown in (c). The white rectangle corresponds to the elemental maps of iridium (purple) and tin (cyan) shown in (d) and (e). The three bright areas in the small black rectangle area are Ir-rich as demonstrated in the corresponding region of the Ir map, indicating the presence of IrO_2 nanocrystals. Both FTs are consistent with IrO_2 or SnO_2 in the tetragonal orientation.

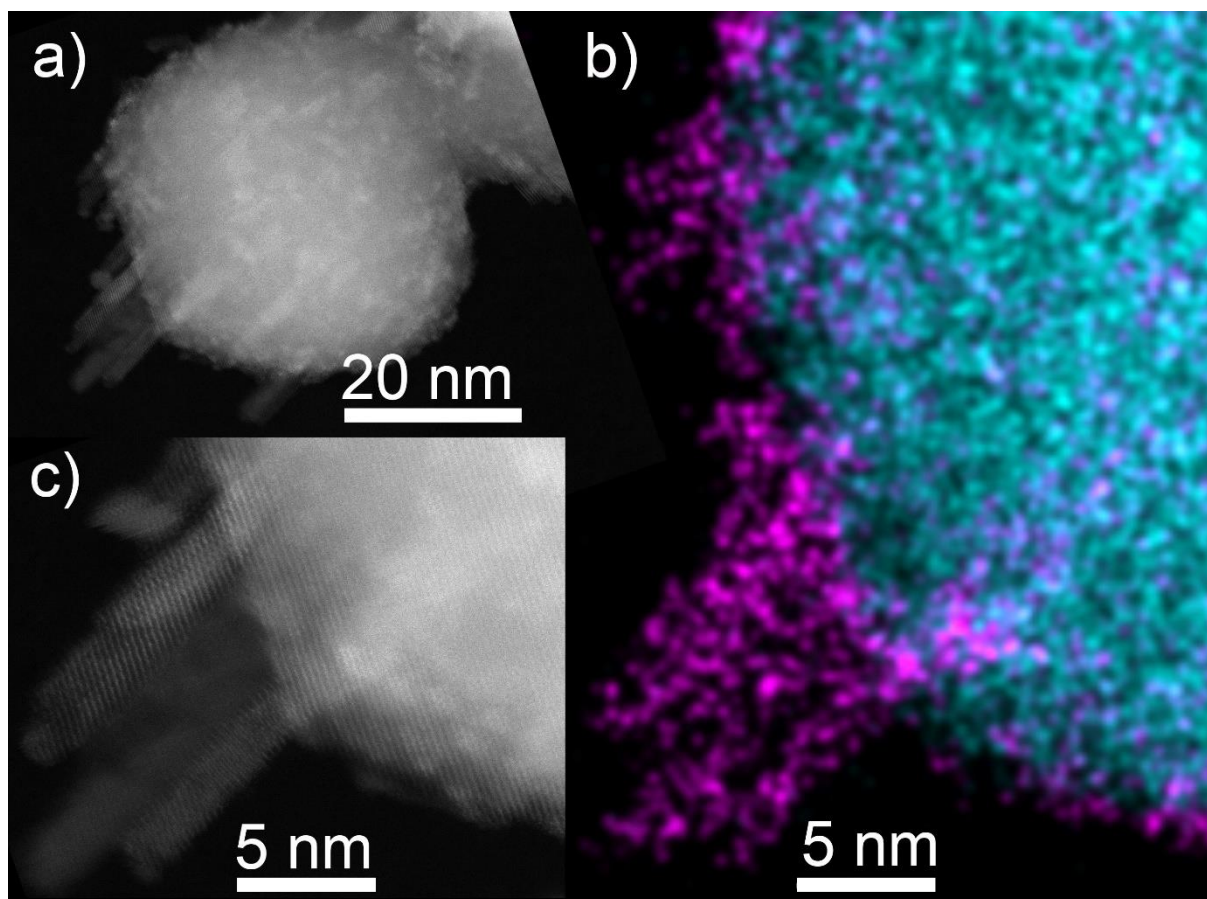


Figure S4-9: (a) HAADF-STEM image of $\text{IrO}_2@\text{SnO}_2_{7\%}$. Most of the supported nanoparticles on the lower left side are crystalline nanorods, oriented in the same direction. (b) EDX map of the lower left side of (a), showing the iridium (purple) and tin (cyan) relative intensities. (c) Magnified detail of the lower left side of (a) showing a very similar periodicity of support and nanorods ($\sim 2.7 \text{ \AA}$), which is close to d_{101} in SnO_2 (2.70 \AA) and IrO_2 (2.58 \AA). The continuation of the periodicity of SnO_2 in IrO_2 indicates an epitaxial relationship between the two phases with rutile structure.

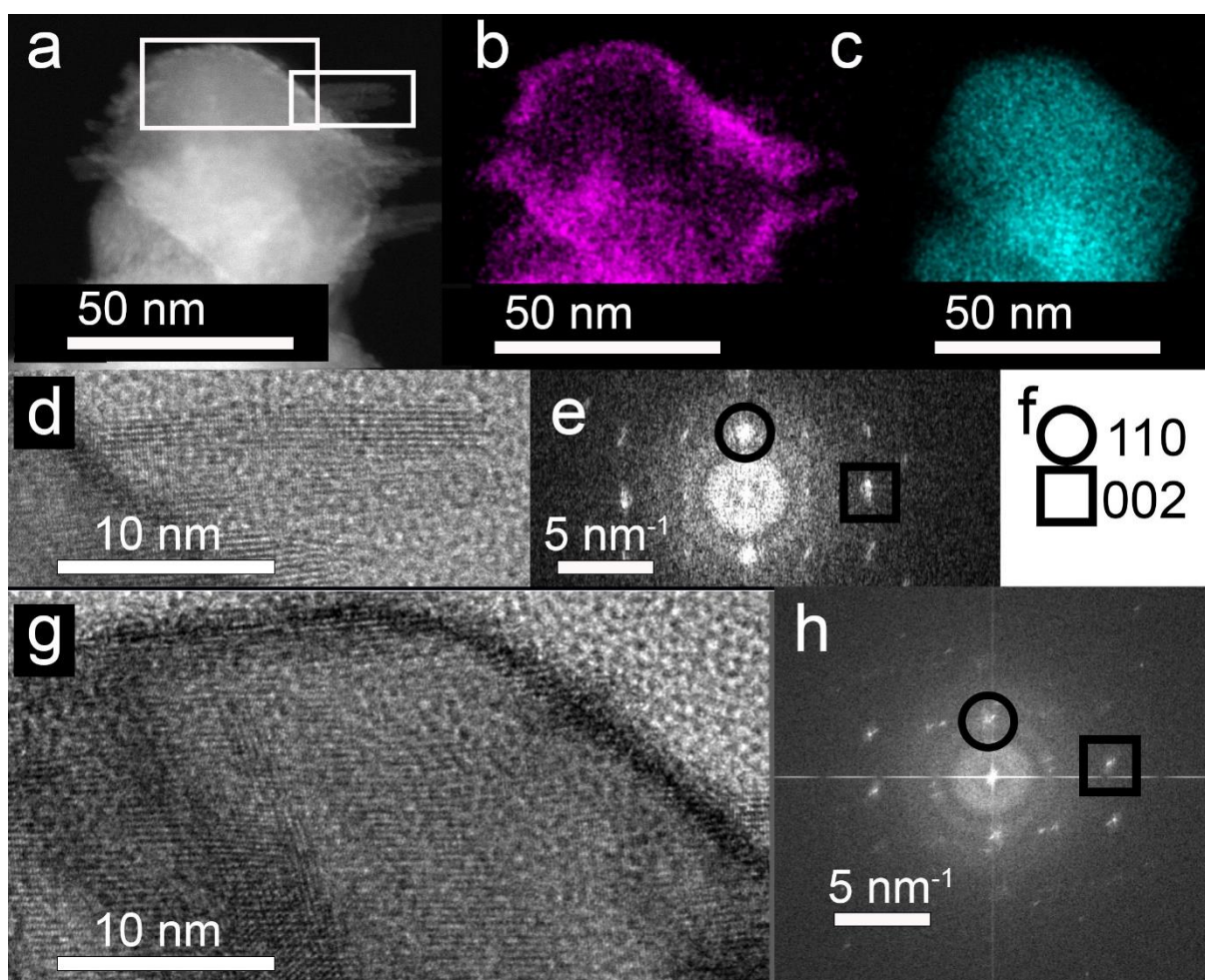


Figure S4-10: (a) STEM-HAADF image of SnO₂ loaded with 21 at% Ir. (b, c) corresponding elemental EDX maps showing the distribution of iridium (purple) and tin (cyan). (d) HRTEM image of the small rectangle in (a) and its corresponding FT (e)). By combining elemental maps (d and e) with the indexing of the Fourier peaks shown in (f), the nanorods can be identified as IrO₂ elongated along [001]. (g) HRTEM image of the large rectangle in (a), showing primarily the same lattice planes as observed in (d), as also confirmed in the corresponding FT shown in (h).

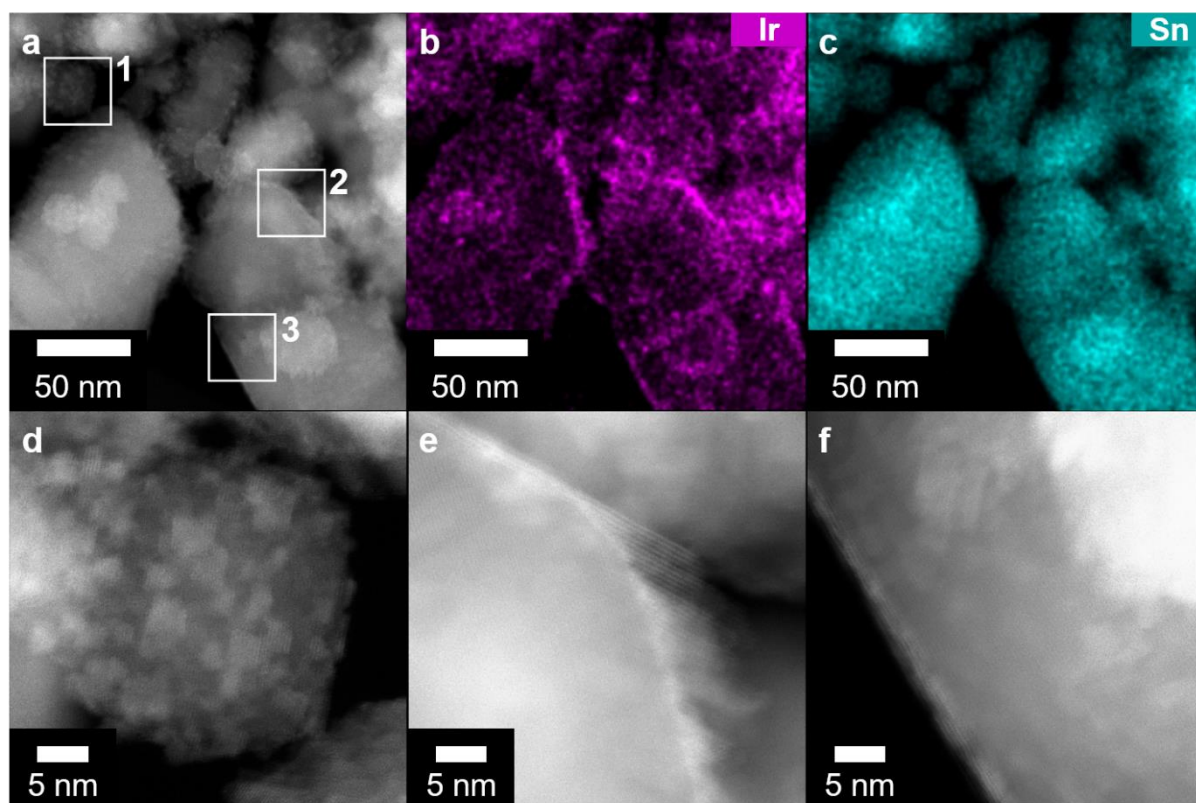


Figure S4-11: (a) STEM-HAADF image of SnO₂ loaded with 7 at% Ir after CVA experiments. (b, c) corresponding elemental EDX maps showing the distribution of iridium (purple) and tin (cyan). (d) STEM-HAADF image of the small rectangle 1 in (a) shows interconnected IrO₂ particle structure. (e) STEM-HAADF image of the small rectangle 2 in (a) shows the elongated IrO₂ rod-like feature and (f) STEM-HAADF image of the small rectangle 3 in a comprising a roughly 1–2 nm thick IrO₂ layer.

EDX Quantitative Measurement of Specimens:

Table S4-3: Composition of nominal IrO₂@SnO₂_7_at%.

Element	Atomic%
Sn	92.4
Ir	7.6
Total	100

4.6. Appendix

Table S4-4: Composition of nominal 14 at% IrO₂@SnO₂_14_at%.

Element	Atomic%
Sn	86.3
Ir	13.7
Total	100

Table S4-5: Composition of nominal 7at% IrO_x@TiO₂_7_at%.

Element	Atomic%
Ti	91.6
Ir	8.4
Total	100

Table S4-6: Composition of nominal 14at% IrO_x@TiO₂_14_at%.

Element	Atomic%
Ti	86.3
Ir	13.7
Total	100

4. Chemical Epitaxy of Iridium Oxide on Tin Oxide Enhances Stability of Supported OER Catalyst

Conductivity Values from DC Cell Measurements:

Table S4-7: Conductivity values in $S\text{ cm}^{-1}$. All conductivities were measured in the ohmic region after oxidation in molten NaNO_3 salt at 375°C for 1h.

Ir at%	Electrical Conductivity in $S\text{ cm}^{-1}$	
	$\text{IrO}_x@\text{SnO}_2$	$\text{IrO}_x@\text{TiO}_2$
0	1.2×10^{-6}	4.2×10^{-5}
7	1.2×10^{-3}	1.1×10^{-3}
14	4.2×10^{-1}	2.0×10^{-2}

4.6. Appendix

Additional static electrode cyclic voltammetry measurements:

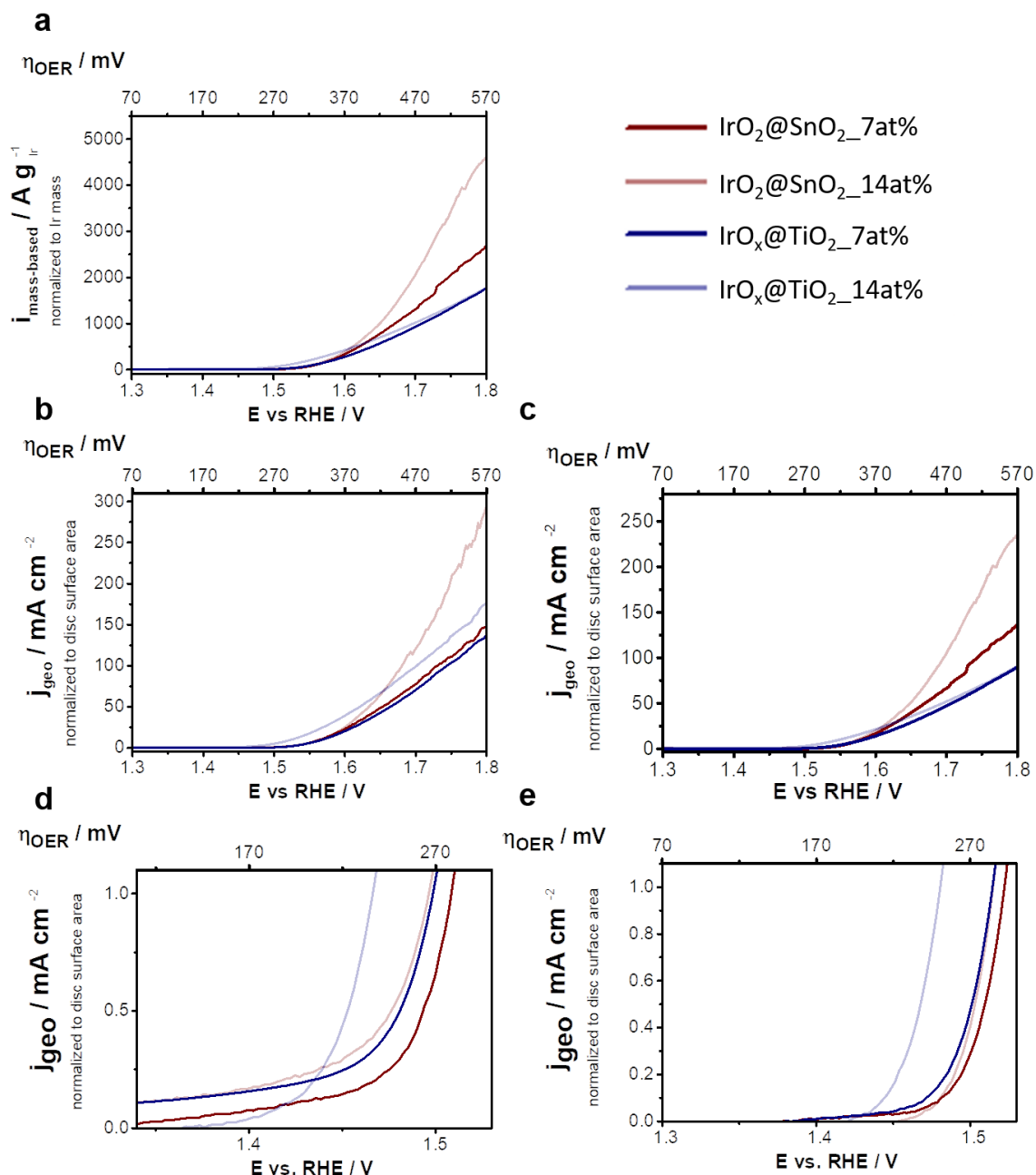


Figure S4-12: Cyclic voltammograms of $\text{IrO}_x @ \text{MO}$ catalysts on stationary FTO electrode (anodic scan only is shown): a) mass-based activity (current normalized to the total mass of Ir in the electrode layer) for the 20th scan; area-based activity (current normalized to the geometric surface area of the electrode) for b) the 2nd scan, with the close-up view in the area of onset potentials in d), and c) the 20th scan, with the close-up view in the area of onset potentials in e).

4. Chemical Epitaxy of Iridium Oxide on Tin Oxide Enhances Stability of Supported OER Catalyst

Table S4-8: Mass-based activity of IrO₂@MO catalysts extracted from CVA measurements. Shown in Fig. 4-4d and Figure S4-5-9.:

Ir at%	CVA cycle	IrO ₂ @SnO ₂		IrO _x @TiO ₂	
		Mass-based current [A gr ⁻¹]			
		@ 300 mV	@ 500 mV	@ 300 mV	@ 500 mV
7	2	77.9	2054.4	185.5	1963.2
	20	46.1	1914.7	58.0	1243.0
14	2	69.7	3536.1	265.8	2475.9
	20	63.8	3145.1	147.4	1283.0

Uncategorized References

1. Bolzan, A. A.; Fong, C.; Kennedy, B. J.; Howard, C. J., Structural studies of rutile-type metal dioxides. *Acta Crystallographica Section B: Structural Science* **1997**, 53 (3), 373-380.

CHAPTER 5

Fabrication of Functional 3D Nanoarchitectures Using Atomic Layer Deposition on DNA Origami Crystals

5. Fabrication of Functional 3D Nanoarchitectures Using Atomic Layer Deposition on DNA Origami Crystals

This chapter is based on the following publication:

Arthur Ermatov^{1,†}, Melisande Kost^{2,†}, Xin Yin¹, Paul Butler^{3,4}, Mihir Dass¹, Ian D. Sharp^{3,4}, Tim Liedl¹, Thomas Bein^{2,*}, Gregor Posnjak^{1,*} *J. Am. Chem. Soc.*, 2025.

1 Faculty of Physics and CeNS, Ludwig-Maximilians-Universität München, Germany

2 Department of Chemistry and CeNS, Ludwig-Maximilians-Universität München, Germany

3 Walter Schottky Institute, Technical University of Munich, Germany

4 Physics Department, TUM School of Natural Sciences, Technical University of Munich, Germany

† These authors contributed equally to this project.

<https://doi.org/10.1021/jacs.4c17232>

Following contributions are from the Author M. Kost:

Performed ALD coverage of SiO₂-stabilized samples with IrO₂ and TiO₂ (TTIP process),
Performed FIB lithography and electrocatalysis experiments, SEM and EDX measurements,
designed electrocatalysis experiments, analyzed and interpreted resulting data, conceived and
designed the ALD experiments

* Corresponding authors: Thomas Bein (thomas.bein@cup.lmu.de) and Gregor Posnjak (gregor.posnjak@physik.lmu.de).

Abstract

While DNA origami is a powerful bottom-up fabrication technique, the physical and chemical stability of DNA nanostructures is generally limited to aqueous buffer conditions. Wet chemical silicification can stabilize these structures but does not add further functionality. Here, we demonstrate a versatile three-dimensional (3D) nanofabrication technique to conformally coat micrometer-sized DNA origami crystals with functional metal oxides via atomic layer deposition (ALD). In addition to depositing homogeneous and conformal nanometer-thin ZnO, TiO₂, and IrO₂ (multi)layers inside SiO₂-stabilized crystals, we establish a method to directly coat bare DNA crystals with ALD layers while maintaining the crystal integrity, enabled by critical point drying and low ALD process temperatures. As a proof-of-concept application, we demonstrate electrocatalytic water oxidation using ALD IrO₂-coated DNA origami crystals, resulting in improved performance relative to that of planar films. Overall, our coating strategy establishes a tool set for designing custom-made 3D nanomaterials with precisely defined topologies and material compositions, combining the unique advantages of DNA origami and atomically controlled deposition of functional inorganic materials.

5.1. Introduction

DNA origami¹ is a modular nucleotide-based self-assembly method operating on the molecular level, thereby enabling access to a vast space of advanced nanostructures^{2,3} with diverse capabilities, including single molecule placement,⁴ reactions⁵ and manipulation,⁶ chiral plasmonic nanostructures with tailored⁷ and switchable⁸ optical response, photonic crystals,⁹ super-resolution microscopy,^{10,11} hierarchically¹² and programmable^{13,14} assembled superstructures, drug delivery systems,^{15,16} and nanodevices with medical applications.^{17,18} DNA nanotechnology thus enables the design of material structure and resulting properties on scales from the single nanometer all the way up to multiple micrometers.¹⁴ The programmable binding of DNA sequences provides both the mechanism for the assembly of the DNA itself as well as the possibility of site-specific decoration of the DNA structures with metallic particles,^{7,19} fluorophores,^{10,11} proteins,^{20,21} and more. In the majority of previously demonstrated applications, DNA origami structures have been used in aqueous buffers since the stability of DNA double helices is highly dependent on pH, salt concentrations, and temperature.²² To stabilize DNA origami structures, several approaches have been utilized, including covalent bonding,²³ protein coating,^{24,25} and silicification using sol-gel chemistry.^{26–28} However, the choice of materials that can overgrow DNA by virtue of wet chemistry is limited, and these processes can be difficult to control. Moreover, the materials applied so far have focused on protecting the DNA nanostructure rather than adding further functionality. Coating precisely defined three-dimensional nanostructures with functional materials such as metals,²⁹ metal oxides, or heterojunctions could yield nanostructures that rival or even outperform three-dimensional (3D) lithographic structures and open a path toward rationally designed 3D meta- and nanomaterials. While silicification of DNA structures can greatly enhance their mechanical,²⁸ chemical, and thermal stabilities,^{30,31} this wet chemical process is highly dependent on buffer conditions and is prone to poor reproducibility due to inhomogeneous coverage. Furthermore, significant effort is required to optimize the silica thickness and smoothness for the specific nanostructures to be coated. In addition, this approach introduces spatial design constraints due to the thickness of the silica shell, which cannot be controlled as precisely as with other coating methods such as atomic layer deposition (ALD). For intricate 3D structures with relatively small pores, it would thus be highly beneficial to circumvent the silicification step and grow a broader range of functional materials with precise thickness control directly onto the DNA; however, capillary forces during drying can deform or collapse intricate nanoscale objects. While recent work³² reported freeze-drying

5.1 Introduction

of individual 3D DNA origami structures, this strategy requires uranyl formate incorporation for stability. An alternative drying method that reduces the deleterious effects of surface tension is critical point drying (CPD),³³ where the solvent is replaced with a liquid that can be brought to the supercritical phase and removed without the liquid–gas phase transition. Even though CPD is widely employed for drying of micro- and nanoscale structures^{34,35} and has even been used for extraction of DNA from biological samples,³⁶ it has not been tested for drying of intricate nanoscale structures that can be assembled with DNA nanotechnology.^{37,38} Thus, CPD may offer a route to drying bare DNA origami nanostructures while minimizing structural and morphological deformations. Atomic layer deposition allows the growth of thin, conformal layers of materials such as metal oxides or pure metals. This is achieved by alternate pulsing of precursor gases, which react in a self-limiting fashion with the chemical groups on the surface of the material. Once the chemical groups have reacted with the first precursor, the reaction has saturated, and the chamber is purged with an inert gas before a second precursor is pulsed into the chamber to form the second part of the deposited layer. These steps are repeated in cycles to grow the coating, thereby enabling precise control of the material thickness down to the number of atomic layers.³⁹ Indeed, ALD functionalization of DNA origami structures has been previously shown to be a powerful approach for coating substrate-supported monomeric structures (i.e., flat triangles and triangular prisms) with metal oxides such as aluminum oxide, titanium oxide, and hafnium oxide,⁴⁰ as well as platinum.⁴¹ In addition, vapor-phase chemical processes derived from ALD have been demonstrated to be effective in covering silicified 3D DNA nanostructures with metal oxides.⁴² However, until now, conventional ALD processes have not been demonstrated to fully penetrate complex 3D DNA origami structures, especially in the absence of SiO₂ stabilization layers. In this work, we coat micrometer-sized 3D DNA origami crystals with metal oxides using standard ALD processes, showing conformal coating and excellent penetration through-out crystals in sizes up to 10 μm . Not only do we apply this technique to SiO₂-stabilized crystal structures, but we also use a low-temperature ALD process to coat bare DNA origami crystals prepared via a CPD process, thus demonstrating dry chemical stabilization and functionalization of complex 3D DNA nanostructures while preserving their geometry (Figure 5-1). As a proof-of-concept application of this technique, we demonstrate the functional performance of IrO₂-coated DNA origami crystals deposited on fluorine-doped tin oxide (FTO)/glass supports for the oxygen evolution reaction (OER) via electrocatalytic water oxidation in aqueous environments.

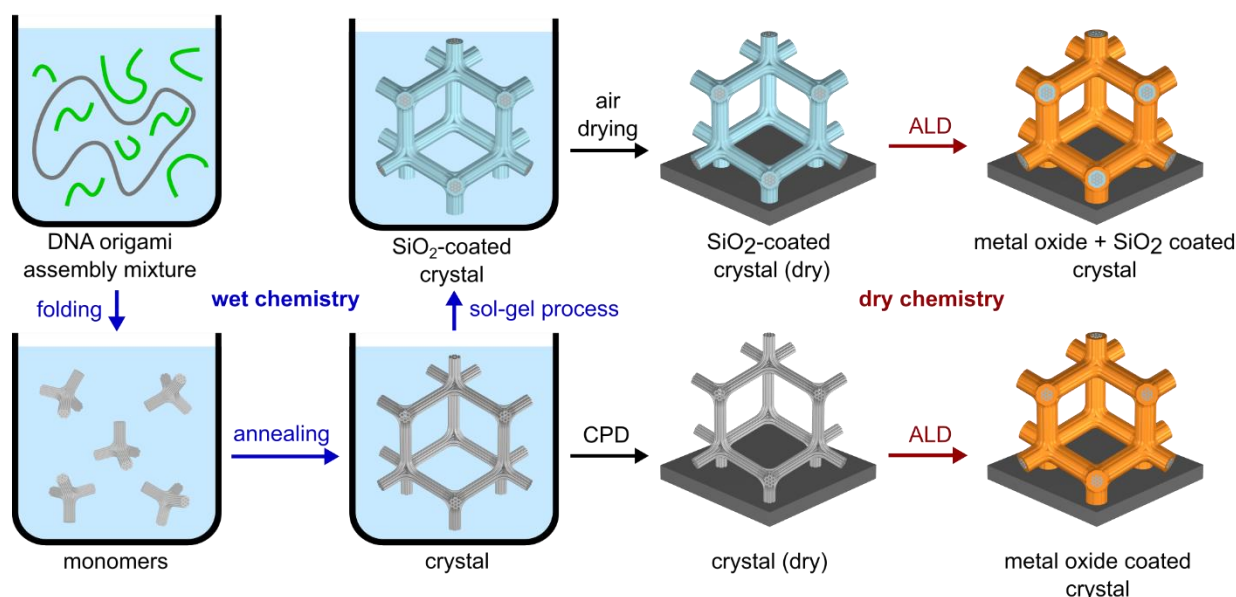


Figure 5-1. Overview of sample preparation. Folding of DNA origami monomers, crystal annealing, and silica growth are performed in an aqueous $1\times$ Tris-EDTA buffer solution comprising a scaffold strand (gray), staple strands (green), and magnesium ions (not shown). The silicified and bare crystals are then transferred to surfaces (glass or silicon) in liquid and dried in air (following silicification) or via CPD (bare structures without silicification). Finally, various functional metal oxide coatings are grown via ALD.

5.2. Results and Discussion

ALD growth on crystals stabilized via sol-gel silicification

As the basis for our functional 3D DNA-based nanomaterials, we used DNA origami tetra pods that are designed to assemble into a rod-connected diamond cubic crystal structure.⁹ The resulting crystals are 5–10 μm in diameter and possess pore sizes of approximately 100 nm. The cross-section of the connecting rods consists of a 24-helix bundle with a diameter of 15 nm. To grow SiO_2 on the DNA origami with a sol–gel process, we first incubated the crystals in an aqueous buffer with N-trimethoxysilyl-propyl-N,N,N-trimethylammonium chloride (TMAPS) before adding tetraethyl orthosilicate (TEOS) and acetic acid^{9,26} (experimental details are provided in the Supporting Information (SI)). The silicification process was halted by washing the crystal with water and isopropanol, resulting in a final 24-helix bundle thickness of around 17 nm (Figures S5-1 and S5-2). It should be noted that SiO_2 does not only form a thin layer on the surface of the DNA but also infiltrates into the cross-section of the DNA origami,⁴³ effectively converting the structure into glass. The silicification mechanically stabilizes the DNA origami crystals, allowing air-drying without deformation of the structures.^{9,30,44} After

5.2 Results and Discussion

the washing steps, the crystals were concentrated and deposited onto silicon or glass surfaces by air-drying a droplet of the liquid containing the washed crystals. Subsequently, metal oxides were grown on the dried crystals using ALD. As a proof-of-concept, we used thermal ALD processes based on metal precursors, including diethylzinc (DEZ), tetrakis(dimethylamino)titanium (TDMAT), titanium tetraisopropoxide (TTIP), and iridium acetylacetonate ($\text{Ir}(\text{acac})_3$) to grow thin layers of ZnO , TiO_2 , and IrO_2 with various thicknesses. Given the thermal stability of SiO_2 -stabilized crystals, standard ALD recipes with reactor temperatures in the range of 175–250 °C were used (see the SI for experimental details). We first analyzed the external surfaces of the ALD-coated crystals with scanning electron microscopy (SEM). In addition, to characterize the interior morphologies of the crystals, we used focused ion beam (FIB) milling to cut open the structures and performed cross-sectional imaging via SEM. The elemental compositions of the inner region of the crystal were subsequently determined by using energy dispersive X-ray spectroscopy (EDX). Figure 5-2a–c shows the monocrystalline morphology of the structures after ALD of TiO_2 . The crystals primarily grew in octahedral shapes (Figure 5-2a), with each of the eight triangular surfaces consisting of $\{111\}$ planes of the diamond cubic lattice and exhibiting a regular hexagonal pattern (Figures 5-2b and S5-3).⁹ Remarkably, the outer surfaces of the crystals feature very few localized defects. Figure 5-2c shows the inner structure of the crystal that was exposed by performing an FIB cut perpendicular to the top crystal surface. The plane of the cut was not aligned with any of the crystal planes, resulting in a moiré pattern of interference fringes, where the periodic variation in thickness (Figures 5-2c and S5-4) originates from different orientations of the cross-section through the local structure of the lattice.

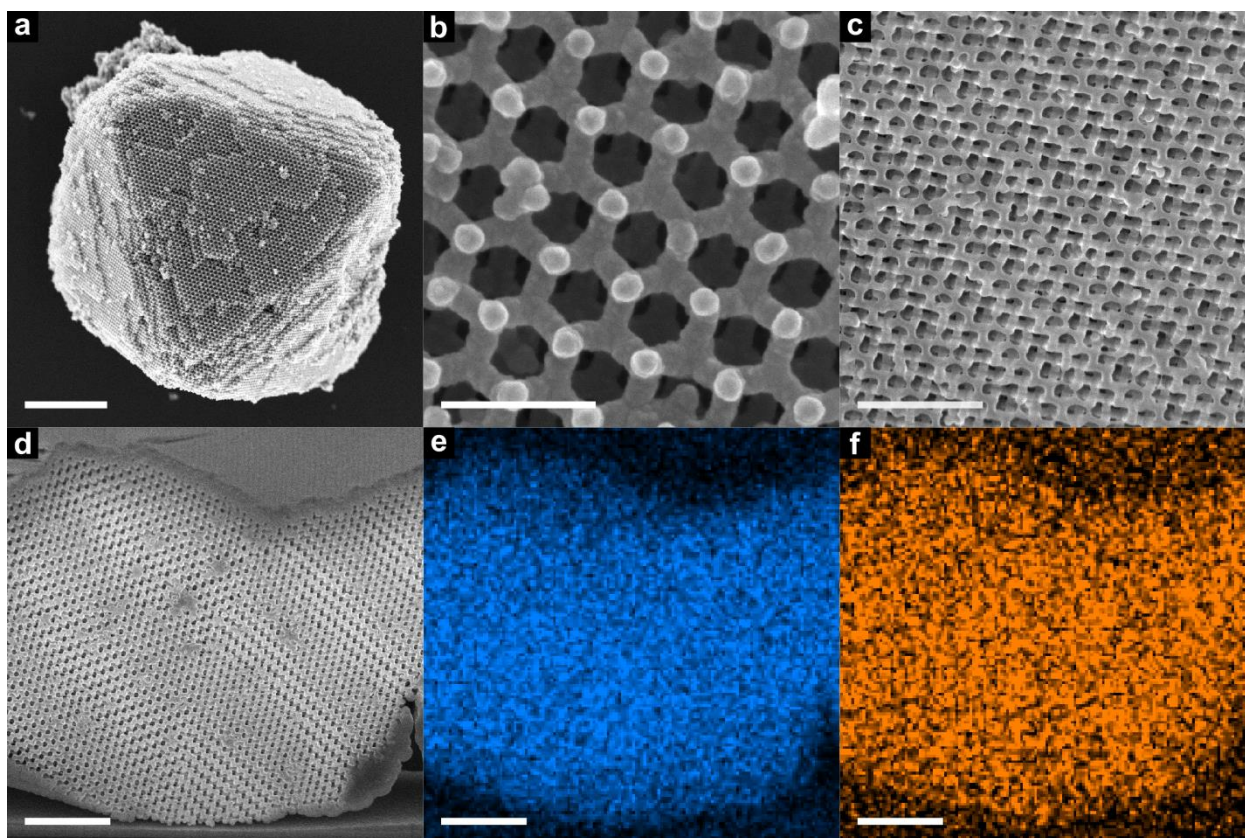


Figure 5-2. SEM images of DNA origami crystals coated with metal oxides. (a) Top view of an air-dried, silicified crystal after conformal coating with 10 nm of TiO_2 using ALD, scale bar 2 μm . (b) Higher magnification image of the surface of the crystal shown in (a), scale bar 200 nm. (c) Image of the inner region of a crystal obtained by FIB milling of the crystal, scale bar 500 nm. (d-f) Image and composition maps obtained following FIB milling of a silicified crystal coated with two consecutive shells of 5 nm TiO_2 (TTIP process) and 5 nm ZnO ; SEM image (d) and corresponding EDX signals for Zn (e) and Ti (f); all scale bars are 1 μm .

Importantly, ALD results in conformal growth of the metal oxide throughout the interior of the crystal, as evidenced by the homogeneous distribution of the deposited material observed by EDX mapping. In particular, there is no discernible gradient in the thickness of the coating from the center toward the outer regions, as would be expected in the case of inhomogeneous infiltration of the ALD precursors. Furthermore, we do not observe selective filling or clogging of the lattice pores near the outer surfaces of the monocrystal. While localized aggregation and uneven thicknesses near the external surfaces of the crystal are observed in Figure 5-2c, their absence in Figure 5-2a indicates that these imperfections are a consequence of the FIB milling process. Moreover, if clogging of the pores would have occurred during ALD, it would have prevented further penetration into the structure, resulting in thinner coatings inside the crystal, which is not observed. Many nanotechnological applications require heterostructures comprising several layers of different materials, each serving different purposes (e.g., passivation, charge separation and transport, photon management, chemical or catalytic function, etc.).^{45,46} To demonstrate the versatility and robustness of our sample preparation

method for the production of mesoscale nanolaminate architectures, we grew heterostructures consisting of two different materials (ZnO and TiO₂, 5 nm thickness each) on top of each other (Figure 5-2d–f). As for the case of a single ALD layer, we observe a homogeneous pore size (Figure 5-2d) and elemental distribution (ZnO in Figure 5-2e and TiO₂ in Figure 5-2f) across the complete cross-section, indicating that the coverage of such heterostructures is comparable to that of a single material (Figure 5-2a–c). Thus, this approach of combining both wet chemical and ALD processes enables the creation of mesostructured nanomaterials with smooth and homogeneous layers, in the present case using three different materials (SiO₂, ZnO, and TiO₂). While this provides a versatile route to a vast range of complex nanomaterials, we now turn to investigating whether the wet chemical silicification step can be eliminated to grow ALD layers directly on DNA origami crystals.

ALD growth on bare DNA origami crystals

In order to apply ALD processes on bare crystals, DNA origami structures must first be transferred from the liquid phase to the dry phase. However, air-drying of bare DNA crystals leads to severe morphological deformations and collapse of the intricate crystalline structures (Figures S5-5 and S5-6). We attribute this instability to mechanical forces generated by surface tension as the liquid–gas interface moves through the crystal during drying. To overcome this problem, we used CPD based on liquid carbon dioxide (CO₂), which allows transition from the liquid to the gaseous phase via a supercritical fluid phase, thereby avoiding the propagation of a surface tension wave through the sample and associated drying artifacts. In our assembly protocol, bare DNA origami crystals are prepared in an aqueous folding buffer. Since water is poorly soluble in both liquid⁴⁷ and supercritical CO₂,⁴⁸ the bare crystals were first washed with isopropanol, an intermediate solvent in which both water and CO₂ are soluble. A liquid droplet containing the crystals was then deposited on an ~1 cm² rectangle cut from a silicon wafer and placed in an isopropanol bath within the critical point dryer. Next, multiple purging steps were performed, during which liquid CO₂ diluted and replaced the isopropanol. Subsequently, the CO₂ was brought to the supercritical phase and removed (for the complete critical point drying process, see the SI). After CPD drying, the crystals show hardly any deformation (Figure S5-7). Once we obtained dried bare DNA origami crystals, we coated them with a 10-nm-thick layer of TiO₂ via ALD using the TDMAT process (see the SI). While the CPD-dried DNA crystals do not show signs of degradation over the course of 6 weeks at room temperature

5. Fabrication of Functional 3D Nanoarchitectures Using Atomic Layer Deposition on DNA Origami Crystals

(Figure S5-8), one of the major obstacles to ALD growth on 3D DNA nanostructures is the potential degradation and deformation of the nanostructure at typical ALD process temperatures.⁴⁹ Such instabilities are particularly pronounced if the DNA structures do not have a protective layer, such as SiO₂, that increases their mechanical and thermal stability. Indeed, initial attempts to apply standard 200 °C ALD processes resulted in considerable deformation of bare DNA origami structures (Figure S5-9). However, by lowering the chamber temperature to 100 °C, we were able to successfully deposit TiO₂ on bare DNA crystals while remaining within the ALD window and preserving their structural integrity (Figure 5-3). The crystal morphology was investigated by using SEM imaging of the crystal surface (Figure 5-3a,b).

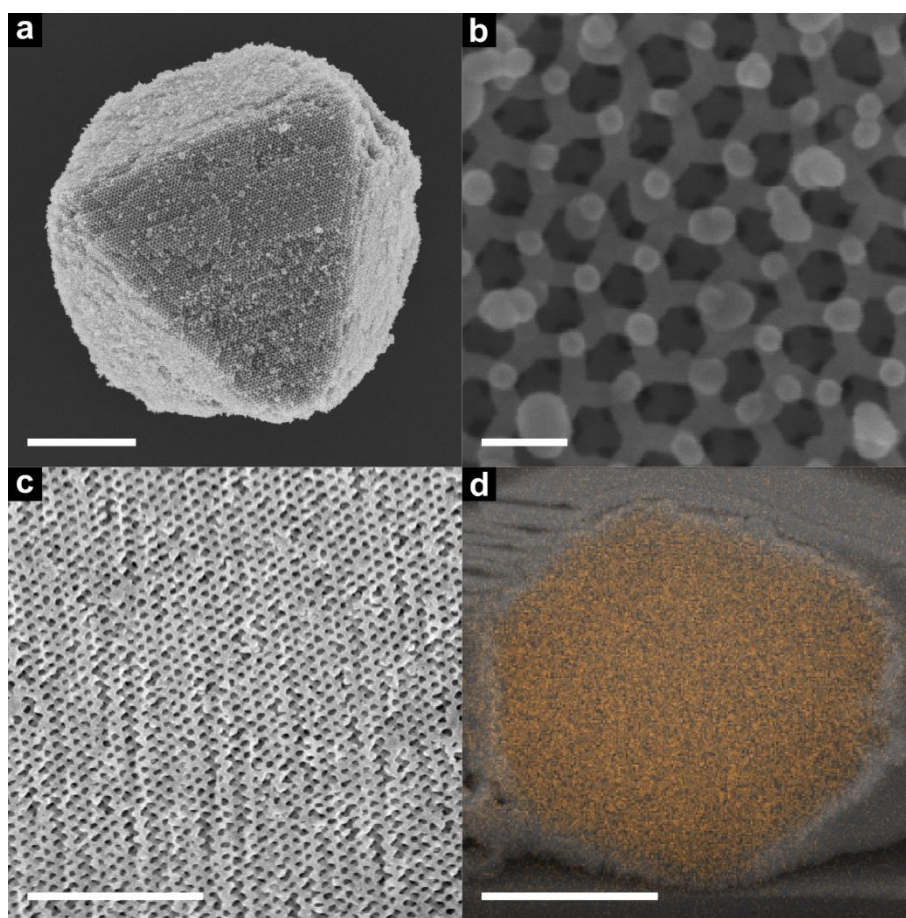


Figure 5-3. SEM images of CPD-dried crystals. (a) Top view of a DNA origami crystal dried using CPD and subsequently coated with 10 nm TiO₂ using ALD (TDMAT process, scale bar 2.5 μm). (b) Close-up view of the crystal shown in (a) (scale bar 100 nm). (c) Cross-sectional FIB cut of a CPD-dried crystal (scale bar 1 μm). (d) Zoomed-out cross-sectional view of a FIB cut crystal, with the Ti EDX signal overlaid in orange (scale bar 2.5 μm).

In contrast to the air-dried bare DNA crystals, which appear deformed and collapsed (Figures S5-5 and S5-6), the CPD-dried and TiO₂-coated DNA crystals retain distinct octahedral shapes (Figure 5-3a) similar to the SiO₂-stabilized crystals (Figure 5-2a–d). While the top surface of the crystal still displays a hexagonal pattern (Figures 5-3b and S5-10), individual hexagons are

slightly distorted and less regular than the ones on the surface of the SiO₂-coated crystals in Figure 5-2a,b. Furthermore, individual tetrahedron arms appear to be slightly bent. These distortions can be attributed to drying artifacts due to the reduced rigidity of the bare DNA structure compared to the silicified crystals. Nevertheless, long-range ordering is retained and future optimization of drying protocols may be applied to minimize these comparatively minor structural distortions. Analogous to the SiO₂-stabilized crystals, the ALD-coated bare crystals were cut using FIB milling, and both their structure and material composition were analyzed using SEM and EDX, respectively. Remarkably, the overall crystal morphology (Figure 5-3c) is preserved during the drying and ALD processes. However, regular moiré patterns that were obtained for SiO₂-stabilized crystals (Figure 5-2c–d) are not observed. We attribute this lack of interference between the cut surface and the crystal planes to the slight distortion of the crystal, resulting from the drying process. Nevertheless, the quality of the deposition of TiO₂ on the bare DNA crystals is comparable to that obtained with the ALD process on SiO₂-stabilized crystals (Figure 5-3d). Similar to the ALD of two different materials shown for SiO₂-coated crystals in Figure 5-2, we expect this process to work equally for several layers of different materials as long as the first material is deposited at chamber temperatures that do not compromise the mechanical stability of the DNA crystal.

IrO₂-facilitated electrocatalytic water splitting

Among many other applications, the ALD-covered DNA origami crystals are potentially interesting for electrochemical,⁵⁰ photoelectrochemical, and photochemical⁵¹ energy conversion due to the large surface-to-volume ratios associated with their porous structures. Furthermore, these crystals could form hierarchical porous systems with diverse topologies and a vast range of scaffold structures, compositions, and surface functionalities, all of which can be tuned to, for example, beneficially promote light absorption, charge carrier transport, mass transport, and catalytic activity. Here, we illustrate these opportunities with a proof-of-concept OER catalyst for electrochemical water splitting based on IrO₂-coated DNA origami crystals. Key questions that can be systematically addressed and ultimately optimized with DNA origami crystals include the electrical contact with a conducting electrode surface, electrical conductivity through the coated origami structure (depending on bulk oxide and Ir-oxide conductivity), catalytic surface area, mechanical stability of crystal attachment, chemical stability of the Ir-oxide phase, and oxygen gas evolution management. The latter will be

5. Fabrication of Functional 3D Nanoarchitectures Using Atomic Layer Deposition on DNA Origami Crystals

strongly dependent on the current density, pore structure, and layer thickness or crystal size. While a systematic study of these important aspects is beyond the scope of this work and will be the subject of future research, here we show that the Ir-oxide-coated DNA crystals indeed feature significant electrocatalytic OER activity. To generate electrochemically active anodes, we coated the DNA origami crystals with an ~ 3 -nm-thick layer of IrO_2 and used them as a catalyst for the OER⁵² (Figure 5-4). Using DNA origami monomers as the basis for the crystal, geometry and pore sizes can be precisely controlled. In this proof-of-concept demonstration, our crystals possess a pore diameter of approximately 100 nm and exhibit a surface-to-volume ratio of $1.88 \times 10^7 \text{ m}^{-1}$ (see the SI for calculation). These dimensions place our system in an intermediate regime compared to previous OER studies that have investigated the impact of pore sizes, either in the range of a few nanometers⁵³ or up to micrometers⁵⁴ in diameter. Silicified crystals were deposited on glass substrates coated with FTO (Figure 5-4a,c-f).

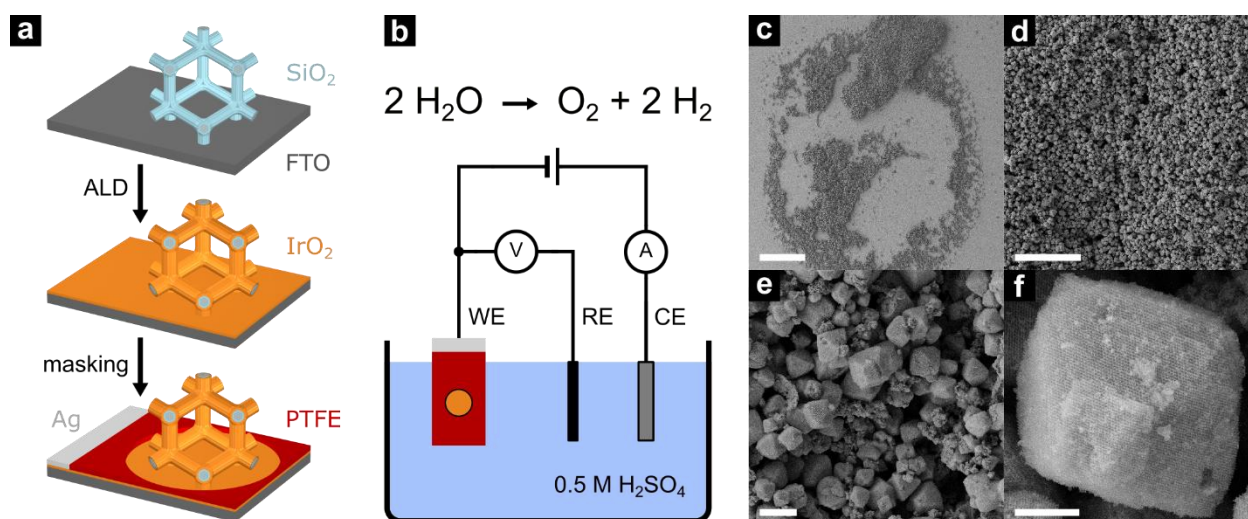


Figure 5-4. Experimental setup for electrocatalytic water oxidation using functionalized DNA origami crystals. (a) Sample preparation: Silicified DNA origami crystals were deposited and air-dried on an FTO-coated glass substrate. A thin layer of IrO_2 was subsequently grown via ALD, resulting in conformal deposition on both the exposed FTO substrate and on the SiO_2 -coated DNA crystals. The substrate was then masked with PTFE, leaving an exposed 5 mm diameter circular area containing all of the DNA crystals. A separate exposed region on the edge of the sample was also defined, on which a Ag contact was placed. (b) Experimental three-electrode setup for electrocatalytic water oxidation with IrO_2 -coated DNA origami crystals. (c-f) Exemplary SEM images of a 3x concentrated DNA origami crystal sample supported on FTO and coated with IrO_2 via ALD at different magnifications ((c) scale bar 500 μm , (d) scale bar 100 μm , (e) scale bar 10 μm , (f) scale bar 2 μm).

Since silicified DNA crystals can be air-dried, a solution containing the crystals can be applied to substrates and air-dried several times in a row, allowing for a degree of control over surface coverage and sample thickness. To determine the impact of surface loading, we examined two different coverages denoted as “1× DNA” and “3× DNA”, where “1× DNA” comprises one deposition cycle with an estimated 0.28 pmol of crystal monomers, resulting in a total IrO_2 -

5.2 Results and Discussion

covered surface of approximately 20 cm^2 , with the corresponding values for “3× DNA” being 3-fold higher (note that these values are estimates based on the origami geometry, see the SI for assumptions and calculation). FTO-coated glass slides without any deposited crystals were used as nominally planar reference samples. After drying, samples were coated with IrO_2 via ALD and subsequently placed in a three-electrode electrochemical cell containing sulfuric acid (Figure 5-4b). Cyclic voltammetry was performed with the IrO_2 -coated samples configured as the working electrode and with a fixed performed from 0 V vs reversible hydrogen electrode (RHE) to 1.8 V vs RHE, all subsequent cycles were run from 1.0 V vs RHE to 1.8 V vs RHE, for a total of 20 cycles. In the following, we discuss the key performance metrics obtained from these proof-of-concept DNA-origami-based electrocatalysts, as well as future opportunities and needs for rational design and improvement of such catalytic systems. An approximately linear enhancement in catalytic activity with increasing crystal concentration is observed and is compared with the reference samples (Figure 5-5c). However, the enhancement is not proportional to the increase in the surface area of the sample; although the “1× DNA” samples had an approximately 100× larger surface area than the reference sample, the catalytic activity is enhanced only by a factor of 1.9 (during cycle 2). For the “3× DNA” samples, the enhancement factor during cycle 2 was approximately 3 (for cycle 20: corresponding enhancement factors were 1.8 for “1×DNA”, 4 for “3× DNA”).

5. Fabrication of Functional 3D Nanoarchitectures Using Atomic Layer Deposition on DNA Origami Crystals

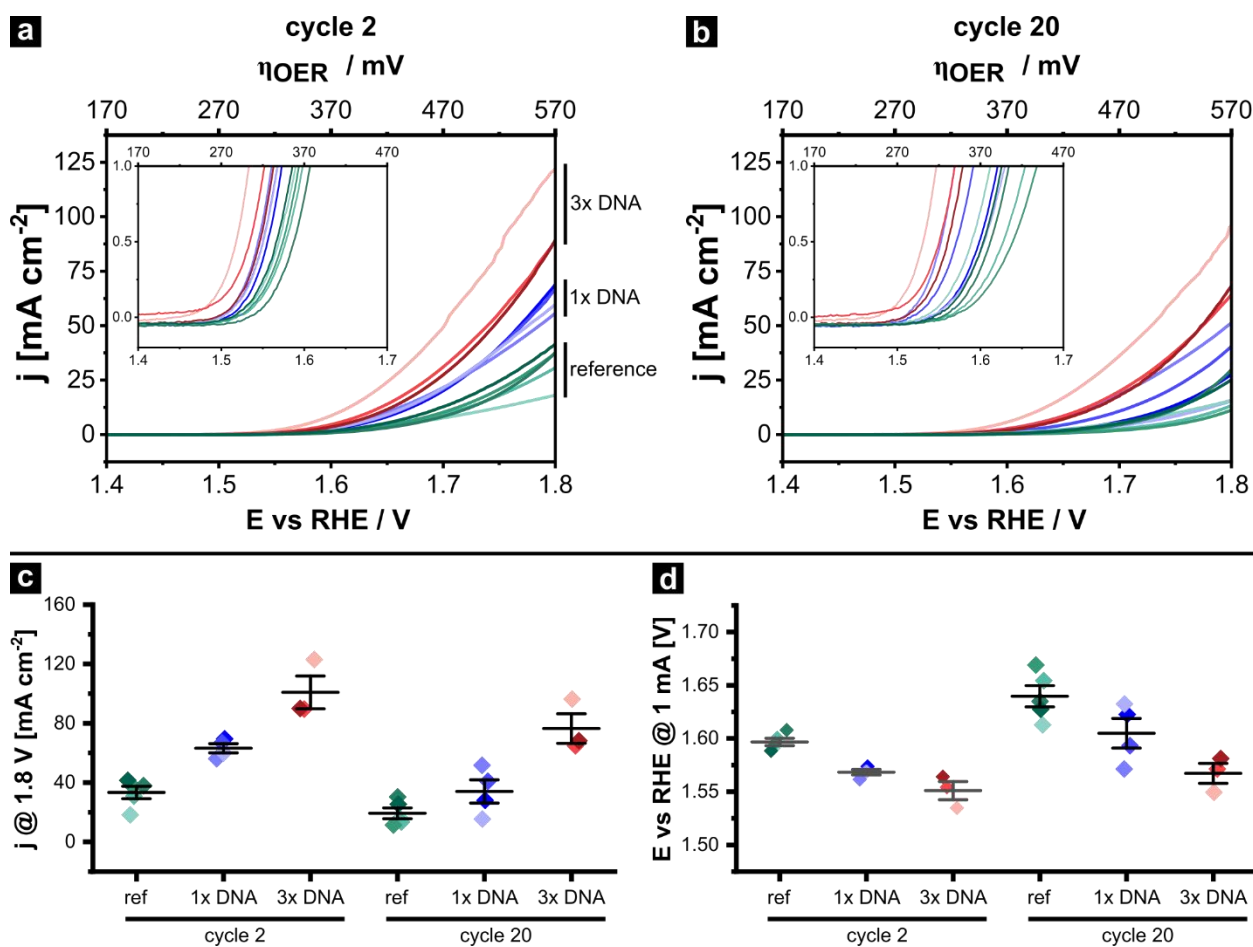


Figure 5-5. Electrolysis of water with IrO₂-coated DNA origami crystals. The specific color shade of each curve and point represents an individual sample. The reference (“ref”) data (green shades) refer to samples that were prepared without adding DNA origami crystals to the FTO-covered glass. “1x DNA” (blue shades) denotes 0.28 pmol of crystal monomers deposited on the FTO-glass surface, “3x DNA” (red shades) denotes samples produced with three times as much material, as described in the text. (a,b) Current density as a function of applied electrochemical potential measured in (a) cycle 2 and (b) cycle 20. Insets show zoomed-in regions near the onset potential. (c) Statistical analysis of current density at 1.8 V vs. RHE. (d) Statistical analysis of the electrochemical potential required to reach a current density of 1 mA/cm².

Nevertheless, we observe a decrease in the onset potential at 1 mA/cm² (Figure 5-5d) with increasing density of crystals, reflecting the increase in the overall electrocatalytic activity. The narrow scatter range of the samples in Figure 5-5d suggests consistent IrO₂ coverage over the catalytically active surface. The moderate current density increases suggest that only a fraction of IrO₂ contributes to the overall activity, which likely originates from two factors that should be addressed in future work. First, while IrO₂ thin films possess high electrical conductivities⁵⁵ and the IrO₂ coverage inside individual crystals is homogeneous (Figure S5-11), the contact between the crystals, and between the crystals and the substrate, may limit electrical transport to and from catalytically active sites. To overcome this limitation, possible future strategies could include the integration of additional conducting layers prior to IrO₂ coating or directed

growth of oriented DNA crystal films on (prefunctionalized) substrates. Second, it is likely that the nanoscale mass transport is limited within the crystals. For example, the oxygen that is produced during the catalytic reaction can be entrapped within the relatively small pores of the crystals and can reduce the contact area of water with the catalyst. This would reduce the catalytically active area and hence limit the reaction rate within the crystal. Previous work suggested that efficient detachment, transport, and coalescence of gas bubbles is also modulated by the 3D geometry of the catalyst, demonstrated by the differences in catalytic activity for pore sizes ranging from 200 to 1200 nm.⁵⁴ This hypothesis can be tested in future experiments by using DNA crystal designs with varying unit cell dimensions and topologies optimized for mass transfer, enabled by the versatile topological and geometric design of DNA crystals. We further observed a decrease in the catalytic activity after 20 CV cycles. We hypothesize that this is due to two reasons. First, IrO₂ is known to slowly dissolve under OER conditions,^{56,57} which is also observed in the present work and manifests for the reference samples as a decrease of the current density and increase of the overpotential between cycle 2 and cycle 20, as shown in Figure 5-5. Second, crystals can detach from the surface (Figure S5-12, blue box) due to mechanical stresses generated during bubble formation and evolution. Here, we note that the crystals are only physically deposited on the surface and adhere due to a combination of weak van der Waals forces and the thin metal oxide layer deposited via ALD, making them prone to mechanical detachment from the sample surface. This is further exacerbated by the “open” configuration of the working electrode electrochemical half-cell, which allows detached crystals to disperse into the bulk electrolyte. By comparison, such effects can likely be suppressed in more confined designs, such as membrane electrode assemblies or through the use of ionomer binders. Interestingly, the crystals not only appear to detach but also to partially reattach to the IrO₂ surface at different locations (Figure S5-12, red boxes), highlighting the dynamic nature of the working interface. Nevertheless, the morphology of the crystals themselves is not altered during the electrochemical experiment (Figure S5-13), indicating significant structural stability under harsh acidic conditions and demonstrating the robustness of the SiO₂- and ALD-coated crystals.

5.3. Conclusion

We demonstrated the fabrication of 3D nanomaterials with controlled pore topologies and dimensions by coating micrometer-sized SiO₂-coated DNA origami crystals with metal oxides such as ZnO, TiO₂, and IrO₂. The porous 3D materials were conformally coated by ALD, with homogeneous layers extending through the complete internal volume of these intricate nanostructures. Furthermore, we demonstrated a method to transfer bare DNA crystals from the liquid to the dry phase while preserving their structures, allowing us to use ALD to grow TiO₂ directly on DNA. As an example application of the developed methods, we show a proof-of-principle study of IrO₂-based electrocatalytic water splitting, demonstrating enhanced catalytic performance compared with planar surfaces. The techniques demonstrated here greatly expand the range of potential applications based on DNA origami-based nano- and mesostructures, providing unique possibilities in terms of the versatile design, precise molecular arrangement, and ALD-based functionalization.

5.4. Experimental Part

Folding and purification of DNA origami tetrapods

The DNA origami tetrapods¹ are designed based on a single 8634 nt long ssDNA scaffold strand and consist of four 35 nm long legs with a 24-helix bundle cross-section, corresponding to a 15 nm diameter. The folding mixture was prepared by mixing the scaffold strand (15 nM) with approximately 200 short staples (Integrated DNA Technologies, HPLC purified, 200 μ M each in water, folding concentration 120 nM) in 100 μ l aliquots containing 1x TE (10 nM Tris-HCl and 1 mM EDTA, pH adjusted to 8.0 with NaOH) and 20 mM MgCl₂. The temperature annealing protocol used for folding is listed in Table S5-1.

Table 5-1. Folding temperature protocol for tetrapod monomer.

Temperature (°C)	Time per °C (min)
67	15
60-50	40
25	storage

The excess staples were removed by PEG precipitation after folding. The DNA origami solution was mixed with PEG solution (15 wt% PEG, 500 mM NaCl, and 1x TE) in a 1:1 ratio. When the volume of the DNA origami solution was less than 1 mL, it was diluted with 1x TE and 20 mM MgCl₂ buffer to 1 mL. This mixture was then centrifuged at 20,000 rcf for 30 min at 4 °C. A pellet was obtained by removing all of the supernatant from the tube. The pellet was re-dissolved in 1x TE and 5 mM MgCl₂ buffer by shaking at 800 rpm at 34 °C for 1 h. The concentration of monomers was then measured using a Nanodrop ND-1000 UV-Vis spectrometer and adjusted to 50 nM with 1x TE and 5 mM MgCl₂ buffer.

Crystal growth

The diamond lattice DNA origami crystals were grown from purified tetrapod monomers (20 nM) mixed with the binding staples (200 nM) and the “mini scaffold” strands (8 μ M) in 70 μ l aliquots with 1x TE and 26 mM MgCl₂. A temperature algorithm was applied to the

5. Fabrication of Functional 3D Nanoarchitectures Using Atomic Layer Deposition on DNA Origami Crystals

solution: first, a temperature ramp from 55 °C to 33 °C was performed at a rate of 2.5 h/°C, followed by incubation at 40 °C for 8 h. Then, 45 µl of supernatant was removed, and a second ramp from 55 °C to 33 °C (at a rate of -2.5 h/°C) was applied.

For CPD drying to obtain bare structures, the crystals were diluted to 2 ml with isopropanol, mixed, and left to sediment for 12 h, at which point the supernatant was carefully removed. This process was then repeated a second time. The crystals were then immediately processed (see Preparation of CPD-dried bare DNA crystal samples).

Silicification

The remaining 20 µl crystal solution was mixed with 110 µl 1x TE and 5 mM MgCl₂ buffer in a 2 ml Eppendorf tube (final monomer concentration approximately 10 nM). After cooling to 4 °C, 1.6 µl of TMAPS (trimethyl[3-(trimethoxysilyl)propyl]ammonium chloride, TCI Germany, 50 % in methanol) diluted in methanol with a 1:3 ratio was added to the solution while shaking. After 30 min, 1.0 µl of TEOS (tetraethyl orthosilicate, Merck) was added to the solution while shaking. After 1 h, 1.3 µl of 0.5 M acetic acid was added while shaking. The temperature was then gradually increased, as summarized in Table 5-2. The silicified crystal was washed twice with water and twice with isopropanol by diluting the mixture to 2 mL, mixing, waiting at least 12 h for the crystals to sediment, and removing the supernatant.

Table 5-2. Temperature protocol for silicification.

Temperature (°C)	Shaking speed (rpm)	Time per °C (h)
4	800	4.5
10	800	2
16	800	2
22	800	16

5.4 Experimental Part

Preparation of air-dried SiO₂-stabilized crystals samples

For SiO₂-stabilized crystal deposition, 1 x 1 cm² Si/SiO₂ chips with a 100 nm thermal oxide layer (MicroChemicals GmbH) were used as substrates. The chips were first washed in acetone for 30 s, then washed in isopropanol for 30 s, and then blow-dried with nitrogen. Afterwards, the chips were cleaned using a PICO plasma cleaner (Diener Electronic GmbH & Co. KG), utilizing an oxygen plasma (45 sccm, 80% power) for 10 min.

After substrate preparation, the SiO₂-stabilized crystal solution (~20 µl) was pipetted onto the substrate and left to air-dry. Following drying, the substrate and supported crystals were coated via ALD according to the protocols described below.

Preparation of CPD-dried bare DNA crystals samples

Bare DNA crystals kept in isopropanol were used immediately after their preparation. The same substrate preparation method was used as for the air-dried SiO₂-stabilized crystals (see above). Approximately 20 µl of bare crystal solution was pipetted onto each substrate and immediately transferred to a K850 Critical Point Drier (Quorum Technologies) chamber. The chamber was then immediately filled with isopropanol, not allowing the isopropanol-covered substrates to dry, and sealed. In all following steps, liquid levels were maintained to ensure full wetting of the substrates at all times until reaching supercriticality. The chamber was first cooled to 18 °C and liquid carbon dioxide (CO₂) was added to the chamber to dissolve and mix in the isopropanol until saturation. The system was then further cooled to 11 °C, where the remaining isopropanol was purged by flushing the chamber with liquid CO₂ for 10 min by fully opening the CO₂ inlet valve while adjusting the draining valve so that the liquid level in the chamber was kept constant. After 10 min of purging, both the drainage and the CO₂ valves were closed and the system was left for approximately 3 min to stabilize the CO₂ level and temperature at 11 °C. During stabilization, the CO₂ inlet valve was opened as needed to adjust the CO₂ level in the chamber. The purging step was performed three times in total. After the last purging step, the chamber was fully filled with liquid CO₂ and cooling was turned off. The chamber was then slowly heated to 35 °C, surpassing the critical point of CO₂ (7.39 MPa, 31.05 °C) and thus transitioning from the liquid to the supercritical phase. After reaching 35 °C, a bleed valve was opened, which slowly reduced the chamber pressure to atmospheric pressure. When atmospheric pressure was reached, heating was turned off and samples were retrieved from the chamber.

Preparation of FTO glass slides for subsequent IrO₂ coating and electrocatalysis

FTO glass (TEC 15, sheet resistance 12-14 Ω/\square) was purchased from XOP GLASS. The glass was cut into 1 x 2 cm² pieces with a diamond glass cutter and the FTO surface cleaned according to the following protocol. In a first step, the glass pieces were separated by spacers to ensure that their surfaces were accessible to the cleaning fluid. Next, 2 ml of Hellmanex II and 100 ml of bi-distilled water were added to cover the entire glass surface, which was then treated in an ultrasonic bath for 15 min. The liquid was then discarded and the samples were washed with bi-distilled water until all Hellmanex II was removed. The glass pieces were then immersed in bi-distilled water and treated in an ultrasonic bath for 15 min, after which the liquid was discarded. In the final treatment step, the glass pieces were fully covered with 100% isopropanol and treated in an ultrasonic bath for 15 min. Subsequently, the glass pieces were dried with nitrogen gas and masked using PTFE tape with a circular 5 mm diameter opening. The masked glass slides were stored in a dust-free container until usage. Before usage, substrates were cleaned using a PICO plasma cleaner (Diener Electronic GmbH & Co. KG), utilizing an oxygen plasma (45 sccm, 80% power) for 10 min.

Six SiO₂-coated DNA origami crystal aliquots à 70 μ l were combined, resulting in an estimated number of monomers of 8.4 pmol (assuming negligible losses in the preparation process, see surface enhancement discussion in SI). The combined aliquots were left to rest for 12 h for sedimentation. Afterwards, the supernatant was removed, and the remaining liquid was fully distributed among 12 “1x DNA” and 6 “3x DNA” samples. This was done by pipetting 0.4 μ l of the combined aliquots onto the center of the exposed region of each masked glass piece and letting it air-dry, repeating this step twice more for the “3x DNA” samples. This process was then repeated until all liquid was consumed or until there was not enough liquid to cover all samples according to the process. Neglecting potential losses, this yielded an estimated tetrapod quantity of 0.28 pmol for “1x DNA” samples and 0.84 pmol for “3x DNA” samples. For the reference samples, no crystals were pipetted onto the masked FTO glass.

All samples were then transferred to the ALD chamber for IrO₂ coating (see below). Before the ALD process, the masks were removed from the FTO glass pieces and after the ALD process the masks were reapplied.

5.4 Experimental Part

Atomic layer deposition (ALD) of ZnO using diethylzinc (DEZ)

ALD deposition was performed using a Picosun R-200 Advanced system (Applied Materials Inc.). The ALD ZnO precursor diethylzinc (DEZ) (Sigma Aldrich, $\leq 100\%$) was acquired from Sigma Aldrich and used as received. ZnO ALD was carried out at 175 °C chamber temperature. The nitrogen carrier gas flow during DEZ pulses was 150 sccm for all lines. DEZ was vaporized from a stainless steel container at room temperature; for this reactor, a precursor vapor pressure between 2 and 10 mbar is typically required to achieve reliable deposition. One ALD cycle included two 0.1 s DEZ pulses followed by 14.9 s of purging with pure gas, alternating with a one 1 s H₂O pulse and subsequent 14 s of purging. Furthermore, a stop-flow protocol was established in order to allow the precursor vapor pressure to build up in the reaction chamber. Within the DEZ pulse, the low-flow protocol started 3 s before the DEZ pulse, at which point the flow in all other lines was reduced to 40 sccm for 8 s. Within this timespan, the chamber evacuation valve was closed 1 s before the precursor pulse and was kept closed for a total of 6 s. For the H₂O pulse, the duration of the low-flow protocol was 7.8 s, whereas the chamber evacuation valve was kept closed for 6.3 s. Here, implemented delay times, as well as the flow rates, were kept the same. Apart from the low-flow rate, the flow rates of DEZ and H₂O were 150 sccm. Using such a recipe, 22 cycles were performed for coating DNA crystals, which resulted in a layer thickness of 4.9 nm, as determined by spectroscopic ellipsometry on Si(100) reference substrates.

Atomic layer deposition (ALD) of TiO₂ samples using titanium tetraisopropoxide (TTIP)

ALD deposition was performed using a Picosun R-200 Advanced system (Applied Materials Inc.). The ALD TiO₂ precursor titanium isopropoxide (TTIP, 98 %) was acquired from Strem Chemicals and used as received. TiO₂ ALD was carried out at a chamber temperature of 250 °C. The nitrogen carrier gas flow was 150 sccm for all lines. TTIP was vaporized from a stainless steel container at 85 °C. One ALD cycle included two 0.1 s TTIP pulses followed by 14.9 s of purging with pure gas, alternating with one 1 s H₂O pulse and subsequent 14 s of purging. Furthermore, a stop-flow protocol was established in order to allow the precursor vapor pressure to build up in the reaction chamber. Within the TTIP pulse, the low-flow protocol started 3 s before the TTIP pulse, at which point the flow in all other lines was reduced to 40 sccm for 8 s. Within this timespan the chamber evacuation valve was closed 1 s before the precursor pulse and was kept closed for a total of 6 s. For the H₂O pulse, the duration of the low-flow protocol was 7.8 s, whereas the chamber evacuation valve was kept closed for 6.3 s.

Here, implemented delay times, as well as the flow rates, were kept the same. Using such a recipe, 160 cycles were used for coating DNA origami structures, which resulted in a layer thickness of 5.1 nm, determined by ex-situ spectroscopic ellipsometry on Si(100) reference substrates.

Atomic layer deposition (ALD) of TiO₂ samples using tetrakis(dimethylamino)titanium (TDMAT)

Titania films were also deposited by a thermal ALD process using a Fiji G2 system from Veeco Instruments Inc. For these depositions, tetrakis(dimethylamido)titanium (TDMAT, 99.999 % Sigma-Aldrich, heated to 75 °C) was used as the titanium precursor and water (filtered at 0.2 µm, VWR Chemicals) was used as the oxidant. The precursor and carrier gas lines were heated to 110 °C, while the chamber walls and substrate stage were heated to 100 °C (200 °C for the sample in Fig. S5-9). In the first half-cycle, the TDMAT was pulsed into the chamber for 0.25 s followed by a 25 s purge; in the second half-cycle, water was pulsed into the chamber for 0.06 s, then the chamber is purged for another 25 s. During the deposition, the chamber was kept at a base pressure of 0.24 Torr, and argon was used as the carrier and purge gas with a flow rate of 420 sccm throughout the entire procedure. The thickness of the resulting titania film was monitored with in-situ spectroscopic ellipsometry measured on a silicon reference chip that was placed in the reactor together with the samples.

Atomic layer deposition (ALD) of IrO₂ samples using iridium acetylacetonate (Ir(acac)₃)

ALD deposition was performed using a Picosun R-200 Advanced system (Applied Materials Inc.). ALD IrO₂ precursor Ir(acac)₃ (98 %) was acquired from Strem Chemicals and used as received. IrO₂ ALD was carried out at a chamber temperature of 188 °C. During pulses, the nitrogen carrier gas flow was 40 sccm for all lines. Ir(acac)₃ was sublimated from a borosilicate glass container at 186 °C. Ozone was supplied by an ozone generator (INUSA AC2025) from a feed of 500 sccm 1 % vol N₂ in O₂ (Air Liquide, 99.9995 %). Each cycle consisted of three Ir(acac)₃ pulses and one ozone pulse, separated by purge intervals. An Ir(acac)₃ half cycle comprised a 1.6 s pulse, 5 s static exposure, and 10 s purge time. For the ozone half cycle, the times were 4 s, 2 s and 10 s, respectively. A total of 80 cycles were used for the OER catalyst coatings, which resulted in a layer thickness of 3.1 nm, as determined by ex-situ spectroscopic ellipsometry on Si(100) reference substrates.

5.4 Experimental Part

Electrocatalytic experiments

Electrochemical characterization was performed in a three-electrode setup in a quartz cell at room temperature. The cell was filled with 20 ml 0.5 M H₂SO₄ (Sigma-Aldrich, Titripur® volumetric standard) electrolyte. A PGSTAT302N potentiostat/galvanostat (Methrohm Autolab B.V.) equipped with a FRA32 M impedance analyzer was connected to a hydroflex reversible hydrogen electrode (Gaskatel Gesellschaft für Gassysteme durch Katalyse und Elektrochemie mbH) or Hg/HgSO₄/K₂SO₄ (sat.) (REF601 radiometer analytical, Hach Company) reference electrode for cyclic voltammetry (CV) and galvanostatic (chronopotentiometry) measurements, respectively.

To avoid artefacts arising from the formation of trapped oxygen bubbles in porous electrode layers, as described in the work of El-Sayed et al.², cyclic voltammetry (CV) measurements were used to determine the electrochemical activity of the catalysts, which allows to reduce oxygen bubbles during each cathodic scan.

The CV measurements were performed with iR-correction (95%) in a potential window of 0.0 – 1.8 V versus RHE with a scan rate of 20 mV/s for the first scan and 1.0 – 1.8 V versus RHE and same scan rate for subsequent 19 scans. Before each CV measurement, impedance spectroscopy was performed at 0.5 V versus RHE to determine the corresponding electrolyte resistance from the high-frequency region (R_s).

SEM and EDX imaging

SEM images in Fig. 5-2a-d, Fig. 5-3c,d, Fig. S9, S11 and S14 were recorded with an FEI Helios Nanolab G3 UC scanning electron microscope equipped with a field emission gun operated at 2 – 20 kV. EDX measurements were recorded at an operating voltage of 20 kV with an X MaxN Silicon Drift Detector with an 80 mm² detector area (Oxford Instruments) and AZTec acquisition software (Oxford Instruments).

SEM images in all other figures were collected using the SEM feature of an eLine electron beam lithography tool (Raith GmbH) operated at 4 kV acceleration voltage, utilizing the in-lens or secondary electron detector. Samples that were not coated using ALD (Fig. S5-5 – S5-7) were sputter coated prior to imaging using a S150 Sputter Coater (Edwards) with a 60:40 Au/Pd target for 30 s, thereby ensuring sufficient electrical conductivity to avoid charging-induced artifacts.

Thickness measurements and fast Fourier transform analysis of the SEM images was done using Fiji³.

Focused ion beam (FIB) milling

The area of interest for a cross section of the oriented DNA origami crystal was covered by a protective 1.5-2 μm thick Pt layer with an ion beam (Fig. S5-14). After depositing the protective coating, the DNA origami crystal was milled with the focused gallium ion beam to form a thin vertical slab. The acceleration energy of the ion beam was 30 kV throughout the process, with an initial beam current of 2.5 nA. The slab thickness was gradually reduced via ion milling until a final thickness of approximately 1-1.3 μm was reached. The beam current was decreased in conjunction with the reduction in the slab thickness to minimize beam damage in the area of interest: 0.77 nA was used down to a thickness of 2 μm , 0.4 nA was chosen in the range 2 - 1.5 μm , and a current of 0.25 nA was then used until the final thickness was reached.

5.5 References

5.5. References

- (1) Rothemund, P. W. K. Folding DNA to Create Nanoscale Shapes and Patterns. *Nature* 2006, 440 (7082), 297–302. <https://doi.org/10.1038/nature04586>.
- (2) Douglas, S. M.; Marblestone, A. H.; Teerapittayanon, S.; Vazquez, A.; Church, G. M.; Shih, W. M. Rapid Prototyping of 3D DNA-Origami Shapes with caDNAno. *Nucleic Acids Res.* 2009, 37 (15), 5001–5006. <https://doi.org/10.1093/nar/gkp436>.
- (3) Douglas, S. M.; Dietz, H.; Liedl, T.; Högberg, B.; Graf, F.; Shih, W. M. Self-Assembly of DNA into Nanoscale Three-Dimensional Shapes. *Nature* 2009, 459 (7245), 414–418. <https://doi.org/10.1038/nature08016>.
- (4) Kuzyk, A.; Schreiber, R.; Fan, Z.; Pardatscher, G.; Roller, E.-M.; Högele, A.; Simmel, F. C.; Govorov, A. O.; Liedl, T. DNA-Based Self-Assembly of Chiral Plasmonic Nanostructures with Tailored Optical Response. *Nature* 2012, 483 (7389), 311–314. <https://doi.org/10.1038/nature10889>.
- (5) Inuma, R.; Ke, Y.; Jungmann, R.; Schlichthaerle, T.; Woehrstein, J. B.; Yin, P. Polyhedra Self-Assembled from DNA Tripods and Characterized with 3D DNA-PAINT. *Science* 2014, 344 (6179), 65–69. <https://doi.org/10.1126/science.1250944>.
- (6) Nickels, P. C.; Wünsch, B.; Holzmeister, P.; Bae, W.; Kneer, L. M.; Grohmann, D.; Tinnefeld, P.; Liedl, T. Molecular Force Spectroscopy with a DNA Origami-Based Nanoscopic Force Clamp. *Science* 2016, 354 (6310), 305–307. <https://doi.org/10.1126/science.aah5974>.
- (7) Wagenbauer, K. F.; Sigl, C.; Dietz, H. Gigadalton-Scale Shape-Programmable DNA Assemblies. *Nature* 2017, 552 (7683), 78–83. <https://doi.org/10.1038/nature24651>.
- (8) Jiang, D.; Ge, Z.; Im, H.-J.; England, C. G.; Ni, D.; Hou, J.; Zhang, L.; Kuttyreff, C. J.; Yan, Y.; Liu, Y. DNA Origami Nanostructures Can Exhibit Preferential Renal Uptake and Alleviate Acute Kidney Injury. *Nature biomedical engineering* 2018, 2 (11), 865–877.
- (9) Sigl, C.; Willner, E. M.; Engelen, W.; Kretzmann, J. A.; Sachenbacher, K.; Liedl, A.; Kolbe, F.; Wilsch, F.; Aghvami, S. A.; Protzer, U.; Hagan, M. F.; Fraden, S.; Dietz, H. Programmable Icosahedral Shell System for Virus Trapping. *Nat. Mater.* 2021, 20 (9), 1281–1289. <https://doi.org/10.1038/s41563-021-01020-4>.

- (10) Gopinath, A.; Thachuk, C.; Mitskovets, A.; Atwater, H. A.; Kirkpatrick, D.; Rothmund, P. W. K. Absolute and Arbitrary Orientation of Single-Molecule Shapes. *Science* 2021, 371 (6531), eabd6179. <https://doi.org/10.1126/science.abd6179>.
- (11) Wintersinger, C. M.; Minev, D.; Ershova, A.; Sasaki, H. M.; Gowri, G.; Berengut, J. F.; Corea, Dilbert, F. E.; Yin, P.; Shih, W. M. Multi-Micron Crisscross Structures Grown from DNA-Origami Slats. *Nat. Nanotechnol.* 2023, 18 (3), 281–289. <https://doi.org/10.1038/s41565-022-01283-1>.
- (12) Ramakrishnan, S.; Ijäs, H.; Linko, V.; Keller, A. Structural Stability of DNA Origami Nanostructures under Application-Specific Conditions. *Computational and Structural Biotechnology Journal* 2018, 16, 342–349. <https://doi.org/10.1016/j.csbj.2018.09.002>.
- (13) Gerling, T.; Kube, M.; Kick, B.; Dietz, H. Sequence-Programmable Covalent Bonding of Designed DNA Assemblies. *Sci Adv* 2018, 4 (8), eaau1157. <https://doi.org/10.1126/sciadv.aau1157>.
- (14) Auvinen, H.; Zhang, H.; Nonappa; Kopilow, A.; Niemelä, E. H.; Nummelin, S.; Correia, A.; Santos, H. A.; Linko, V.; Kostianen, M. A. Protein Coating of DNA Nanostructures for Enhanced Stability and Immunocompatibility. *Advanced Healthcare Materials* 2017, 6 (18), 1700692. <https://doi.org/10.1002/adhm.201700692>.
- (15) Ponnuswamy, N.; Bastings, M. M. C.; Nathwani, B.; Ryu, J. H.; Chou, L. Y. T.; Vinther, M.; Li, W. A.; Anastassacos, F. M.; Mooney, D. J.; Shih, W. M. Oligolysine-Based Coating Protects DNA Nanostructures from Low-Salt Denaturation and Nuclease Degradation. *Nat Commun* 2017, 8 (1), 15654. <https://doi.org/10.1038/ncomms15654>.
- (16) Nguyen, L.; Döblinger, M.; Liedl, T.; Heuer-Jungemann, A. DNA-Origami-Templated Silica Growth by Sol–Gel Chemistry. *Angew. Chem. Int. Ed.* 2019, 58 (3), 912–916. <https://doi.org/10.1002/anie.201811323>.
- (17) Liu, X.; Zhang, F.; Jing, X.; Pan, M.; Liu, P.; Li, W.; Zhu, B.; Li, J.; Chen, H.; Wang, L.; Lin, J.; Liu, Y.; Zhao, D.; Yan, H.; Fan, C. Complex Silica Composite Nanomaterials Templated with DNA Origami. *Nature* 2018, 559 (7715), 593–598. <https://doi.org/10.1038/s41586-018-0332-7>.

5.5 References

- (18) Michelson, A.; Flanagan, T. J.; Lee, S.-W.; Gang, O. High-Strength, Lightweight Nano-Architected Silica. *Cell Reports Physical Science* 2023, 4 (7), 101475. <https://doi.org/10.1016/j.xcrp.2023.101475>.
- (19) Shani, L.; Michelson, A. N.; Minevich, B.; Flegler, Y.; Stern, M.; Shaulov, A.; Yeshurun, Y.; Gang, O. DNA-Assembled Superconducting 3D Nanoscale Architectures. *Nat Commun* 2020, 11 (1), 5697. <https://doi.org/10.1038/s41467-020-19439-9>.
- (20) Majewski, P. W.; Michelson, A.; Cordeiro, M. A. L.; Tian, C.; Ma, C.; Kisslinger, K.; Tian, Y.; Liu, W.; Stach, E. A.; Yager, K. G.; Gang, O. Resilient Three-Dimensional Ordered Architectures Assembled from Nanoparticles by DNA. *Sci. Adv.* 2021, 7 (12), eabf0617. <https://doi.org/10.1126/sciadv.abf0617>.
- (21) Martynenko, I. V.; Erber, E.; Ruider, V.; Dass, M.; Posnjak, G.; Yin, X.; Altpeter, P.; Liedl, T. Site-Directed Placement of Three-Dimensional DNA Origami. *Nat. Nanotechnol.* 2023, 1–7. <https://doi.org/10.1038/s41565-023-01487-z>.
- (22) Zhou, F.; Sun, W.; Zhang, C.; Shen, J.; Yin, P.; Liu, H. 3D Freestanding DNA Nanostructure Hybrid as a Low-Density High-Strength Material. *ACS Nano* 2020, 14 (6), 6582–6588. <https://doi.org/10.1021/acsnano.0c00178>.
- (23) Leskelä, M.; Ritala, M. Atomic Layer Deposition (ALD): From Precursors to Thin Film Structures. *Thin Solid Films* 2002, 409 (1), 138–146. [https://doi.org/10.1016/S0040-6090\(02\)00117-7](https://doi.org/10.1016/S0040-6090(02)00117-7).
- (24) Hui, L.; Nixon, R.; Tolman, N.; Mukai, J.; Bai, R.; Wang, R.; Liu, H. Area-Selective Atomic Layer Deposition of Metal Oxides on DNA Nanostructures and Its Applications. *ACS Nano* 2020, 14 (10), 13047–13055. <https://doi.org/10.1021/acsnano.0c04493>.
- (25) Hui, L.; Chen, C.; Kim, M. A.; Liu, H. Fabrication of DNA-Templated Pt Nanostructures by AreaSelective Atomic Layer Deposition. *ACS Appl. Mater. Interfaces* 2022, 14 (14), 16538–16545. <https://doi.org/10.1021/acsam.2c02244>.
- (26) Michelson, A.; Subramanian, A.; Kisslinger, K.; Tiwale, N.; Xiang, S.; Shen, E.; Kahn, J. S.; Nykypanchuk, D.; Yan, H.; Nam, C.-Y.; Gang, O. Three-Dimensional Nanoscale Metal, Metal Oxide, and Semiconductor Frameworks through DNA-Programmable Assembly and Templating. *Science Advances* 2024, 10 (2), eadl0604. <https://doi.org/10.1126/sciadv.adl0604>.

- (27) Posnjak, G.; Yin, X.; Butler, P.; Bienek, O.; Dass, M.; Lee, S.; Sharp, I. D.; Liedl, T. Diamond-Lattice Photonic Crystals Assembled from DNA Origami. *Science* 2024, 384 (6697), 781–785. <https://doi.org/10.1126/science.adl2733>.
- (28) Wang, Y.; Dai, L.; Ding, Z.; Ji, M.; Liu, J.; Xing, H.; Liu, X.; Ke, Y.; Fan, C.; Wang, P.; Tian, Y. DNA Origami Single Crystals with Wulff Shapes. *Nat Commun* 2021, 12 (1), 3011. <https://doi.org/10.1038/s41467-021-23332-4>.
- (29) Wibowo, A.; Marsudi, M. A.; Amal, M. I.; Ananda, M. B.; Stephanie, R.; Ardy, H.; Diguna, L. J. ZnO Nanostructured Materials for Emerging Solar Cell Applications. *RSC Adv.* 2020, 10 (70), 42838–42859. <https://doi.org/10.1039/D0RA07689A>.
- (30) Zhao, Y.; Sarhan, R. M.; Eljarrat, A.; Kochovski, Z.; Koch, C.; Schmidt, B.; Koopman, W.; Lu, Y. Surface-Functionalized Au–Pd Nanorods with Enhanced Photothermal Conversion and Catalytic Performance. *ACS Appl. Mater. Interfaces* 2022, 14 (15), 17259–17272. <https://doi.org/10.1021/acsami.2c00221>.
- (31) Stone, H. W. Solubility of Water in Liquid Carbon Dioxide. *Ind. Eng. Chem.* 1943, 35 (12), 1284–1286. <https://doi.org/10.1021/ie50408a015>.
- (32) Sabirzyanov, A. N.; Il'in, A. P.; Akhunov, A. R.; Gumerov, F. M. Solubility of Water in Supercritical Carbon Dioxide. *High Temperature* 2002, 40 (2), 203–206. <https://doi.org/10.1023/A:1015294905132>.
- (33) Johnson, R. W.; Hultqvist, A.; Bent, S. F. A Brief Review of Atomic Layer Deposition: From Fundamentals to Applications. *Mater. Today* 2014, 17 (5), 236–246. <https://doi.org/10.1016/j.mattod.2014.04.026>.
- (34) Qi, J.; Zhang, W.; Cao, R. Porous Materials as Highly Efficient Electrocatalysts for the Oxygen Evolution Reaction. *ChemCatChem* 2018, 10 (6), 1206–1220. <https://doi.org/10.1002/cctc.201701637>.
- (35) Bathla, A.; Lee, J.; Younis, S. A.; Kim, K.-H. Recent Advances in Photocatalytic Reduction of CO₂ by TiO₂– and MOF–Based Nanocomposites Impregnated with Metal Nanoparticles. *Materials Today Chemistry* 2022, 24, 100870. <https://doi.org/10.1016/j.mtchem.2022.100870>.

5.5 References

- (36) Chen, Z.; Duan, X.; Wei, W.; Wang, S.; Ni, B.-J. Iridium-Based Nanomaterials for Electrochemical Water Splitting. *Nano Energy* 2020, 78, 105270. <https://doi.org/10.1016/j.nanoen.2020.105270>.
- (37) Abbott, D. F.; Lebedev, D.; Waltar, K.; Povia, M.; Nachtegaal, M.; Fabbri, E.; Copéret, C.; Schmidt, T. J. Iridium Oxide for the Oxygen Evolution Reaction: Correlation between Particle Size, Morphology, and the Surface Hydroxo Layer from Operando XAS. *Chem. Mater.* 2016, 28 (18), 6591–6604. <https://doi.org/10.1021/acs.chemmater.6b02625>.
- (38) Kim, Y. J.; Lim, A.; Kim, J. M.; Lim, D.; Chae, K. H.; Cho, E. N.; Han, H. J.; Jeon, K. U.; Kim, M.; Lee, G. H.; Lee, G. R.; Ahn, H. S.; Park, H. S.; Kim, H.; Kim, J. Y.; Jung, Y. S. Highly Efficient Oxygen Evolution Reaction via Facile Bubble Transport Realized by Three-Dimensionally Stack-Printed Catalysts. *Nat Commun* 2020, 11 (1), 4921. <https://doi.org/10.1038/s41467-020-18686-0>.
- (39) Bernt, M.; Schramm, C.; Schröter, J.; Gebauer, C.; Byrknes, J.; Eickes, C.; Gasteiger, H. A. Effect of the IrO_x Conductivity on the Anode Electrode/Porous Transport Layer Interfacial Resistance in PEM Water Electrolyzers. *J. Electrochem. Soc.* 2021, 168 (8), 084513. <https://doi.org/10.1149/1945-7111/ac1eb4>.
- (40) Alia, S. M.; Reeves, K. S.; Cullen, D. A.; Yu, H.; Kropf, A. J.; Kariuki, N.; Park, J. H.; Myers, D. J. Simulated Start-Stop and the Impact of Catalyst Layer Redox on Degradation and Performance Loss in Low-Temperature Electrolysis. *J. Electrochem. Soc.* 2024, 171 (4), 044503. <https://doi.org/10.1149/1945-7111/ad2bea>.
- (41) Cherevko, S.; Geiger, S.; Kasian, O.; Kulyk, N.; Grote, J.-P.; Savan, A.; Shrestha, B. R.; Merzlikin, S.; Breitbach, B.; Ludwig, A.; Mayrhofer, K. J. J. Oxygen and Hydrogen Evolution Reactions on Ru, RuO₂, Ir, and IrO₂ Thin Film Electrodes in Acidic and Alkaline Electrolytes: A Comparative Study on Activity and Stability. *Catalysis Today* 2016, 262, 170–180. <https://doi.org/10.1016/j.cattod.2015.08.014>.
- (42) El-Sayed, H. A.; Weiß, A.; Olbrich, L. F.; Putro, G. P.; Gasteiger, H. A. OER Catalyst Stability Investigation Using RDE Technique: A Stability Measure or an Artifact? *J. Electrochem. Soc.* 2019, 166 (8), F458. <https://doi.org/10.1149/2.0301908jes>.

5.6. Appendix

Estimation of surface enhancement due to DNA origami crystals

The calculation of the enlarged surface area by crystal deposition on the FTO glass slide is based on several assumptions:

- the folding yield of the DNA origami tetrapods is 100%,
- there are no losses in the tetrapod purification process,
- there are no losses in the crystal washing steps,
- all crystals remain in solution (i.e., do not stick to tube walls or pipette tips before deposition),
- all crystals in solution are distributed between the FTO glass substrates according to the pipetted volume, and
- no crystals are swept away due to external forces during the ALD process.

The following calculation therefore only provides approximate estimates for the order of magnitude of the surface area. From experience with the system, we estimate the errors to be around 20 % of the values obtained by the calculation.

One crystal aliquot à 70 µl contains 20 nM of scaffold. Assuming perfect yield, this results in

$$n_{\text{tetrapod}} = V_{\text{aliquot}} \cdot c_{\text{scaffold}} = 70 \mu\text{l} \cdot 20 \text{ nM} = 1.4 \cdot 10^{-12} \cdot N_A = 1.4 \text{ pmol}$$

per aliquot (for six combined aliquots, the number of tetrapods is therefore 8.4 pmol).

The surface of every tetrapod can be approximated by four cylinders of length 35 nm, ignoring the circular surfaces that are covered by adjacent tetrapods. The radius is given by half the thickness of the DNA origami (~7.5 nm), the SiO₂ layer (~2.5 nm) and the IrO₂ layer (~ 3.1 nm), resulting in a total radius of 13.1 nm. The resulting surface area per aliquot is therefore

$$\begin{aligned} A_{\text{surface, aliquot}} &= n_{\text{tetrapod}} \cdot 4 \cdot l_{\text{cylinder}} \cdot 2\pi \cdot (r_{\text{DNA}} + r_{\text{SiO}_2} + r_{\text{IrO}_2}) \\ \Rightarrow A_{\text{surface, aliquot}} &= 1.4 \cdot 10^{-12} \cdot N_A \cdot 4 \cdot 35 \cdot 10^{-9} \text{ m} \cdot 2\pi \cdot ((7.5 + 2.5 + 3.1) \cdot 10^{-9} \text{ m}) \\ &\Rightarrow A_{\text{surface, aliquot}} = 9.7 \cdot 10^{-3} \text{ m}^2 = 97 \text{ cm}^2 \end{aligned}$$

Since 6 aliquots combined resulted in the equivalent of 30 “1x DNA” or 10 “3x DNA” samples, this means that, per sample, the surface is given by

5.6. Appendix

$$A_{1\times \text{DNA}} = \frac{6 \cdot A_{\text{surface, aliquot}}}{30} = 19 \cdot 10^{-4} \text{ m}^2 \approx 20 \text{ cm}^2,$$

and

$$A_{3\times \text{DNA}} = 3 \cdot A_{1\times \text{DNA}} = 57 \cdot 10^{-4} \text{ m}^2 \approx 60 \text{ cm}^2,$$

respectively.

Supplementary Figures

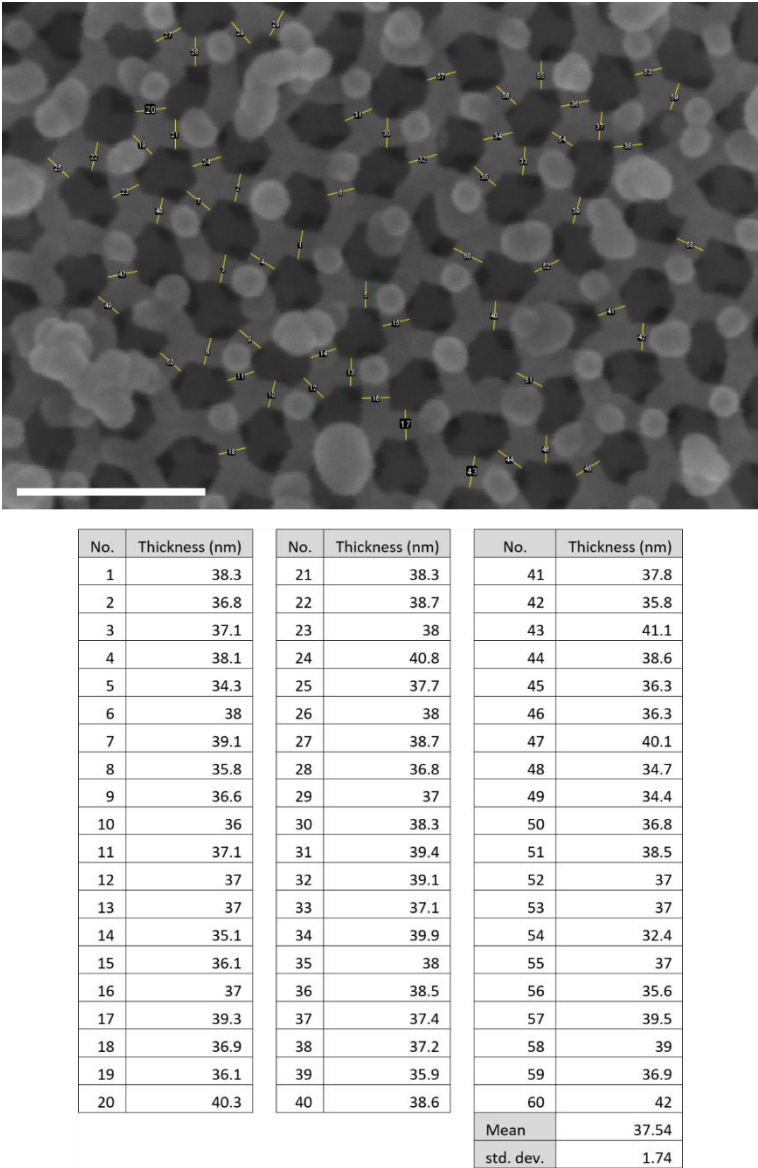
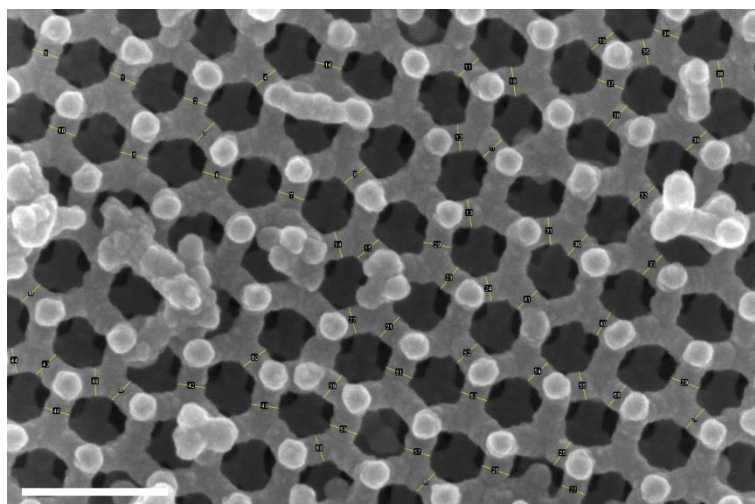


Figure S5-1. Thickness measurement for a CPD-dried DNA origami crystal, with subsequent ALD deposition of 10 nm of TiO₂. The locations of thickness measurements are marked in the SEM image, and the measured values listed in the table below. To achieve high resolution with SEM imaging, the DNA origami structure has to be covered with a conductive layer. In this case, ALD deposition of TiO₂ provides a conductive layer with a well-defined thickness, which was measured with spectroscopic ellipsometry on a flat Si chip (details in Methods). The structure is covered with 10 nm of TiO₂ from all sides, so the thickness of the underlying structure is 37.5 nm – 20 nm = 17.5 nm. Scale bar 200 nm.



No.	Thickness (nm)	No.	Thickness (nm)	No.	Thickness (nm)
1	39.5	22	37.9	43	38
2	34.2	23	38.3	44	35.2
3	36.5	24	35.4	45	34.7
4	34.6	25	39.2	46	35.3
5	38.6	26	38.3	47	36.2
6	39.8	27	35.1	48	39.5
7	37.8	28	36.5	49	37.1
8	37	29	40.5	50	38
9	37.6	30	39.4	51	38.7
10	39.1	31	37.5	52	38.4
11	35.8	32	39.9	53	37.3
12	36.8	33	38	54	36
13	37.8	34	36.5	55	40
14	37.4	35	35.9	56	37.1
15	38.5	36	39.1	57	35.9
16	37.3	37	38.2	58	39.2
17	35.3	38	38.6	59	39.8
18	39.8	39	38.5	60	37.8
19	38.7	40	36	61	34.8
20	38.8	41	37.1	Mean	37.5967213
21	39.4	42	38.2	std. dev.	1.6008297

Figure S5-2. Thickness measurement for a SiO₂-coated DNA origami crystal with subsequent ALD deposition of 10 nm of TiO₂. The locations of thickness measurements are marked in the SEM image, and the measured values listed in the table below. To achieve high resolution with SEM imaging, the SiO₂-coated structure has to be covered with a conductive layer. In this case, ALD deposition of TiO₂ provides a conductive layer with a well-defined thickness, which was measured with spectroscopic ellipsometry on a flat Si chip (details in Methods). The structure is covered with 10 nm of TiO₂ from all sides, so the thickness of the underlying structure is 37.6 nm – 20 nm = 17.6 nm. In the case of silica growth protocol, we used in this study, the thickness increase is small compared to ALD-coated bare DNA origami crystals from Fig. S5-1. This is consistent with most silica being incorporated between the double helices of DNA as demonstrated by small angle x-ray scattering measurements in ref. 34. Scale bar 200 nm.

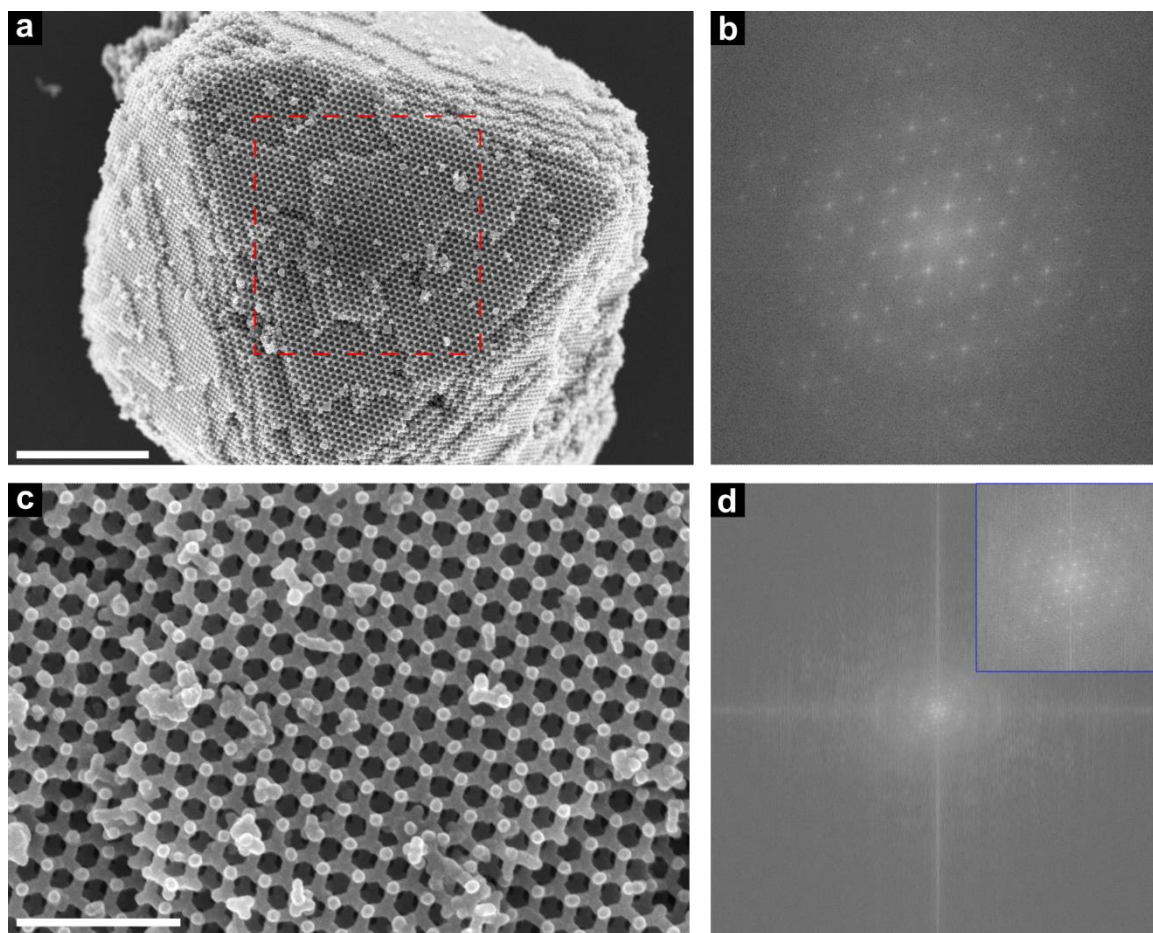


Figure S5-3. Fast Fourier Transform (FFT) analysis of SEM images of a $\{111\}$ crystal plane of DNA origami crystals covered in SiO_2 and 10 nm of ALD deposited TiO_2 . (a,b) The red dashed rectangle in (a) shows the analyzed region from Fig. 5-2a, with FFT shown in (b). (c) Wider view image of Fig. 5-2b and (d) the FFT of this region. The inset in the blue square in (d) is a zoomed-in view of the central area of (d). In both FFTs a hexagonal symmetry is clearly visible, reflecting the crystallinity of the structure. Scale bars: (a) 2 μm ; (c) 500 nm.

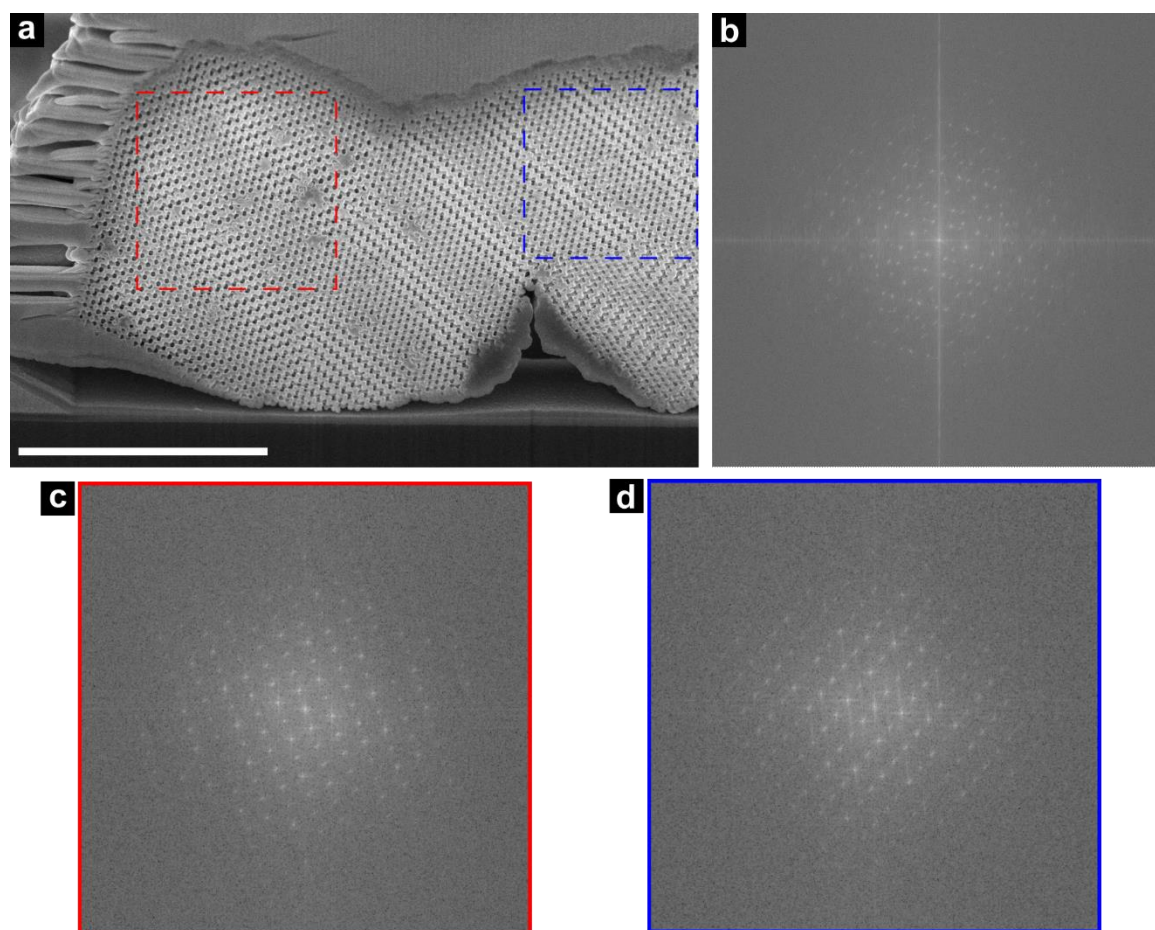


Figure S5-4. Fast Fourier Transform (FFT) analysis of SEM images of FIB milling cross-section of a DNA origami crystal covered in SiO_2 and two 5 nm layers of ALD deposited TiO_2 and ZnO from Fig. 2d. (a) The FIB-milled cross-section with the position of different analyzed regions. (b) FFT of the whole image in (a). Two overlapping patterns can be observed, signifying two differently aligned crystalline lattices in (a). (c) FFT of the area marked with a red dashed rectangle in (a) displays a single lattice, representing a monocrystalline region of the crystal. (d) FFT of the area marked with a blue dashed rectangle in (a) also displays a single lattice, representing a different monocrystalline region of the crystal. Scale bar: 3 μm .

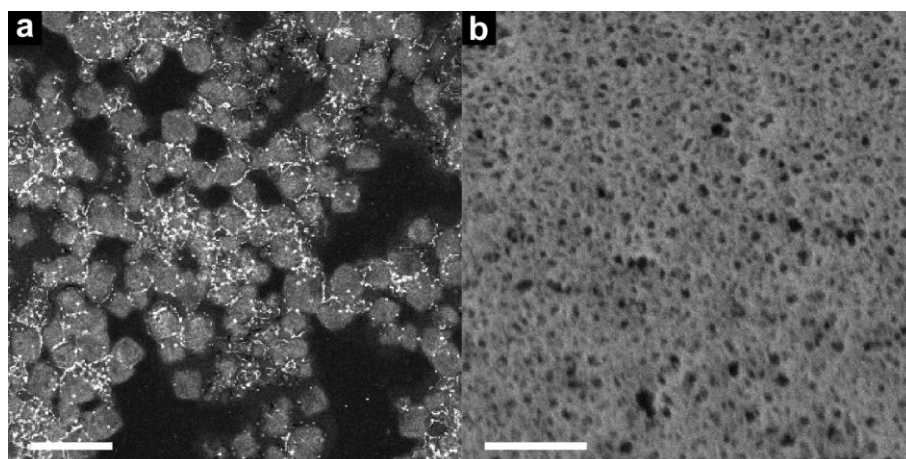


Figure S5-5. Bare crystals air-dried from buffer solution. (a) Plan-view SEM image of bare crystals air-dried from the buffer solution (crystals were coated by sputtering Au/Pt for SEM imaging, see Methods section), scale bar 20 μm . (b) Zoomed-in image of an exemplary bare crystal shown in (a), scale bar 400 nm.

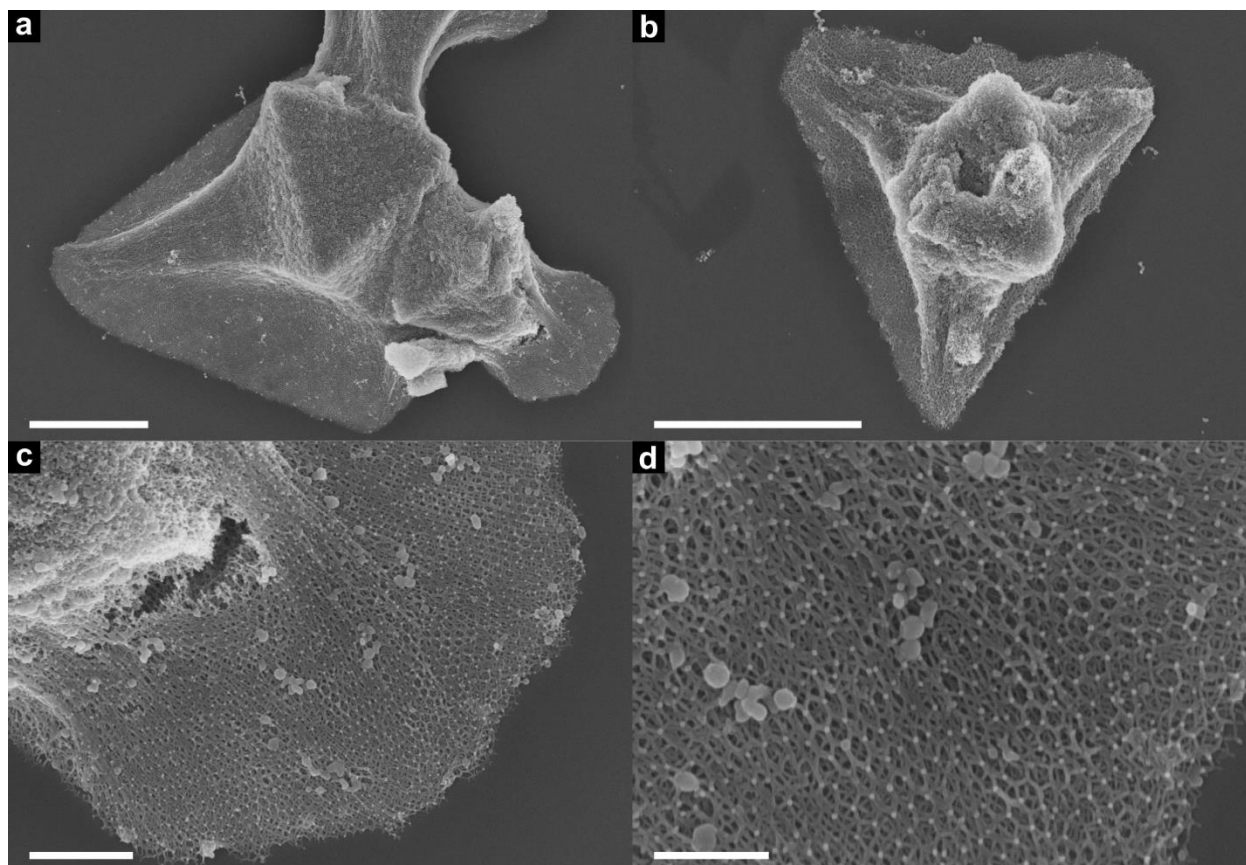


Figure S5-6. SEM images of bare DNA origami crystals, air-dried from isopropanol solution. 30 μl of crystal growth solution was diluted to 2 ml with isopropanol, shaken and left to stand for 24 h before removing 1.9 ml of supernatant and repeating the isopropanol wash. In (a) and (b) it can be seen how the bottom side of the octahedral crystal that was in contact with the substrate kept its triangular shape, whereas the rest of the crystal collapsed during drying. (c) and (d) close-ups of the deformed DNA origami lattice. Scale bars: (a) and (b) 5 μm , (c) 1 μm and (d) 500 nm.

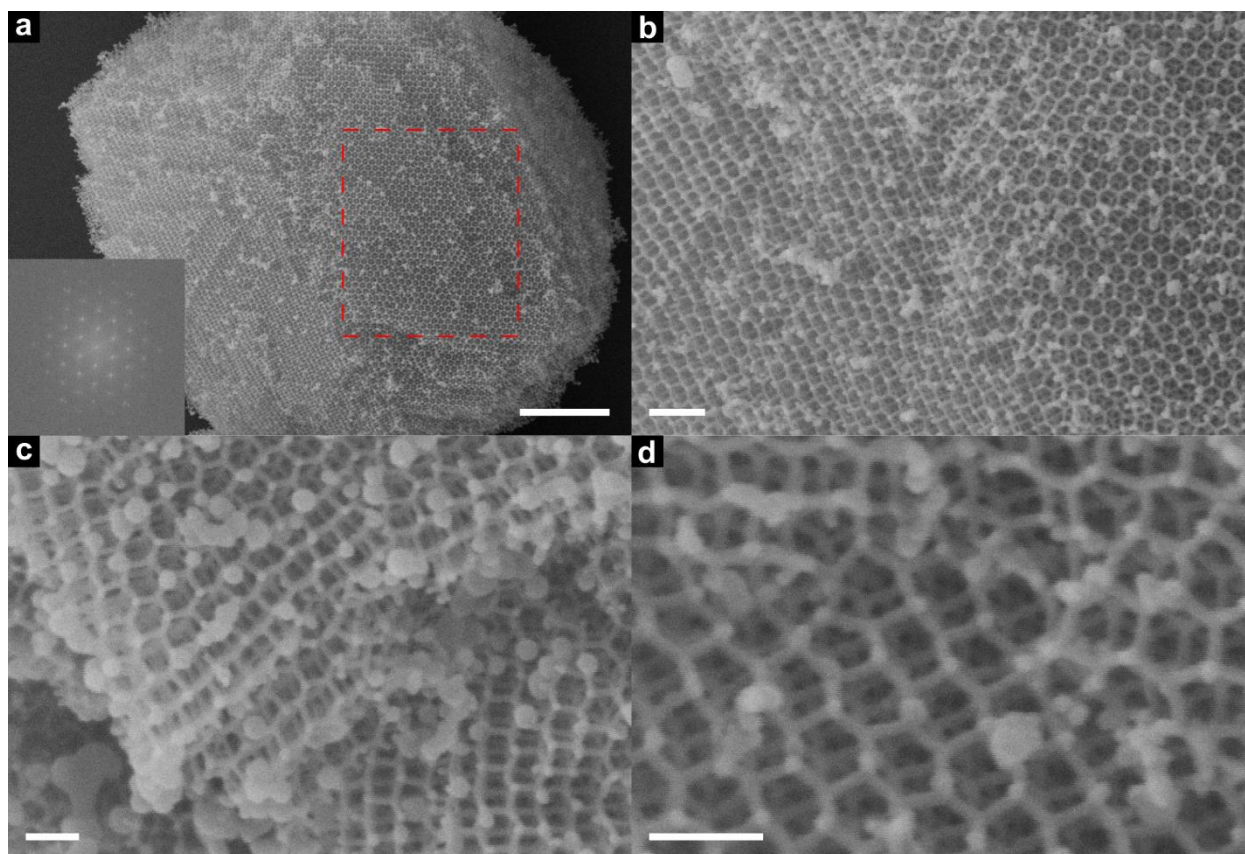


Figure S5-7. CPD-dried DNA origami crystal without ALD coating. These crystals were sputter coated with Au/Pd as described in the Methods section to increase the conductivity of the sample for SEM imaging. The inset in (a) is the FFT of the {111} region marked with a dashed red rectangle in (a). Scale bars: (a) 1 μm , (b) 200 nm, (c) and (d) 100 nm.

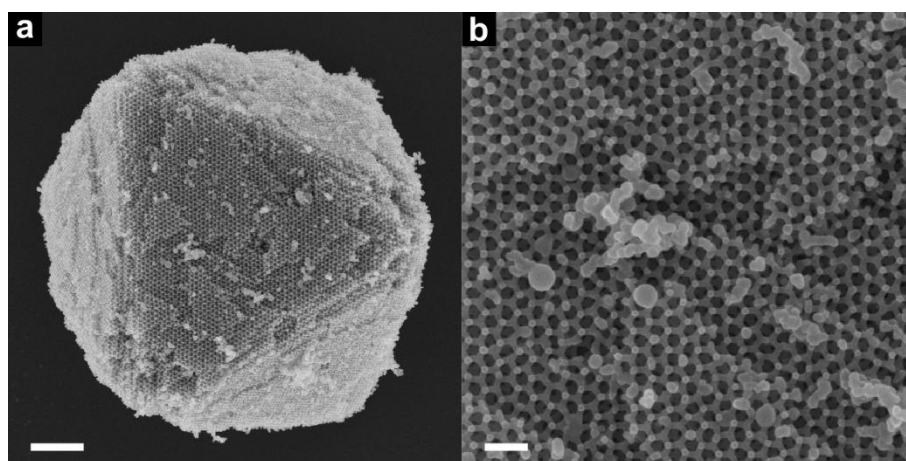


Figure S5-8. CPD-dried crystal stored under ambient conditions for six weeks and subsequent coating with 10 nm of TiO_2 using the TDMAT process. (a) scale bar 1 μm . (b) Zoomed-in view of (a), scale bar 200 nm.

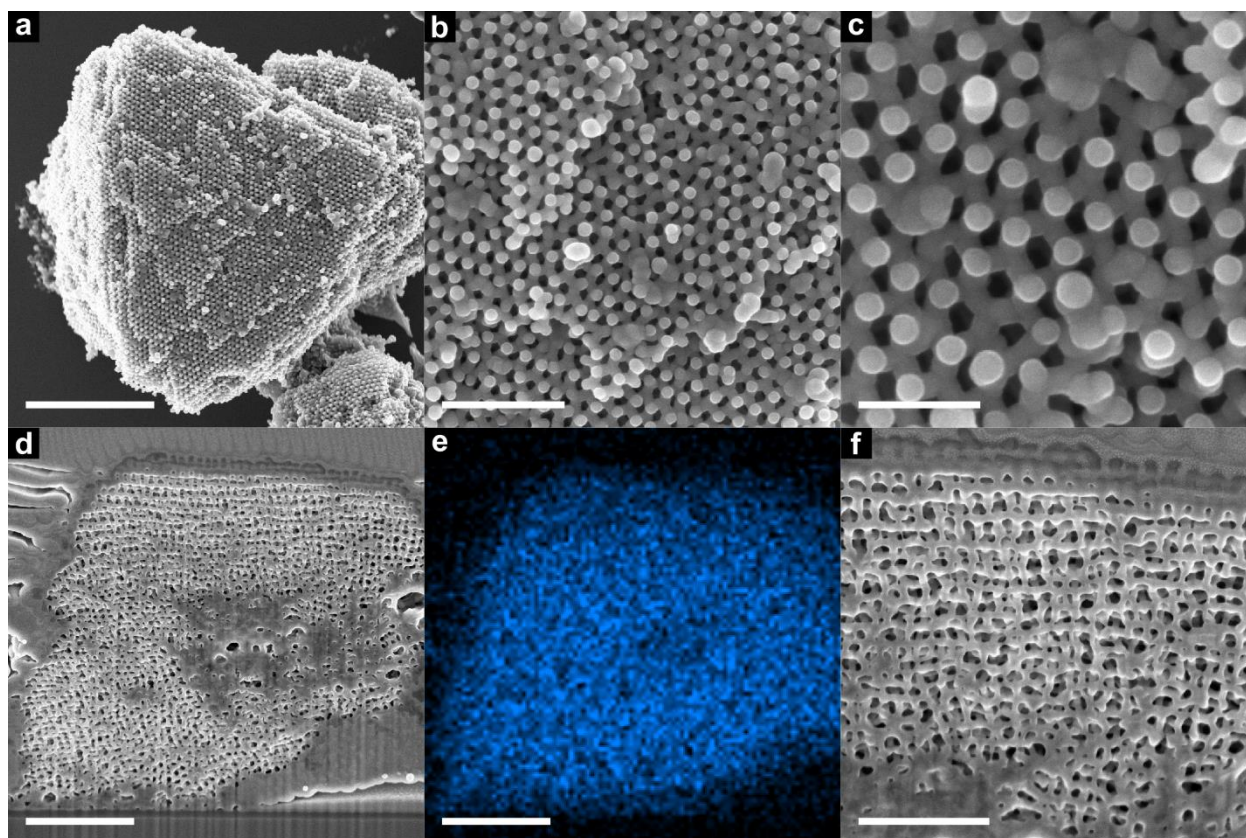


Figure S5-9. CPD-dried bare crystals coated in TiO_2 (TDMAT process) using a chamber temperature of 200 °C. (a), SEM image of an exemplary crystal, scale bar 2 μm . (b-c) Zoomed-in images of (a), scale bar 500 nm (b) and 200 nm (c). (d) SEM images of the interior of a CPD-dried, bare crystal coated in 10 nm TiO_2 using FIB milling, scale bar 1 μm . (e) Ti EDX signal of the cut crystal shown in (d), scale bar 1 μm . (f) Zoomed-in image of crystal shown in (d), scale bar 500 nm.

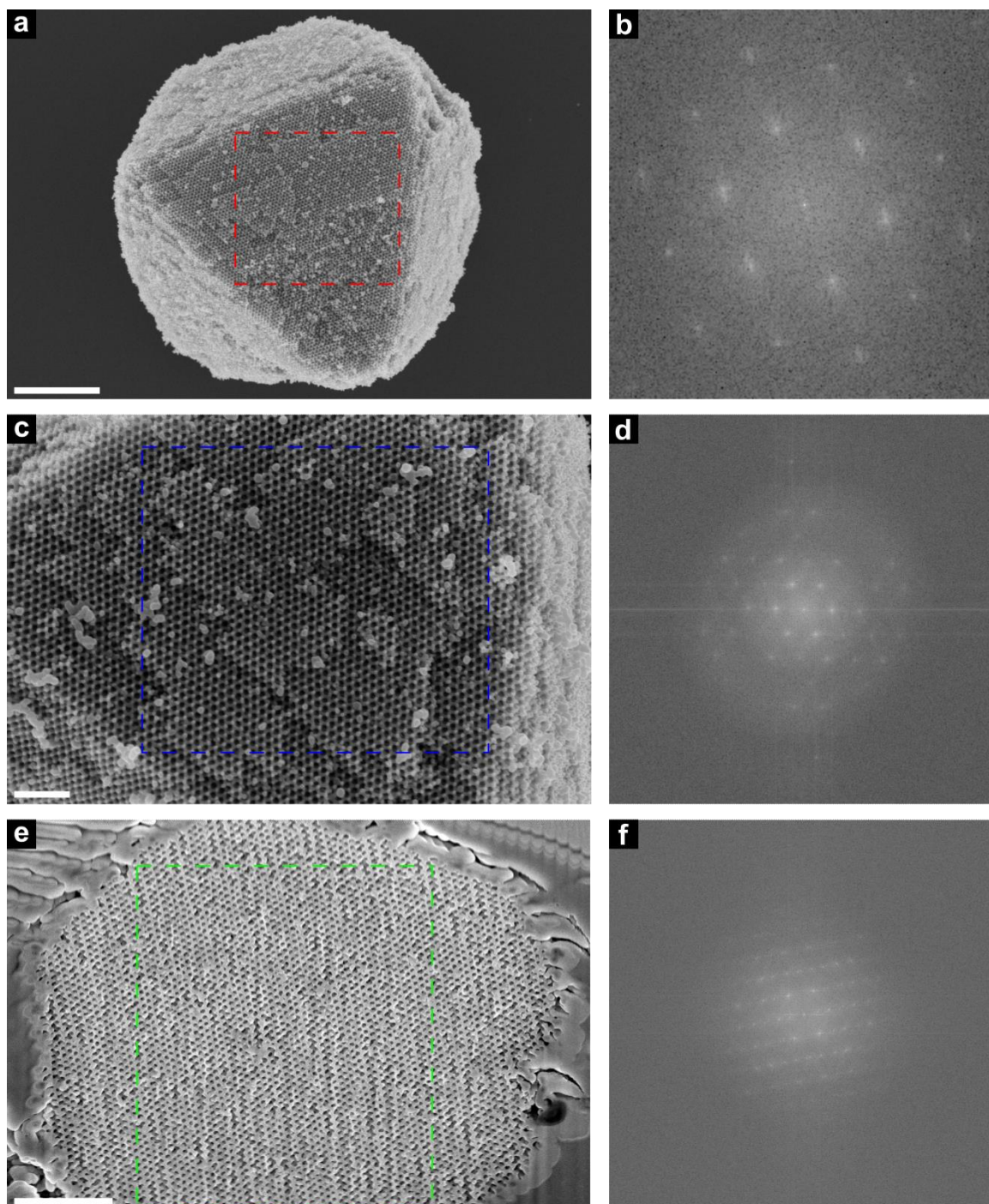


Figure S5-10. Fast Fourier Transform (FFT) analysis of SEM images of CPD-dried DNA origami crystals covered in 10 nm of ALD deposited TiO₂ (TDMAT process). (a,b) The red dashed rectangle in (a) shows the region of a {111} crystal plane from Fig. 5-3a that was analyzed with FFT, as shown in (b). (c) Zoomed-in view of a {111} crystal plane of a CPD-dried crystal, covered in 10 nm of TiO₂. (d) FFT of the region marked with a dashed blue rectangle in (c). (e) FIB-milled cross-section of a CPD-dried crystal with 10 nm of TiO₂. (f) FFT of the region marked with a dashed green rectangle in (e). Both FFT patterns in (b) and (d) are hexagonal, and all three patterns (b,d,f) have fewer points compared to the ones in Fig. S5-3 and S5-7, showing lower spatial coherence of the CPD-dried crystalline lattice after ALD treatment. Scale bars: (a) 2 μ m; (c) 500 nm; (e) 1 μ m.

5. Fabrication of Functional 3D Nanoarchitectures Using Atomic Layer Deposition on DNA Origami Crystals

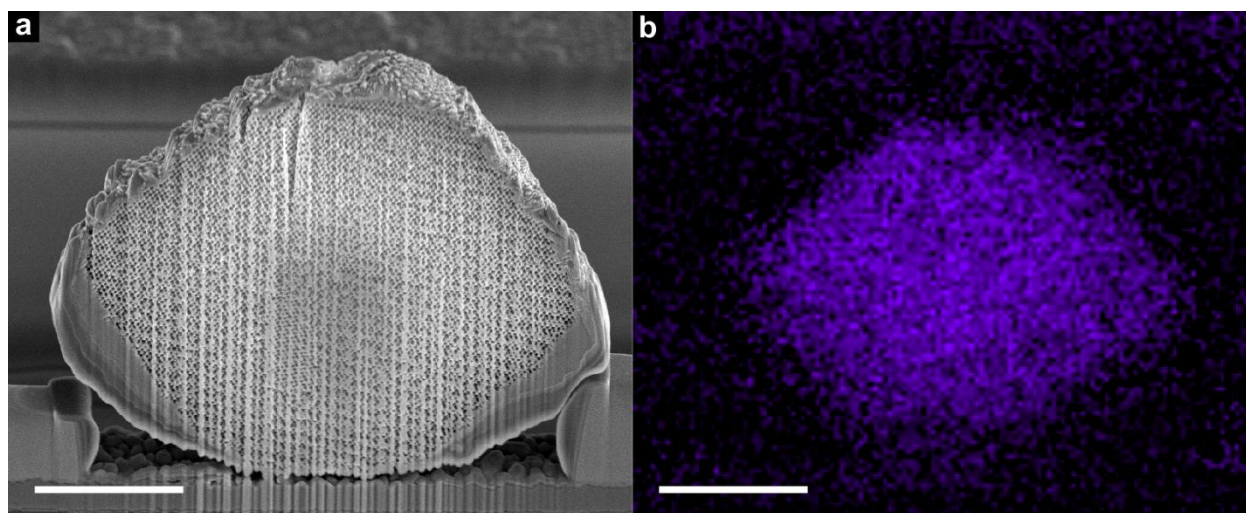


Figure S5-11. Silicized DNA origami crystal coated with ALD IrO_2 . (a) Cross-sectional SEM images of the interior of an SiO_2 -stabilized crystal coated in IrO_2 , scale bar $2.5\ \mu\text{m}$. Note that the damage to the surface and the stripe-like artefacts are a result of the FIB milling process. (b) Ir EDX signal of the cut crystal, scale bar $2.5\ \mu\text{m}$.

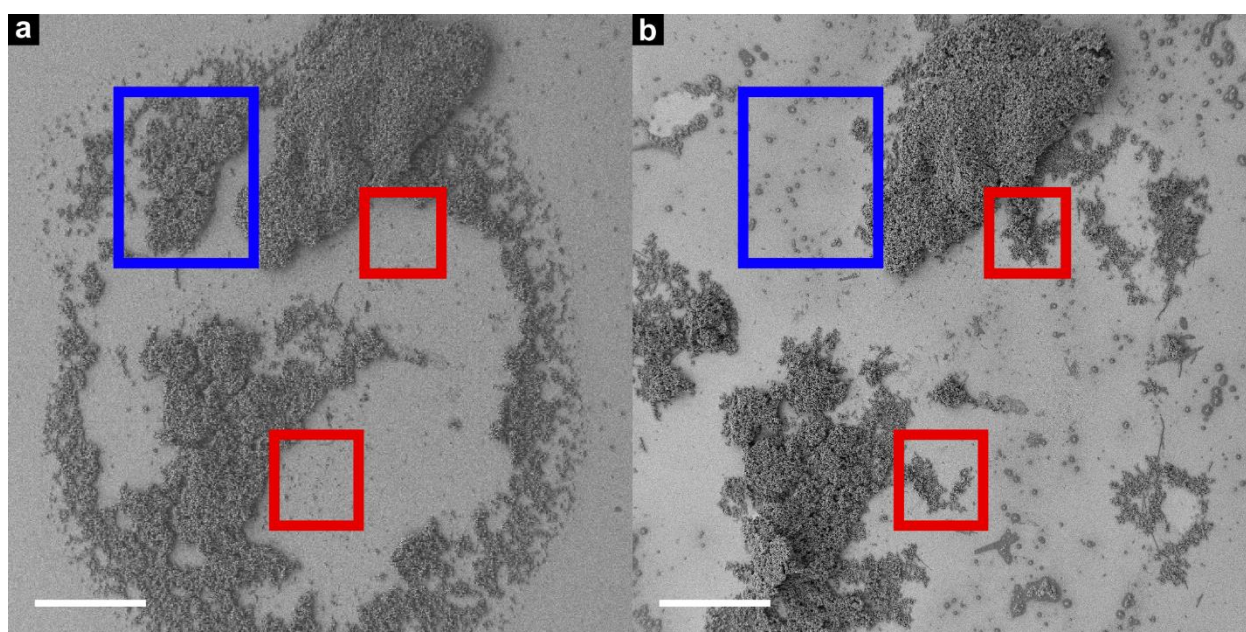


Figure S5-12. Comparison between “3x DNA” catalyst samples before and after electrocatalysis. (a) “3x DNA” sample before electrocatalysis (same as Fig. 5-4c), scale bar $500\ \text{nm}$. (b) “3x DNA” sample after 20 cycles of electrocatalysis (same as Fig. S5-13a), scale bar $500\ \text{nm}$. Note the change in crystal distribution: in some regions, crystals detach during the experiment (exemplary region shown in blue box) and re-attach at different locations (exemplary regions shown in red boxes). Both scale bars $500\ \text{nm}$.

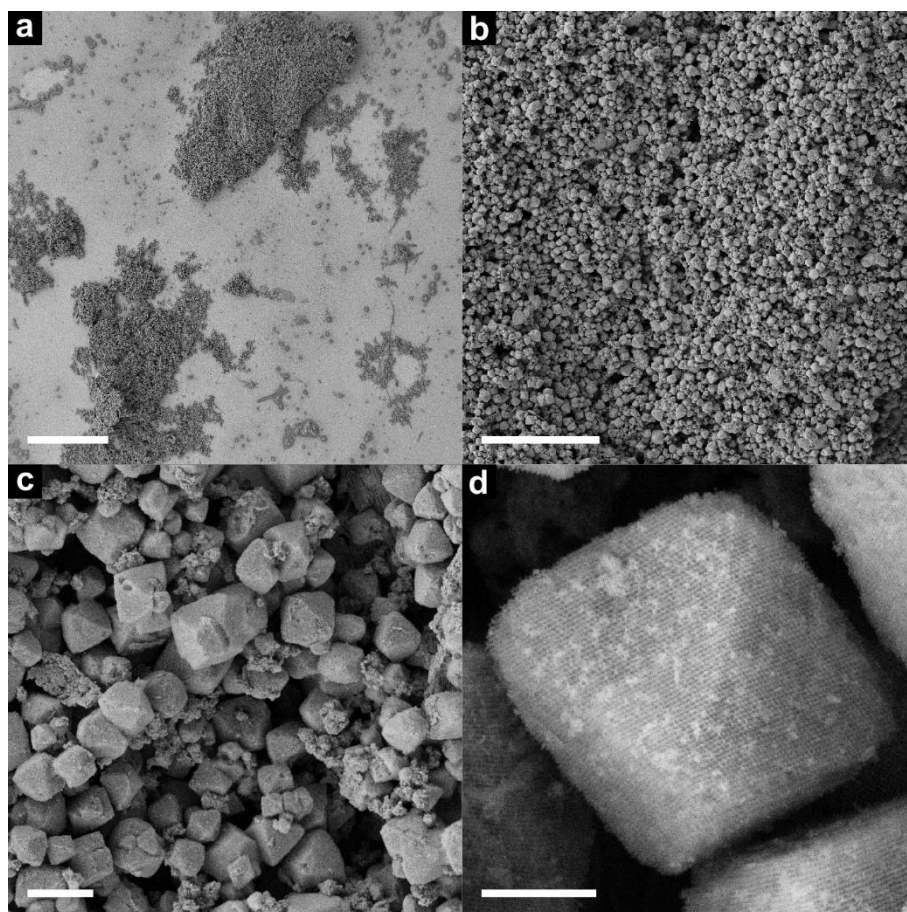


Figure S5-13. SEM images of “3x DNA” electrocatalysis sample of Fig. 5-4c-f after 20 cycles of electrocatalysis at different magnifications. (a) scale bar 500 μm . (b) scale bar 100 μm . (c) scale bar 10 μm . (d) scale bar 2 μm .

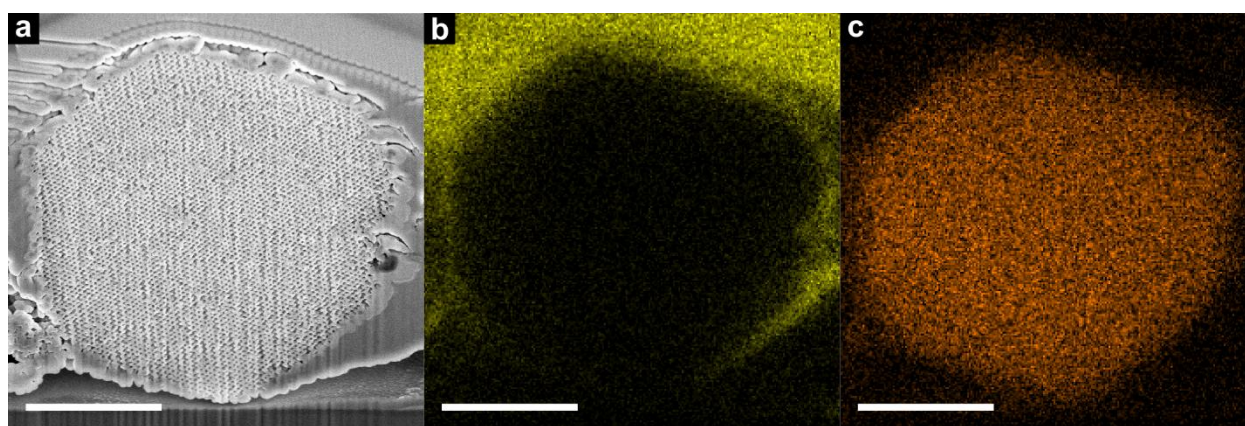


Figure S5-14. Crystal preparation for FIB milling. (a) SEM imaging of cut crystal. (b) Pt EDX signal of (a), depicting the Pt layer that protects the area of interest from gallium ion bombardment. Ion milling of the remaining crystal not covered in Pt yields a cross-section, allowing observation of the inner morphology of the DNA crystal shown in (a). (c) Ti EDX signal of (a), showing the signal of interest inside the DNA crystal. All scale bars 2 μm .

Uncategorized References

- (1) Posnjak, G.; Yin, X.; Butler, P.; Bienek, O.; Dass, M.; Lee, S.; Sharp, I. D.; Liedl, T. Diamond-Lattice Photonic Crystals Assembled from DNA Origami. *Science* **2024**, 384 (6697), 781–785. <https://doi.org/10.1126/science.adl2733>.
- (2) El-Sayed, H. A.; Weiß, A.; Olbrich, L. F.; Putro, G. P.; Gasteiger, H. A. OER Catalyst Stability Investigation Using RDE Technique: A Stability Measure or an Artifact? *J. Electrochem. Soc.* **2019**, 166 (8), F458. <https://doi.org/10.1149/2.0301908jes>.
- (3) Schindelin, J.; Arganda-Carreras, I.; Frise, E.; Kaynig, V.; Longair, M.; Pietzsch, T.; Preibisch, S.; Rueden, C.; Saalfeld, S.; Schmid, B.; Tinevez, J.-Y.; White, D. J.; Hartenstein, V.; Eliceiri, K.; Tomancak, P.; Cardona, A. Fiji: An Open-Source Platform for Biological-Image Analysis. *Nat Methods* **2012**, 9 (7), 676–682. <https://doi.org/10.1038/nmeth.2019>.

CHAPTER 6

Conclusion and Outlook

6. Conclusion

A reduction in iridium content of OER catalysts for PEM electrolysis with stable performance remains a significant challenge for the establishment of this electrolysis technique for the production of green hydrogen.

This thesis demonstrates various strategies for addressing the constraints of PEM catalysts through nanostructuring to synthesize OER catalysts with overall low-iridium density. The stability of the materials may be influenced by varying the crystallization process via the choice of support morphology, support material as well as the oxidation temperature. Optimization of these factors may allow for an extension of the service life of such systems.

In the initial project, a filamentous morphology was introduced and decorated with iridium oxide. The produced catalyst exhibited enhanced activity when subjected to different oxidation temperatures in air, with a temperature optimum identified at 375 °C. TEM data acquisition facilitated the visualization of crystallization processes in ex-situ mode, and additional in-situ data were collected. If the oxidation temperature is too low, the energy supplied is inadequate for the crystallization process, resulting in an amorphous iridium oxide layer that is electrochemically less stable than the crystalline phase. Conversely, a temperature above the optimum leads to the formation of isolated iridium oxide crystallites and reduced conductivity and thus reduced activity. The precise mechanisms underlying crystallization on this substrate remain unclear. However, besides changes of percolation pathways, changes in the tortuosity may also lower the conductivity and thus indirectly the activity of the catalyst. To validate these hypotheses, further mechanistic investigations are required. Overall, the fabrication of this electrocatalyst comprises two key processes: firstly, the scalable production of the SnO₂ substrate through electrospinning, and secondly, the scalable deposition of iridium oxide onto the substrate. This renders the system suitable for potential upscaling and testing in a single-cell electrolyzer. In addition to the component optimization, which is crucial for the application, the conductivity of the catalysts is also of particular importance. With the help of this information, a suitable iridium content can be identified to achieve the most stable and efficient operation of the electrolyzer.

In light of the learnings from the initial project, the second work was designed to address identified shortcomings. The impact of the substrate material itself on the crystallinity of the emerging IrO₂ phase was examined using a less complex nanoparticulate morphology. In this manner, epitaxial growth of IrO₂ on SnO₂ could be achieved, with lattice constants of the two

compounds exhibiting a high degree of similarity as both comprise the rutile structure. This phenomenon could not be observed in the case of anatase TiO_2 , with nanoparticles exhibiting a morphology very similar to that of SnO_2 . In electrochemical laboratory tests under OER conditions, the IrO_2 on SnO_2 epitaxy resulted in enhanced conductivity, activity, and stability at industrially attractive potentials. It was demonstrated that a reduction of the iridium content was feasible through the judicious selection of the substrate material. It is expected that by modifying the reaction conditions, it will be possible to conduct batch production of the catalyst on a larger scale. Furthermore, additional tests, particularly accelerated stress tests and protocols spanning several thousand hours, could be performed to investigate the stability and aging phenomena in an electrolyzer stack.

The final project of this thesis was the implementation of a novel 3D crystalline DNA origami architecture as a catalyst substrate for PEM electrolysis. This new electrocatalyst with diamond topology featuring thin connecting struts was designed by depositing an ultra-thin IrO_2 layer via ALD on the surface of the silicified DNA origami. The catalyst exhibited promising potential for OER catalysis, as evidenced by the proof-of-concept data collected in this project. Further detailed studies are required to validate the acquired data and to further develop this system. It may be beneficial to modify the scaling of the DNA origami architecture and investigate the impact of the pore size to optimize gas transport through the structure upon OER. Similarly, it is conceivable that the framework conductivity could be increased by depositing a TiN layer by ALD between the SiO_2 and IrO_2 layers of the origami. This could potentially enable the deposition of an even thinner IrO_2 layer which would allow for a further lowered precious metal use and make this system attractive for applications. Moreover, mechanistic insights gained from these well-defined porous model systems could also possibly be transferred to more easily scalable porous support systems generated by alternative synthesis strategies.

All of the electrochemical catalysts presented in this thesis are distinguished by an overall low iridium content, straightforward production, and the stability in highly oxidizing environments such as acidic conditions and high potentials. Nevertheless, further studies are necessary to address the long-term stability of epitaxial systems in an electrolyzer, ascertain the structural stability of the fibrous support morphology and to optimize the pore size and scalability of the DNA origami with regard to potential industrial applications.

In conclusion, this thesis presents original and innovative methods for reducing the iridium content of OER catalysts and provides encouraging data for catalysts with a promising potential for industrial application. Novel catalysts were demonstrated to not only withstand the harsh, highly oxidizing environment of PEM electrolyzers but also to exhibit high activity. These findings have the potential to help to advance the field of electrochemical catalysis, promote PEM electrolysis and ultimately boost facilitation of a more sustainable hydrogen production.

CHAPTER 7

Publications and Presentation

7. Publications and Presentations

7.1. Publications

1. Melisande Kost, Matthias Kornherr, Peter Zehetmaier, Hannah Illner, Djung Sue Jeon, Hubert Gasteiger, Markus Döblinger*, Dina Fattakhova-Rohlfing* and Thomas Bein*, Chemical Epitaxy of Iridium Oxide on Tin Oxide Enhances Stability of Supported OER Catalyst, *Small*, **2024**, 351, 989-1002. [\[link\]](#)
2. Arthur Ermatov†, Melisande Kost†, Xin Yin, Paul Butler, Mihir Dass, Ian D. Sharp, Tim Liedl, Thomas Bein*, and Gregor Posnjak*, Fabrication of Functional 3D Nanoarchitectures Using Atomic Layer Deposition on DNA Origami Crystals, *J. Am. Chem. Soc.*, **2025**. [\[link\]](#)
3. Melisande Kost, Jean Felix Dushimineza, Knut Müller-Caspary and Thomas Bein* Optimized Oxidation Temperature Enhances OER Performance of IrO₂-Loaded SnO₂ Nanofibers – Role of Charge Carrier Percolation Pathways, *Accepted*, **2025**.

† These authors contributed equally

7.2. Presentations

Oral presentations

1. Wet-chemical Synthesis of Tin Oxide and Titania Supported Iridium Oxide Nanoparticles with Ultralow Iridium Density as Novel Catalysts for PEM Electrolysis; Materials Research Society (MRS) Spring Meeting, San Francisco 2023, USA.
2. Strategies Towards Low-Ir-Catalysts for PEM Electrolysis: From Support Material and Morphology to Depositing Iridium Oxide; Materials Research Society (MRS) Spring Meeting 2024, Seattle, USA.

Poster presentations

1. Electrospinning of OER Supports and IrO₂ Coating; Kopernikus P2X Tag 2020, Frankfurt, Germany.
2. Development of Electrospun Niobium-Doped Titanium Oxide Supports for OER Catalysis; Kopernikus P2X Tag 2021, Frankfurt, Germany. (Online-Presentation)
3. Nanofibrous Supports for OER Catalysts; Kopernikus P2X Tag 2022, Frankfurt, Germany.
4. Nanosized OER Catalysts and High Surface Area Conductive Oxide Supports; E-Conversion Conference 2022, Venice, Italy.
5. High Stability of SnO₂-Supported Crystalline IrO₂ Rods as Novel OER Catalysts; Center for NanoScience (CeNS)/SFB1032 Retreat Kleinwalsertal 2023, Austria.
6. Sweet Spot in Oxidation Temperature Enhances Conductivity and OER Activity for IrO₂-Coated SnO₂ Nanofibers; Center for NanoScience (CeNS)/e-Conversion Conference 2024, Venice, Italy.
7. Epitaxy Promotes OER Stability of IrO₂-Coated SnO₂ Nanoparticles in PEM Electrolysis; Electrochemical Society (ECS) PRiME Meeting 2024, Honolulu, USA.

CHAPTER 8

Curriculum Vitae

8. Curriculum Vitae